

ACTA DE EVALUACIÓN DE LA TESIS DOCTORAL
(FOR EVALUATION OF THE ACT DOCTORAL THESIS)

Año académico (academic year): 2018/19

DOCTORANDO (candidate PHD): **JIMÉNEZ RODRÍGUEZ, MARCO**
D.N.I./PASAPORTE (Id.Passport): ******9858M**
PROGRAMA DE DOCTORADO (Academic Committee of the Programme): **D441-ELECTRÓNICA: SISTEMAS ELECTRÓNICAS AVANZADOS. SISTEMAS INTELIGENTES**
DPTO. COORDINADOR DEL PROGRAMA (Department): **ELECTRÓNICA**
TITULACIÓN DE DOCTOR EN (Phd title): **DOCTOR/A POR LA UNIVERSIDAD DE ALCALÁ**

En el día de hoy 12/11/18, reunido el tribunal de evaluación, constituido por los miembros que suscriben el presente Acta, el aspirante defendió su Tesis Doctoral **con Mención Internacional** (In today assessment met the court, consisting of the members who signed this Act, the candidate defended his doctoral thesis with mention as International Doctorate), elaborada bajo la dirección de (prepared under the direction of) **FERNANDO BERNABÉ NARANJO VEGA // MIGUEL GONZÁLEZ HERRÁEZ**.

Sobre el siguiente tema (Title of the doctoral thesis): **DEVELOPMENT OF PASSIVE ULTRAFAST FIBER LASERS AT TELECOM WAVELENGTHS USING INDIUM NITRIDE AS SATURABLE ABSORBER**

Finalizada la defensa y discusión de la tesis, el tribunal acordó otorgar la CALIFICACIÓN GLOBAL¹ de **(no apto, aprobado, notable y sobresaliente)** (After the defense and defense of the thesis, the court agreed to grant the GLOBAL RATING (fail, pass, good and excellent): **SOBRESALIENTE**

Alcalá de Henares, a 12 de NOVIEMBRE de 2018


Fdo. (Signed): JUAN D. ANIA


Fdo. (Signed): CÉSAR TAUREGUI


Fdo. (Signed): OSCAR ESTEBAN

FIRMA DEL ALUMNO (candidate's signature),

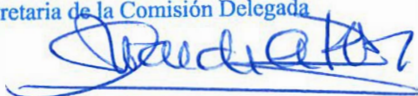


Fdo. (Signed): MARCO JIMÉNEZ

Con fecha 19 de noviembre de 2018 la Comisión Delegada de la Comisión de Estudios Oficiales de Posgrado, a la vista de los votos emitidos de manera anónima por el tribunal que ha juzgado la tesis, resuelve:

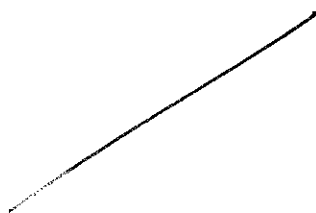
- ☒ Conceder la Mención de "Cum Laude"
☐ No conceder la Mención de "Cum Laude"

La Secretaria de la Comisión Delegada



¹ La calificación podrá ser "no apto" "aprobado" "notable" y "sobresaliente". El tribunal podrá otorgar la mención de "cum laude" si la calificación global es de sobresaliente y se emite en tal sentido el voto secreto positivo por unanimidad. (The grade may be "fail" "pass" "good" or "excellent". The panel may confer the distinction of "cum laude" if the overall grade is "Excellent" and has been awarded unanimously as such after secret voting.).

INCIDENCIAS / OBSERVACIONES:
(Incidents / Comments)





Universidad
de Alcalá

COMISIÓN DE ESTUDIOS OFICIALES
DE POSGRADO Y DOCTORADO

En aplicación del art. 14.7 del RD. 99/2011 y el art. 14 del Reglamento de Elaboración, Autorización y Defensa de la Tesis Doctoral, la Comisión Delegada de la Comisión de Estudios Oficiales de Posgrado y Doctorado, en sesión pública de fecha 19 de noviembre, procedió al escrutinio de los votos emitidos por los miembros del tribunal de la tesis defendida por *JIMÉNEZ RODRÍGUEZ, MARCO*, el día 12 de noviembre 2018, titulada *DEVELOPMENT OF PASSIVE ULTRAFAST FIBER LASERS AT TELECOM WAVELENGTHS USING INDIUM NITRIDE AS SATURABLE ABSORBER*, para determinar, si a la misma, se le concede la mención "cum laude", arrojando como resultado el voto favorable de todos los miembros del tribunal.

Por lo tanto, la Comisión de Estudios Oficiales de Posgrado **resuelve otorgar** a dicha tesis la

MENCIÓN "CUM LAUDE"

Alcalá de Henares, 20 de noviembre de 2018
EL VICERRECTOR DE INVESTIGACIÓN Y TRANSFERENCIA



F. Javier de la Mata de la Mata

Copia por e-mail a:

Doctorando: JIMÉNEZ RODRÍGUEZ, MARCO

Secretario del Tribunal:

Directores de Tesis: FERNANDO BERNABÉ NARANJO // VEGA MIGUEL GONZÁLEZ HERRÁEZ



Universidad
de Alcalá

ESCUELA DE DOCTORADO
Servicio de Estudios Oficiales de
Posgrado

DILIGENCIA DE DEPÓSITO DE TESIS.

Comprobado que el expediente académico de D./D^a _____
reúne los requisitos exigidos para la presentación de la Tesis, de acuerdo a la normativa vigente, y habiendo
presentado la misma en formato: ☐ soporte electrónico ☐ impreso en papel, para el depósito de la
misma, en el Servicio de Estudios Oficiales de Posgrado, con el nº de páginas: _____ se procede, con
fecha de hoy a registrar el depósito de la tesis.

Alcalá de Henares a _____ de _____ de 20____



Fdo. El Funcionario



Programa de doctorado en Electrónica:

Sistemas Electrónicos Avanzados. Sistemas Inteligentes

DEVELOPMENT OF PASSIVE ULTRAFAST FIBER
LASERS AT TELECOM WAVELENGTHS USING
INDIUM NITRIDE AS SATURABLE ABSORBER

Tesis doctoral presentada por

MARCO JIMÉNEZ RODRÍGUEZ

Directores

Dr. Fernando B. Naranjo Vega

Dr. Miguel González Herráez

2018

Either write something worth reading

or do something worth writing

Benjamin Franklin (1706-1790)

Do not be afraid

and get InN!

Dr. Fernando Bernabé Naranjo Vega, Profesor Titular de la Universidad de Alcalá.

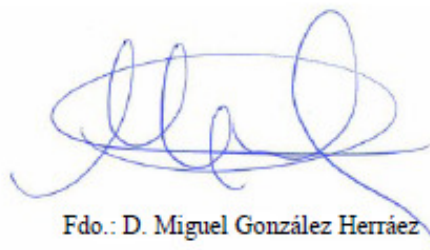
Dr. Miguel González Herráez, Catedrático de la Universidad de Alcalá.

INFORMAN que la Tesis Doctoral titulada "*Development of Passive Ultrafast Fiber Lasers at Telecom Wavelengths using Indium Nitride as Saturable Absorber*", presentada por D. Marco Jiménez Rodríguez, bajo la dirección del Dr. Fernando Bernabé Naranjo Vega y del Dr. Miguel González Herráez, dentro del campo de Tecnología Electrónica, reúne los méritos de calidad y originalidad para optar al Grado de Doctor.

Para que así conste y surta los efectos oportunos, se firma el presente informe en Alcalá de Henares a 22 de 06 de 2018



Fdo.: D. Fernando B. Naranjo Vega



Fdo.: D. Miguel González Herráez



Dr. Miguel González Herráez, Coordinador de la Comisión Académica del Programa de Doctorado en Electrónica: Sistemas Electrónicos Avanzados. Sistemas Inteligentes.

INFORMA que la Tesis Doctoral titulada "*Development of Passive Ultrafast Fiber Lasers at Telecom Wavelengths using Indium Nitride as Saturable Absorber*", presentada por D. Marco Jiménez Rodríguez, bajo la dirección del Dr. Fernando Bernabé Naranjo Vega y del Dr. Miguel González Herráez, reúne los requisitos científicos de originalidad y rigor metodológicos para ser defendida ante un tribunal. Esta Comisión ha tenido también en cuenta la evaluación positiva anual del doctorando, habiendo obtenido las correspondientes competencias establecidas en el Programa.

Para que así conste y surta los efectos oportunos, se firma el presente informe en Alcalá de Henares a 22 de junio de 2018

Fdo.:

Agradecimientos

Hay mucha gente que agradecer en esta gran aventura, desde que comenzara tras aquella entrevista por junio de 2013 cuando conocí a los doctores Miguel González Herráez y Fernando B. Naranjo (uno de esos días en los que vestir camisa de manga larga). Gracias a ellos pude embarcarme en este maravilloso proyecto profesional y personal de más de cuatro años. Os estaré eternamente agradecido por todo lo que me habéis enseñado, por hacerme parte de esta gran familia y por vuestra honestidad. De todos y cada uno de mis compañeros, pero muy especialmente de vosotros dos he aprendido muchísimo, he crecido día a día, me he formado, he reído, sufrido, pero, sobre todo, he disfrutado.

Quisiera agradecer a la Dra. Eva Monroy por todo lo relacionado con el tiempo tan maravilloso que pasé en Grenoble (Francia) y por todas sus correcciones y sugerencias en cada uno de los artículos. Gracias a ella esta tesis es un poco mejor.

Me gustaría también agradecer especialmente a los Dres. Óscar Esteban y Sonia Martín, por tantos buenos consejos, y por ayudarme a lidiar con los jefes de la mejor manera posible: con humor.

A los Dres. Juan Diego Ania, Pedro Corredera y a Francesca Gallazzi les agradezco por su colaboración en este proyecto y por las discusiones varias.

Llegados a este punto, se me vienen a la mente decenas de historias y momentos con mis compañeros GRIFO, así que intentaré no olvidar a ninguno (¡habéis sido tantos!). Todos han sido muy importantes para mí. Gracias a Laura y Arantxa (¡ya Dras., pero en la amistad os tuteo!) por enseñarme infinidad de cosas desde mi llegada, por soportarme tantos años y hasta reiros conmigo. Habéis hecho que cada día fuera mucho más fácil. A Alejandro y a Juan, por vuestra amistad y

tomaros siempre la vida con humor. A todos vosotros, os he echado mucho de menos desde que os fuisteis. Por supuesto, gracias a los que seguimos dando el callo cada día para mantener el GRIFO a flote. A Piedad, gracias por esta gran amistad inesperada. A Andrés, por tu (a veces hasta peculiar) adictiva forma de ser y tu buen sentido del humor. A Javier N. y Rosario, por vuestra honestidad y compartir vuestra sabiduría. A Hugo, por traer otros idiomas al grupo (Laura, Alejandro y Rosario, un poco vosotros también en esta parte...) y por integrarte tan bien en nuestras tonterías y costumbres. A Regina y Luis, por traer alegría y futuro al grupo. A Laura (Monroy), por convertir mi aburrida etapa de escritura final en algo mucho más ameno. A todos los demás GRIFO y *former* GRIFO que, aunque no hayamos podido compartir tantos momentos, también os tengo un aprecio especial: Alexia, Xabi, Javier (Tejedor), Paco, Ana, Sirona, Rodrigo, Pablo, Alberto. Os quiero dedicar un abrazo muy especial a todos vosotros.

Quiero agradecer a mis amigos Laura, Miguel, Inés y Susel, por ayudarme a afrontar el día a día con una sonrisa y por superar ese gran tópico de convertir compañeros de trabajo en grandes amigos. También a mis compañeros GEISER Javier M. y Javier S. por ayudar a traer la diversión después de la calma.

No puedo dejar de agradecer a Lorena por aguantarme tantos años. Querría agradecerle por infinidad de cosas, y no se me ocurriría por dónde empezar. En el fondo, tú me conoces perfectamente, y sabes todo lo que has hecho por mí. No sería quien soy y no habría podido llegar hasta aquí sin tu ayuda, sin que me enseñaras a terminar lo que empecé, sin que me apoyaras y me alegraras en tantos días difíciles y estuvieras conmigo haciendo todos los días fáciles. Gracias por todo. Te quiero. Desde siempre.

A mis padres, por quererme, por hacerme tal y como soy, y por siempre haberme enseñado a perseguir mis sueños y hacer lo que me gusta. Por enseñarme a esforzarme por el camino. Muy especialmente a mi madre, por haberse desvivido tanto por mi hermano como por mí. Nos has enseñado lo que es el amor (a veces,

hasta demasiado). Eso me lleva a pensar en mi hermano, una persona maravillosa. En el fondo, la única que se, espero, y deseo con todas mis fuerzas que siempre va a estar ahí, en todo momento, aunque no estemos cerca. Aunque no nos veamos ni hablemos todos los días. Por supuesto, nadie puede ser tan bueno sin alguien capaz de aguantar su sombra, y a la vez de brillar con su luz. Por todo ello, Noe, quiero que sepas que eres como una hermana para mí. Os quiero.

Gracias a todos los que he nombrado, pero también a los que me han faltado por nombrar. Gracias a mi familia y al resto de amigos. Gracias a ti, lector, por adentrarte en este trabajo, que es el fruto de tantos años y horas de esfuerzo y sacrificio. Permíteme advertirte que a partir de aquí ya empieza lo serio. Espero no decepcionarte.

Marco Jiménez Rodríguez

Abstract

This thesis focuses on the research of new technologies for fabrication of passive ultrafast mode-locked fiber lasers, operating at telecom wavelengths (C-band, 1.53-1.57 μm). For this purpose, novel semiconductor saturable absorbers are proposed, namely InN bulk thin layers and multiple InN/InGaN quantum wells (MQWs). All the structures have been growth by molecular beam epitaxy, on a commercial GaN-on-sapphire substrate. The use of III-nitrides is justified because of their unique properties such as direct band gap energies, high thermal and chemical stability, and high radiation hardness.

The saturable absorbers have been studied in detail. Their morphological and structural properties have been introduced. A complete study of the optical properties has been carried out. From the linear optical measurements, the bulk samples have proved to be resonant at telecom wavelengths, with band gap energies around 0.8 eV (1.55 μm). Through the performed nonlinear characterization, it has been found that the bulk structures exhibit huge nonlinear effects, with modulation depths higher than 30 %, but also high saturation fluences, larger than 200 $\mu\text{J}/\text{cm}^2$. In addition, it has been demonstrated that the InN-based saturable absorbers can support over 100 mJ/cm^2 , with no sign of apparent optical damage, converting them in promising devices for very high-energy applications. Furthermore, an InN-based semiconductor saturable absorber mirror has been implemented, by depositing a thin layer of Al on one of the bulk InN devices. This procedure should introduce benefits such as increase

of the absorption region and larger effective thickness. The MQW have not demonstrated to be efficient enough saturable absorber devices.

Placing the proposed bulk InN-based saturable absorbers within a fiber resonator that uses an Er-doped fiber amplifier as gain medium, it has been possible to achieve passively mode-locked lasers. The lasers delivered ultrashort pulses with time widths as short as 220-250 fs, with a repetition rate close to 5 MHz. Using the devices in transmission configuration, pulses with a peak power up to 26.5 kW and pulse energy up to 5.8 nJ have been achieved. Using the device in reflection, these values have been increased up to 42 kW and 10 nJ. For a good comparison between the developed lasers, in all the analyzed cases the gain medium used has been the same. Moreover, the use of InN-based saturable absorbers makes the laser polarization independent. All the demonstrated lasers have proved self-starting operation and have been designed as dispersion managed cavities.

With all the experiments that have been carried out in this thesis, we have demonstrated that InN-based structures are promising saturable absorbers for application in the development of ultrafast lasers, operating at telecom wavelengths.

Resumen

Esta tesis doctoral se centra en la investigación de nuevas tecnologías para la fabricación de láseres ultrarrápidos de fibra óptica anclados en modos (*mode-locked*), con emisión a la longitud de onda de las telecomunicaciones (Banda-C, 1.53-1.57 μm). Para ello, se proponen los siguientes absorbentes saturables: InN en estado masivo (*bulk*) y pozos cuánticos de InN/InGaN. Todos los dispositivos han sido depositados sobre el mismo sustrato comercial (zafiro con GaN como capa amortiguadora) mediante la técnica de epitaxia de haces moleculares. Ciertas propiedades de los nitruros del grupo III los hace ideales para esta aplicación: su energía prohibida (*band gap energy*) es directa, tienen alta estabilidad térmica y química y poseen una gran resistencia frente a la radiación.

A lo largo de esta tesis se ha realizado un estudio en profundidad de los absorbentes saturables. Por un lado, comenzaremos viendo desde un punto de vista formal sus propiedades morfológicas y estructurales. Por otro lado, se ha llevado a cabo una completa caracterización de las propiedades ópticas de estos materiales, entre las que se han realizado medidas de óptica lineal, a partir de las cuales se ha estimado una energía prohibida de 0.8 eV (1.55 μm) para las muestras *bulk*. En relación a la caracterización óptica no lineal de las estructuras, se ha conseguido demostrar que estos materiales poseen un comportamiento muy no lineal, llegando a mostrar profundidades de modulación que superan el 30 %, pero también altas fluencias de saturación, por encima de los 200 $\mu\text{J}/\text{cm}^2$. Sin embargo, todas las estructuras estudiadas han demostrado que pueden ser bombeadas con hasta 100 mJ/cm^2 , sin llegar a mostrar indicios de daño óptico. Con lo cual, podría

tratarse de dispositivos muy prometedores para aplicaciones a altas energías. También se ha desarrollado y caracterizado un espejo de absorción saturada basado en semiconductor, depositando para ello una capa de Al sobre una de las muestras de InN *bulk*. Este nuevo dispositivo debería aportar al sistema beneficios adicionales como por ejemplo mayor longitud neta de absorción y una mayor longitud de la capa efectiva. En relación a los pozos cuánticos, los resultados no han sido concluyentes, ya que su respuesta no lineal no ha demostrado ser tan elevada como en el caso de las muestras de InN masivo, y, por lo tanto, se debe asumir que dichos dispositivos no son tan eficientes.

Se ha conseguido anclar en modos un láser de fibra óptica, utilizando para ello un amplificador de fibra dopada con Erbio como medio de ganancia e introduciendo el absorbente saturable en el seno del resonador. Los resultados obtenidos son prometedores, puesto que los láseres emiten pulsos ultracortos, cuya duración temporal es de 220-250 fs, con una tasa de repetición aproximada de 5 MHz. Utilizando los absorbentes saturables en transmisión, se ha obtenido una potencia de pico de hasta 26.5 kW y una energía por pulso de 5.8 nJ. Estos valores aumentan en el caso del absorbente saturable en reflexión, obteniendo hasta 42 kW y 10 nJ. Se ha utilizado el mismo medio de ganancia en todos los láseres desarrollados, para poder comparar correctamente los resultados obtenidos. Además, el hecho de introducir estos dispositivos basados en InN, hace que los láseres muestren independencia de la polarización. Todos los láseres estudiados tienen un arranque automático (*self-starting*), y sus cavidades han sido diseñadas según la técnica de *dispersion management*.

Los experimentos realizados a lo largo de esta tesis sitúan al InN como un material muy prometedor para su aplicación en el diseño de láseres ultrarrápidos con emisión en la longitud de onda de las telecomunicaciones.

Contents

Chapter 1	Introduction.....	1
1.1	Motivations.....	1
1.1.1	Highlights of passive ultrafast fiber lasers at telecom wavelengths	2
1.1.2	Why indium nitride as saturable absorber?	3
1.2	Aim of this Thesis.....	5
1.3	Brief description of this Thesis.....	6
Chapter 2	Introduction to III-Nitrides Semiconductors	9
2.1	General introduction to III-nitrides.....	9
2.1.1	Structural properties.....	10
2.1.2	Polarization in III-nitrides	12
2.1.3	Linear optical properties.....	17
2.1.4	Nonlinear optical properties.....	19
2.2	Growth of III-nitrides.....	22
2.2.1	Plasma-Assisted Molecular Beam Epitaxy.....	22
2.2.2	Sputtering.....	25
Chapter 3	Optical Effects in Materials	29
3.1	Introduction to light properties.....	29
3.1.1	Maxwell equations	29

3.1.2	Propagation of light.....	31
3.2	Linear optical effects in semiconductors	42
3.2.1	Complex refractive index.....	43
3.2.2	Absorbance, transmittance and reflectance.....	45
3.2.3	Optical transitions	45
3.3	Nonlinear optical effects in semiconductors.....	49
3.3.1	Second-order nonlinear optical effects.....	51
3.3.2	Third-order nonlinear optical effects.....	52
Chapter 4	Ultrafast Fiber Lasers	61
4.1	Introduction to silica optical fibers.....	63
4.1.1	Single-mode fiber	64
4.1.2	Erbium-doped fiber amplifiers	64
4.2	Light propagation in optical fibers	66
4.2.1	The Nonlinear Schrödinger Equation (NLSE)	67
4.2.2	Linear effects in optical fibers.....	69
4.2.3	Nonlinear effects in optical fibers.....	71
4.2.4	Introduction to solitons	77
4.3	Ultrafast fiber lasers.....	82
4.3.1	Passively mode-locked fiber lasers	84
4.3.2	State of the art	89
Chapter 5	Experimental Methods.....	93
5.1	Semiconductor characterization methods	93
5.1.1	Structural characterization	93

5.1.2	Optical characterization methods	95
5.2	Characterization methods of pulsed laser sources.....	106
5.2.1	Basic laser concepts	107
5.2.2	Autocorrelation.....	108
5.2.3	Laser spectra measurements	111
5.2.4	ESA and oscilloscope measurements.....	112
Chapter 6	Characterization of InN-Based Saturable Absorbers.....	115
6.1	Study of the InN-based samples: structure and growth details	115
6.2	Structural characterization.....	117
6.3	Optical characterization	120
6.3.1	Linear optical properties.....	120
6.3.2	Nonlinear optical properties.....	124
6.4	Conclusions	131
Chapter 7	Ultrafast Fiber Lasers using InN as Saturable Absorber in Transmission	135
7.1	InN-based ultrafast fiber lasers.....	135
7.1.1	Ultrafast fiber laser using bulk InN-based saturable absorber without buffer.....	138
7.1.2	Ultrafast fiber laser using bulk InN-based saturable absorber with buffer layer	145
7.2	Discussion.....	148
7.2.1	Principle of operation	148
7.2.2	Comparison with other ultrafast fiber lasers.....	151

7.3	Conclusions	152
Chapter 8	Ultrafast Mode-Locked Fiber Laser using InN-Based Semiconductor Saturable Absorber Mirror	155
8.1	SESAM fabrication and characterization	155
8.2	Ultrafast fiber laser using InN-based SESAM	159
8.2.1	Laser characterization using 90/10 fiber coupler	161
8.2.2	Laser characterization using 70/30 fiber coupler	164
8.2.3	Laser characterization using 50/50 fiber coupler	166
8.3	Ultrafast laser using commercial SESAM	168
8.4	Discussion	172
8.5	Conclusions	175
Chapter 9	General Conclusions and Future Work	177
9.1	General conclusions	177
9.1.1	InN-based saturable absorbers	177
9.1.2	InN-based ultrafast fiber lasers	179
9.2	Future work	183
9.2.1	Saturable absorbers	183
9.2.2	Ultrafast fiber laser design	184
	List of Publications	187
	Bibliography	191

List of Figures

Fig. 1.1: Band gap given in energy and wavelength as a function of the lattice constant for different semiconductor family groups. [WBCF12]	4
Fig. 2.1: Different crystalline structures of the III-nitrides: (a) wurtzite (α -phase), (b) zinc-blende (β -phase) and (c) rocksalt (γ -phase). [Hana09]	11
Fig. 2.2: Atomic structure of III-nitrides wurtzite represented by (a) its primitive cell [Münc09] and (b) the stacking sequence (aBbA...) along the [0001] axis. [Hana09]	12
Fig. 2.3: Representation of the different spontaneous polarization on wurtzite III-nitrides with (a) metal-polarity and (b) N-polarity. [Mont15]	13
Fig. 2.4: Representation of the conduction and valence bands of wurtzite InN near the Γ point. [Wu09]	18
Fig. 2.5: Scheme of typical PAMBE chamber for III-nitrides growth. [Laho09]	23
Fig. 2.6: Types of MBE growth, where Θ is the degree of coverage. (a) Frank-Van der Merwe; (b) Volmer-Weber; (c) Stranski-Krastanov. [Kais00]	24
Fig. 2.7: Sputtering system used in this work placed in the GRIFO facilities at the University of Alcala. The figure shows the gas bottle and the installation (right).....	26
Fig. 2.8: Scheme of the bombardment process of the target in a typical sputtering system for Ar plasma generation. [PFSG14].....	27

Fig. 3.1: Representation of the propagation of a harmonic electromagnetic wave. [Hech02].....	32
Fig. 3.2: Normalized simulated 50-fs Gaussian pulse centered at 1550 nm neglecting the phase, showing the electric field, $\hat{E}(t)$, with blue line, the amplitude, $\bar{E}_0(t)$, by black line, and the temporal optical intensity, $I(t)$, with red line.....	33
Fig. 3.3: Comparison of a 1-ps FWHM pulse following a Gaussian shape function (black line) and sech^2 shape function (red line).	35
Fig. 3.4: 20-fs Gaussian pulse, centered at 1550 nm showing: (a) Electric field, with $\varphi_0 = 0$ (blue line) and $\varphi_0 = \pi$ (red line). For the case of $\varphi_0 = 0$: (b) Temporal optical intensity (blue line) and phase (red dashed line), (c) Optical spectrum versus frequency. (d) Optical spectrum versus wavelength.....	37
Fig. 3.5: 20-fs Gaussian pulse, centered at 1550 nm with linear phase ($\varphi_1 = 30\text{rad} / \text{fs}$) showing: (a) Electric field. (b) Temporal optical intensity (blue line) and phase (red dashed line). (c) optical spectrum versus frequency. (d) Optical spectrum versus wavelength.....	38
Fig. 3.6: 20-fs Gaussian pulse, centered at 1550 nm with quadratic phase ($\varphi_2 = -300\text{rad} / \text{fs}^2$), or positive (up) chirp exhibiting: (a) Electric field. (b) Temporal optical intensity (blue line) and phase (red dashed line). (c) optical spectrum versus frequency. (d) Optical spectrum versus wavelength.	39
Fig. 3.7: 20-fs Gaussian pulse, centered at 1550 nm with quadratic phase ($\varphi_2 = 300\text{rad} / \text{fs}^2$), or negative (down) chirp exhibiting: (a) Electric field. (b) Temporal optical intensity (blue line) and phase (red dashed line). (c) optical spectrum versus frequency. (d) Optical spectrum versus wavelength.	40
Fig. 3.8: Photon absorption from a semiconductor. [BaTe91].....	46

Fig. 3.9: Non-radiative transitions: (a) Intra-band and (b) inter-band. [BaTe91]	47
Fig. 3.10: Radiative transitions in semiconductors presenting: (a) Spontaneous emission and (b) stimulated emission. [BaTe91]	48
Fig. 3.11: Normalized to arbitrary unit intensity (blue line) and change of instantaneous frequency (red line) of an initially unchirped 20-fs pulse propagating through Kerr media.	56
Fig. 3.12: Illustration of self-acting effects derived from Kerr effect (a) Self-focusing; (b) Self-trapping of light; (c) Laser beam break-up. [Boyd08]	57
Fig. 3.13: Nonlinear absorptive processes in direct band gap semiconductors: (a) Saturable absorption effect. (b) Two-photon absorption. [Vald11]	59
Fig. 4.1: (a) (Up) Illustration of an optical fiber cross-section showing the core, the cladding and the jacket. (Down) Qualitative refractive index profile of each of the parts. (b) Loss spectrum of single-mode silica fiber, where dashed line represents the losses from Rayleigh scattering. [Agra01]	63
Fig. 4.2: (a) The three-level energy diagram for Er-doped silica fiber showing the 980 nm and 1480 nm pump bands, and the 1500-1600 nm emission. (b) Amplified spontaneous emission (ASE) spectrum of the EDFA used in this thesis.	65
Fig. 4.3: Temporal broadening induced by the chromatic dispersion for Gaussian pulses. [Agra01]	71
Fig. 4.4: Illustration of SPM effect giving from up to down the incident electrical field and its normalized intensity, the change induced by the material to the refractive index and the phase change. [Gonz04],[Mart06]	73
Fig. 4.5: Simulation of spectral broadening induced by SPM effect of a 200-fs Gaussian pulse propagating through 15-m long SMF. $\gamma \approx 0.8W^{-1}km^{-1}$, $P_0 \approx 1kW$	74

Fig. 4.6: Pulse spectrum variation as a result of the modulation instability effect as a function of: (a) dispersion and (b) pump power. [Mart06].....	76
Fig. 4.7: Temporal evolution of the third-order soliton over one soliton period. [Agra01]	79
Fig. 4.8: Experimental measured spectra for increasing powers (from down to up) of a 475-fs pulse propagating through 52-m-long optical fiber. [MiMo86] ...	81
Fig. 4.9: 1-mW average power laser emission centered at 1.55 μm with 10 MHz repetition rate showing the optical intensity (a) and optical spectrum (b) for continuous wave operation. Same laser in mode-locking operation regime, delivering 100-fs pulses, showing the optical intensity (c) and optical spectrum (d).	83
Fig. 4.10: Typical evolution of gain (black line) and losses (red line) in a passive mode-locked laser. The laser only deliver pulses when the losses are reduced under the gain level, denote by the intensity, $I(t)$ (blue line). [Kell03].....	85
Fig. 4.11: Saturable absorber in reflection characterization curve showing its relevant parameters. [Kell03]	87
Fig. 4.12: First ultrafast fiber lasers developed: (a) Figure-of-8 laser configuration [Duli91b]; (b) NPR-based laser configuration [TaHI92].	89
Fig. 5.1: (a) Representation of AFM experimental setup. (b) Different AFM measurement modes. [Núñez17]	94
Fig. 5.2: Experimental setup for linear optical transmittance measurements with normal incidence of light onto the sample.	95
Fig. 5.3: Simulations of z-scan measurements in: (a) open aperture (OA) (with $S = 1$) and (b) closed aperture (CA) (with $S = 0.2$). Material properties: $L_{\text{eff}} = 500\mu\text{m}$, $\alpha_2 = -1000\text{cm} / \text{GW}$, $n_2 = 5 \cdot 10^{-2}\text{cm}^2 / \text{GW}$	100
Fig. 5.4: Z-scan experimental setup using a 1.5 μm fiber laser as pumping source and Ge-photodetector as light collector.	101

Fig. 5.5: Setup for SESAM characterization comparing reflectivity of the measured device to a known HR-mirror. Using a beam splitter (BS) and a chopper, it is possible to separate in time the four possible states generated between the two branches of the BS.....	103
Fig. 5.6: Measurement of a HR-mirror after calibration with linear fitting and an InGaAs SESAM, with fit to equation (5.9), represented with blue line, and neglecting the induced absorption, represented with green line. [MRBI08]	104
Fig. 5.7: Pump and probe setup configured for transmittance measurements. [Vald11]. PBS: Polarized Beam Splitter	105
Fig. 5.8: Scheme of an ultrafast fiber laser characterization setup from the laser output of a fiber laser. Two fiber couplers are placed in cascade, allowing to send a small signal to the power meter and the OSA.	106
Fig. 5.9: Basic laser concepts schematically explained such as average and peak power, pulse energy, pulse width, pulse energy and repetition rate.	108
Fig. 5.10: Standard autocorrelation setup with second harmonic generation (SHG) from two identical pulses introducing a delay to one of the pulses. [Treb12]	109
Fig. 5.11: Typical autocorrelator trace (black line) with Gaussian fitting (blue triangles) for InN-based ultrafast fiber laser used in this thesis.....	110
Fig. 5.12: Typical linear (black line) and logarithmic (green line) spectrum from InN-based ultrafast fiber laser used in this thesis, with Gaussian fit (red dashed line). [JMMG17]	111
Fig. 5.13: Train of pulses of ultrafast fiber laser presenting: ESA (a) and oscilloscope (b) measurements.	112
Fig. 6.1: Scheme of the InN-based structures as saturable absorbers, presenting (a) Bulk InN layer without buffer (S1), (b) Bulk InN with MQW buffer layer	

between substrate and InN (S2), and (c) 41xMQWs heterostructures (S3, S4, S5).	117
Fig. 6.2: 2x2 μm^2 AFM images of InN-based structures, corresponding to (a) S1; (b) S2; (c) S3; (d) S4; (e) S5. [Vald11].....	118
Fig. 6.3: HRXRD measurements (black line) of bulk InN without buffer (S1) and MQWs heterostructures (S3, S4, S5). Best fit to experimental data obtained by theoretical calculations (orange line) is presented for each case. The measurements have been shifted upwards for clarity. [Vald11], [NKVC11].....	119
Fig. 6.4: Dark field TEM picture ($g=0002$) of: (a) Bulk InN with buffer layer (S2), and (b) the $\text{In}_{0.9}\text{Ga}_{0.1}\text{N}$ MQW sample (S3). [VRNR12].....	119
Fig. 6.5: Optical spectra comparison of the five InN-based structures proposed as SA (S1-S5).	121
Fig. 6.6: Representations of $(\alpha E)^2$ versus E for Tauc's fit, to estimate the optical bandgap of bulk InN-based SA without buffer, S1 (black line with dashed fit curve), and bulk InN SA with buffer layer, S2 (blue line with dotted fit curve). [JMMG17],[JMMG18].....	122
Fig. 6.7: Low temperature PL emission spectra of: (a) Samples S1 (red) and S2 (cyan). (b) Samples S1, S3 and S4. No PL was observed for S5. Inset shows the estimated recombination energies as a function of the In content for the cases of fully relaxed structure (hollow squares) and fully strained on InN (filled squares). Filled red circles are the experimental PL peak energies. [NKVC11].....	123
Fig. 6.8: Relaxation curve measured by pump and probe technique for S2 and S3 samples. [VRNR12].....	125
Fig. 6.9: Z-scan experimental data points of 325 μm -thick commercial silicon substrate, using the setup described in Chapter 5. Solid red line corresponds to fitting curve.	126

Fig. 6.10: Z-scan analysis of the InN bulk structures. S1 is represented by red circles, and S2 by blue triangles. Solid lines correspond to the fittings. Black crosses correspond to measurements of the substrate alone.....	127
Fig. 6.11: Comparison of the z-scan measurements of the MQW heterostructures. Magenta squares represent S3. Orange diamonds represent S4. Green stars S5. Solid lines correspond to the fittings. Black crosses correspond to measurements of the substrate alone.	128
Fig. 6.12: Z-scan measurements at different incident peak intensities for S2.	129
Fig. 6.13: Representation of the transmittance as a function of the fluence impinged to the materials for saturable absorption characterization. S1 represented by red circles, S2 by blue triangles, S3 by magenta squares, S4 by orange diamonds and S5 by green stars. Fitting is represented for each sample.	130
Fig. 7.1: Scheme of the C-band ultrafast mode-locked fiber laser using InN bulk as saturable absorber. [JMMG17]	136
Fig. 7.2: Electrical spectrum of the bulk InN-based SA without buffer ultrafast laser cavity at ML operation. [JMMG18]	137
Fig. 7.3: For the minimum attenuation in the cavity: (a) Autocorrelator trace with a temporal duration of 252 fs; (b) Typical laser spectrum, centered at 1562 nm, with a FWHM of 16 nm. [JMMG17].....	138
Fig. 7.4: Characterization of the ultrafast fiber laser using S1 as SA. (a) Variation of the peak power as a function of the average output power, showing the different laser operation regimes. The normalized linear spectra, centered at 1.56 μm with a span of 100 nm, are shown for each regime. (b) Time-Bandwidth Product as a function of the ring average power. The solid line represents the sech^2 limit. [JMMG17]	139

Fig. 7.5: Laser stability for different cavity lengths (from the standard configuration to +200 m of additional fiber): (a) Autocorrelator traces (vertically shifted for clarity), (b) normalized optical spectra (vertically shifted for clarity), and (c) Normalized electrical spectra. [JMMG17].....141

Fig. 7.6: Electrical spectrum of the laser output when inserting (a) 2.3 km of additional fiber, and (b) 1.1 km of additional fiber.143

Fig. 7.7: Ultrafast mode-locked fiber oscillator using InN saturable absorber with output fiber gain: (a) spectra, and (b) autocorrelator traces for different amplification values, operating close to the oscillator threshold, with master oscillator output average power of 5.5 mW. The legend indicates the average output power in each case. The green line corresponds to the case of minimum attenuation in the oscillator, i.e. far from the threshold, with master oscillator output average power of 9.7 mW, and minimum output amplification ($P_{Av} = 207$ mW). [JMMG17]144

Fig. 7.8: Typical laser output without variable attenuator at 30.6 mw output average power showing: (a) Experimental autocorrelator trace and (b) linear optical spectrum, giving FWHM values for each case. (c) Laser analysis as a function of the average output power, presenting the estimated peak power (fill black circles) and the time-bandwidth product (empty blue triangles). [JMMG18]146

Fig. 7.9: Experimental measured spectrum for laser using S1 as saturable absorber and a 70/30 fiber coupler.148

Fig. 7.10: Oscilloscope traces showing the train of pulses delivered by the laser, with the laser operating in (a) stable mode-locking range, and (b) the transition range.....150

Fig. 8.1: Curve of the measured reflectance (%) of InN-based SESAM (blue circles) and a 300-nm-thick Al mirror deposited on a GaN-on-sapphire substrate

(black triangles), as a function of the incident fluence ($\mu\text{J}/\text{cm}^2$) where symbols are the experimental data and the line represents the fitting to Eq. (5.9).....156

Fig. 8.2: For the commercial InGaAs-based SESAM: (a) Linear reflectance, measured at low intensity incident beam. (b) Simulation of the reflectance as a function of the fluence impinging the structure.158

Fig. 8.3: Scheme of the 1.5 μm ultrafast mode-locked laser using InN based SESAM. The black arrow denotes the direction of the light travelling along the cavity. [JMGN18]159

Fig. 8.4: Frequency-domain spectrum of the ultrafast InN-based fiber laser. [JMGN18]160

Fig. 8.5: Experimental results of the laser presented in Fig. 8.3 including a fiber attenuator, for a 90/10 fiber coupler: (a) Representation of the typical normalized linear spectra centered at 1565 nm, with 100 nm span for each operation regime (CW, transition range and ML). (a) Peak power calculated as a function of the output power for the 90/10 fiber coupler. Black circles represent the results for the SESAM-based laser, and blue squares for the laser using SA in transmission. For each laser results, the empty marker denotes both the CW measurements and the transition range, while filled markers represent the ML results.....162

Fig. 8.6: Results for the SESAM-based laser, namely the variation of the pulse duration (black squares, left axis) and time-bandwidth product (red triangles, right axis) as a function of the output average laser power in mode-locking range. [JMGN18]163

Fig. 8.7: Experimental measurements (black squares) and fits (red lines) when using a 90/10 fiber coupler for output pulses presenting: (a) Autocorrelator trace and (b) optical linear spectrum. [JMGN18]163

Fig. 8.8: Experimental results of the laser using a 70/30 fiber coupler: (a) Peak power as a function of average output power. Insets show normalized linear

spectra centered at $1.56\ \mu\text{m}$ with $100\ \text{nm}$ span for each operation regime. (b) Variation of the pulse duration (black squares, left axis) and time-bandwidth product (red triangles, right axis) as a function of the output average laser power in mode-locking range. [JMGN18]165

Fig. 8.9: Spectra comparison at maximum possible average power using 70/30 fiber coupler for the laser using SESAM and with the SA in transmission. [JMGN18]166

Fig. 8.10: Experimental measurements (black squares) and fits (red lines) when using a 50/50 fiber coupler presenting: (a) Autocorrelator trace and (b) optical linear spectrum. The spectrum at maximum average power for the laser in transmission using the same fiber coupler is represented in blue line. [JMGN18]167

Fig. 8.11: Scheme of the $1.5\ \mu\text{m}$ ultrafast mode-locked laser using commercial GaAs-based SESAM, similar to the one presented in Fig. 8.3, but including a polarization controller. The black arrow denotes the direction of the light propagation in the cavity.168

Fig. 8.12: (a) Representation of the peak power as a function of the average output power of the laser using the GaAs-based commercial SESAM. Different operation modes have been observed, namely CW and transition range (empty markers, in not ML operation), standard ML (with fundamental solitons), and ML with high-harmonic solitons circulating in the resonator (filled markers). (b) For high-output-power of $P_{out} = 28\text{mW}$ in the ML regime, oscilloscope traces with Y-axis-offset for observation of the fundamental soliton (black) and the 2nd and 3rd harmonics (red and blue lines, respectively).169

Fig. 8.13: Typical results for ultrafast fiber laser using GaAs commercial SESAM at $P_{out}=28\ \text{mW}$, presenting: (a) Autocorrelator trace, and (b) optical

spectrum. The figures have been obtained for particular case of minimum
attenuation.170

Fig. 8.14: Spectra taken at high-output power ($P_{out} = 34.4mW$) varying the
polarization in the cavity. The operation with the 2nd and 3rd harmonics was
stable, while operation with fundamental soliton was highly unstable.171

List of Abbreviations and Symbols

Abbreviations	
AC	Autocorrelator
AFM	Atomic force microscopy
CW	Continuous wave
EDFA	Er-doped fiber amplifier
ESA	Electrical spectrum analyzer
FWHM	Full-width half maximum
GaN	Gallium nitride
GVD	Group velocity dispersion
InN	Indium nitride
ML	Mode-locking
MOPA	Master oscillator power amplifier
NLSE	Nonlinear Schrödinger equation
NPR	Nonlinear polarization rotator
OSA	Optical spectrum analyzer
PAMBE	Plasma-Assisted Molecular Beam Epitaxy
PL	Photo-luminescence
PM	Power meter
QW / QD	Quantum wells / Quantum dots
RSA	Reverse saturable absorption
SA	Saturable absorber
SESAM	Semiconductor saturable absorber mirror
SHG	Second-harmonic generation
SMF	Standard single mode fiber
SPM	Self-phase modulation
TBP	Time-bandwidth product
TEM	Transmission electron microscopy

Symbols

A	Optical absorbance
A_{eff}	Optical fiber effective core area
c	Light speed
D	Chromatic dispersion
E_g	Band gap energy
E_p	Pulse energy
F	Optical fluence
f_{rep}	Repetition rate
F_{sat}	Saturation fluence
g	Optical gain
I	Intensity, irradiance
I_0	Peak intensity
I_{sat}	Saturation intensity
$k(\omega); \beta(\omega)$	wave number
L	Material thickness
L_{eff}	Effective material thickness
n_i	i-th order coefficient of refractive index
P_{ave}	Average power
P_p	Peak power
R	Optical reflectance
T	Optical transmittance
$T_{\text{lin}}; R_{\text{lin}}$	Linear transmittance / reflectance
$T_{\text{ns}}; R_{\text{ns}}$	Non-saturable transmittance / reflectance
$w(z)$	Beam radius
z_0	Rayleigh length
α_i	i-th order coefficient of absorption
Υ	Effective nonlinear coefficient
$\Delta T; \Delta R$	Modulation depth, measured in transmission or reflection
$\Delta\lambda$	Spectral pulse width (wavelength domain)

$\Delta\nu$	Spectral pulse width (frequency domain)
$\Delta\tau$	Pulse width (time domain)
ε	Electric susceptibility
λ	Wavelength
τ	Semiconductor relaxation time
ϕ	Field phase
χ_i	i-th order of electric susceptibility tensor
ω	Angular frequency

Chapter 1 Introduction

This chapter has been divided into three sections. The first section briefly introduces the state of the art of the passively mode-locked ultrafast fiber lasers and the benefits of using III-nitrides as saturable absorbers. Then, the aim and objectives of the thesis will be introduced. Finally, the organization of this manuscript is given.

1.1 Motivations

Since the report of the first laser by T. H. Maiman in 1960 [Maim60], this field has become one of the most relevant to scientists nowadays. Particularly, the generation of very short pulses was demonstrated some years after, by locking the resonant modes in the cavity, in a process called mode-locking. This can be achieved either using an active device [HaFP64], or with the introduction of a material whose absorption can be saturated passively when being pumped by very high intensities [IpSD72], in order to modulate the intracavity losses. Mode-locking leads to the generation of ultrashort pulses (in the range of ps or fs), thus we usually refer to these devices as ultrafast lasers. At present, a wide range of ultrafast lasers is available, relying on a large variety of fabrication technologies: gas lasers, semiconductor lasers, dye lasers, solid-state lasers or fiber lasers [Haus00].

The generation of ultrashort pulses led to high peak powers, which is one of the main features of ultrafast lasers. The application of ultrafast lasers to different research fields has led to a fast evolution in many fields, as for example in medicine, micromachining, communications, optical sensing and metrology and terahertz generation, to name some [FeGS02],[Kell03].

1.1.1 Highlights of passive ultrafast fiber lasers at telecom wavelengths

Despite optical fibers were discovered in the 19th Century, it was not until the 1960s when the first optical fiber amplifiers were developed by doping the silica fiber with rare-earths [KoSn64]. However, the development of fiber lasers remained almost in standby until the achievement of the first Er-doped fiber amplifier (EDFA) in 1987 [MRJP87], by doping silica fiber with Er^{3+} ions. This type of optical amplifier presents its gain in the C-band (telecom wavelengths, 1530-1570 nm) and will be the devices used as the gain medium of all the lasers developed in this thesis. Nevertheless, there exist fiber amplifiers doped with other rare-earth elements, thus operating at different wavelengths such as Yb-doped fiber amplifiers (YDFAs) or Tm-doped fiber amplifiers (TDFAs) with the gain centered at 1030 nm and 1850 nm, respectively. Similarly to other kind of lasers, fiber lasers can be mode-locked actively, typically using an acousto-optic or electro-optic device in the cavity, or passively, with a saturable absorber (SA).

The first passive mode-locked fiber lasers were developed in the last decade of the 20th Century, based on the Kerr effect, which typically appears in optical fibers at high powers. Particularly, they were developed using either nonlinear amplifying loop mirrors [Duli91a] or nonlinear polarization rotators (or NPRs) [TaHI92],[TIHN93], acting as saturable absorbers. Despite very short pulses

(below 100 fs) were generated using these techniques, they present the great inconvenience of being highly polarization dependent.

More recently, many research groups have proposed graphene and carbon nanotubes as saturable absorbers at 1.5 μm , generating pulses as short as the previous techniques, but with great limitation of the maximum energy as they have a low damage threshold [SYTJ04],[PSHC12].

The use of semiconductors as saturable absorbers in Er-doped fiber lasers is not yet as extended as in other kind of lasers, such as Ti-sapphire [JKMS97]. The main problem with these devices is that, since they are developed in free space, either the guided light must be launched at first instance and coupled again into the fiber or they can be positioned at the end of an optical fiber, typically increasing considerably the system losses. Moreover, they are usually polarization dependent. On the contrary, typically their damage thresholds are much larger than other materials like for example in the case of graphene or carbon nanotubes. The most extended materials for this purpose are doped GaAs-based semiconductors. Particularly it is more common to find these GaAs-based devices forming heterostructures, such as quantum wells (QWs) or quantum dots (QDs), than in bulk state, due to the enhancement of their nonlinear properties [SSPS93],[CGNK11],[HTFH17].

In this thesis, we will show the development of passive mode-locked fiber lasers, using InN-based saturable absorbers for the first time to our knowledge, and operating at telecom wavelengths.

1.1.2 Why indium nitride as saturable absorber?

Group III-nitrides have been largely studied lately due to their applications in a wide range of wavelengths. As it is shown in Fig. 1.1, III-nitrides cover wider range of the spectrum than any other family of semiconductors, from middle

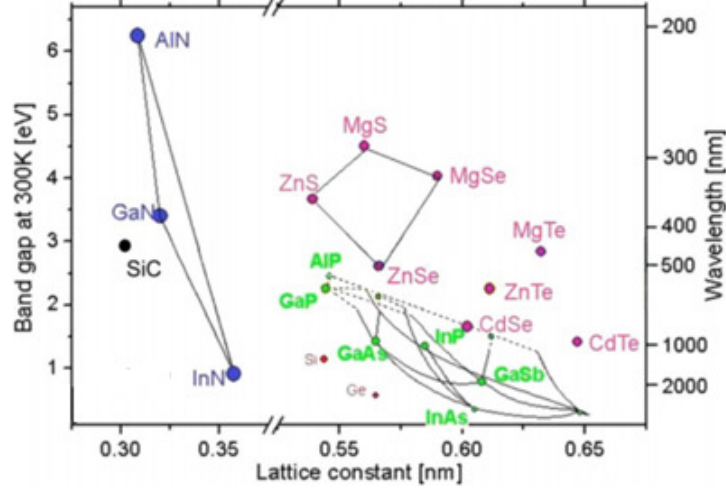


Fig. 1.1: Band gap given in energy and wavelength as a function of the lattice constant for different semiconductor family groups. [WBCF12]

ultraviolet (6.2 eV band gap energy for AlN [SWNV00]) to near infrared (0.64 eV for InN [WWSY03]). Furthermore, this group of semiconductors has demonstrated unique properties such as radiation hardness or thermal and chemical stability [SWNV00]. These properties, along with their direct band gap in binary and ternary III-nitrides makes them feasible for light emission and absorption applications.

Particularly, InN attracted much attention more recently, due to the difficulty of growing layers of this material with high quality. During the 1980s and 1990s, InN layers were mainly deposited by sputtering or chemical vapor deposition, leading to a band gap close to 1.8-1.9 eV [TaFo86]. However, in the early 2000s, finally high quality InN was fabricated by means of molecular beam epitaxy, leading to a band gap energy ranging from 0.64 eV to 0.85 eV [WWSY03]. Interestingly for this thesis, this material is highly resonant at telecom wavelengths (1.53-1.57 μm ; 0.79-0.81 eV). InN layers are typically grown on sapphire or silicon substrates usually in wurtzite structure [MONH02]. This hexagonal structure presents very high symmetry (type 6mm in international

notation). When InN layers are being pumped by electromagnetic radiation along the growth direction, the second-order nonlinear optical effects can be neglected and the third-order coefficients of the susceptibility are equal in the two remaining directions, converting this material in almost polarization independent [Boyd08]. This feature is extremely interesting for the development of ultrafast fiber lasers, which typically are very sensitive to polarization changes. Moreover, our research group was pioneer in the characterization of the nonlinear absorption of bulk InN layers and InN-based multiple quantum-wells (MQW), showing a large nonlinearity of $\alpha_2 = -1450 \text{ cm} / \text{GW}$ and $\alpha_2 = -9150 \text{ cm} / \text{GW}$, respectively, which is a main condition of saturable absorbers. These measurements are in good agreement with Ahn *et al.*, that reported very large SA effect in resonant thin InN films, where the nonlinear absorption coefficient can be estimated between $\alpha_2 = -10^3 \text{ cm} / \text{GW}$ and $\alpha_2 = -10^4 \text{ cm} / \text{GW}$ [AhLC14].

In this thesis, we propose InN as the active layer for the development of saturable absorber devices in the telecom wavelength band of 1.55 μm .

1.2 Aim of this Thesis

The aim of this work is the development of ultrafast fiber lasers operating at telecom wavelengths using InN-based saturable absorbers. More specifically, the objectives of this thesis are:

- To study new nitride-based saturable absorber devices operating at telecom wavelengths. For this purpose, the nonlinear properties of bulk InN and InN/InGaN MQWs will be investigated. In particular, the saturation fluence and the modulation depth will determine the efficiency of these devices.

- To fabricate passive ultrafast fiber lasers centered at the C-band of telecom wavelengths using InN-based structures as saturable absorbers.
- To fully characterize the properties of the developed ultrafast fiber lasers using InN-based saturable absorbers.

This work has been carried out within the framework of the following research projects from different institutions:

- Spanish Government projects: CISTER (TEC2012-37958-C02-01); ANOMALOS (TEC2015-71127-C2-2-R).
- Community of Madrid projects: SINFOTON (S2013/MIT-2790).
- Alcalá University projects: DESLAP (CCG2013/EXP-052); SOLARSEN (CCG2014/EXP-051); Autocorrelador para la medida de pulsos ultracortos (UAH INFR.B 2017-009).
- Spanish Government grant for PhD: FPI-2013.

1.3 Brief description of this Thesis

This manuscript is divided into nine chapters, considering this first chapter as the introduction. Chapter 2 gives an introduction to semiconductors, particularly to III-nitrides. This chapter also includes an overview of the different growth techniques used for the fabrication of the devices and the state-of-the-art of III-nitrides.

Chapter 3 explains theoretically the different optical effects that appear in the semiconductors used in this thesis. Chapter 4 introduces optical effects in optical fibers and formally sets the theory of ultrafast mode-locked fiber lasers. In this chapter, the state-of-the-art of these kind of lasers, operating at 1.55 μm , can be

found. Chapter 5 describes the different techniques for a complete characterization of the structures proposed.

Chapter 6 to Chapter 8 show the experimental results obtained in this work. Particularly, Chapter 6 presents the characterization results of the structures proposed. The following two chapters show the different ultrafast fiber lasers that have been developed. In Chapter 7, fiber resonators using the saturable absorber structures in transmission are displayed, while Chapter 8 introduces the developed laser using the InN-based saturable absorber mirror.

Finally, Chapter 9 summarizes the general conclusions established in this thesis. This chapter also provides new perspectives for the improvement of some of the results obtained and proposes new ideas to carry on with this work.

Chapter 2 Introduction to III-Nitrides Semiconductors

This chapter summarizes the general aspects concerning III-nitride semiconductors. Particularly, structural and optical properties of AlN, GaN and InN are shown, providing most accepted values of important parameters as for example the lattice constants, elastic and polarization coefficients and linear and nonlinear optical coefficients. Finally, the semiconductor growth techniques used to develop the nitride structures studied along this thesis are presented.

2.1 General introduction to III-nitrides

The high bonding energy between the nitrogen and the III-group metal atoms (Al, In, Ga) is one of the main properties of these compounds, as it shows a strong covalent component. This feature implies the thermal stability of III-nitrides to be very high [VoKP97]. Among the binary nitrides compounds that will be discussed in this thesis, InN presents the lower bond energy, while this value increases for GaN and is maximum for AlN. III-nitrides also present a high melting point, estimated theoretically by J. A. van Vechten, finding values of 2146 K, 2791 K and 3487 K for InN, GaN and AlN respectively [Vech73]. However, it is not possible the growth at these temperatures, since the materials decompose at much lower temperatures [Poro97]. Particularly, the properties of

InN presented in this chapter would be of particular interest for the purpose of this thesis.

When considering ternary compounds based on III-nitrides (like $A_{1-x}B_xN$), a linear fit is usually a good approximation for the estimation of a parameter characteristic of the ternary material. It consists in an interpolation between the parameter corresponding to each of the binary compounds constituents. Equation (2.1) defines this law:

$$C = C_A^0 (1 - X) + C_B^0 (X) \quad (2.1)$$

where A and B are III-group metals, characterized by C_A^0 and C_B^0 . X is the concentration of metal B and C is a physical parameter to be estimated for the ternary compound. Particularly, it is called Vegard's Law when estimating the lattice constant [Vega21]. It must be pointed out that not always the experimental properties of a ternary can be fit linearly. In these cases, it is necessary to make use of the bowing parameter, b , by adding the term $bX(1 - X)$ to eq. (2.1) [AACM07],[Hana09].

2.1.1 Structural properties

Among all the possible lattice structures, III-nitride semiconductors (AlN, GaN, InN and their alloys) most commonly crystalize in wurtzite structure, which corresponds to two interpenetrating hexagonal close-packed lattices (HCP), usually known as wurtzite (α -phase). However, under some circumstances, zinc-blende (β -phase), and rock-salt structures (γ -phase) can be obtained [Edga94],[VoKP97],[SWNV00],[VuMe03]. These two latter structures (β - and γ -phase) are formed by two interpenetrating face-centered cubic lattices. The difference between them is the relative position of the two lattices. Fig. 2.1. depicts the three structures. Wurtzite and zinc-blende structures have tetrahedral

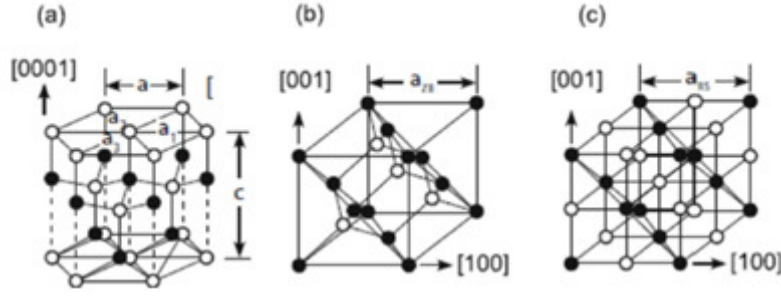


Fig. 2.1: Different crystalline structures of the III-nitrides: (a) wurtzite (α -phase), (b) zinc-blende (β -phase) and (c) rocksalt (γ -phase). [Hana09]

coordination, meaning that each atom has four atoms of the opposite group as nearest neighbors. Nevertheless, only wurtzite nitrides will be considered along this thesis.

The wurtzite structure in III-nitrides is the most thermodynamically stable phase at room temperature. As a hexagonal structure, it is common to employ four indices in the Miller notation to denote the structure planes $(hkil)$, instead of the standard (hkl) , where $i=-(h+k)$, and $[hki\bar{l}]$ denotes the direction perpendicular to the $(hkil)$ plane. The basic cell vectors are usually defined by $\{\vec{a}_1, \vec{a}_2, \vec{a}_3, \vec{c}\}$, where $\vec{a}_1, \vec{a}_2, \vec{a}_3$ are three equivalent axes which are in the basal plane, and are perpendicular to \vec{c} . It is possible to define $\vec{a}_3 = -(\vec{a}_1 + \vec{a}_2)$. The interplanar distance can be expressed as follows:

$$\frac{1}{d_{hkl}^2} = \frac{4(h^2 + k^2 + hk)}{3a^2} + \frac{l^2}{c^2} \quad (2.2)$$

In an ideal wurtzite, two HCP sub-lattices coexist and are separated by the $u = 3c / 8$ parameter. Usually, the growth direction for nitrides is the $[0001]$, i.e. along the c -axis of the hexagonal prism, where the c lattice constant characterizes its height. In the (0001) plane, the a lattice constant is the edge length of the basal hexagon. In an ideal HCP structure, the c / a ratio is 1.633, while the u / c ratio is 0.375. For real III-nitrides wurtzite, as represented in Fig. 2.2(a), u

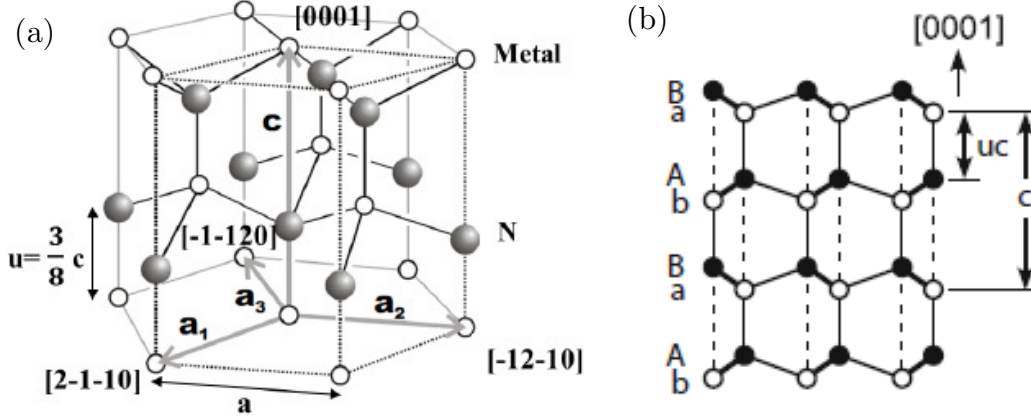


Fig. 2.2: Atomic structure of III-nitrides wurtzite represented by (a) its primitive cell [Münc09] and (b) the stacking sequence (aBbA...) along the [0001] axis. [Hana09]

defines the metal-nitrogen bond length, and the ratios are deviated from the ideal values, as indicated in Table 2.1. Fig. 2.2(b) shows the stacking sequence along the [0001] direction, which for a typical wurtzite III-nitride corresponds to AaBb..., where uppercase letters correspond to N atoms and lowercase to metal atoms. Furthermore, it is easier to shorten the interlayer distances between A-b and B-a than to shorten those between A-a and B-b because the former can be done mostly with angle deformation of the bond pairs [Hana09].

Table 2.1 Lattice parameters of the wurtzite bulk binary nitrides at room temperature (a,c) and metal-nitrogen bond length, normalized to parameter c.

Parameter	AlN	GaN	InN	Ref.
a (Å)	3.112	3.189	3.545	[VuMe03]
c (Å)	4.982	5.185	5.703	[VuMe03]
u/c	0.380	0.376	0.377	[VuMe03]

2.1.2 Polarization in III-nitrides

In this section, two different sources of polarization will be introduced: the spontaneous polarization, \vec{P}_{sp} , and the piezoelectric polarization, \vec{P}_{pz} . The sum of these two terms lead to the total polarization of a crystal (\vec{P}_{tot}). The polarization is of great importance in III-nitrides, since it affects to both, the electrical and

optical properties. As a consequence of this polarization, an internal electric field emerges inside the crystal, defined by Eq. (2.3)

$$\vec{E}_{tot} = -\frac{\vec{P}_{tot}}{\epsilon_0 \epsilon_r} \quad (2.3)$$

where ϵ_0 is the vacuum permittivity, and ϵ_r is the dielectric constant of the material.

2.1.2.1 Spontaneous polarization

In III-nitride semiconductors, the c-axis corresponds to a polar axis where the inversion of symmetry does not hold. Thus, the crystal is different along the [0001] and [000-1] directions. This effect is due to a deformation that occurs in the tetrahedrons formed by the N and metal (Al, Ga and In) atoms. The electronegativity of the N atoms (3.04) is higher than the metal atoms (1.61, 1.81, 1.78 for Al, Ga, In respectively), so the valence electrons of the metal tend to be attracted by the nitrogen atoms, inducing a small dipole in each tetrahedron. The contribution of all the tetrahedrons present in the crystal, produces the generation of a macroscopic spontaneous polarization in the crystal, \vec{P}_{sp} . Fig. 2.3 depicts the two possible polarities that can arise in the wurtzite III-nitrides. Thereby, if metal atoms are found in the top of the bilayer, the structure is referred as metal-

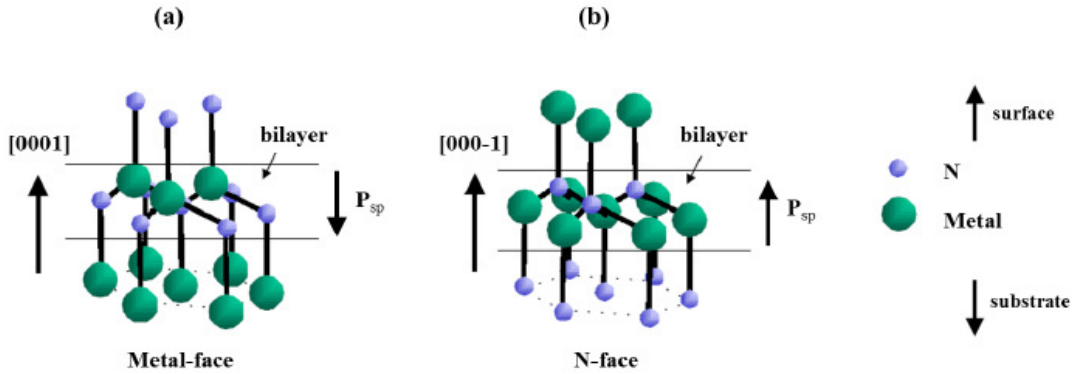


Fig. 2.3: Representation of the different spontaneous polarization on wurtzite III-nitrides with (a) metal-polarity and (b) N-polarity. [Mont15]

polarity [Fig. 2.3(a)]. On contrary, if nitrogen atoms are on the top of the bilayer, the structure is called nitrogen-polarity [Fig. 2.3(b)]. In both cases, \vec{P}_{sp} points from the metal monolayer to the nitrogen one, which by convention is considered as $[000-1]$ direction.

Table 2.2 summarizes the \vec{P}_{sp} coefficients for the III-nitride family. The highest value, which was estimated for AlN, comes from the largest deformation of the tetrahedrons on this material compared to the ideal case, as its parameter u / c was the most deviated from the ideal $u / c = 3 / 8 = 0.375$ (see Table 2.1).

Table 2.2 Spontaneous polarization of wurtzite III-nitrides

Parameter	AlN	GaN	InN	Ref.
\vec{P}_{sp} (C/m ²)	-0.090	-0.034	-0.042	[VuMe03]

2.1.2.2 Piezoelectric polarization

When a crystal is under mechanical stress, the position of the atoms is changed with respect to the corresponding one to free standing conditions, leading to a differential change in spatial distribution of the charges. This change could induce the appearance of a dipole, which is macroscopically known as piezoelectric polarization, \vec{P}_{pz} . Due to the lack of substrates for homoepitaxial growth, III-nitrides are typically grown on substrates such as Si, SiC or sapphire heteroepitaxially, and they present strain from the lattice-mismatch between the layer and the substrate. The piezoelectric polarization under these circumstances emerges naturally.

From Hooke's Law, the stress induced in a material (σ_{ij}) and the strain (ϵ_{ij}) are related by the elastic tensor of the material (C_{ij}) as follows [Love44]:

$$\begin{pmatrix} \sigma_{xx} \\ \sigma_{yy} \\ \sigma_{zz} \\ \sigma_{yz} \\ \sigma_{zx} \\ \sigma_{xy} \end{pmatrix} = \begin{pmatrix} C_{11} & C_{12} & C_{13} & 0 & 0 & 0 \\ C_{12} & C_{11} & C_{13} & 0 & 0 & 0 \\ C_{13} & C_{13} & C_{33} & 0 & 0 & 0 \\ 0 & 0 & 0 & C_{44} & 0 & 0 \\ 0 & 0 & 0 & 0 & C_{44} & 0 \\ 0 & 0 & 0 & 0 & 0 & \frac{C_{11} - C_{12}}{2} \end{pmatrix} \times \begin{pmatrix} \epsilon_{xx} \\ \epsilon_{yy} \\ \epsilon_{zz} \\ \epsilon_{yz} \\ \epsilon_{zx} \\ \epsilon_{xy} \end{pmatrix} \quad (2.4)$$

When the crystal grows along the direction [0001], the strain coefficients ϵ_{ij} with $i \neq j$ are equal to zero because the stress along that direction is zero too ($\sigma_{zz} = 0$). In this same case, the in-plane stress is uniform ($\sigma_{xx} = \sigma_{yy}$). With these assumptions, the Eq. (2.4) can be simplified as follows:

$$\begin{pmatrix} \sigma_{xx} \\ \sigma_{yy} \\ 0 \end{pmatrix} = \begin{pmatrix} C_{11} & C_{12} & C_{13} \\ C_{12} & C_{11} & C_{13} \\ C_{13} & C_{13} & C_{33} \end{pmatrix} \times \begin{pmatrix} \epsilon_{xx} \\ \epsilon_{yy} \\ \epsilon_{zz} \end{pmatrix} \quad (2.5)$$

The elastic coefficients of the III-nitrides can be found in Table 2.3. The relation between the in-plane and out-plane strain coefficients along the direction [0001] is given by (2.6):

$$\epsilon_{zz} = -\frac{2C_{13}}{C_{33}}\epsilon_{xx} \quad (2.6)$$

The stress in the plane (0001) is uniform, given by the Eq. (2.7):

Table 2.3 Coefficients of elastic tensor for the binary III-nitrides.

Coefficient (Gpa)	AlN	GaN	InN	Ref.
C_{11}	396	390	223	[Wrig97],[VuMe03]
C_{12}	137	145	115	[Wrig97],[VuMe03]
C_{13}	108	106	92	[Wrig97],[VuMe03]
C_{33}	373	398	224	[Wrig97],[VuMe03]
C_{44}	116	105	48	[PoGG96],[Wrig97]

$$\epsilon_{xx} = \epsilon_{yy} = \frac{a - a_0}{a_0} \quad (2.7)$$

And the out-plane stress is:

$$\epsilon_{zz} = \frac{c - c_0}{c_0} \quad (2.8)$$

Where a, c are the lattice parameters of the grown material, and a_0, c_0 correspond to the lattice parameters in a relaxed state.

The piezoelectric polarization induced from the stress present in the wurtzite III-nitrides is defined by Eq. (2.9):

$$\vec{P}_{pz} = \begin{pmatrix} 0 & 0 & 0 & 0 & e_{15} & 0 \\ 0 & 0 & 0 & e_{15} & 0 & 0 \\ e_{31} & e_{31} & e_{33} & 0 & 0 & 0 \end{pmatrix} \times \begin{pmatrix} \epsilon_{xx} \\ \epsilon_{yy} \\ \epsilon_{zz} \\ \epsilon_{yz} \\ \epsilon_{zx} \\ \epsilon_{xy} \end{pmatrix} \quad (2.9)$$

The wurtzite is the structure with the highest symmetry compatible with piezoelectric polarizations. Because of that, only three piezoelectric coefficients (e_{ij}) are independent in this structure. The most common growth direction in III-nitrides is along the [0001] direction. In this case, the components of the piezoelectric polarization vector are defined as follows:

$$\begin{aligned} \vec{P}_{pz}^X &= 0 \\ \vec{P}_{pz}^Y &= 0 \\ \vec{P}_{pz}^Z &= 2 \frac{a - a_0}{a_0} \left(e_{31} - e_{33} \frac{C_{13}}{C_{33}} \right) \end{aligned} \quad (2.10)$$

This means that the piezoelectric polarization in III-nitrides only affects to the direction [0001]. When the crystal is under compressive stress, \vec{P}_{pz}^Z points to the

Table 2.4 Piezoelectric tensor coefficients of the binary III-nitrides.

Coefficient (C/m ²)	AlN	GaN	InN	Ref.
e_{31}	-0.50	-0.35	-0.57	[VuMR01]
e_{33}	1.79	1.27	0.97	[VuMR01]

[0001] direction, while \vec{P}_{pz}^Z points to the [000-1] direction if it is under tensile in-plane stress. The coefficients of the piezoelectric tensor can be found in Table 2.4.

2.1.3 Linear optical properties

As it was mentioned before, all wurtzite binary III-nitrides (AlN, GaN, InN) and their alloys present a direct optical band gap. This means that the position (in k-space) of the point of minimum energy in conduction band coincides with the maximum position of the valence band, placed at the center of the Brillouin zone (point Γ , see Fig. 2.4). Fig. 2.4 depicts the conduction (CB) and heavy (HH) and light holes (LH) valence bands for the wurtzite InN at Γ point. The crystal field band (CH) is also represented. The crystal field splitting energy was estimated in $\Delta_{cr} \approx 40meV$ for InN [Wu09].

In direct band gap semiconductors, as it is the case of III-nitrides, optical transitions like absorption and emission can involve only photons. In general, every semiconductor presents a certain band gap value, which has a dependency with temperature, described by empirical Varshni equation:

$$E_g(T) = E_{g,0} - \frac{\gamma T^2}{T + \beta} \quad (2.11)$$

Where $E_{g,0}$ is the band gap energy at 0 K, γ is a proportionally constant and β is associated with the Debye temperature.

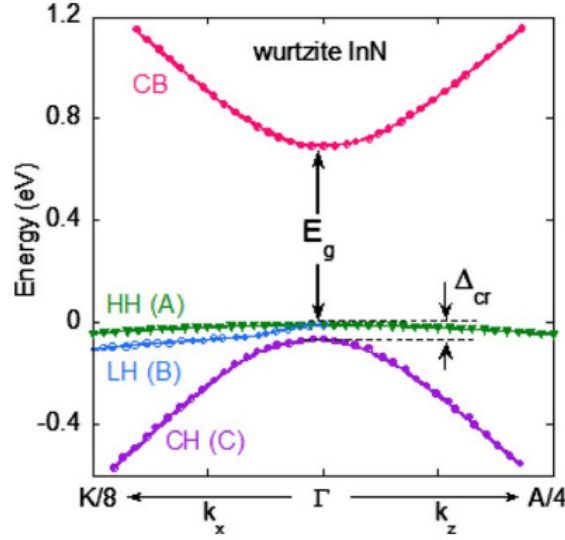


Fig. 2.4: Representation of the conduction and valence bands of wurtzite InN near the Γ point. [Wu09]

The most accepted experimental values of the optical band gap at low and room temperatures for III-nitrides are summarized in Table 2.5. Moreover, with the formation of III-nitride ternaries with $A_{1-x}B_xN$ composition, a wide energy band gap values can be achieved, from the ultraviolet region (AlN, $E_g = 6.14\text{eV}$, i.e. 198 nm) covering all the visible region up to the near infrared (InN, $E_g = 0.64\text{eV}$, i.e. 1936 nm), just by changing the content of the III-metal.

InN is of particular importance for the purpose of this thesis, as it will be seen later. Despite the first reported synthesis of InN date from 1938 [JuHa38], the physical parameters of this semiconductor have been of a large controversy until

Table 2.5 Band gap energies at low and room temperatures (0K and 300K), and Varshni fitting coefficients (γ , β) for wurtzite binary III-nitrides.

Coefficient (C/m ²)	AlN	GaN	InN	Ref.
$E_{g,0}$ (eV)	6.25	3.51	0.69, 0.69*	[VuMe03], [WWSY03]*
γ (meV/K)	1.799	0.909	0.245, 0.41*	[VuMe03], [WWSY03]*
β (K)	1462	830	624, 454*	[VuMe03], [WWSY03]*
$E_{g,300}$ (eV)	6.14	3.43	0.64, 0.64*	[VuMe03], [WWSY03]*

the 2000s due to the difficulty to obtain good quality crystals. In the 1970s and 1980s a band gap of $\sim 1.9\text{-}2.0$ eV was estimated from the films grown by RF sputtering or metalorganic vapor phase epitaxy. These techniques usually produce polycrystalline samples with high carrier concentrations, typically $>10^{19}$ cm $^{-3}$ [Wu09]. At last, in the new millennium, good quality crystals of InN were developed by molecular beam epitaxy technique (MBE), leading to an optical band gap as low as 0.64 eV at room temperature [WWYA02],[MONH02],[WWSY03]. Additional information about all this controversy was given by Butcher and Tansley [BuTa05].

2.1.4 Nonlinear optical properties

In this section, the nonlinear optical properties present in III-nitrides will be discussed in the near infrared effects, when possible. However, some values at other wavelengths might be cited, for a wider overview of this family of semiconductors. The formalism of the nonlinear optical effects in semiconductors will be presented in detail in Chapter 3. As a brief introduction, when light is propagating through the growth direction (z-axis) of wurtzite III-nitrides, these materials do not exhibit the second-order of the susceptibility, $\chi^{(2)} = 0$, since all the non-zero terms depend on z , and the electric field only has x, y components. Thus, the effective susceptibility can be described as [Boyd08]:

$$\tilde{\chi}_{eff} = \tilde{\chi}^{(1)} + \frac{3}{4} \tilde{\chi}^{(3)} |E_0|^2 \quad (2.12)$$

Being $\chi^{(1)}$ the linear (first-order) susceptibility tensor and $\chi^{(3)}$ the third-order susceptibility tensor. The susceptibility is related to the absorption and refractive index of the material. Considering their nonlinear terms as a function of the optical intensity, they can be described as follows:

$$\alpha(I, \lambda) = \alpha_0(\lambda) + \alpha_2(\lambda)I \quad (2.13)$$

$$n(I, \lambda) = n_0(\lambda) + n_2(\lambda)I \quad (2.14)$$

Where $\alpha_2(\lambda)$ and $n_2(\lambda)$ are the nonlinear absorption and Kerr coefficients, respectively. When the material exhibits saturable absorption effect (SA), then $\alpha_2(\lambda) < 0$. On contrary, $\alpha_2(\lambda) > 0$ (also referred as β in many cases) occurs when it presents reverse saturable absorption (RSA), typically due to the two-photon absorption process (TPA). These nonlinear coefficients are related to $\chi^{(3)}$ as it will be shown in Chapter 3.

The study of nonlinear effects in III-nitrides has been mainly focused on the fabrication of waveguides or devices for Photonics Integrated Circuits (PICs) such as optical switches. Nonlinear optical effects in GaN have been largely studied, due mainly to the relevance of this semiconductor in the photonics community. In this way, Lin *et al.* reported in 2003 huge TPA for resonant bulk GaN, finding a value of $\beta \approx 1500 \text{ cm} / \text{GW}$ at 362 nm, near the band gap energy [LCHK03]. This value measured was more than 100 times larger than former off-resonance reported nonlinear absorption coefficients of $\beta \approx 15 \text{ cm} / \text{GW}$ at 400 nm [SLWK00]. C. K. Sun *et al.* estimated a very high Kerr coefficient of $n_2(\lambda) = -1 \times 10^{-12} \text{ cm}^2 / \text{W}$ near the resonance [SHLG00]. More recently, Fazio *et al.* reported in 2007 a Kerr coefficient of $n_2(\lambda) = -7.3 \times 10^{-14} \text{ cm}^2 / \text{W}$ at 800 nm (below half the band gap energy of GaN). Although thermally and chemically stable, bulk GaN never appear to exhibit large nonlinear optical properties in the infrared.

On contrary, GaN/AlN-based heterostructures, such as QWs or QDs have demonstrated to present high nonlinearities at resonant wavelengths. Particularly, Yao *et al.* studied theoretically strained GaN/AlN QDs, reporting that the maximum nonlinear behavior typically appears in the range of 0.85-0.90 eV (~ 1375 -1450 nm) [YYLJ09]. At the same time but independently,

these heterostructures were experimentally studied in the Group of Photonics Engineering (GRIFO) at University of Alcalá [VNGF08], finding a third order susceptibility of $\chi^{(3)} = 1.3 \times 10^{-6} esu$ for QDs and $\chi^{(3)} = 2.4 \times 10^{-7} esu$ for QWs, with excited carriers lifetime of $\tau \approx 100 fs$, at telecom wavelengths. However, these structures were strong polarization dependent.

Regarding InN bulk, our group was pioneer in investigating its nonlinearities at telecom wavelengths. In 2007, Naranjo *et al.* found a third order susceptibility of $\chi^{(3)} = 5 \times 10^{-10} esu$ [NGFS07], and later estimated a nonlinear absorption coefficient of $\alpha_2 = -1450 cm / GW$ for bulk InN, and $\alpha_2 = -9150 cm / GW$ for InN/InGaN MQW [NKVC11], demonstrating a large nonlinear absorption, with almost independency on the impinging polarization. Ahn *et al.* carried out in 2014 a large experimental study, demonstrating nonlinear absorption effect for InN in a wide wavelength range in the near infrared from 700 nm to 1600 nm [AhLC14]. Particularly, from the data they reported, the nonlinear absorption coefficient of a close-to-resonant 1400 nm-thick InN layer was in the order of $\alpha_2 = -10^3 cm / GW$ to $\alpha_2 = -10^4 cm / GW$, at a wavelength of 1600 nm. This study also demonstrated that excitation of the samples at off-resonant shorter wavelengths (larger energies) proved great reduction of the nonlinear absorption for shorter wavelengths of the impinging light. This effect was experimentally observed and previously reported by Miller *et al.* in 1981 and referred as the band-filling model. Further information can be read in [MSPS81]. Tsai *et al.* had previously proved this same effect by measuring bulk InN thin-films by z-scan technique far from the resonance, at 720-790 nm [TWLW09], reporting a nonlinear absorption cross section of $\sigma \approx 4 \times 10^{-17} cm^2$, about two orders of magnitude lower than resonant InN measured by Ahn *et al.* [AhLC14], but in good agreement with the band-filling model. This value is directly related to the

nonlinear absorption coefficient as $\alpha_2 = -\sigma\alpha_0\tau / \hbar\omega$, where τ is the impinging pulse duration and $\hbar\omega$ the incident photon energy.

The nonlinearities of RF-sputtering InN were also studied in 2007 by Zhang [ZHGS07], estimating the third- and fifth-order of the susceptibility near its band gap energy, at 800 nm. They estimated nonlinear refractive indices of $n_2 = -2.5 \times 10^{-11} \text{ cm}^2 / \text{W}$ and $n_4 = 2.1 \times 10^{-19} \text{ cm}^4 / \text{W}^2$, but small RSA effect of $\beta = 2.3 \text{ cm} / \text{GW}$. In our group, the two-photon absorption of bulk InN thin films deposited by RF-sputtering were explored at telecom wavelengths, finding a much larger RSA coefficient of $\beta = 167 \text{ cm} / \text{GW}$ [VMMG12].

2.2 Growth of III-nitrides

The layers of III-nitrides studied in this thesis have been grown by plasma assisted molecular beam epitaxy (PAMBE). Also, a sputtering system has been used for the growth of aluminum mirrors, as it will be presented later. In this section, these two deposition techniques will be briefly introduced. Further information about them can be found extensively in previous thesis of our group [Vald11],[Mont15],[Núñez17]

2.2.1 Plasma-Assisted Molecular Beam Epitaxy

The deposition of a crystalline layer on a crystalline substrate is known as epitaxy. The III-nitrides used in this work were grown by PAMBE under the supervision of Dr. Eva Monroy, in the INAC-SP2M laboratories of CEA (Grenoble, France). A scheme of a typical PAMBE chamber for the growth of III-nitrides is shown in Fig. 2.5. An ultra-high vacuum environment inside the chamber (in the order of 10^{-9} mBar or lower) is crucial for obtaining good quality crystals. The III-group metals (Al, In, Ga) are evaporated from the effusion cells,

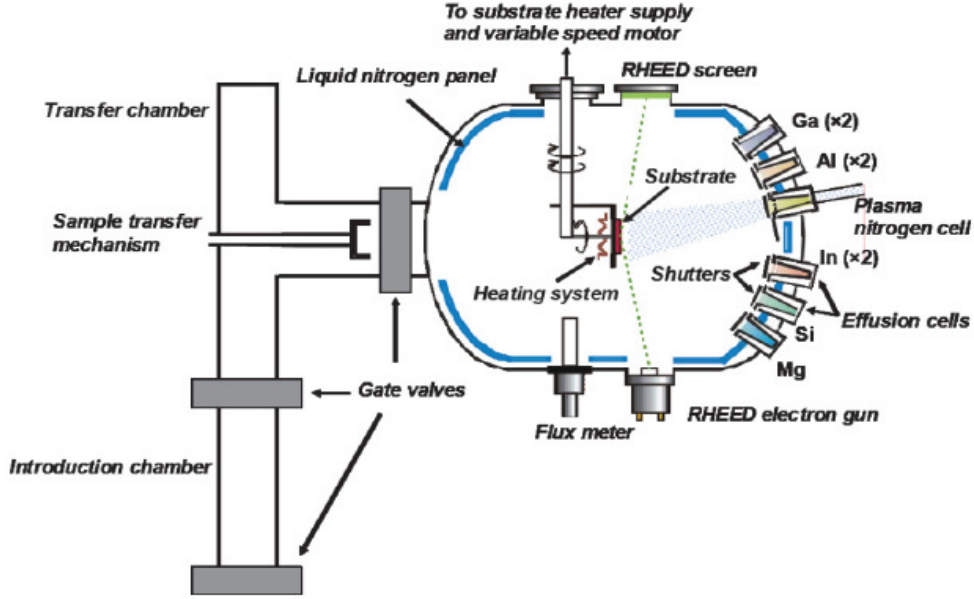


Fig. 2.5: Scheme of typical PAMBE chamber for III-nitrides growth. [Laho09]

while the nitrogen is provided by a radio-frequency (RF) plasma cell by the excitation and dissociation of the N_2 molecules, which are resonant at a RF of 13.56 MHz. Finally, the evaporated atoms impinge on a substrate, where they condense and form the layer. The substrate temperature is an important parameter in the deposition control, since several processes can occur during the growth. The atoms are usually adsorbed by the surface, but also can diffused on it, or they can grow in clusters instead of layer by layer or even be desorpted. Depending on different parameters such as the substrate temperature, the growth rate, the mobility or the grade of coverage (the number of atoms or molecules to fulfill a whole layer), three different growth modes can occur (see Fig. 2.6):

- Frank-Van der Merwe growth [FrMe49]: In this method, the adatom mobility is good enough to ensure a layer by layer growth [Fig. 2.6(a)]. This is the ideal case for bulk or quantum well structures (2-dimensional) and has been the method used for the fabrication of all the structures present in this thesis.
- Volmer-Weber growth [VoWe26]: In this method, the adatom mobility is very low and the molecules tend to form pyramids

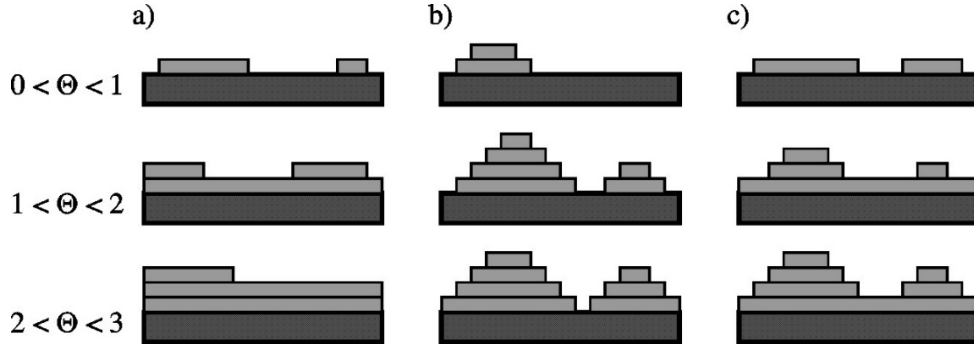


Fig. 2.6: Types of MBE growth, where Θ is the degree of coverage. (a) Frank-Van der Merwe; (b) Volmer-Weber; (c) Stranski-Krastanov. [Kais00]

(3-dimensional), since the growth rate is faster than the diffusion velocity [Fig. 2.6(b)].

- Stranski-Krastanow growth [StKr38]: This method is a combination of the two others presented before. The deposition begins as a Frank-Van der Merwe growth, but after a critical layer is reached, the formation of pyramids becomes more stable energetically [Fig. 2.6(c)].

The layer surface can be precisely characterized using a Reflection High-Energy Electron Diffraction (RHEED). This *in situ* technique is based on the diffraction of an electron beam produced by the layer that is being deposited. The beam is launched from an electron gun and collected at a screen. Additional information about this technique is given by Ino Shozo [Ino77].

The particular PAMBE chamber used for the deposition of the samples of this thesis can keep a vacuum under 10^{-11} mBar. The substrate can rotate during the growth, can be heated and the temperature can be precisely controlled by means of a thermocouple. The N active species are generated by an RF plasma source. Despite being an expensive technique, PAMBE presents some great advantages upon other deposition techniques, namely:

- High layer thickness control *in situ*.

- Fabrication of bulk or heterostructures.
- Growth of binary, ternary or quaternary alloys.
- Good control of dopant concentrations.
- Very high-quality crystals.

2.2.2 Sputtering

One of the most extended uses of a sputtering chamber is the fabrication of metals. Besides the deposition of metals, this low-cost technique also allows the deposition of semiconductors and insulators, the etching, and the deposition at low (even room) and high temperature over rigid or flexible substrates. The sputtering chamber used in this work is an ATC ORION-3-HV from AJA international (see Fig. 2.7), placed in the *Grupo de Ingeniería Fotónica* (GRIFO) at the University of Alcala facilities. Using this technique, thin layers of aluminum acting as the high-reflectivity mirror of a SEmiconductor Saturable Absorber Mirror (SESAM) have been growth.

In this technique, atoms of a gas are ionized to form a plasma and accelerated to impact a target (usually a metal). Atoms from the target are ejected (or sputtered) and can be deposited onto a substrate. Not only ejection of atoms from the target is produced, but also the emission of secondary electrons, which are accelerated to maintain the plasma discharge active. This technique can achieve a high vacuum, with pressures lower than 10^{-7} mBar. The generation of the plasma comes from the application of a voltage in a low-pressure gas. This voltage can be produced by DC or radiofrequency (RF). For the deposition of Al thin films only DC voltage has been used. In this case, the cathode is placed in contact with the target while the anode is in contact with surrounded area of the magnetron gun. However, a wide range of III-nitride materials growth using both RF or DC can be found in previous thesis of our group [Vald11],[Mont15],[Núñez17]. Fig. 2.8

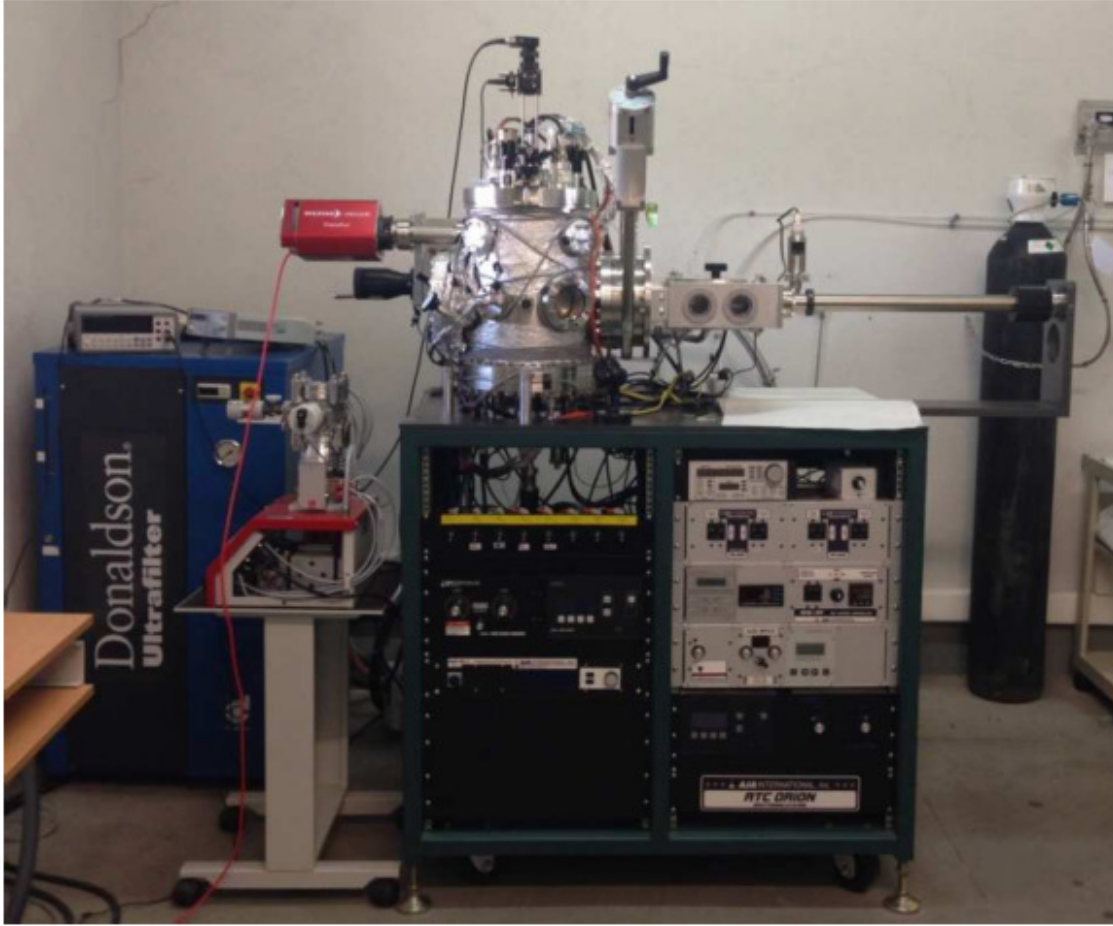


Fig. 2.7: Sputtering system used in this work placed in the GRIFO facilities at the University of Alcalá. The figure shows the gas bottle and the installation (right).

depicts schematically the bombardment process in a sputtering system, using Ar as the gas for plasma generation.

The sputtering yield is defined as the average number of atoms of the target ejected per incident ion. This parameter is related to the properties of the incident ions (incident angle, energy and mass of the ion, etc.) and the atoms in the target (binding energy). Depending on the energy of the ions that reach the target atoms, they can be reflected (low energy), they can produce the atoms ejection (energy higher than the surface binding energy) or they even can produce ion implantation (very high energy).

The Al-mirrors deposited in this work have approximately a thickness of 300 nm, being the deposition rate approximately 240-250 nm/h. They have been

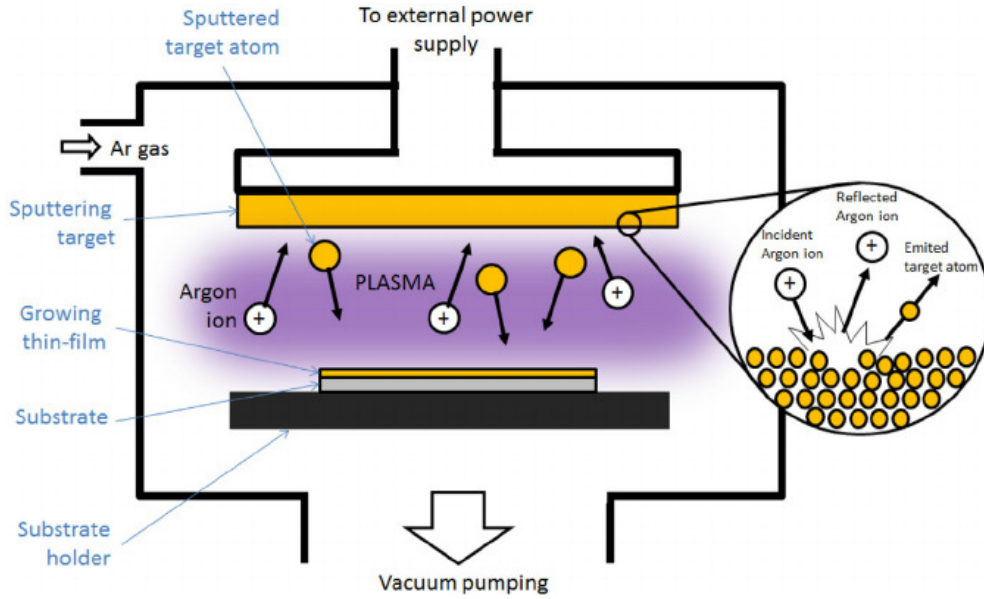


Fig. 2.8: Scheme of the bombardment process of the target in a typical sputtering system for Ar plasma generation. [PFSG14].

fabricated at room temperature, under a flux of Ar of 2 sccm. The power applied to the Al magnetron was 75 W, and the chamber pressure during the growth was stabilized at 5 mTorr. Particularly, the sputtering system used in this thesis (Fig. 2.7) presents the parts described below:

- High vacuum system, in the order of 10^{-8} mBar, achieved from a mechanical pump (up to 12 m³/h) and a turbo-molecular pump (up to 210 l/s).
- Two gas sources: Ar (5N) and N₂ (6N)
- Two RF power sources (up to 300 W) and one DC (up to 750 W) with three possible targets.
- Three 2-inch magnetron guns, two of them with Al (5N) targets and the other with In (4N5) target.
- Two quartz lamps to heat the substrate up to 850 °C.
- A substrate rotation system with a 4-inch substrate holder.

- A quartz crystal microbalance for *in situ* measuring thin films thickness.
- An introduction chamber with a mechanical and turbomolecular pumps that can reach a vacuum in the order of 10^{-7} mBar.

Chapter 3 Optical Effects in Materials

This chapter summarizes the most relevant optical effects concerning semiconductors which are important for a complete understanding of this thesis. We begin introducing some basic concepts of light and its propagation in either vacuum or dispersive media. Afterwards, linear optical effects in semiconductors are introduced, with a full mathematical description of the complex refractive index and a qualitative description of optical transitions in semiconductors. Finally, nonlinear optical effects in semiconductors are introduced, where a detailed analysis of the third-order nonlinearities has been performed, making a distinction between effects that affect the index of refraction (such as self-phase modulation or self-focusing) and those that affect the absorption (such as saturable absorption or two-photon absorption).

3.1 Introduction to light properties

Some basic and intrinsic properties of the light will be introduced in this section, which are of great relevance for the purpose of this thesis.

3.1.1 Maxwell equations

Historically, the light not only has been one of the most scientific studied subjects in nature, but also probably the one that has been surrounded by the largest controversy. It was not until late 19th century that James Clerk Maxwell demonstrated that light could propagate as an electromagnetic wave, after

reformulating Ampere's Law (3.2), introducing a term that he called *electric displacement field*, \vec{D} . This field depends on the free charges, but it is also related to the electric field, \vec{E} and the polarization, \vec{P} , which depends on the internal charges of a medium, as defined by the following constitutive equation:

$$\vec{D} = \epsilon_0 \vec{E} + \vec{P} = \epsilon \vec{E} \quad (3.1)$$

Being ϵ_0 and ϵ the electric susceptibility for vacuum and for a medium, respectively. This contribution, along with the generalization of previous existing formulas, allowed describing the light behavior with only four equations, which are currently known as Maxwell's equations:

$$\nabla \times \vec{H} = \vec{J} + \frac{\partial \vec{D}}{\partial t} \quad (3.2)$$

$$\nabla \cdot \vec{B} = 0 \quad (3.3)$$

$$\nabla \cdot \vec{D} = \rho \quad (3.4)$$

$$\nabla \times \vec{E} = -\frac{\partial \vec{B}}{\partial t} \quad (3.5)$$

Where \vec{H} is the magnetizing field, \vec{J} is the current density, $\partial \vec{D} / \partial t$ is the displacement current density, \vec{B} is the magnetic field and ρ is the free charge density. Equations (3.3) and (3.4) are the Gauss's electric and magnetic equations. The first one describes the absences of magnetic monopoles, while the second one relates the flux of the electric field and the sources that generate that flux. Faraday's induction law (3.5) establishes how to "convert magnetism into electricity", as he quoted himself in 1822 [Hech02]. Maxwell's equations show the perpendicularity between \vec{E} and \vec{B} .

3.1.2 Propagation of light

It is possible to derive a wave equation for the propagation of the light in vacuum or a medium, from the Maxwell equations, containing only the electric field. Taking the curl of eq. (3.5), and using the relation (3.1), along with $\vec{B} = \mu \vec{H}$ where μ is the magnetic susceptibility, we find that:

$$\nabla \times (\nabla \times \vec{E}) + \frac{1}{v^2} \frac{\partial^2 \vec{E}}{\partial t^2} = -\frac{1}{\epsilon_0 v^2} \frac{\partial^2 \vec{P}}{\partial t^2} \quad (3.6)$$

Using the mathematical identity $\nabla \times (\nabla \times \vec{E}) = \nabla(\nabla \cdot \vec{E}) - \nabla^2 \vec{E}$, the first term can be neglected, resulting in [Boyd08]:

$$\nabla^2 \vec{E} - \frac{1}{v^2} \frac{\partial^2 \vec{E}}{\partial t^2} = \frac{1}{\epsilon_0 v^2} \frac{\partial^2 \vec{P}}{\partial t^2} \quad (3.7)$$

Where $v = 1 / \sqrt{\epsilon \mu}$ is the light speed in the medium. If light is propagating in vacuum, we find that $v = c = 1 / \sqrt{\epsilon_0 \mu_0}$, where μ_0 is the magnetic susceptibility in vacuum, and the right term of eq. (3.7) can be neglected as well, since no polarization is present in vacuum. Thus, we can write the light propagation wave equation for vacuum as follows:

$$\nabla^2 \vec{E} - \frac{1}{c^2} \frac{\partial^2 \vec{E}}{\partial t^2} = 0 \quad (3.8)$$

This expression, known as the Helmholtz equation, is also usually valid in the case of isotropic, linear, homogeneous and non-magnetic media with instantaneous response, but propagating at speed $v = c / n$, where n is the refractive index of the medium. In these media, the solution to the wave equation in the time domain, as depicted in Fig. 3.1, is:

$$\vec{E}(t) = \vec{E}_0(t) \cos(k\vec{r} - \omega_0 t + \phi(t)) = \frac{1}{2} \hat{E}_0(t) \exp\{i(k\vec{r} - \omega_0 t)\} + c.c. \quad (3.9)$$

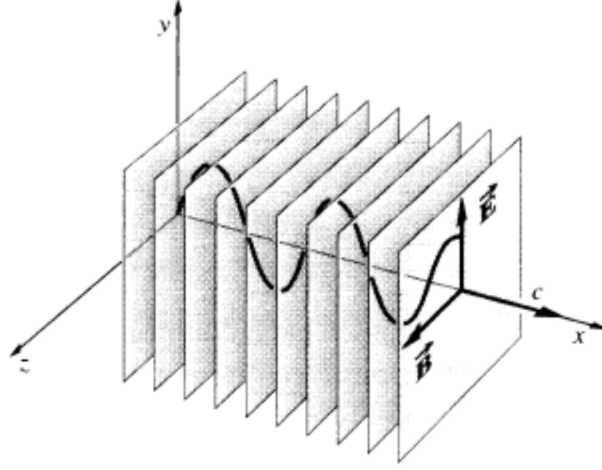


Fig. 3.1: Representation of the propagation of a harmonic electromagnetic wave.
[Hech02]

Where $k = 2\pi / \lambda$ is the propagation number, with λ the wavelength and ω_0 the angular central frequency. Furthermore, we have defined the amplitude of (3.9) as:

$$\hat{E}(t) = \vec{E}_0(t) \exp[-i\varphi(t)] \quad (3.10)$$

The terms $\vec{E}_0(t)$ and $\varphi(t)$ in eq. (3.10) refer to the amplitude of the pulse and its temporal phase, respectively, and they will be discussed afterwards. Eq. (3.10) is essentially (3.9), ignoring the spatial evolution of the pulse, and considering that the values $\vec{E}_0(t)$ and $\exp[-\varphi(t)]$ vary slowly, compared to $\exp(-i\omega_0 t)$, which is in general a good assumption, except for very short pulses exhibiting only few cycles, which is not the case of this thesis. Thus, in most of the cases along this chapter, only time evolution of pulses will be considered, as expressed in (3.10). As an example, blue line of Fig. 3.2 depicts a 50 fs Gaussian pulse, centered at 1550 nm, with no phase given. In this figure, numerous cycles can be observed. The ultrashort pulses generated in this thesis typically present 4-times larger time widths, but on the other hand they will have some phase. Nevertheless, they can not be considered as few-cycle pulses. Fig. 3.2 also depicts the amplitude of the pulse and its optical intensity, denoted by black and red lines, respectively.

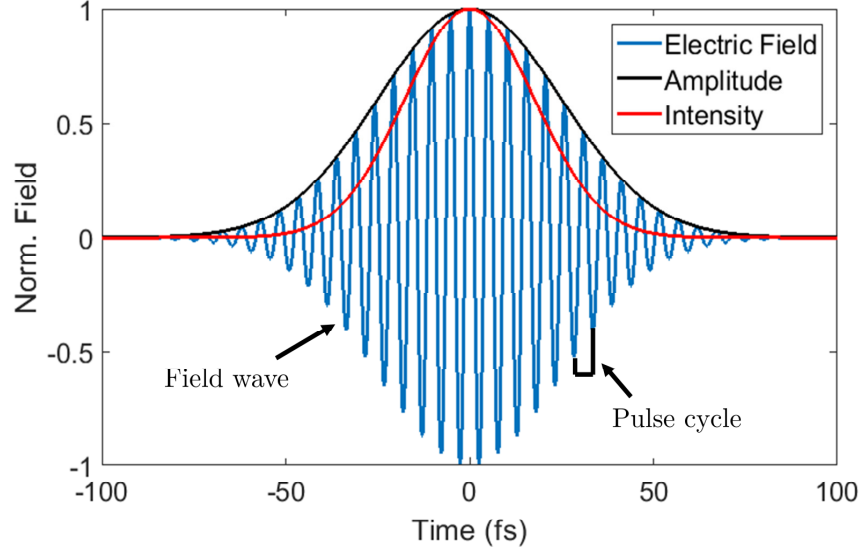


Fig. 3.2: Normalized simulated 50-fs Gaussian pulse centered at 1550 nm neglecting the phase, showing the electric field, $\hat{E}(t)$, with blue line, the amplitude, $\bar{E}_0(t)$, by black line, and the temporal optical intensity, $I(t)$, with red line.

The temporal optical intensity is related to the amplitude of the electric field as expressed in eq. (3.11):

$$I(t) = \frac{nc\mathcal{E}_0}{2} \left| \hat{E}_0(t) \right|^2 \quad (3.11)$$

The temporal optical intensity is defined as the amount of optical power per unit area, and is usually expressed in $[I] = [W / cm^2]$. In optics, generally there is no distinction between the terms irradiance and optical intensity. However, strictly speaking, the irradiance is the power per unit area that is measured at a certain target, while the intensity is the power per solid angle from a radiation source. In spite of this difference, these two terms will be used indistinctly along this thesis.

It is often very common and useful in optics to treat electric fields in the frequency domain. This can be achieved by just applying the Fourier transform to (3.9), in the form:

$$\vec{E}(\omega) = \int_{-\infty}^{\infty} \vec{E}(t) \exp\{i\omega t\} dt \quad (3.12)$$

Where, similarly to the previous case, we can define a spectral amplitude as:

$$\hat{E}(\omega) = \vec{E}_0(\omega) \exp[-i\varphi(\omega)] \quad (3.13)$$

Similarly as in the time domain, the optical intensity in frequency, $I(\omega)$ (also labelled as $S(\omega)$), is related to the field amplitude as: $\vec{E}_0(\omega) \propto \sqrt{S(\omega)}$. The term $S(\omega)$ is usually referred as the optical spectrum of the pulse and $\varphi(\omega)$ as the spectral phase. It is important to note that, despite we have written $\varphi(\omega)$ and $\varphi(t)$ using the same Greek symbol, these two phases are not directly related. These magnitudes are related through the Fourier transform of the whole field.

In many cases, it is also very common to give the spectra as a function of the wavelength, $I(\lambda)$, instead of the frequency. This can be done by means of eq. (3.14), and taking into account that $\omega = 2\pi c / \lambda$:

$$S(\lambda) = \frac{2\pi c}{\omega^2} S(\omega) \quad (3.14)$$

3.1.2.1 Pulse profiles and time-bandwidth product (TBP)

Having in mind the purpose of this thesis, it will be very fruitful to define the two most common temporal pulse profiles that are typically generated by ultrafast lasers: the gaussian and the squared hyperbolic-secant (sech^2) distributions. These are the most common profiles that ultrashort pulses envelopes, $\vec{E}_0(t)$, follow. Fig. 3.3 depicts a graphical comparison between both. Gaussian and sech^2 distributions are mathematically described through (3.15) and (3.16), respectively:

$$E_{0,Gaussian}(t) = \frac{A_{Gaussian}}{\tau_{Gaussian} \sqrt{2\pi}} \exp\left\{-\frac{1}{2} \left(\frac{t-t_0}{\tau_{Gaussian}}\right)^2\right\} \quad (3.15)$$

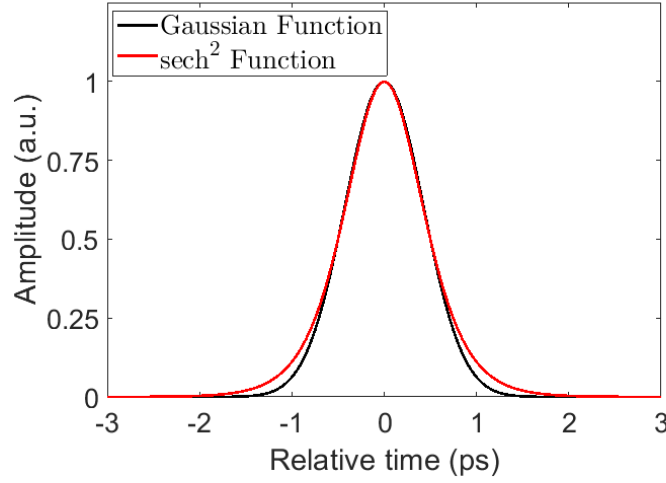


Fig. 3.3: Comparison of a 1-ps FWHM pulse following a Gaussian shape function (black line) and sech^2 shape function (red line).

$$E_{0,\text{sech}^2}(t) = A_{\text{sech}^2} \left(\frac{1}{\exp\left\{\left(t - t_0/\tau_{\text{sech}^2}\right)^2\right\}} + \frac{1}{\exp\left\{-\left(t - t_0/\tau_{\text{sech}^2}\right)^2\right\}} \right)^2 \quad (3.16)$$

Where A is the area of the function and τ in each case is related to the temporal duration of the pulse, or pulse width. The pulse width, $\Delta\tau$, is defined as the full-width at half maximum (FWHM) of the pulse temporal optical intensity. If the pulses follow a Gaussian distribution, then $\Delta\tau = \tau_{\text{Gaussian}} \cdot 2\sqrt{2\ln 2} \approx 2.355 \cdot \tau_{\text{Gaussian}}$, while for pulses following a sech^2 distribution $\Delta\tau = \tau_{\text{sech}^2} \cdot 2\text{arc cosh}(\sqrt{2}) \approx 1.763 \cdot \tau_{\text{sech}^2}$ [LaDG95].

Analogously, the frequency width, $\Delta\nu$, is defined as the full-width at half maximum of the pulse spectrum.

Having defined these two FWHM values, the time-bandwidth product, or TBP, is defined as the product of the time width and the frequency width, as expressed in eq. (3.17):

$$\Delta\tau \cdot \Delta\nu \geq K \quad (3.17)$$

where K denotes the lower limit, which depends on the pulse shape. The TBP is usually considered as a value of the pulse quality. When the TBP is exactly K it is said that the pulse is in the transform-limited situation. This feature implies the minimum possible time width for a certain given spectrum. Particularly, this limit is $K_{Gaussian} \approx 0.441$ for Gaussian pulses, and $K_{sech^2} \approx 0.315$ for sech pulses. In these particular cases, the phase is typically constant or linear, as it will be discussed afterwards.

3.1.2.2 Temporal phase and pulse distortions

The instantaneous angular frequency, $\omega_{ins}(t)$, and instantaneous frequency, $\nu_{ins}(t)$ are defined as:

$$\omega_{ins}(t) = \omega_0 - \frac{d\varphi(t)}{dt} \quad (3.18)$$

$$\nu_{ins} = \nu_0 - \frac{d\varphi(t)}{2\pi dt} \quad (3.19)$$

The temporal phase in (3.18) can be written as a Taylor series as follows:

$$\varphi(t) = \varphi_0 + \varphi_1 \cdot t + \varphi_2 \frac{t^2}{2} + \varphi_3 \frac{t^3}{6} + \dots \quad (3.20)$$

Where φ_i is the i -th order of the phase coefficient. For well-behaved pulses, as it is the case of many of the ultrashort pulses generated, it is usually reasonable to just consider the first few coefficients of eq. (3.20).

When pulses are propagating through dispersive media, such as the case of III-nitride semiconductors, the phase typically does not remain unaffected, but is changing. Since the temporal phase normally contains information about frequency constant of the pulse versus time, these phase changes can have implications in any of the domains, as it is visible through eq. (3.18). We will briefly introduce next how pulses are affected for different phase terms.

It should be noted that, analogously to the time domain, the spectral phase, $\phi(\omega)$, contains information of frequency versus time. Moreover, it is usually common to write $\phi(\omega)$ as a Taylor series, and a similar expression to (3.18) can be found, which is known as group delay, $t_{\text{group}}(\omega) = d\phi(\omega) / d\omega$.

Constant temporal phase

It is important to realize that a constant phase, i.e. a phase of the zeroth-order, just indicates where is the peak of the field inside the envelope. This constant phase can be seen as a relative phase, since only *moves* the field waves. Moreover, a constant phase operates in equal form in both domains. Fig. 3.4(a) shows a shift of π in the phase for a 20-fs gaussian pulse, centered at 1550 nm. It is very clear from the figure how the maxima and minima of the field have changed their positions, but the envelope, and therefore the intensity, remain unaltered. For the case of zero phase, it has been plotted the temporal optical intensity of this pulse in Fig. 3.4(b). Fig. 3.4(c) and (d) represent the optical spectrum as a function of

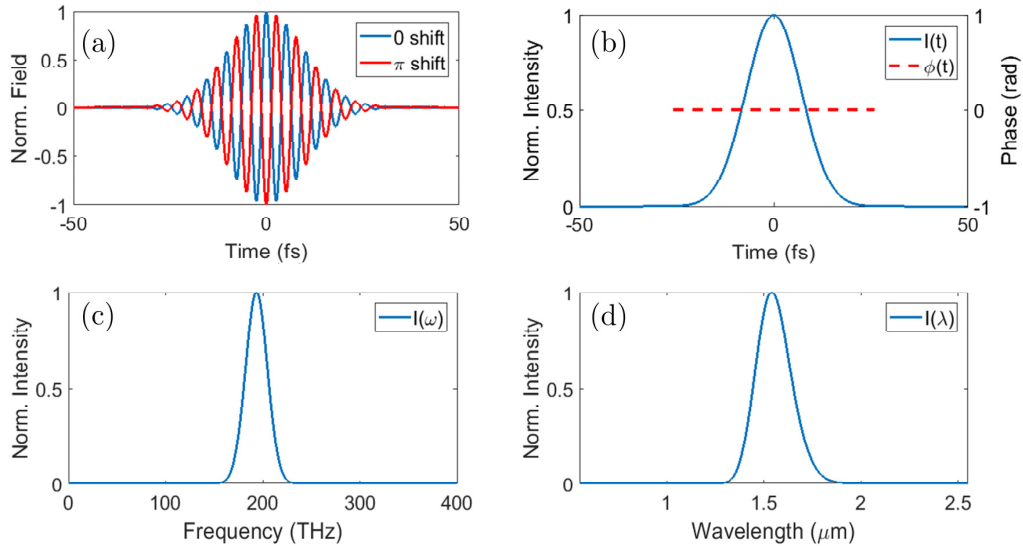


Fig. 3.4: 20-fs Gaussian pulse, centered at 1550 nm showing: (a) Electric field, with $\phi_0 = 0$ (blue line) and $\phi_0 = \pi$ (red line). For the case of $\phi_0 = 0$: (b) Temporal optical intensity (blue line) and phase (red dashed line), (c) Optical spectrum versus frequency. (d) Optical spectrum versus wavelength.

the frequency and wavelength, respectively. It is observable from the figures that the pulse is centered at 193 THz and 1550 nm, respectively.

Linear temporal phase

It is said that a pulse presents linear temporal phase when all the coefficients in (3.20) are zero, except for φ_1 . This feature implies that instantaneous angular frequency (hence instantaneous frequency), given in (3.18), is constant, which leads to a shift in frequency of the pulse, as it is depicted in Fig. 3.5(c). In this case, a linear temporal of $\varphi_1 = 30 \text{ rad} / \text{fs}$ was given for the 20-fs Gaussian pulse, represented in Fig. 3.4. Depending on the sign of this coefficient, the shift can be to shorter or larger frequencies, and opposite in the case of representing the spectrum as a function of wavelength [see Fig. 3.5(d)]. Moreover, despite the introduction of a linear phase does not affect to the envelope or the pulse intensity in the time domain as it can be observed in Fig. 3.5(b), it affects to the number of cycles of the pulse [see Fig. 3.5(a)]. Particularly, this phase given has reduced in two the total number of cycles, while an opposite phase sign would increment

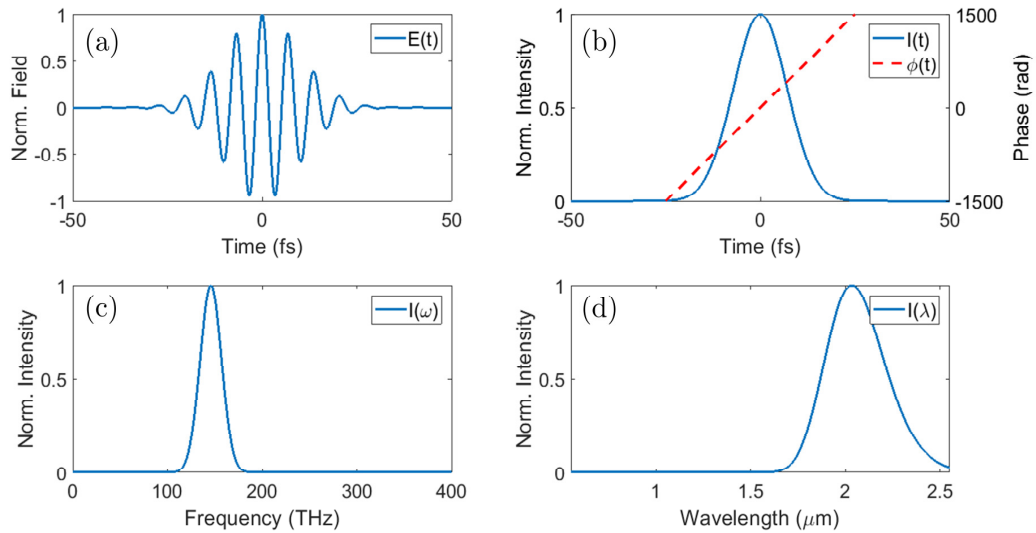


Fig. 3.5: 20-fs Gaussian pulse, centered at 1550 nm with linear phase ($\varphi_1 = 30 \text{ rad} / \text{fs}$) showing: (a) Electric field. (b) Temporal optical intensity (blue line) and phase (red dashed line). (c) optical spectrum versus frequency. (d) Optical spectrum versus wavelength.

this value. A shift in the spectrum is usually of great interest in ultrashort pulse generation, since it is directly related to the pulse energy. Note that a pulse with constant or linear phase can still be in the transform-limited situation, since $\Delta\tau$ and $\Delta\nu$ are typically unaffected.

In an analogous analysis, a linear spectral phase introduces a positive or negative shift in the time domain. Contrary to the case of spectral shifting, a shift in time usually lacks interest for the photonics community, except for some few cases, such as developing interferometric methods.

Quadratic temporal phase, or linear chirp

When the temporal phase follows quadratic variation, in the form of $\phi(t) = \phi_2 t^2 / 2$, the instantaneous frequency grows or decreases linearly with time. This is usually referred to as linear chirp. Particularly, it is called positive (or up) chirp when ω_{ins} rises with time, and negative (or down) chirp in the opposite case. Fig. 3.6 depicts the case of positive linear chirp, with

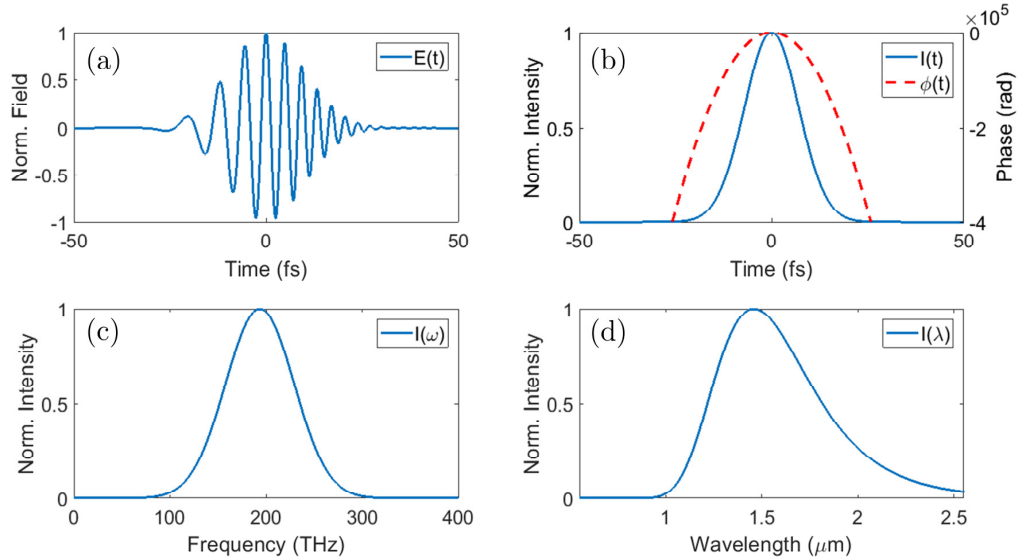


Fig. 3.6: 20-fs Gaussian pulse, centered at 1550 nm with quadratic phase ($\phi_2 = -300 \text{ rad} / \text{fs}^2$), or positive (up) chirp exhibiting: (a) Electric field. (b) Temporal optical intensity (blue line) and phase (red dashed line). (c) optical spectrum versus frequency. (d) Optical spectrum versus wavelength.

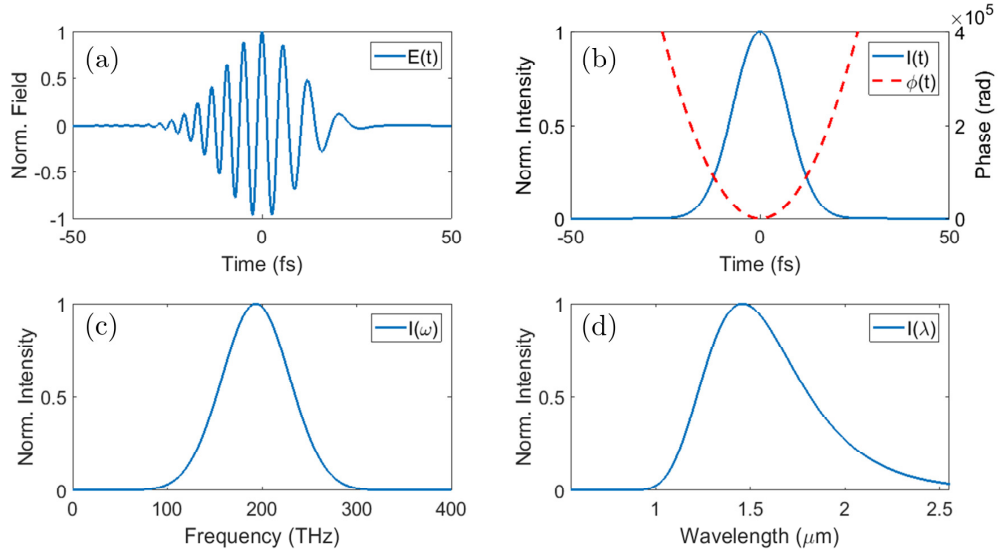


Fig. 3.7: 20-fs Gaussian pulse, centered at 1550 nm with quadratic phase ($\varphi_2 = 300 \text{ rad} / \text{fs}^2$), or negative (down) chirp exhibiting: (a) Electric field. (b) Temporal optical intensity (blue line) and phase (red dashed line). (c) optical spectrum versus frequency. (d) Optical spectrum versus wavelength.

$\varphi_2 = -300 \text{ rad} / \text{fs}^2$, while Fig. 3.7 shows the effect of negative chirp for $\varphi_2 = +300 \text{ rad} / \text{fs}^2$. It can be appreciated that this quadratic phase distorts significantly the electric field of the pulse, while temporal intensity remains unaltered. However, the spectrum gets wider and wider for larger values of φ_2 .

Most materials introduce some type of chirp, when pulses are propagating through them. Therefore, assuming an incident transform-limited pulse propagating through a material, the spectral width will be typically increased while pulse width remains unaffected. This feature implies the pulse to drive away from the transform-limited situation, being now the product of $\Delta \tau$ and $\Delta \nu$ larger than the K limit, given in (3.17). On the other hand, this property can also be used in our benefit in many cases, since the time width of pulses being initially chirped can be reduced, by propagation of the pulse in a medium introducing chirp of opposite sign. Techniques such as chirp-pulse amplification (CPA) used this idea [StMo85]. Nevertheless, this is out of the scope of this thesis.

High-order phases

Well-behaved pulses commonly have one of the phases described above. However, usually other phase distortions, such as quadratic or higher-order chirps, can appear for pulses propagating through different kind of media, that affect to both the time and frequency domain. These high-order phases can usually also break the transform-limited condition, by modifying the values of $\Delta \tau$ or $\Delta \nu$. Nevertheless, we will not go further along this thesis, but there are several texts that discuss these effects [Wein09],[Treb12].

3.1.2.3 Phase velocity and group velocity

For pulses propagating either through space or in a medium, the phase velocity, v_p , is defined as the rate at which the phase of one wave is travelling and the group velocity, v_g , as the derivative of the phase velocity, which represents how the envelope of the pulse is propagating in space or in the medium:

$$v_p = \frac{\omega}{k(\omega)} = \frac{c}{n_p(\omega)} \quad (3.21)$$

$$v_g = \frac{d\omega}{dk} = \frac{c}{n_g(\omega)} \quad (3.22)$$

Where $n_p(\omega)$ and $n_g(\omega)$ are the phase and group index, respectively, and c represents the speed at which the pulse is propagating. Taking into account the dispersion relation from (3.21), $k(\omega) = n_p \omega / c$, the phase velocity and the group velocity (or their indexes) are related as follows:

$$\frac{dk}{d\omega} = \frac{n_p(\omega)}{c} \frac{d\omega}{d\omega} + \frac{\omega}{c} \frac{dn_p(\omega)}{d\omega} \quad (3.23)$$

$$n_g(\omega) = n_p(\omega) + \omega \frac{dn_p(\omega)}{d\omega} \quad (3.24)$$

The group velocity dispersion (GVD) gives the dependence of v_g on the frequency or wavelength:

$$GVD = \frac{\partial}{\partial \omega} \frac{1}{v_g} = \frac{\partial^2 k}{\partial \omega^2} \quad (3.25)$$

The GVD is related to the time broadening that a pulse suffers when propagating through dispersive media.

The group delay, t_{group} , which was introduced above, was defined similarly as the group velocity. The group delay indicates the delay that a pulse acquires when after propagating through a medium. Analogously, we can also define the group delay dispersion, or GDD, as:

$$GDD = \frac{dt_{group}}{d\omega} = \frac{d^2 \varphi(\omega)}{d\omega^2} \quad (3.26)$$

The GDD is related to the dispersion introduced by a medium, as it will be discussed in Chapter 4.

3.2 Linear optical effects in semiconductors

From this point in this chapter, we will strictly consider light propagating through optical media. Taking into account the constitutive relation given by eq. (3.1), which related the electric field, \vec{E} , to the displacement field, \vec{D} , and the intrinsic charges from the medium inducing a polarization, \vec{P} , we can write the polarization vector for homogeneous and isotropic dielectric materials, in which the polarization and the electric field vectors follow the same direction, as:

$$P_i = \epsilon_0 \sum_{ij} \tilde{\chi}_{ij} E_j \quad (3.27)$$

Where $i, j = x, y, z$ and $\tilde{\chi}_{ij}$ is the electric susceptibility tensor, intrinsic of the material. From now on, the symbol indicating a tensor, \tilde{A} , will be removed for

simplicity on the notation. Note that eq. (3.27) is an approximation that considers the response of the material as linear and instantaneous. However, this is not common for real materials. In this case, the induced polarization, $\vec{P}(t)$, is caused by an applied field, $\vec{E}(t')$, at any previous time, $t \leq t'$. Thus, the linear component of the polarization can be expressed as the convolution of the electric field and the susceptibility:

$$\vec{P}(t) = \epsilon_0 \int_{-\infty}^{\infty} \chi(t-t') \cdot \vec{E}(t') dt' \quad (3.28)$$

The relative permittivity of the material is a relation between the dielectric tensor of the material and the vacuum permittivity:

$$\epsilon_r = \frac{\epsilon}{\epsilon_0} = 1 + \chi \quad (3.29)$$

From the interaction of light with matter, many different linear and nonlinear optical effects can occur. The main difference between them is that the nonlinear optical effects have a dependence on the intensity of incident light. It must be pointed out that only the effects that are relevant for the understanding of this thesis will be treated in detail.

3.2.1 Complex refractive index

Light propagates slower in a medium than in vacuum. As explained in sub-section 3.1.2, the refractive index, n , indicates the relation between these velocities (eq. (3.30))

$$n = \frac{c}{v} \quad (3.30)$$

Where v is the light speed in the medium. Light rays do not pass through any optical medium unaltered, since, on one hand, the refractive index typically depends on the optical frequency (or wavelength) of incident light, and on the

other hand the medium absorbs part of the radiation. The complex refractive index takes into account these facts:

$$\hat{n}(\lambda) = n(\lambda) - i\kappa(\lambda) \quad (3.31)$$

In (3.31), $\kappa(\lambda)$ is the extinction coefficient, and is related to the absorption coefficient of the material, $\alpha(\lambda)$:

$$\alpha(\lambda) = 4\pi \frac{\kappa(\lambda)}{\lambda} \quad (3.32)$$

Note that scattering losses in the above relations have been neglected. The complex refractive index is related to the relative permittivity through $\hat{n} = \sqrt{\epsilon_r}$. The relative permittivity can also be described as a complex tensor, $\epsilon_r = \epsilon_r' + i\epsilon_r''$. The relation between ϵ_r , n and κ is shown in (3.33):

$$\begin{aligned} \epsilon_r' &= n^2 - \kappa^2 \\ \epsilon_r'' &= 2n\kappa \end{aligned} \quad (3.33)$$

Neglecting wavelength dependence in the refractive index, we can introduce \hat{n} in the solution to the wave equation (3.9), with zero phase, finding that:

$$\vec{E}(t) = \frac{1}{2} \hat{E}_0(t) \exp \left[i \left(\omega t - \frac{2\pi(n - i\kappa)z}{\lambda} \right) \right] \quad (3.34)$$

That can be reformulated as:

$$\vec{E}(t) = \frac{1}{2} \hat{E}_0(t) \exp \left(-\frac{2\pi\kappa z}{\lambda} \right) \exp \left[i(\omega t - k_n z) \right] \quad (3.35)$$

where k_n only depends on the real part of the refractive index. Thus, the envelope for light propagating in a media is exponentially attenuated as a function of the absorption coefficient and the distance covered, z :

$$\vec{E}_{0,medium}(t) = \frac{1}{2} \hat{E}_0(t) \exp\left(-\frac{\alpha z}{2}\right) \quad (3.36)$$

3.2.2 Absorbance, transmittance and reflectance

When light interacts with matter, part of the incident light is absorbed by the medium, $A(\lambda)$. Transmittance, $T(\lambda)$, is the fraction of the light intensity that passes through the material and reflectance, $R(\lambda)$, is the light intensity that is deviated backwards from the material. Since the total energy is conserved, the following equation can be written:

$$A(\lambda) + T(\lambda) + R(\lambda) = 1 \quad (3.37)$$

Neglecting scattering losses, transmittance and absorbance are related by the Beer-Lambert's Law as follows:

$$T(\lambda) = e^{-A(\lambda)} \quad (3.38)$$

Where $T(\lambda)$ is the ratio of light intensity measured before (I_0) and after (I) the material, and the absorbance is $A(\lambda) = \alpha_0 L$, where α_0 is the absorption coefficient and L the material thickness. Thus, the Beer-Lambert's Law can be expressed as follows:

$$I(\lambda) = I_0(\lambda) e^{-\alpha_0(\lambda)L} \quad (3.39)$$

3.2.3 Optical transitions

A qualitative overview of the possible quantum transitions in semiconductors occurring upon illumination with light will be given in this section. For a more detailed analytic description of these processes, including the decayment rates and the Einstein's coefficients, the reader might explore the books from Griffiths [Grif99] or Bahae and Teich [BaTe91].

It was previously introduced in Chapter 2 that III-nitrides present a direct optical bandgap. The main difference between direct and indirect bandgap materials is that, in the first, typically no phonons are involved in the absorption and emission processes. As the scope of this thesis is limited to III-nitride materials, only optical transitions in direct band gap materials will be discussed in this section. Nevertheless, in all types of semiconductors, band-to-band (inter-band) and free carrier (intra-band) transitions can occur.

3.2.3.1 Excitation

In the interaction between light and matter, electrons in the medium can be excited in an inter-band transition from the valence band to the conduction band, through the absorption of a photon. This usually occurs if the photon energy is approximately equal or above the bandgap energy, $h\nu \geq E_g$. The transition of the electron to the conduction band, generates a hole in the valence band, in what is usually called an electron-hole pair [Fig. 3.8(a)].

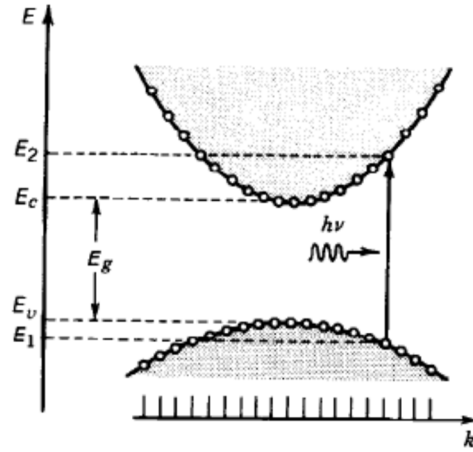


Fig. 3.8: Photon absorption from a semiconductor. [BaTe91]

3.2.3.2 Non-radiative transitions

Non-radiative transitions are optical transitions in which no radiation, i.e. photons, are involved. It is common in semiconductors that, after the excitation,

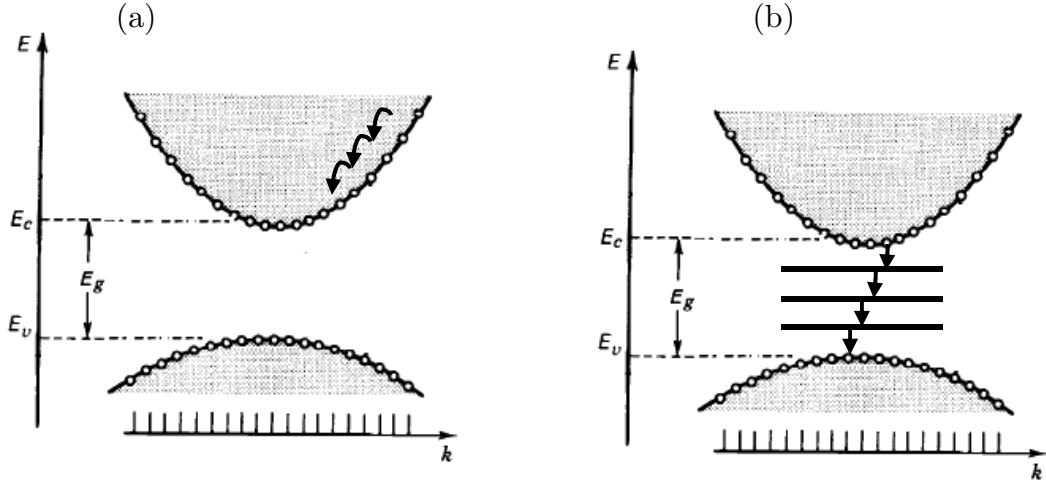


Fig. 3.9: Non-radiative transitions: (a) Intra-band and (b) inter-band. [BaTe91]

an electron reaches a state with larger energy than the lowest point of the conduction band. Once the electron-hole pair has been generated, the electron tends to decay to its equilibrium state in the valence band after a time delay called the relaxation time, τ . This relaxation can occur through transitions either in the same band [Fig. 3.9(a)] or band-to-band [Fig. 3.9(b)]. In the first case, the electron may interact with other electrons (where the conservation of energy must be fulfilled) or with phonons of the medium, transferring energy to the lattice in the form of an increase of the temperature.

The most common non-radiative inter-band transitions occur when an electron relaxes to lower energy states that may exist in the forbidden energy region because of the defects that are present in the semiconductor [as shown in Fig. 3.9(b)]. However, other processes can occur, as for example the Auger recombination, where three carriers are involved. In Auger recombination, an electron-hole pair recombines, giving the resulting energy to a second electron, which will finally collide with other particles in the lattice, transferring the energy to the lattice.

3.2.3.3 Radiative transitions

In radiative transitions, photons are directly involved, leading to the emission of radiation. When an electron-hole pair is formed by the excitation process, there is a certain probability that the pair will recombine spontaneously after a relaxation time, resulting in the emission of a photon. This process is known as spontaneous emission and is responsible of almost all the light that we *see* around us every day [Fig. 3.10(a)]. However, if a material is being pumped with light of a certain wavelength (with a photon energy above the band gap), it is possible that an incoming photon interacts with a previously excited electron, stimulating its relaxation. This process releases a new photon with the same direction, polarization state and wavelength than the impinging photon, in what is called stimulated emission [Fig. 3.10(b)]. The stimulated emission is the physical basis of light amplifiers and lasers. However, sometimes the electron-hole pair can last for some time, due to Coulomb attraction. The quasi-particle formed by an electron-hole pair is referred as exciton. Both particles, the electron and the hole, each belonging to its own band, can move along the lattice just as a single entity.

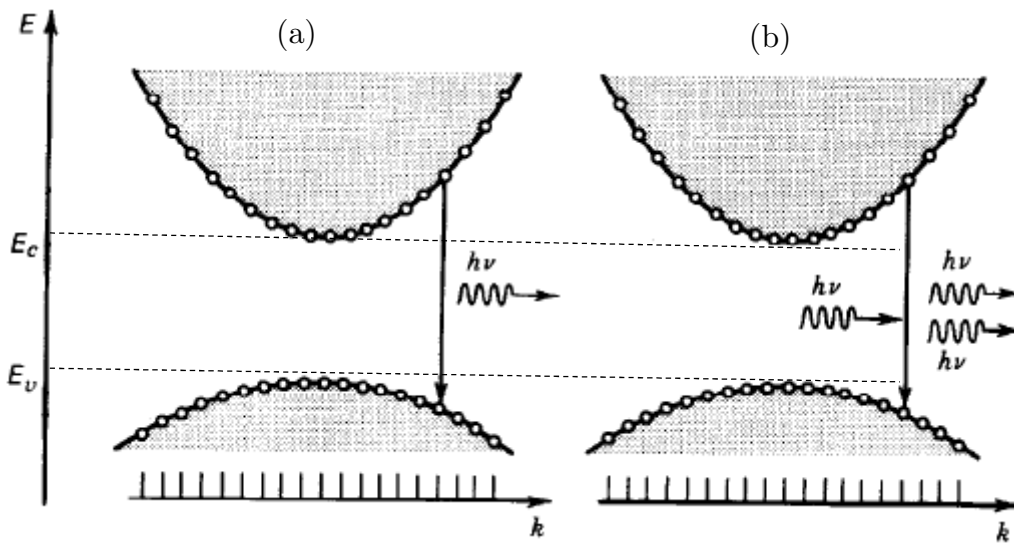


Fig. 3.10: Radiative transitions in semiconductors presenting: (a) Spontaneous emission and (b) stimulated emission. [BaTe91]

Excitons are typically the dominant radiative phenomena in many semiconductors, including III-nitrides, but not particularly in InN at room temperature, since the binding energy of the exciton is around 9 meV, much lower than the thermal energy at room temperature (~ 26 meV) [Wu09].

With independence if the transition is an absorption or emission process, two basic rules should always be satisfied: the conservation of energy and the conservation of momentum. In this analysis, only direct optical transitions will be considered:

- Conservation of Energy. The absorption/emission of a photon with associated energy $h\nu$ involves two states with energy E_1 and E_2 . Thus, the following condition must be satisfied:

$$E_2 - E_1 = h\nu \quad (3.40)$$

- Conservation of Momentum. Analogously to the conservation of energy, the momentum must be conserved. In direct band gap semiconductors, the two states involved lie in the same direction of the wave vector, \vec{k} , as it can be observed in Fig. 3.8 and Fig. 3.10. Therefore, in optical transitions in direct band gap semiconductors we have: $\vec{k}_1 = \vec{k}_2$.

Note that for indirect band gap semiconductors, these two conservation rules may also be applied. However, this typically occurs with the assistance of phonons, which are directly involved in the transition. Further reading about these processes can be found in M. S. Dresselhauss lecture notes [Dres01].

3.3 Nonlinear optical effects in semiconductors

When materials are affected by light of very high intensity, nonlinear optical effects can appear. In spite of the fact that nonlinear optical effects are present in any material, not all materials exhibit nonlinear behavior at similar power levels. This depends mainly on the nonlinear coefficients of the material, which in turn

are related to its internal structure and composition. Typically, only laser light is sufficiently intense to generate nonlinear optical effects.

For the mathematical description of these effects, we must express eq. (3.27), of the induced polarization in the medium, as a Taylor series, which leads to:

$$P_i(\vec{E}) = \epsilon_0 \left(\sum_j \chi_{ij}^{(1)} \vec{E}_j + \sum_{j,k} \chi_{ijk}^{(2)} \vec{E}_j \vec{E}_k + \sum_{j,k,l} \chi_{ijkl}^{(3)} \vec{E}_j \vec{E}_k \vec{E}_l + \dots \right) \quad (3.41)$$

Where $i, j, k, l = x, y, z$. In (3.41), $\chi^{(n)}$ is the n -th order of the susceptibility, corresponding to a tensor of rank $n+1$, with 3^{n+1} components. This equation can be expressed as:

$$\begin{aligned} \vec{P}(t) &= \vec{P}^{(1)}(t) + \vec{P}^{(2)}(t) + \vec{P}^{(3)}(t) + \dots \\ \vec{P}(t) &= \vec{P}^L(t) + \vec{P}^{NL}(t) \end{aligned} \quad (3.42)$$

Where $\vec{P}^{(i)}(t)$ is the i -th order of the polarization vector, which can be group into $\vec{P}^L(t)$ as the linear contribution and $\vec{P}^{NL}(t)$ as the nonlinear contribution to the polarization vector. Thus, eq. (3.8) can be written in the form:

$$\nabla^2 \vec{E}(t) - \frac{1}{v^2} \frac{\partial^2 \vec{E}(t)}{\partial t^2} = \frac{1}{\epsilon_0 c^2} \frac{\partial^2 \vec{P}^{NL}(t)}{\partial t^2} \quad (3.43)$$

As it was introduced for linear propagation, optical media typically do not exhibit instantaneous response. In this case, eq. (3.41) must be expressed as:

$$\begin{aligned} \vec{P}(t) &= \epsilon_0 \int_{-\infty}^{\infty} \chi^{(1)}(t-t') \cdot \vec{E}(t') dt' + \\ &+ \epsilon_0 \int_{-\infty}^{\infty} \int_{-\infty}^{\infty} \chi^{(2)}(t-t', t-t'') : \vec{E}(t') \vec{E}(t'') dt' dt'' + \\ &+ \epsilon_0 \int_{-\infty}^{\infty} \int_{-\infty}^{\infty} \int_{-\infty}^{\infty} \chi^{(3)}(t-t', t-t'', t-t''') : \vec{E}(t') \vec{E}(t'') \vec{E}(t''') dt' dt'' dt''' + \\ &+ \dots \end{aligned} \quad (3.44)$$

The first term in the right-hand side of (3.44) represents $\vec{P}^L(t)$, while following terms represent $\vec{P}^{NL}(t)$. However, for simplicity in the analysis, we will assume

that media do not have *memory*, i.e. they are instantaneous. The slowly varying envelope approximation (SVEA) can be considered if the condition (3.45) is fulfilled:

$$\left| \frac{\partial \vec{E}_0}{\partial t} \right| \ll \omega_0 |\vec{E}_0| \quad (3.45)$$

For short pulses, this only happens if $\Delta\omega \ll \omega_0$, which is not valid for pulses exhibiting only few cycles, but this will not occur in this thesis, as it was shown above, since the pulses generated in this work will be even larger than the one shown in Fig. 3.2.

In the following analysis, two considerations will be made for incident pulses: the SVEA approximation and monochromatic incident plane waves, travelling along z-axis (i.e. along the growth direction of the wurtzite III-nitride semiconductor). From the second approach, the electric field would only present components in x, y directions.

3.3.1 Second-order nonlinear optical effects

If we consider only one monochromatic incident beam along one direction in the form of:

$$\vec{E}(t) = \frac{1}{2} \hat{E}_0(t) \exp(i\omega_0 t) \quad (3.46)$$

We find that the second order contribution can be expressed as:

$$\vec{P}^{(2)}(t) = \epsilon_0 \chi^{(2)} \vec{E} \vec{E} = \frac{1}{2} \epsilon_0 \chi^{(2)} \hat{E}_0 \hat{E}_0^* + \frac{1}{4} \epsilon_0 \chi^{(2)} \hat{E}_0^2 \exp(i2\omega_0 t) + c.c. \quad (3.47)$$

The first term of eq. (3.47) corresponds to a constant field (DC). This term is related to a nonlinear optical process called optical rectification, which was first reported in 1962 by M. Bass *et. al.* [BFWW62]. The second term, which is

oscillating at double frequency of the incident beam, is related to second harmonic generation (SHG). Thus, two fields coincide at the output of the material, oscillating at frequencies ω_0 and $2\omega_0$, which are related to the fundamental incident field and the SHG, respectively. Other second-order effects can appear if we consider an incident field which contains two different oscillating frequencies, ω_1, ω_2 , such as sum- or difference-frequency generation [BFHP62],[Boyd08].

However, none of these second-order nonlinear optical effects will be observed in this thesis, since, as it was introduced in Chapter 2, wurtzite III-nitrides are dihexagonal-pyramidal crystals of type 6mm, under the international (Hermann-Mauguin) notation. This feature implies that there are only 7 non-zero elements of the 27 total $\chi_{ijk}^{(2)}$ elements, due to the crystal symmetry [Boyd08]:

$$\begin{aligned}
 \chi_{xxz}^{(2)} &= \chi_{yyz}^{(2)}, \\
 \chi_{xzx}^{(2)} &= \chi_{yzy}^{(2)}, \\
 \chi_{zxx}^{(2)} &= \chi_{zyy}^{(2)}, \\
 \chi_{zzz}^{(2)} &
 \end{aligned} \tag{3.48}$$

Considering incident light along the z-axis, the electric field will only present E_x, E_y components, and therefore the second-order nonlinear effects can be considered negligible (i.e. no non-zero component considering only the x-y plane).

3.3.2 Third-order nonlinear optical effects

For the third-order contribution, a similar analysis to what was carried out for the second order polarization can be done, finding that:

$$\vec{P}^{(3)}(t) = \epsilon_0 \chi^{(3)} \vec{E} \vec{E} \vec{E} = \frac{3}{8} \epsilon_0 \chi^{(3)} \hat{E}_0^2 \hat{E}_0^* \exp(i\omega_0 t) + \frac{1}{8} \epsilon_0 \chi^{(3)} \hat{E}_0^3 \exp(i3\omega_0 t) + c.c. \tag{3.49}$$

The second term of Equation (3.49) describes a field oscillating at three times the fundamental frequency, which corresponds to the physical phenomenon of

third-harmonic generation (THG). On the contrary, the first term is oscillating at the same frequency of the input field, implying a change of the complex refractive index of the optical medium, which shows dependence on the intensity. This effect will be explained in the next sub-section.

In this case, the following 21 elements of the total 81 of $\chi_{ijkl}^{(3)}$, are non-zero [Boyd08]:

$$\begin{aligned} \chi_{xxxx}^{(3)} = \chi_{yyyy}^{(3)} = \chi_{xxyy}^{(3)} + \chi_{xyyx}^{(3)} + \chi_{xyxy}^{(3)}, & \begin{cases} \chi_{xxyy}^{(3)} = \chi_{yyxx}^{(3)}, \\ \chi_{xyyx}^{(3)} = \chi_{yxyx}^{(3)}, \\ \chi_{xyxy}^{(3)} = \chi_{yxxy}^{(3)}, \end{cases} \\ \chi_{yyzz}^{(3)} = \chi_{xxzz}^{(3)}, & \\ \chi_{zzyy}^{(3)} = \chi_{zzxx}^{(3)}, & \\ \chi_{zyyz}^{(3)} = \chi_{zzxz}^{(3)}, & \\ \chi_{yzzy}^{(3)} = \chi_{xzzx}^{(3)}, & \\ \chi_{yzyz}^{(3)} = \chi_{xxzx}^{(3)}, & \\ \chi_{zyzy}^{(3)} = \chi_{zzzx}^{(3)}, & \\ \chi_{zzzz}^{(3)} & \end{aligned} \quad (3.50)$$

Therefore, for light propagating through z-axis, the only non-zero terms are:

$$\chi_{xxxx}^{(3)} = \chi_{yyyy}^{(3)} = \chi_{xxyy}^{(3)} + \chi_{xyyx}^{(3)} + \chi_{xyxy}^{(3)} \quad (3.51)$$

3.3.2.1 Nonlinear refractive index

If we consider light propagation through the z-axis of wurtzite III-nitrides, we can approximate $\chi_{ijk}^{(2)} = 0$ and $\chi_{ijkl}^{(3)} = \chi_{xxxx}^{(3)} = \chi_{yyyy}^{(3)}$. Therefore, the change of the complex refractive index can be found from the first term of (3.49), oscillating at the fundamental frequency:

$$\vec{P}(t) = \vec{P}^{(1)}(t) + \vec{P}^{(3)}(t) = \epsilon_0 \left(\chi^{(1)} + \frac{3}{4} \chi^{(3)} \hat{E}_0 \hat{E}_0^* \right) \frac{1}{2} \hat{E}_0 \exp(i\omega_0 t) + c.c. \quad (3.52)$$

Thus, considering eq. (3.46):

$$\vec{P}(t) = \epsilon_0 \left(\chi^{(1)} + \frac{3}{4} \chi^{(3)} \hat{E}_0 \hat{E}_0^* \right) \vec{E} + c.c. = \epsilon_0 \chi \vec{E} \quad (3.53)$$

The complex refractive index can be expressed in terms of the susceptibility as:

$$\hat{n} = \sqrt{1 + \chi} = \sqrt{1 + \chi^{(1)} + \frac{3}{4} \chi^{(3)} \hat{E} \hat{E}^*} = \sqrt{1 + \chi^{(1)} + \frac{3}{4} \chi^{(3)} |\hat{E}|^2} \quad (3.54)$$

If we remember the definition for the intensity given in eq. (3.11) and assuming transparent media ($\alpha_0 \approx 0$), we can rewrite (3.54) as follows:

$$\hat{n} = \sqrt{1 + \chi^{(1)} + \frac{3}{2} \frac{\chi^{(3)}}{c \epsilon_0 n_0} I} \quad (3.55)$$

Using the following Taylor expansion: $\left(1 + \chi^L + \chi^{NL}\right)^{1/2} \approx n_0 \left(1 + \chi^{NL} / 2n_0^2\right)$, eq. (3.55) can be written in the form:

$$\hat{n} = n_0 + \frac{3}{4} \frac{\chi^{(3)}}{c \epsilon_0 n_0^2} I \quad (3.56)$$

Thus, we can express nonlinear coefficients of the refraction (n_2) and the absorption (α_2) as a function of the third-order susceptibility for transparent media as follows:

$$n_2 = \frac{3}{4n_0^2 \epsilon_0 c} \text{Re} \left\{ \chi^{(3)} \right\} \quad (3.57)$$

$$\alpha_2 = \frac{3\pi}{\lambda n_0^2 \epsilon_0 c} \text{Im} \left\{ \chi^{(3)} \right\} \quad (3.58)$$

In the cases that will be presented in this thesis, the assumption transparency does not hold. The analysis for absorbing media can be found in Coso *et. al.*, finding the following expressions [CoSo04]:

$$n_2 = \frac{3}{4\epsilon_0 c (n_0^2 + \kappa_0^2)} \left[\operatorname{Re}\{\chi^{(3)}\} + \frac{\kappa_0}{n_0} \operatorname{Im}\{\chi^{(3)}\} \right] \quad (3.59)$$

$$\alpha_2 = \frac{3\pi}{\lambda \epsilon_0 c (n_0^2 + \kappa_0^2)} \left[\operatorname{Im}\{\chi^{(3)}\} - \frac{\kappa_0}{n_0} \operatorname{Re}\{\chi^{(3)}\} \right] \quad (3.60)$$

In summary, the refractive index and the absorption of any optical medium depends on the optical intensity as follows:

$$n(I) = n_0 + n_2 I \quad (3.61)$$

$$\alpha(I) = \alpha_0 + \alpha_2 I \quad (3.62)$$

3.3.2.2 Nonlinear refractive effects

As we have seen before, nonlinear refraction (Kerr effect) occurs in all nonlinear optical media, regardless of the symmetry in its internal structure. As it was discussed before, these effects become relevant at high pump optical intensities and lead to a change in refractive index proportional to the intensity: $\Delta n = n_2 I$, where n_2 is the Kerr coefficient, which specifically depends on the characteristics of the medium. This gives rise to a self-modulation of the phase of the optical pulse, as we will see next

Self-phase modulation

Supposing an incident Gaussian pulse propagating through a Kerr medium, the Kerr effect can induce a change in the phase velocity, due to the variation of the refractive index:

$$\frac{dn(I)}{dt} = n_2 \frac{dI}{dt} = n_2 I_0 \left(-\frac{2t}{\tau^2} \right) \exp\left(-\frac{t^2}{\tau^2} \right) \quad (3.63)$$

This fact implies a change in the instantaneous frequency (and the acquisition of some type of chirp by the pulse), given by:

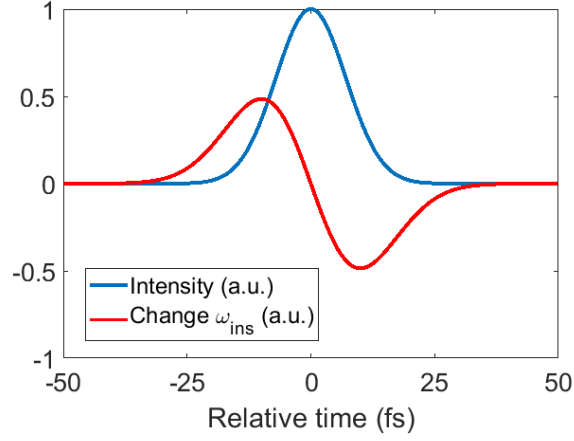


Fig. 3.11: Normalized to arbitrary unit intensity (blue line) and change of instantaneous frequency (red line) of an initially unchirped 20-fs pulse propagating through Kerr media.

$$\omega_{ins}(t) = \omega_0 - \frac{d\phi(t)}{dt} = \omega_0 - \frac{2\pi L}{\lambda_0} \frac{dn(I)}{dt} \quad (3.64)$$

Fig. 3.11 depicts an initially unchirped 20-fs pulse propagating in a Kerr medium. The red line represents the change in the instantaneous frequency, inducing a positive chirp in the pulse. Analogously, a medium with a negative Kerr coefficient, $n_2 < 0$ will induce a negative chirp in the propagating pulse. Eq. (3.65) defines the phase change per unit of optical power:

$$\gamma_{SPM} = \frac{2\pi L}{\lambda} n_2 \left(\frac{\pi}{2} w^2 \right)^{-1} = \frac{4Ln_2}{\lambda w^2} \quad (3.65)$$

Where w is the beam radius and L the medium length.

Self-focusing and other self-action effects

Some spatial self-action effects induced by the high intense beam itself will be discussed here qualitatively. When an intense beam induces Kerr effect in a material, the material behaves as a positive lens, inducing the beam to come to a focus. This is known as self-focusing effect of light and is represented in Fig. 3.12(a).

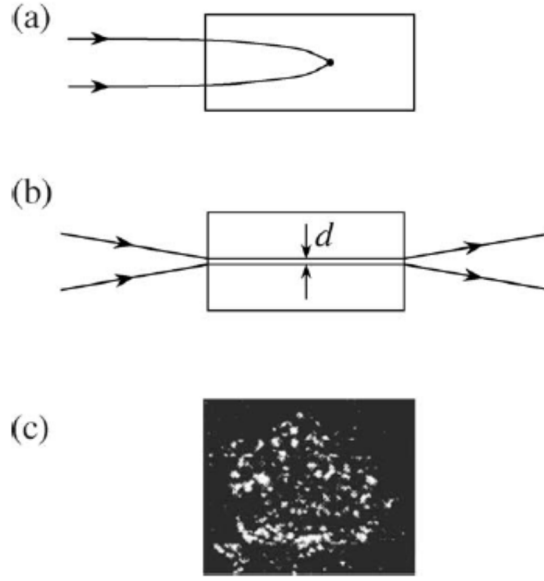


Fig. 3.12: Illustration of self-acting effects derived from Kerr effect (a) Self-focusing; (b) Self-trapping of light; (c) Laser beam break-up. [Boyd08]

If there exists an exact balance between the self-focusing effect and diffraction effects present in the material, self-trapping of light can occur, represented in Fig. 3.12(b). This is the spatial equivalent of the temporal soliton, that will be discussed in Chapter 4. In self-trapping, the beam propagates through the medium with a constant diameter. The condition for self-trapping to occur is that the power carried by the beam is exactly a critical power, P_{cr} , given by [Boyd08]:

$$P_{cr} = \frac{\pi (0.61)^2 \lambda_0^2}{8n_0 n_2} \quad (3.66)$$

If the power that the beam carries is much larger than the critical power ($P \gg P_{cr}$), then a beam break-up process can occur. In this effect, the beam breaks into as many filaments as necessary, having each of the filaments a power approximately equal to P_{cr} . Fig. 3.12(c) shows this effect.

3.3.2.3 Nonlinear absorptive effects

These effects are related to the nonlinear effects that imply changes in the absorption processes. For the purpose of this thesis, only saturable absorption (SA) and two-photon absorption (TPA), which is a particular case of reverse saturable absorption (RSA), will be treated.

Mathematically, these effects can be described through a generalization of the Beer-Lambert law:

$$\frac{dI}{dz} = -\alpha_0 I - \alpha_2 I^2 \quad (3.67)$$

Where α_2 is the nonlinear absorption coefficient (also referred sometimes as β for TPA). Integrating this equation directly from $z = 0$ to $z = L$, being L the total thickness of the material, we find:

$$I = I_0 \frac{\alpha_0 \exp\{-\alpha_0 L\}}{\alpha_0 + \alpha_2 I_0 (1 - \exp\{-\alpha_0 L\})} \quad (3.68)$$

Where L_{eff} can be defined as:

$$L_{eff} = \frac{1 - \exp\{-\alpha_0 L\}}{\alpha_0} \quad (3.69)$$

The effective length, L_{eff} , is the length of a material with no absorption which has the same nonlinear impact as a material with absorption α_0 . Note from eq. (3.69) that $L_{eff} = L$ when $\alpha_0 = 0$, and $L_{eff} < L$ for real materials, in which $\alpha_0 > 0$. Note also that $L_{eff} \rightarrow 1 / \alpha_0$ for very thick materials ($L \rightarrow \infty$) [Thév11].

For materials with small linear absorption, $\alpha_0 \approx 0$, equation (3.68) can be simplified to:

$$I = I_0 \frac{1}{1 + \alpha_2 I_0 L} \quad (3.70)$$

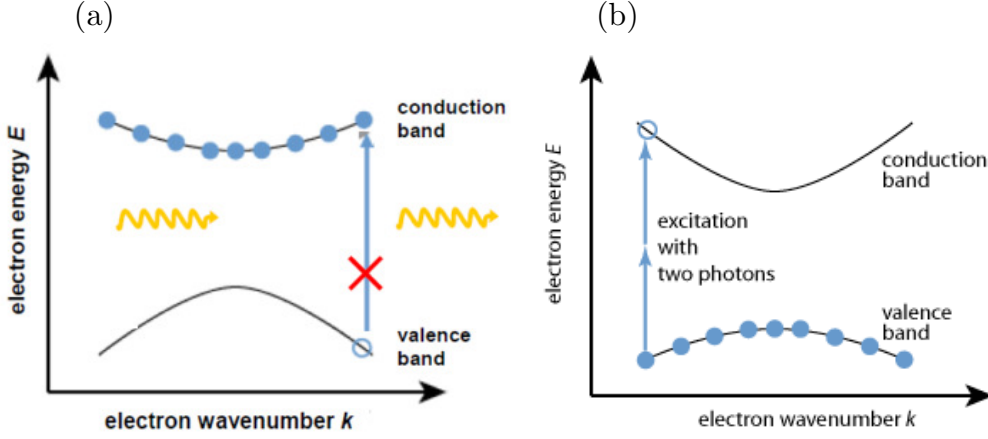


Fig. 3.13: Nonlinear absorptive processes in direct band gap semiconductors: (a) Saturable absorption effect. (b) Two-photon absorption. [Vald11]

Saturable absorption (SA)

When pumped with very high light intensity, certain absorptive materials can reduce or even saturate their absorption. Particularly, for semiconductors, if the incident photons are of approximately the same energy than the band gap energy, most of the photons will be absorbed before the spontaneous decay time, resulting in many electrons jumping to the conduction band. For high enough optical intensities, the electrons can saturate the conduction band, leading to a reduction of the available number of free states for the photons arriving afterwards. This implies that the next photons to reach the semiconductor experience a reduced absorption probability, leading to an increase in the transmission of the material (effectively, a reduction of the absorption coefficient). This effect is known as saturable absorption, implying negative values of the nonlinear absorption coefficient, $\alpha_2 < 0$. The decrease of the total absorption, α , as a function of the intensity, is generally described by eq. (3.71):

$$\alpha = \frac{\alpha_0}{1 + I/I_s} \quad (3.71)$$

Where I_s is a parameter known as the saturation intensity. Fig. 3.13(a) depicts schematically the absorption saturation in a direct band gap semiconductor.

Two-photon absorption

Reverse saturable absorption is a process in which the total absorption of the material increases when it is pumped with very high optical intensities. In opposition to SA, RSA leads to positive values of the nonlinear absorption coefficient, $\alpha_2 > 0$ (i.e. an increase in the absorption with the light intensity). Two-photon absorption is a particular case of RSA, where two photons with energy below the band gap energy are absorbed by a material simultaneously. For semiconductors, as depicted in Fig. 3.13(b), the sum of the energies of the two photons must be approximately equal or larger than the band gap energy. The first photon absorbed induces an electron to jump to a virtual state, which is in the forbidden energy band. The second photon makes possible the transition to the conduction band if the lifetime of the electron in the virtual state is larger than the time of the second photon to be absorbed.

Chapter 4 Ultrafast Fiber Lasers

This chapter introduces the concepts required for the complete understanding of passive ultrafast mode-locked (ML) fiber lasers. First, some linear and nonlinear optical effects present in optical fibers are introduced, showing how these effects affect to the solution of the nonlinear Schrödinger equation (NLSE). Afterwards, ultrafast fiber lasers are introduced. Particularly, passive mode-locked fiber lasers that use saturable absorbers based on semiconductors are introduced in detail, since they are the kind of lasers that will be experimentally demonstrated in the following chapters. Finally, the state of the art of ultrafast fiber lasers operating at telecom wavelengths is briefly summarized.

The most relevant advantages and disadvantages of using fiber lasers are discussed below:

Advantages:

- Fiber lasers tend to present very high stability and reproducibility. This is mainly due to the fact that optical fibers are very stable, even in the presence of high optical power.
- The optical pulses generated present a very high quality, compared to other kinds of lasers. Spatially, they can be focused to extremely small spot sizes, which is useful in many applications.
- Optical fibers are immune to external electromagnetic radiation.

- Fiber laser resonators are easy-to-fabricate. Moreover, due to the flexibility of optical fibers, ring resonators are also very simple to develop and pack into a small volume, requiring no mirrors in the resonator.
- Related to the previous point, the repetition rate of the laser is quite easily tuned, just with the addition or removal of optical fiber, modifying the total length of the resonator.
- Since optical fiber is so flexible, fiber lasers can present a compact form factor. Moreover, the light is confined inside the optical fiber. Thus, fiber lasers can be easily transported, eliminating the risk of damaging or altering the resonator.

Disadvantages:

- Alterations of external conditions such as temperature, vibrations or stress typically induce changes to the signal that is propagating through the optical fiber, leading to variations in the behavior of the laser.
- Undesired nonlinear optical effects might appear at high pulse energies, such as SPM or Raman scattering.
- There is a lack of fiber amplifiers at arbitrary wavelengths. Most common are Ytterbium- and Erbium-doped fiber amplifiers (YDFAs and EDFAs respectively), which typically have operation wavelengths ranging from 1025 nm to 1075 nm and 1530 nm to 1565 nm, respectively. However, the lack of amplifiers makes difficult to cover all the wavelengths where optical fibers have low losses (typically in the near infrared region).
- The achievement of very short pulses, of less than 30 fs, is still considered a challenge.

4.1 Introduction to silica optical fibers

Optical fibers are formed by a high-refractive-index core, covered by a lower-refractive-index cladding, made of the same material, all protected by a plastic jacket against external perturbations, which also provides strength to the cable and helps to prevent damage due to stress. Fig. 4.1(a) depicts schematically the cross-section of an optical fiber. Total internal reflection occurs between the core and the cladding, allowing the light to be guided mainly inside the optical core. Although this effect was well known more than hundred years ago, it was not until the second term of the 20th Century when optical fibers started to attract much attention from the photonics community. This was mainly due to the huge reduction in optical losses that optical fibers have experienced since ~1970 until the present days (from tens of dB to less than 0.2 dB/km at 1550 nm for the particular case of silica fibers). Fig. 4.1(b) shows the typical loss spectrum of single-mode silica fibers, which is the kind of optical fiber that will be used in this thesis. The transmitted power, P_T follows the Beer-Lambert law:

$$P_T = P_0 \exp\{-\alpha L\} \quad (4.1)$$

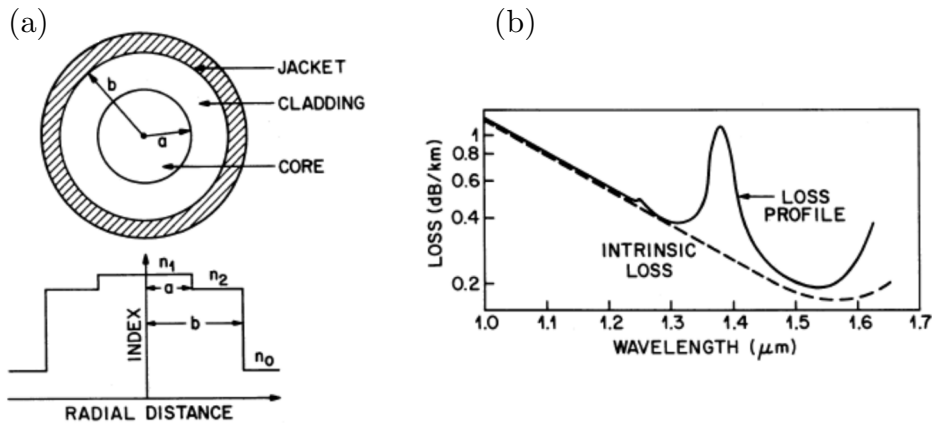


Fig. 4.1: (a) (Up) Illustration of an optical fiber cross-section showing the core, the cladding and the jacket. (Down) Qualitative refractive index profile of each of the parts. (b) Loss spectrum of single-mode silica fiber, where dashed line represents the losses from Rayleigh scattering. [Agra01]

Where α is the attenuation in the fiber, expressed in km^{-1} . However, it is very common to express this coefficient in $dB \cdot km^{-1}$, using the relation to convert a magnitude to decibels, $R(dB) = 10 \log_{10} R$ [Agra01], finding that:

$$\alpha(dB \cdot km^{-1}) \approx 4.34 \cdot \alpha(km^{-1}) \quad (4.2)$$

In current fibers, most of the losses come from Rayleigh scattering, denoted with the dashed line in Fig. 4.1(b), $\alpha_R = C_R / \lambda^4$, where the constant C_R depends on the fiber core material. The standard value for silica optical fibers ranges between $\alpha_R = 0.12 - 0.15 dB \cdot km^{-1}$ near $\lambda = 1.55 \mu m$ [Agra01].

4.1.1 Single-mode fiber

Depending on the diameter of the core, just the fundamental mode or several modes can be transmitted along the fiber simultaneously. In this thesis, only standard single-mode fiber (SMF28) will be used [Corn02]. This fiber presents a very low attenuation of just $\alpha = 0.2 dB / km$ and a dispersion value of $D_{SMF} = +18 ps / nm \cdot km$ at $\lambda = 1.55 \mu m$. The core has around $8 \mu m$ diameter, and the numerical aperture is typically in the order of $NA = 0.1$ for silica fibers.

4.1.2 Erbium-doped fiber amplifiers

To develop a fiber laser, an optical fiber amplifier becomes indispensable. In the wavelength band used in this thesis (~ 1550 nm), the ideal gain medium is an erbium-doped fiber amplifier (EDFA). In an EDFA, the fiber core is doped with Er ions, to provide gain at the wavelength band signal, when optically pumped at the right wavelength. Fig. 4.2(a) depicts schematically the three-levels that intervene in the absorption and emission process in this type of fibers. EDFAs are usually pumped at 980 nm and 1480 nm, to induce the stimulated emission at 1500-1600 nm. Er ions excited to level 3 have a fast decay to level 2 through a

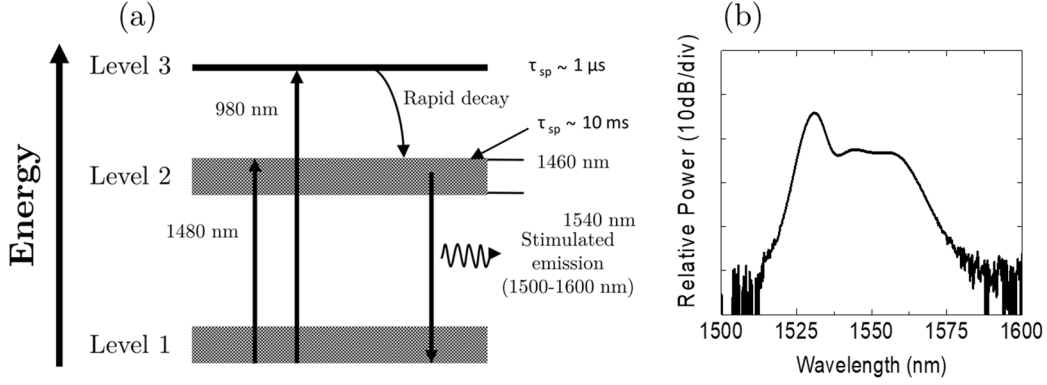


Fig. 4.2: (a) The three-level energy diagram for Er-doped silica fiber showing the 980 nm and 1480 nm pump bands, and the 1500-1600 nm emission. (b) Amplified spontaneous emission (ASE) spectrum of the EDFA used in this thesis.

non-radiative process. From this level, they decay to the first level through spontaneous or stimulated emission, making possible the laser generation.

In the first case, photons can be emitted spontaneously in all possible directions. Therefore, a proportion of the total emitted photons will be emitted in a direction in which they can be captured and guided by the fiber. The captured photons may then interact with other dopant ions and are thus amplified by stimulated emission. The initial spontaneous emission is amplified in the same manner as the signals. For this reason, this effect is referred to as Amplified Spontaneous Emission, or ASE, and is a very important factor for lasers to self-start, providing the necessary power to feed the process. ASE is emitted by the amplifier in both directions (forward and reverse to the signal). It is common to eliminate the reverse ASE by introducing a fiber isolator before the EDFA. On the other hand, forward ASE is directly related to the noise introduced by the amplifier, since it co-propagates with the incident signal. Fig. 4.2(a) depicts the amplified spontaneous emission (ASE) spectrum of the EDFA used in this thesis as gain medium for the developed fiber lasers (Accelink, TV Series, up to 24 dBm

output optical power). This ASE spectrum is usually approximately the same than the gain spectrum of the amplifier.

4.2 Light propagation in optical fibers

Optical fibers are dielectric materials in which the total electric charge density is zero, since no electric charges are present ($\rho = 0 \rightarrow \vec{J} = 0$). Moreover, they are non-magnetic media, so the magnetization vector, \vec{M} , is also assumed to be zero, leading to the equation $\vec{B} = \mu\vec{H}$ [Hera03]. The polarization field vector is related to the electric field through the linear and nonlinear susceptibility tensors, as it was introduced in eq. (3.41).

From the Helmholtz equation considering nonlinear effects, which was previously introduced in the time domain in (3.43), and taking into account the following Fourier transform in the electric field, between $\vec{E}(\vec{r}, t)$ and $\tilde{E}(\vec{r}, \omega - \omega_0)$:

$$\tilde{E}(\vec{r}, \omega - \omega_0) = \int_{-\infty}^{\infty} \vec{E}(\vec{r}, t) \exp\{i(\omega - \omega_0)t\} dt \quad (4.3)$$

We can find the wave propagation equation in the frequency domain [Thév11]:

$$\nabla^2 \cdot \tilde{E} + (n \cdot k_0)^2 \tilde{E} + k_0^2 \tilde{P}_{NL}(\omega) = 0 \quad (4.4)$$

Where the term $\tilde{P}_{NL}(\omega)$ is the nonlinear component of the polarization field in the frequency domain, n is the refractive index of the optical fiber (neglecting the losses) considering the nonlinear contribution and $k_0 = \omega / c$. When working with optical fibers, it is usually very common to make use of the wave number, $\beta(\omega) = n \cdot k_0$ (note that in Chapter 3 the wave number was referred as $k(\omega)$), which can be expressed as a Taylor series as follows:

$$\begin{aligned}\beta(\omega) &= n(\omega) \cdot k_0 = \beta_0 + \beta_1(\omega - \omega_0) + \beta_2(\omega - \omega_0)^2 + \dots \\ \beta_m &= \left(\frac{d^m \beta}{d\omega^m} \right)_{\omega=\omega_0}, (m = 0, 1, 2, \dots)\end{aligned}\tag{4.5}$$

4.2.1 The Nonlinear Schrödinger Equation (NLSE)

A brief introduction on how to find the nonlinear Schrödinger equation from the pulse propagation equation introduced in (4.4) will be presented here. Further information can be found in many references in the literature [Agra01],[Niel06],[Thév11],[Feli16].

Assuming weak coupling between the transverse (z) and longitudinal (x, y) modes, $\tilde{E}(\vec{r}, \omega - \omega_0)$ can be separated into products:

$$\tilde{E}(\vec{r}, \omega - \omega_0) = F(x, y) \tilde{A}(z, \omega - \omega_0) \exp\{i\beta_0 z\}\tag{4.6}$$

Where $\beta_0 = \beta(\omega_0)$. We will only consider the analysis in the transverse mode, i.e. the light propagation direction. Analogously to the electric field, the nonlinear component of the polarization can be expressed as:

$$\tilde{P}_{NL} = P_{NL}(\omega) \exp\{i\beta_0 z\}\tag{4.7}$$

Substituting (4.6) in (4.4), we can reach the next equation [Thév11]:

$$\frac{\partial^2 A}{\partial z^2} + 2i\beta_0 \frac{\partial A}{\partial z} + (\beta^2 - \beta_0^2) A + k_0^2 P_{NL} = 0\tag{4.8}$$

Considering that the complex amplitude $A(z, t)$ is a slowly varying function of z and t (SVEA approximation, as introduced in Chapter 3), we can neglect the second-order derivatives. Hence, we can write (4.8) as [Thév11]:

$$\frac{\partial A}{\partial z} - i(\beta - \beta_0) A - i \frac{k_0^2}{2\beta_0} P_{NL} = 0\tag{4.9}$$

Where the approximation $\beta^2 - \beta_0^2 \cong 2\beta_0(\beta - \beta_0)$ has been used. We can express again A in the time domain, using the inverse of Fourier transform:

$$A(z, t) = \frac{1}{2\pi} \int_{-\infty}^{\infty} \tilde{A}(z, \omega - \omega_0) \exp\{-i(\omega - \omega_0)t\} d\omega \quad (4.10)$$

During the Fourier transform, the operation $\omega - \omega_0$ is replaced by the operator $i(\partial / \partial t)$. Therefore, the light propagation in optical fibers can finally be expressed in time domain:

$$\frac{\partial A(z, t)}{\partial z} + \beta_1 \frac{\partial A(z, t)}{\partial t} + i \frac{\beta_2}{2} \frac{\partial^2 A(z, t)}{\partial t^2} = i\Delta\beta A(z, t) \quad (4.11)$$

Where the term $\Delta\beta$ contains information about the optical fiber losses and the fiber nonlinearity (see G. P. Agrawal's for the complete description of this term, [Agra01]). Considering these effects, we can write again (4.11) as follows:

$$\frac{\partial A(z, t)}{\partial z} + \beta_1 \frac{\partial A(z, t)}{\partial t} + i \frac{\beta_2}{2} \frac{\partial^2 A(z, t)}{\partial t^2} + \frac{\alpha}{2} A(z, t) = i\gamma |A|^2 A(z, t) \quad (4.12)$$

Eq. (4.12) is the well-known Nonlinear Schrödinger Equation, or NLSE. In this equation, the amplitude units are assumed to be normalized, so that $P = |A|^2$, β_1 and β_2 are the dispersion coefficients, that will be introduced later, α represents the losses and γ is the nonlinear coefficient, related to the Kerr coefficient and defined as:

$$\gamma = \frac{n_2 \omega_0}{c A_{eff}} \quad (4.13)$$

In (4.13), n_2 is the Kerr coefficient and A_{eff} is the effective core area. Typical values for SMF and EDF at 1550 nm are $A_{eff,SMF} = 78.5 \mu m^2$ and $A_{eff,EDF} = 28.3 \mu m^2$, respectively [ChSG11].

In case of having gain in the medium, an additional term must be included to equation (4.12), resulting in the following equation:

$$\frac{\partial A}{\partial z} + \beta_1 \frac{\partial A}{\partial t} + \frac{i\beta_2}{2} \frac{\partial^2 A}{\partial t^2} + \frac{\alpha}{2} A(z, t) - \frac{g}{2} A(z, t) = i\gamma |A|^2 A(z, t) \quad (4.14)$$

Being g the gain coefficient. Note that g will follow a saturation behavior with the optical power, as in the case of Er-doped fiber amplifiers.

4.2.2 Linear effects in optical fibers

4.2.2.1 Chromatic dispersion

Chromatic dispersion refers to the dependence of the group velocity of light with the frequency (or wavelength). Considering eq. (4.5), it can be shown that β_1 is the inverse of the group velocity, and β_2 is known as the GVD coefficient. In optical fibers, phase and group velocities are almost equal to $2 \cdot 10^8 \text{ m/s}$ [Gonz04],[Mart06]. Chromatic dispersion is usually expressed as a function of the wavelength, and is related to β by the following equation:

$$D = \frac{\partial \beta_1}{\partial \lambda} = -\frac{2\pi c}{\lambda^2} \beta_2 \quad (4.15)$$

Being D measured as $[D] = \text{ps} / \text{nm} \cdot \text{km}$, and $[\beta_2] = \text{ps}^2 / \text{km}$.

It is possible to study the effect of the GVD in optical pulses propagating in linear dispersive media directly from eq. (4.14), neglecting the attenuation, gain and nonlinearities, by setting $\beta_1 = \alpha = g = \gamma = 0$:

$$\frac{\partial A}{\partial z} + \frac{i\beta_2}{2} \frac{\partial^2 A}{\partial T^2} = 0 \quad (4.16)$$

Where T is measured in a frame of reference moving with the pulse at the group velocity, v_g , and is defined as: $T = t - z / v_g$. We can write $A(z, t)$ as a function of a normalized amplitude, $U(z, t)$ as follows:

$$A(z, t) = U(z, t) \sqrt{P_0} \exp \left\{ -\frac{\alpha z}{2} \right\} \quad (4.17)$$

Being P_0 the peak power of the pulse. The solution to equation (4.16) is:

$$U(z, T) = \frac{1}{2\pi} \int_{-\infty}^{\infty} \tilde{U}(0, \omega) \exp \left(\frac{i}{2} \beta_2 \omega^2 z - i\omega T \right) d\omega \quad (4.18)$$

The dispersion usually introduces a temporal broadening of the pulse. For example, for Gaussian incident pulses in the form of:

$$U(0, T) = \exp \left(-\frac{T^2}{2\tau^2} \right) \quad (4.19)$$

Being τ the pulse width. Introducing (4.19) in (4.18), we find that:

$$U(z, T) = \frac{\tau}{(\tau^2 - i\beta_2 z)^{1/2}} \exp \left(-\frac{T^2}{2(\tau^2 - i\beta_2 z)^{1/2}} \right) \quad (4.20)$$

Thus, a Gaussian pulse maintains its shape, but experiments a change in the time width, when propagates a distance z , given by:

$$T_1(z) = \tau \left[1 + (z/L_D)^2 \right]^{1/2} \quad (4.21)$$

Where $L_D = \tau^2/|\beta_2|$ is the dispersion length. This temporal broadening effect is shown in Fig. 4.3 and can be found explained in more detail in [Agra01].

At the same time that temporal broadening occurs, the pulse propagating through the fiber acquires some type of chirp, depending on the sign of β_2 . Particularly, it is usually referred as normal-dispersion to the case when $\beta_2 > 0$ ($D < 0$). In this case, the group velocity of the components with higher frequencies is lowered, i.e. the red components travel faster than blue components. This fact leads to the generation of a positive chirp. On the contrary, it is called

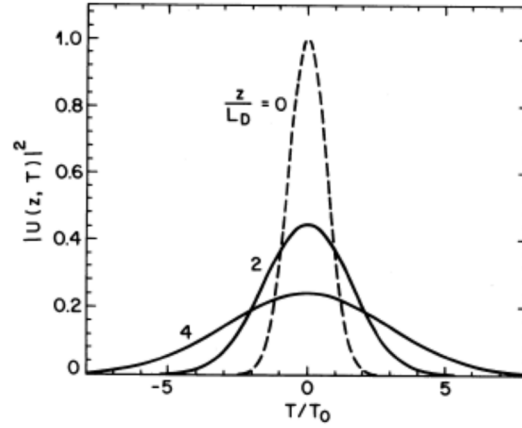


Fig. 4.3: Temporal broadening induced by the chromatic dispersion for Gaussian pulses. [Agra01]

anomalous-dispersion to the case when $\beta_2 < 0$ ($D > 0$). Opposite to the previous case, a negative chirp is generated due to the increased group velocity of higher-frequency components (blue components travel faster than red components) [Agra01]. Examples of optical fibers with normal dispersion are EDF or dispersion compensation fibers, whereas SMF typically presents anomalous dispersion.

4.2.3 Nonlinear effects in optical fibers

As explained in the previous chapter, nonlinear optical effects appear when the optical intensities of incident light are very high. Among all the nonlinear effects that can occur in optical fibers, only those relevant for the understanding of the following sections and chapters will be introduced. Particularly, the Kerr coefficient for silica-based optical fibers is very small, $n_2 \approx 2 \cdot 10^{-20} m^2 W^{-1}$. However, this small coefficient can induce some important effects if the applied power is high enough and/or the propagation length is long enough.

4.2.3.1 Self-Phase modulation (SPM) in optical fibers

As it was introduced in Chapter 3 for the case of semiconductors, the SPM effect is a change in the phase of a pulse, induced by the same intense optical pulse, which is propagating through dispersive media. The refractive index of the

material is affected by the pulse, resulting in the pulse modulating its own phase according to its intensity profile [Thév11].

In order to study this effect when light is propagating through optical fibers (following the NLSE), the normalized amplitude of the field, $U(z, T)$, as introduced in equation (4.17), will be used in eq. (4.14), where attenuation, dispersion and gain have been neglected ($\alpha, \beta, g = 0$):

$$\frac{\partial U(z, t)}{\partial z} = i\gamma P_0 |U(z, t)|^2 U(z, t) \quad (4.22)$$

At $z = L$ we find the solution:

$$U(L, t) = U(0, t) \exp\{i\phi_{NL}\} \quad (4.23)$$

Being ϕ_{NL} the nonlinear phase that introduces the SPM effect, and is related to the nonlinear coefficient of the fiber, γ , as follows:

$$\phi_{NL} = \gamma P_0 |U(0, t)|^2 L \quad (4.24)$$

It is evident from (4.24) that the nonlinear phase of the signal is affected not only by the power of the incident wave, but also by its shape. We can write the variation of the instantaneous frequency of the signal as:

$$\delta\omega(t) = -\frac{\partial\phi_{NL}}{\partial t} = -\gamma P_0 L \frac{\partial}{\partial t} \left(|U(0, t)|^2 \right) \quad (4.25)$$

For instance, supposing an incident Gaussian pulse in the form of (4.19), the frequency shift due to SPM effect will be:

$$\delta\omega(t) = -\frac{\partial\phi_{NL}}{\partial t} = 2\gamma P_0 L t \exp\left\{-\left(\frac{t}{\tau}\right)^2\right\} \quad (4.26)$$

Fig. 4.4 depicts schematically the SPM effect for an incident pulse, whose electric field is given by E_1 . The change in refractive index associated to the

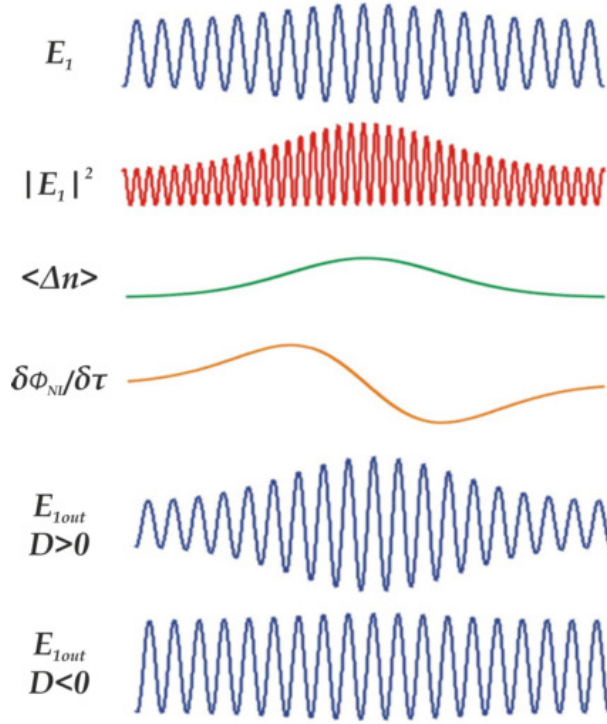


Fig. 4.4: Illustration of SPM effect giving from up to down the incident electrical field and its normalized intensity, the change induced by the material to the refractive index and the phase change. [Gonz04],[Mart06]

nonlinear SPM effect is shown in the figure. It can be appreciated how the first part of the pulse (leading edge), is being shifted to longer wavelengths ($\Delta\omega < 0$) while the last part of the pulse (trailing edge), is being shifted to lower wavelengths ($\Delta\omega > 0$).

The change in the temporal phase, given in (4.24), induces a spectral broadening, which is associated to a chirp generated in the pulse. Particularly, Fig. 4.5 depicts a simulation of this broadening in the spectrum for a 200-fs Gaussian pulse propagating through 15 m of SMF. A real experimentally measured value of the SMF fiber nonlinearity coefficient of $\gamma \approx 0.8 W^{-1} km^{-1}$ has been used in this simulation [SSLS16], while the peak power of the pulse was assumed to be $P_0 = 1 kW$. From the figure, the pulse broadening can be clearly observed, but also the appearance of symmetrical frequencies at both sides of the initial pulse (red-shifted or Stokes and blue-shifted or anti-Stokes).

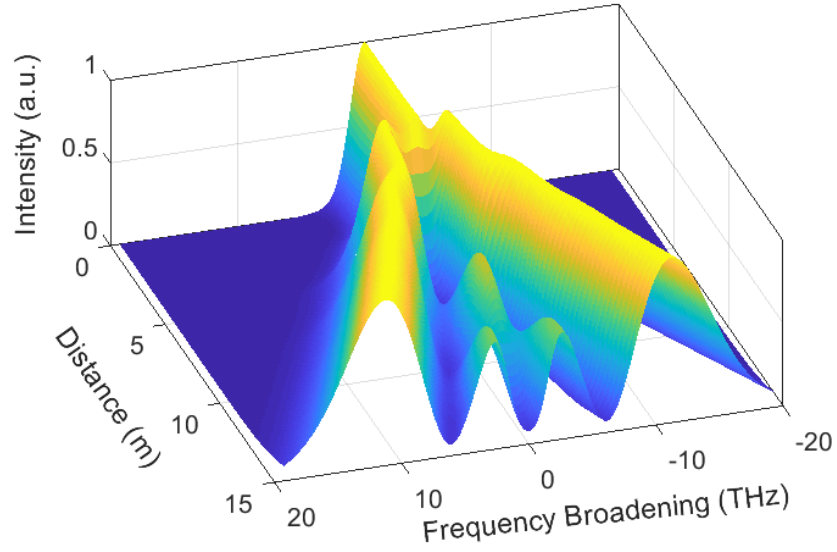


Fig. 4.5: Simulation of spectral broadening induced by SPM effect of a 200-fs Gaussian pulse propagating through 15-m long SMF. $\gamma \approx 0.8W^{-1}km^{-1}$, $P_0 \approx 1kW$

4.2.3.2 Modulation instability (MI)

Modulation instability is a phenomenon that arises in many nonlinear systems, when taking into account the interplay of both dispersive and nonlinear effects. As a result of this effect, continuous-wave beam breaks into a train of ultrashort optical pulses. This effect can be qualitatively understood from Fig. 4.4, assuming a continuous-wave with small fluctuations in the intensity profile. The Kerr effect would produce a refractive index variation, being larger at the points where the intensity is higher, producing a nonlinear phase shift, ϕ_{NL} , as introduced above. This phase shift, which can be considered as a frequency chirp, similarly as explained in 4.2.3.1, affects the signal by shifting the leading edge towards the red and the trailing edge towards the blue. Taking in mind this nonlinear effect, it is important now to consider the effect of dispersion. If the dispersion is normal ($\beta_2 > 0, D < 0$), the positive chirp generated induces a temporal broadening, leading to an outspread of the intensity perturbation. On the contrary, if the

dispersion is anomalous ($\beta_2 < 0, D > 0$), the negative chirp generated leads to a sharpening of the profile of the intensity perturbation, which at the same time strengthens the whole process, leading to the amplification of the intensity perturbation [Agra01],[Thév11].

To explore the analytical solution, we must begin considering eq. (4.14), neglecting the optical losses and the gain ($\alpha = g = 0$):

$$i \frac{\partial A}{\partial z} = \frac{\beta_2}{2} \frac{\partial^2 A}{\partial T^2} - \gamma |A|^2 A \quad (4.27)$$

Being $T = t - z / v_g$ and v_g the group velocity. As shown before, a solution to this equation is:

$$A(z, t) = \sqrt{P_0} \exp\{i\gamma P_0 z\} \quad (4.28)$$

It is interesting to test if the steady-state solution (4.28) is stable under small perturbations. For this purpose, we introduce a small amplitude perturbation, $a(z, t)$, in the form $A(z, t) = \left(\sqrt{P_0} + a(z, t)\right) \exp\{i\gamma P_0 z\}$, and we substitute it in equation (4.27) [Gonz04],[Mart06],[Angu14]:

$$i \frac{\partial a}{\partial z} = \frac{\beta_2}{2} \frac{\partial^2 a}{\partial T^2} - \gamma P_0 (a + a^*) \quad (4.29)$$

Because of the complex term, a^* , when solving equation (4.29) in the frequency domain, the Fourier frequencies Ω and $-\Omega$ are coupled. Therefore, solutions to (4.29) will be in the form [Agra01]:

$$a(z, T) = a_1 \exp\{i(Kz - \Omega T)\} + a_2 \exp\{-i(Kz - \Omega T)\} \quad (4.30)$$

Where K and Ω are the wave number and frequency of the perturbation, respectively. Substituting (4.30) in (4.29), a set of two homogeneous equations arise for a_1 and a_2 . This set has a nontrivial solution only when K and Ω satisfy the following dispersion relation [Agra01]:

$$K = \pm \frac{1}{2} |\beta_2 \Omega| \sqrt{\Omega^2 + \text{sgn}(\beta_2) \frac{4\gamma P_0}{|\beta_2|}} \quad (4.31)$$

Equation (4.31) shows the critical dependence of propagation with the GVD. In the case of normal dispersion ($\beta_2 > 0$), K is always real, and the steady state solution is stable against small perturbations. On the contrary, if the GVD is anomalous ($\beta_2 < 0$) and $\Omega < \sqrt{4\gamma P_0 / |\beta_2|}$, K is imaginary, and therefore the perturbation $a(z, T)$ grows exponentially with z . Therefore, MI manifests experimentally as an exponential gain of noise perturbations separated less than $\sqrt{4\gamma P_0 / |\beta_2|}$ from the optical pump.

The gain spectrum of modulation instability can be obtained from equation (4.31), setting $\text{sgn}(\beta_2) = -1$ and $g(\Omega) = 2\text{Im}(K)$, where the factor 2 converts $g(\Omega)$ into power gain [Mart06]:

$$g(\Omega) = |\beta_2 \Omega| \sqrt{\frac{4\gamma P_0}{|\beta_2|} - \Omega^2} \quad (4.32)$$

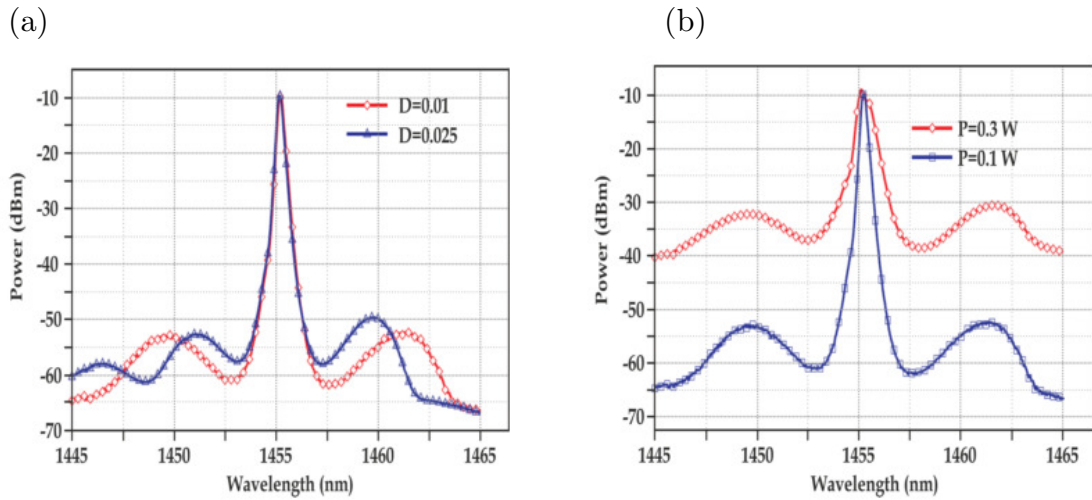


Fig. 4.6: Pulse spectrum variation as a result of the modulation instability effect as a function of: (a) dispersion and (b) pump power. [Mart06]

The gain reaches a maximum at $\Omega_{\max} = \sqrt{2\gamma P_0 / |\beta_2|}$, leading to the value of gain $g_{\max} = g(\Omega_{\max}) = 2\gamma P_0$. Fig. 4.6(a) depicts the effect of dispersion on the modulation instability spectrum at a given pump power. The more dispersive the medium is, the thinner the sidebands appear. Fig. 4.6(b) depicts the modulation instability spectra obtained for the same dispersion and different input powers. It can be appreciated how the sidebands increase their level.

4.2.4 Introduction to solitons

In optics, the term soliton usually refers to a wave that does not change during its propagation due to the existence of a balance between the nonlinear effects and dispersion. This is the case of the first-order or fundamental soliton, whose shape does not change when propagating. To study these soliton waves, the NLSE can be normalized introducing the following three dimensionless variables given in eq. (4.33) [Agra01]:

$$U = \frac{A}{\sqrt{P_0}}, \quad \xi = \frac{z}{L_D}, \quad \tau_0 = \frac{T}{\tau} \quad (4.33)$$

$$i \frac{\partial U}{\partial \xi} = \text{sgn}(\beta_2) \frac{1}{2} \frac{\partial^2 U}{\partial \tau_0^2} - N^2 |U|^2 U \quad (4.34)$$

Where P_0 is the peak power of the pulse and τ its temporal width. The parameter N gives the soliton-order, and is defined as:

$$N^2 = \frac{\gamma P_0 \tau^2}{|\beta_2|} \quad (4.35)$$

We can suppress the parameter N from the equation by defining the variable u as $u = NU$, finding the original form of the NLSE, with the assumption of anomalous GVD ($\text{sgn}(\beta_2) = -1$):

$$i \frac{\partial u}{\partial \xi} + \frac{1}{2} \frac{\partial^2 u}{\partial \tau_0^2} + |u|^2 u = 0 \quad (4.36)$$

Eq. (4.36) has a solution in the form (see [MoGo06] or [Agra01] for a complete analysis):

$$u(\xi, \tau) = \text{sech}(\tau) \exp\left\{\frac{i\xi}{2}\right\} \quad (4.37)$$

Equation (4.37) is the analytical solution to (4.36) for the case of fundamental soliton ($N = 1$). It is useful to express this field wave as a function of all the physical variables [Thév11]:

$$U(z, \tau) = \sqrt{P_0} \text{sech}\left(\tau \sqrt{\frac{\gamma P_0}{\beta_2}}\right) \exp\left\{i \frac{\gamma P_0}{2} z\right\} \quad (4.38)$$

It can be seen from (4.38) that a great balance between the dispersion of the fiber, the peak power and pulse duration is required, in order to achieve the undistorted transmission of these soliton waves. On contrary, higher-order solitons ($N > 1$) are typically breathing or evolving periodically with distance propagation. Fig. 4.7 depicts the temporal evolution of the third-order soliton over one soliton period, z_0 , which is defined as:

$$z_0 = \frac{\pi T_0^2}{2|\beta_2|} \quad (4.39)$$

It is clearly visible from the figure the pulse collapse, splitting and finally the recovery of the soliton wave over this one-soliton-period. Since these high-order solitons are very unstable, it is more usual that they split into several fundamental solitons during their propagation along the optical fiber [Thév11], and transfer part of the energy to generated dispersive waves [BHZW87].

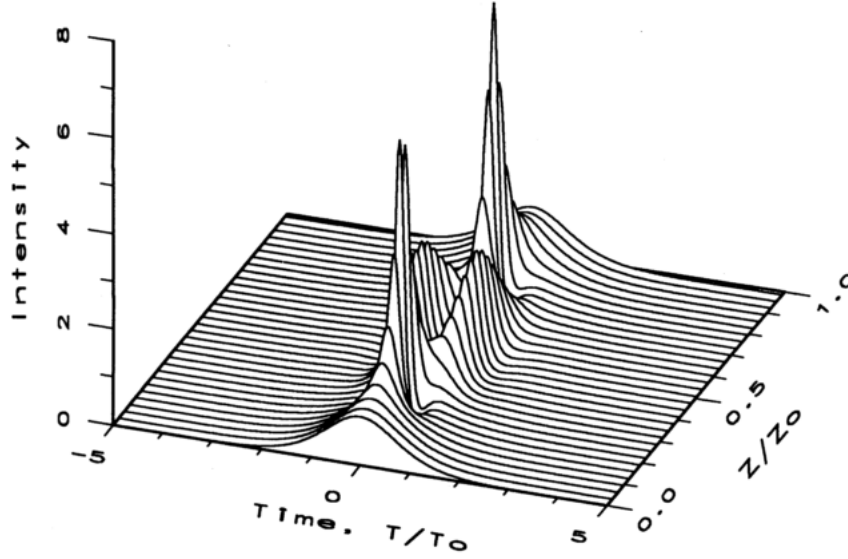


Fig. 4.7: Temporal evolution of the third-order soliton over one soliton period. [Agra01]

Despite there are many types of solitons known and widely accepted by the scientific community, such as dispersion-managed solitons, dark solitons, dissipative solitons, etc., only the first ones will be introduced in this manuscript.

4.2.4.1 Dispersion managed solitons

When solving NLSE, it is assumed that the GVD parameter (β_2) is constant. However, in many cases (particularly in fiber lasers) the dispersion is not constant but follows a periodic dispersion map by combining fibers with different characteristics such that the average GVD in each period is quite low while the local GVD at every point along the fiber link is relatively large. This technique is known as dispersion-management, and for the case of soliton propagation leads to a breathing pulse across the resonator length [Agra01]. In practice, just two kinds of fibers with opposite signs of β_2 are combined to reduce the average dispersion to a small value. When designing fiber laser resonators, dispersion-managed cavities are very useful, as they allow to use well differentiated regions of EDF and SMF. It must be taken into account that the amplitude and the

width of dispersion-managed solitons are continuously oscillating, depending on through which sign of β_2 they are travelling. Nevertheless, dispersion-managed solitons are generally chirped, leading to a pulse shape that usually presents a more likely Gaussian shape rather than the “sech²” shape of fundamental solitons, obtained for the case of constant-dispersion fibers. A further analysis of dispersion-managed solitons can be found in [TuBF12] and [MoGo06].

4.2.4.2 Soliton self-frequency shift

When high-power solitons are propagating through optical fibers the spectrum can suffer of a continuous downshift of the central frequency (redshift). This effect is known as soliton self-frequency shift, and it was first experimentally observed in 1986 by F. M. Mitschke and L. F. Mollenauer [MiMo86], and theoretically explained by J. P. Gordon in same year [Gord86], all of them working in the AT&T Bell Laboratories. This effect, also known as Raman self-frequency shift or intrapulse Raman-scattering [Agra90] is a phenomenon in which the higher-frequency components of the pulse act as a Raman gain pump to the lower-frequency components, transferring energy to the redder part of the spectrum via stimulated Raman scattering. Therefore, it is more common for very short pulses, since they typically present broader spectra and higher powers.

Fig. 4.8 depicts the first experimental observation of this effect for a 475-fs pulse propagating through 52-m-long optical fiber at different input powers, showing the strong dependence between this effect and the power associated to the pulse [MiMo86]. Moreover, Mitschke and Mollenauer showed experimentally that soliton self-frequency shift was related to the pulse width as well, particularly to $\Delta\tau^{-4}$. J. P. Gordon theoretically calculated the relation between the rate of frequency shift as a function of propagated distance, $d\nu / dz$, and the pulse width $(\Delta\tau)$, as follows [Gord86]:

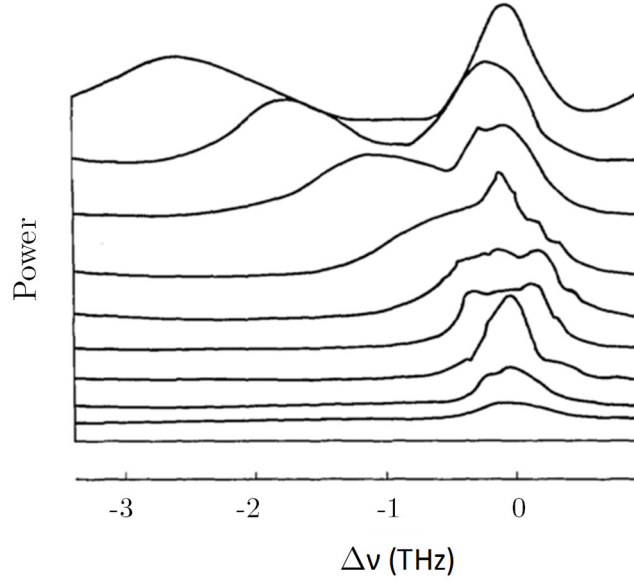


Fig. 4.8: Experimental measured spectra for increasing powers (from down to up) of a 475-fs pulse propagating through 52-m-long optical fiber. [MiMo86]

$$\frac{d\nu}{dz} \propto \frac{h(\Delta\tau)}{\Delta\tau^4} \quad (4.40)$$

Where $h(\Delta\tau)$ is a function integrated from the Raman gain spectrum [Gord86]. Soliton self-frequency shift effect can be directly integrated to the NLSE, by adding the following term to the right part of eq. (4.14) [Agra90]:

$$-t_R U \frac{\partial |U|^2}{\partial t} \quad (4.41)$$

Where t_R is related to the Raman response [Agra01]. It should be taken into account that during propagation through the optical fiber, the rate of the frequency shift often slows down, because the pulse duration is increased, due to dispersive effects.

For further reading about these or other higher-order nonlinear optical effects present in optical fibers, it is highly recommended to read books such as [Agra01] or [Thév11]. However, no other higher-order nonlinear optical effect will be studied in this thesis.

4.3 Ultrafast fiber lasers

After the discovery of fiber amplifiers, many different kinds of fiber lasers came up. As it occurs in other kind of lasers (gas, semiconductor, diode, etc.), fiber lasers can run in different operation modes such as continuous wave (CW), Q-Switching or mode-locking (ML). From the point of view of this thesis, only CW and ML operation are relevant.

When a laser is operating in continuous wave mode, the output power that the laser delivers is constant over time, which is usually called average power, P_{av} . Despite P_{av} is relatively stable, sometimes it can exhibit variations due to random oscillation of the several modes in the laser cavity. It is common that CW lasers emit photons in the form of monochromatic plane waves, introduced by equation (3.9), with constant amplitude, $E_0(t)$. This feature implies that the associated spectrum is very thin (ideally a Dirac-delta), at a frequency of ω_0 (or wavelength, λ_c).

In some cases, many of the modes oscillating in the laser cavity can be locked with the use of some element, which produces the formation of ultrashort pulses (in the order of ps or fs) circulating in the resonator. This operation mode is referred as mode-locking. The generated ultrashort pulses, as introduced in Chapter 3, are usually delimited by a Gaussian or sech envelope. The pulses are typically emitted with a separation time (T_{rep}), given by the total resonator length (in the case of ring resonators, or twice for linear resonators). ML lasers only present laser emission in the form of these ultrashort pulses. Therefore, all the power is concentrated in a short time, leading to extremely high powers, called peak power ($P_p = P_{av} T_{rep} / \tau$). Also, ML lasers present much broader optical

spectra than in the case of CW, with spectral and pulse widths inversely related, as it was introduced by the TBP in Chapter 3.

Fig. 4.9 shows a simulated comparison between CW and ML operation modes of a 20-m-long fiber laser ($T_{rep} = 100\text{ns}$) with $P_{av} = 1\text{mW}$, and emission centered at $1.55\text{ }\mu\text{m}$. In the case of ML operation, ultrashort pulses with $\tau = 100\text{fs}$ have been assumed. Fig. 4.9 (a) and (c) represent the temporal optical intensity for CW and ML, respectively. It can be clearly observed from the figure that the CW is emitting a constant power level, while in the ML operation a very short pulse with 1 kW peak power is emitted, while the emission is zero for the rest of time. Fig. 4.9 (b) and (d) show the optical spectra for each case, where the difference

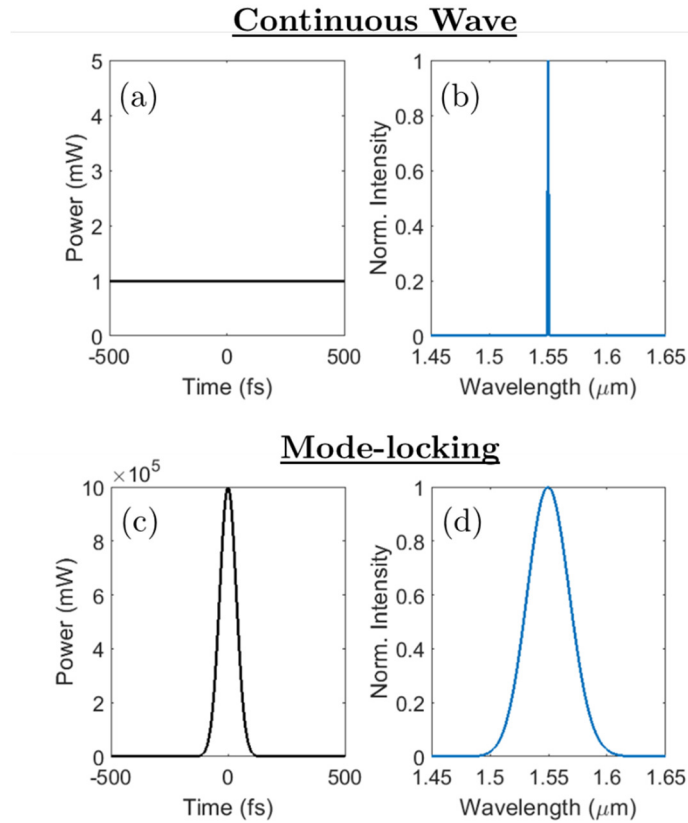


Fig. 4.9: 1-mW average power laser emission centered at $1.55\text{ }\mu\text{m}$ with 10 MHz repetition rate showing the optical intensity (a) and optical spectrum (b) for continuous wave operation. Same laser in mode-locking operation regime, delivering 100-fs pulses, showing the optical intensity (c) and optical spectrum (d).

between the thin spectrum from the CW and the broader spectrum in the case of ML is remarkable, both centered at the same wavelength.

Particularly, mode-locked lasers will be discussed in detail, due to their relevance in this thesis. The inserted element in the cavity for the achievement of mode-locking can operate either in an active or passive way [Pasc08]:

- Active mode-locking. The random modes in the laser cavity are usually locked by the insertion of a modulator, typically an electro-optic modulator, which modulates the resonator losses in exact synchronism with the resonator round-trips. The circulating pulse goes through the modulator at times where the losses are smallest, and the slightly higher losses in the pulse wings slightly shorten the pulses. With this technique, the repetition rate can be easily controlled. However, ultrafast pulses of less than 20 ps are hardly achieved, due to the limitations in the electronic response of the modulator.
- Passive mode-locking. In this technique, the loss modulation is carried out by a saturable absorber, such as NPR (Nonlinear Polarization Rotator), Kerr-based SA or Semiconductor Saturable Absorber Mirror (SESAM). This mechanism allows to generate shorter pulses (< 1 ps) than with active mode locking. The reason is that the shorter the circulating pulses become, the faster the loss modulation is. The pulse duration is determined by a balance of various effects, including the pulse shaping action of the saturable absorber, the pulse broadening by the limited gain bandwidth, the cavity dispersion and the optical nonlinearities.

4.3.1 Passively mode-locked fiber lasers

One of the most accepted ways to generate ultrashort pulses in a laser cavity is by passively mode-locking the random modes within the cavity. For this purpose, a saturable absorber must be placed inside the resonator to modulate

the optical losses in the cavity, considering the gain as stable. Fig. 4.10 shows schematically this effect, where it can be appreciated how only optical laser signal is generated when the level of losses is below the gain. The separation between consecutive peaks of the optical power gives the repetition rate of the laser, which is related to the cavity length. Particularly, most ultrafast fiber lasers are developed by placing a saturable absorber within the cavity that modulates the losses via Kerr effect or saturable absorption. In this thesis, III-nitride semiconductor saturable absorbers will be introduced as the mechanism of ultrashort pulse generation, being the first time that these materials have been used for this purpose at 1.5 μm . However, lasers fabricated with other devices will be introduced too, in order to give an overview of the state of the art.

The basic analytical model that describes the mode-locking of a laser was introduced by H. Haus [Haus00], which derivates from the NLSE, and is a particularization of the Ginzburg-Landau equation [KuAK98]:

$$T_R \frac{\partial A(T, t)}{\partial T} = \left(-iD \frac{\partial^2}{\partial t^2} + i\delta |A|^2 \right) A + \left(g - \alpha + D_{g,f} \frac{\partial^2}{\partial t^2} - q(T, t) \right) A \quad (4.42)$$

In this equation, $A(T, t)$ represents the slowly varying electrical field envelope that describes the pulses on two-time scales, the soliton or retarded time, t , and

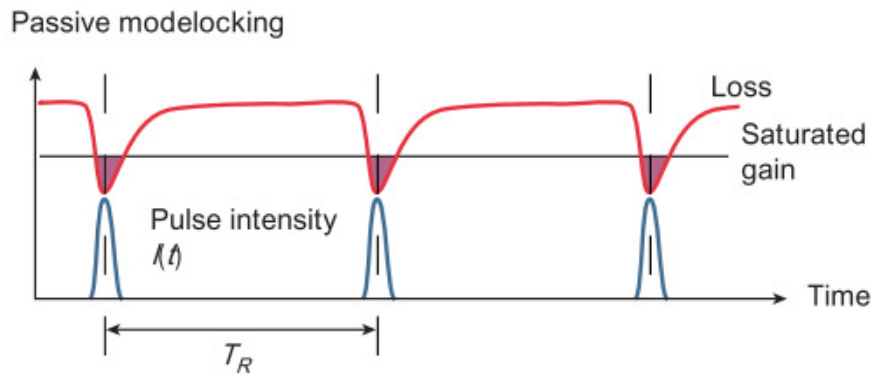


Fig. 4.10: Typical evolution of gain (black line) and losses (red line) in a passive mode-locked laser. The laser only deliver pulses when the losses are reduced under the gain level, denote by the intensity, $I(t)$ (blue line). [Kell03]

the slow time, T , of multiple round trips. T_R is the total round-trip time. D is the intracavity GDD and $D_{g,f}$ is the frequency dependence of the gain. The factor $\delta = (2\pi n_2 / \lambda A_{eff})l$ is the SPM coefficient, α represents the losses in each round-trip and $g(T)$ is the saturated gain, defined as [KuAK98]:

$$g(T) = \frac{g_0}{1 + \frac{E_p(T)}{P_L T_R}} \quad (4.43)$$

Where some terms of the gain medium must be defined: g_0 is the small signal gain, P_L its saturation power, and $E_p(T) = \int_{-\infty}^{\infty} |A(T, t)|^2 dt$ gives the pulse energy. Finally, $q(T, t)$ represents the evolution of the saturable absorber along the time, that will be discussed in next sub-section.

4.3.1.1 Fast and slow Saturable Absorbers

As it was introduced in Chapter 3, saturable absorbers are materials that present a nonlinear change of their intrinsic absorption when pumped by high enough optical intensities. A saturable absorber can be considered as fast if its recovery time is shorter than the pulse duration or slow if the recovery time is comparable or larger than the pulse that is being generated in the laser. Note that, following this definition, the same saturable absorber could be considered sometimes as fast and others as slow, depending on the duration of the pulses generated with the laser system. The behavior of fast saturable absorbers is defined by equation (4.44), where q_0 represents the linear losses and P_{sat} the saturation power of the saturable absorber [KuAK98]:

$$q(T, t) = \frac{q_0}{1 + \frac{|A(T, t)|^2}{P_{sat}}} \quad (4.44)$$

Slow saturable absorbers follow a first-order equation (4.45):

$$\frac{dq(T, t)}{dt} = \frac{q(T, t) - q_0}{\tau} - q(T, t) \frac{|A(T, t)|^2}{E_{sat}} \quad (4.45)$$

Being τ and E_{sat} the recovery time and the saturation energy of the saturable absorber, respectively. Note from equation (4.44) that a fast SA can be considered as instantaneous, in terms of simulations. Note also that for very short τ , equation (4.45) approaches to (4.44). Further reading about the differences between fast and slow saturable absorbers is given as references [Haus75a], [Haus75b], [KuAK98], [Haus00].

A SA can be placed within a laser cavity in two configurations: transmission or reflection. For the latter case, a mirror is deposited on one end of the device, which typically is based on semiconductor, known as SESAM. Fig. 4.11 depicts the typical reflection (or transmission) of a SESAM (or SA) device as a function of the input pulse fluence. As it can be seen, in these devices the reflectance (transmittance) grows with the input fluence until it reaches a maximum, which

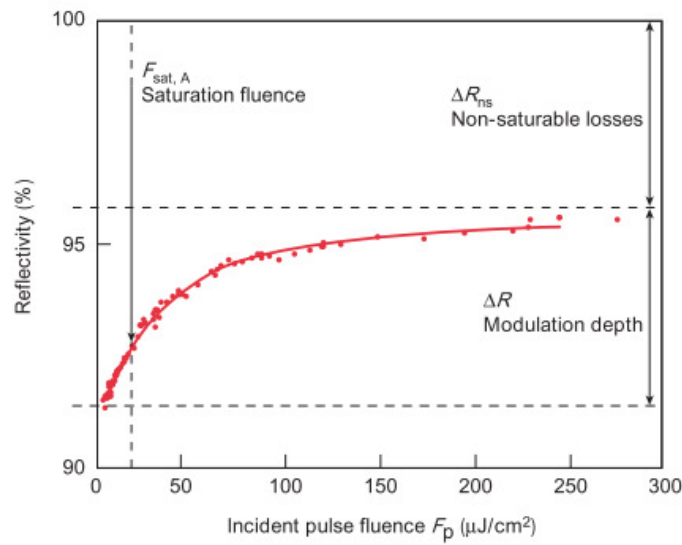


Fig. 4.11: Saturable absorber in reflection characterization curve showing its relevant parameters. [Kell03]

is due to a fall in the material absorption. The following definitions are therefore necessary with independence on whether a SA is fast or slow:

- Linear losses, (T_{lin}, R_{lin}) , is defined as the intrinsic loss that light experiences when travelling through the SA due to linear absorption (i.e. at low incident fluences). Can be seen in terms of the transmittance or the reflectance.
- Non-saturable losses, (T_{ns}, R_{ns}) , are losses which cannot be saturated as a result, typically, of the defects of the material. Scattering effects contribute to this term, along with the residual reflection or transmission in the cases of SA or SESAM, respectively. Can be seen in terms of the transmittance or the reflectance.
- The modulation depth of a SA, ΔT or ΔR , is defined as the maximum change (in transmittance or reflectance) that the device can experience. Haus demonstrated that for larger values of modulation depth, usually shorter pulses were achieved in the laser [Haus75a],[Haus75b].
- The recovery time (τ_{rec}) of the SA is the average decay time of the carriers from an excited state to the ground state.
- Saturation fluence, (F_{sat}) , is the necessary amount of fluence (defined as energy per area unit) required to saturate the absorption to $1/e$. Very often other physical quantities are used as well, as for example the saturation energy, saturation power or saturation intensity.
- The damage threshold of a SA denotes the upper threshold limit over which the material can suffer optical damage.
- Typically, it is said that a SA that has been placed inside a laser resonator is fully saturated when the following condition occurs [Kell03]:

$$E_p > E_{sat,L} E_{sat,A} \Delta R \quad (4.46)$$

Where E_p is the intracavity energy, $E_{sat,L}$ the saturation energy of the laser medium, and $E_{sat,A}$ the saturation energy of the absorber.

Normally, when the condition (4.46) is fulfilled, the laser enters in a stable mode-locking range.

4.3.2 State of the art

In this section, the literature of Er-doped ultrafast fiber lasers, delivering ultrashort pulses in the C-Band (few ps and under-ps) will be reviewed as an introduction to the ultrafast lasers developed in this thesis.

Ultrafast fiber lasers were first demonstrated in the early 1990s, where the most representative works included figure-of-8 lasers (F8), in which the mode-locking was performed by a nonlinear amplifying loop mirror (NALM). The mode-locking mechanism in these lasers is based on the Kerr effect that naturally occurs in the optical fiber. Also, fiber ring lasers mode-locked by nonlinear polarization rotation (NPR) and additive pulse mode-locking (APM) mechanisms were developed. Fig. 4.12 shows the typical configuration of each of these lasers.

NALM mode-locked lasers are based on the Sagnac interferometer, generating pure solitons with sech-shape. Duling was the first to develop this type of lasers, delivering pulses up to 2 ps time-width, with 1.5 mW of average power and

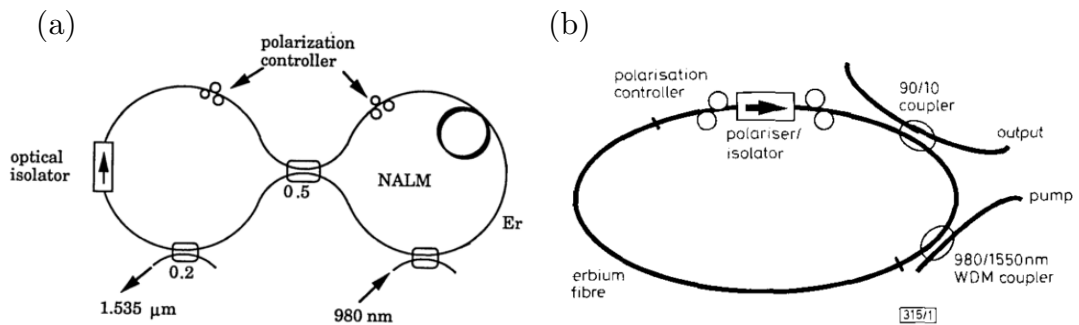


Fig. 4.12: First ultrafast fiber lasers developed: (a) Figure-of-8 laser configuration [Duli91b]; (b) NPR-based laser configuration [TaHI92].

5-10 MHz repetition rate [Duli91b],[Duli91a]. The generation of pure solitons made these lasers very limited in the amount of power which could be obtained, since they usually produce either instabilities in the soliton generation or higher-order solitons. De-chirping at the laser output, 427 fs pulses were demonstrated [NiAn06]. More recently it has been demonstrated the generation of even shorter pulses with this technique, up to 247 fs and high repetition rate, 2.45 GHz, achieving higher harmonics solitons [ChFB17].

Lasers using NPR as mode-locking mechanism can generate very short pulses, of just tens of fs. These lasers were strongly studied by Tamura *et al.* in the last decade of the last century and beginning of 2000s [TaHI92],[TJIH93]. A 77-fs pulsed laser was developed based on a dispersion-managed cavity [TIHN93]. Dispersion-managed fiber lasers produce Gaussian pulses with greatly suppressed temporal wings, [HOHF92], [TIHN93] (compared to the sech^2 -shaped pulses of pure soliton lasers) and eliminating spectral sidebands. More recently, using the same principle, less than 50 fs pulses have been achieved [TaZh07],[MCZZ10]. It must be highlighted that this technique is mostly used in the fabrication of commercial lasers by fiber laser manufacturers, allowing the master oscillator power amplifier (MOPA) configuration and very stable soliton generation.

Along with the two techniques introduced previously for ultrafast fiber laser generation, the use of semiconductor saturable absorbers was the third technique that attracted more attention. Typically, all-normal dispersion fiber lasers are fabricated using this technique, generating dissipative solitons [GrAk12]. In these lasers, saturable absorbers with a very large modulation depth are needed. Almost the majority of Er-doped fiber lasers developed by this principle used GaAs-based semiconductors. De Souza *et al.* developed bulk doped structures delivering 320 fs pulses which were almost transform-limited [SSPS93]. In 1995, Barnett *et al.* reported a high-power laser with 2 ps pulse width and 2.3 nJ pulse energy

[BRIC95]. From this point, researchers focused their interest in heterostructures, typically based on MQW or MQD, as Cabasse *et al.* did [COMH08],[CGNK11].

More recently, two new types of saturable absorbers are being used, namely carbon-based, such as graphene or carbon nanotubes (CNTs) and all-fiber lasers with topological SA in D-shape fibers. The first ones are of particular relevance, since they are being widely investigated with very positive perspectives. In 2004 Set *et al.* developed mode-locked lasers based on CNT-based SAs in both transmission and reflection configurations. They generated pulses as short as 320 fs [SYTJ04]. Many groups have contributed to the development of this kind of lasers and among them, Popa *et al.* demonstrated a 74-fs CNTs-based SA laser [PSHC12]. On the other hand, graphene-based SA lasers were also developed a little later, presenting in general larger pulse durations and reduced peak power. Moreover, the damage threshold of graphene is much lower than for CNTs [SHTP10],[ZTKZ10]. It must be highlighted the Yamashita's contributions to this topic, with in-depth investigation on both CNT-SA and graphene-SA [YaMX14].

All-fiber lasers with topological SA in D-shape fibers present the great advantage that an all-fiber laser resonator can be fabricated. Also, very high repetition rates can usually be achieved, reaching higher harmonics due to the great reduction of the total losses. As an example, Lee *et al.* developed a fiber laser using Bi₂Te₃-based SA, reaching a repetition rate of 775 MHz, but not less than 630 fs [LKJL14],[LKJL15]. Also high repetition rates, up to 3 GHz with 800 fs, were achieved using a MoSe₂-based SA [KPLJ16].

In summary, semiconductor-based SA are barely used in dispersion managed cavities, but they are typically used to generate dissipative solitons, where very complicated heterostructures are designed to achieve a large modulation depth. The shortest pulses usually come from lasers using CNTs- or NPR-based SAs. The first ones present the inconvenience of a very small modulation depth, with

large non-saturable losses and low damage threshold. On the other hand, NPR-based lasers can deliver very short pulses (with just few fs pulse-width) and are the preferred choice by the fiber laser industry. However, a strong-dependence on the polarization and, thus, the need of periodical readjustments is a great disadvantage of this kind of lasers.

Chapter 5 Experimental Methods

This chapter introduces the different experimental methods and measurement techniques used in the following chapters. Firstly, the semiconductor characterization methods are presented. In this way, a difference is made between the methods that apply, on one hand, to the study of the semiconductors structure and, on the other hand, to the methods that optically characterize the semiconductors in both, linear and nonlinear regime. Finally, the equipment and the methods for characterization of ultrafast fiber lasers are introduced.

5.1 Semiconductor characterization methods

For the structural characterization, techniques such as atomic force microscopy (AFM) have been used. Through different optical characterization techniques, the linear and nonlinear coefficients of the absorption and refractive index can be studied, along with an estimation of the relaxation time of the carriers after excitation by means of the pump and probe method.

5.1.1 Structural characterization

5.1.1.1 Atomic force microscopy (AFM)

The surfaces of the materials can be characterized by AFM, through images showing its topography. Besides obtaining information about the surface

morphology, this technique also allows the quantitative estimation of the surface roughness.

In the AFM technique, a tip is fixed at a cantilever, located close to the material surface. When the tip is close enough to the surface of the material, as depicted in Fig. 5.1(a), a Van der Waals interaction between sample and tip atoms arises. A laser beam is continuously illuminating the cantilever and the reflected laser beam is collected by a detector. The bending of the cantilever in the z-axis, perpendicular to the surface of the material which is being characterized, is continuously monitored *in situ*. The cantilever can also move in the x-y plane, parallel to the surface.

An atomic force microscope can usually run under three working modes, depending on the interaction between the tip and the surface. The three different operation modes are illustrated in Fig. 5.1(b). We refer as contact mode when the distance between the tip and the surface is typically less than 1 Å. The non-contact mode analyzes the inter-atomic force between the tip and the surface. When the tip and the surface are close enough, the Van der Waals interaction between them becomes relevant, leading to changes in the tip oscillation frequency. Variations of the z-position of the tip during the scanning are plotted

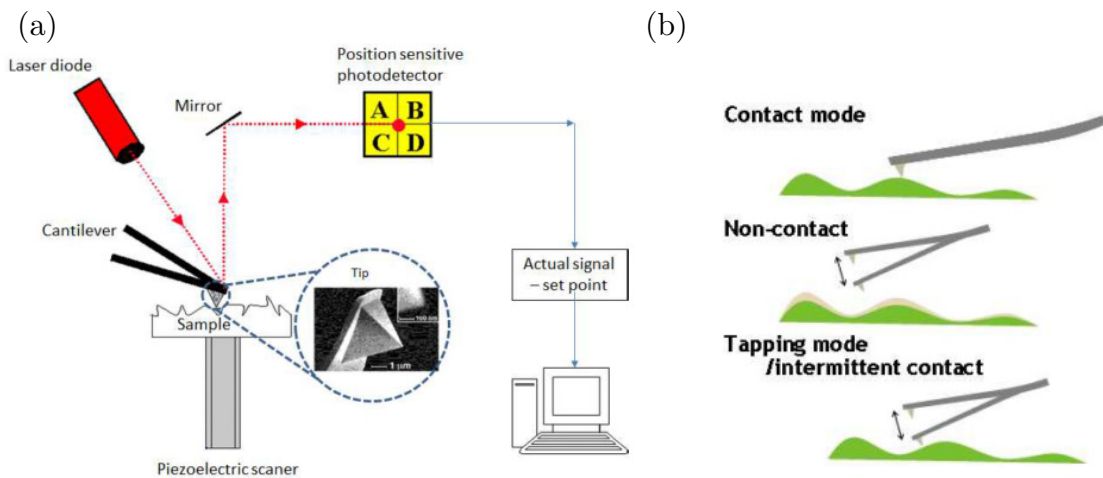


Fig. 5.1: (a) Representation of AFM experimental setup. (b) Different AFM measurement modes. [Núñez17]

as a function of the position of the tip on the x-y plane to compose the surface height image.

The AFM measurements for this thesis have been carried out using the tapping mode. In this mode, the tip oscillates near its resonance frequency. These measurements have been performed by Dr. Eva Monroy in the CEA-Grenoble facilities, using a Veeco Dimension 3100 microscope in tapping mode and probe tips Bruker OTESPA with a resonant frequency of 300-50 kHz.

5.1.2 Optical characterization methods

5.1.2.1 Linear optics

In general, all the samples used in this thesis have been optically characterized under normal incidence, i.e. parallel to the growth direction, the z-axis. Under this condition, the reflectance, R , of the samples is minimum. R can be estimated theoretically using the transfer matrix method [Grif99],[PeYF03].

The linear optical transmittance of the layers has been estimated under a simple linear transmittance characterization setup, as depicted in Fig. 5.2. A halogen lamp, emitting a wide spectrum light ranging from ultraviolet to near infrared, has been used as the excitation source. After passing through the samples, the light is finally collected using a 20x-microscope objective into a

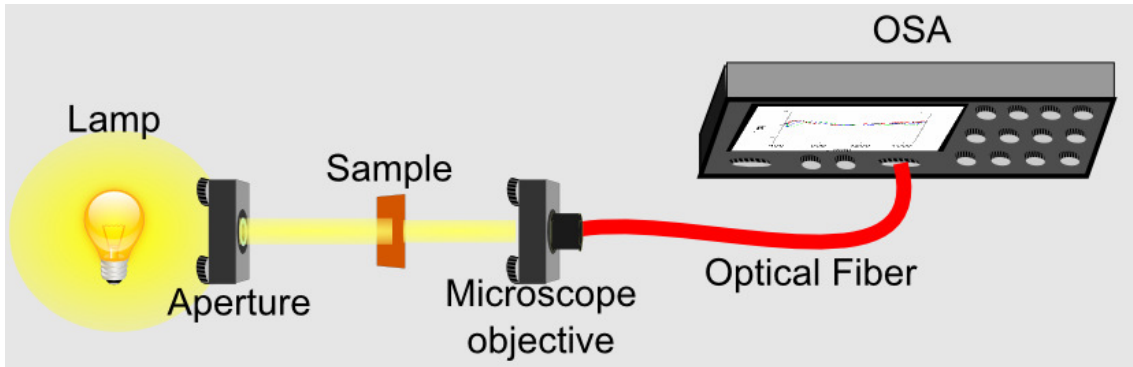


Fig. 5.2: Experimental setup for linear optical transmittance measurements with normal incidence of light onto the sample.

multimode optical fiber of approximately 1-mm-diameter core, connected to an optical spectrum analyzer (OSA). The used OSA was a Yokogawa AQ-6315B, which can measure the average power in a wide wavelength range, from 350 nm to 1700 nm. Additionally, a commercial Perkin-Elmer Lambda 1050 UV/Visible/IR spectrophotometer has been used. With this technique, we have measured wide spectra ranging from 0.5-2.9 μm . These measurements were performed by Dr. Susana Fernández in the CIEMAT, Madrid.

Knowing the layer length of the analyzed sample and from the Beer-Lambert relation introduced in Chapter 3, we can estimate the linear absorption coefficient of the material, α_0 .

From the spectra, the band gap energy of a semiconductor can be estimated using a sigmoidal approximation. With this approximation, the effective band gap energy, $E_{g,eff}$, and the absorption edge broadening, ΔE , can be obtained, taking into account that the absorption coefficient and the transmittance are related through $\alpha(E) \propto -\ln(T)$ [MMOS99],[NSCC02], neglecting the reflection losses in the sample surfaces and interfaces:

$$\alpha(E) = \frac{\alpha_0}{1 + \exp(E_{g,eff} - E/\Delta E)} \quad (5.1)$$

The band gap energy of semiconductors can also be obtained using the Tauc's plot, through the representation of the magnitude $(\alpha E)^n$ as a function of E , where n varies depending on the semiconductor properties [Tauc68] ($n = 1/2$ for direct band gap semiconductors). With a representation of $(\alpha E)^n$ versus E and fitting the linear part of this curve, the value of E_g can be estimated from the crossing point of this linear fitting with the z-axis.

The real part of the refractive index, n_0 , can be estimated too from the transmittance measurements using the Transfer Matrix Method and a Sellmeier approximation in the transparency region [ANMV03]. However, all the samples proposed in this thesis typically operate in the absorption region. Nevertheless, despite the refractive index of the semiconductors is not of great relevance for the characterization of saturable absorbers, it has been theoretically estimated, as it will be seen in Chapter 6.

5.1.2.2 Nonlinear optics

The nonlinear optical properties have been characterized by different techniques. On one hand, the z-scan technique allows to estimate the nonlinear absorption and refractive index coefficients, α_2 and n_2 , respectively. Using this setup, the intrinsic parameters of the saturable absorbers have been estimated from the changes in transmittance (obtained as the peak-to-valley differences) of the curves obtained at different pump powers, i.e. as a function of the peak intensity or the fluence. The SESAMs devices have been characterized using a different setup, comparing the reflection to a high-reflectivity (HR) reference mirror. These setups have been fully built and characterized for this thesis. Finally, the recovery times of the semiconductors were estimated using a pump-and-probe system.

Z-scan technique

The z-scan is a widely used technique in the scientific community for determining both, α_2 and n_2 , of nonlinear optical materials. This technique was first developed and fully described by M. Sheik-Bahae *et al.* [BSWH90]. In z-scan technique, a high-power pumping radiation source (typically mode-locked laser) emits a beam which is focused with an optical lens. The sample is moving along the z-axis (the optical axis of the system), close to the focal region of the beam.

Finally, the beam is usually collimated using another lens and measured using a photodetector.

Assuming a Gaussian profile for the incident beam, the intensity profile along the z -axis can be described as [Svel10]:

$$I(r, z) = I_0(z) \exp\left(-\frac{2r^2}{w(z)^2}\right) \quad (5.2)$$

Where r is the radial distance from the center axis of the beam, z is the axial distance from the beam focus, $I_0(z)$ is the incident intensity and $w(z)$ the beam radius. The beam radius is defined as the distance measured in the plane perpendicular to the propagation direction (z) at which the beam intensity falls to $1/e$ and can be defined as [Svel10]:

$$w(z) = w_0 \sqrt{1 + \left(\frac{\lambda z}{\pi w_0^2}\right)^2} \quad (5.3)$$

Being $w_0 = w(z=0)$ the beam radius at the beam focus (beam waist). The Rayleigh length, z_0 , is related to w_0 as [Svel10]:

$$z_0 = \frac{\pi w_0^2}{\lambda} \quad (5.4)$$

Thus, we can write (5.3) as [Svel10]:

$$w(z) = w_0 \sqrt{1 + \left(\frac{z}{z_0}\right)^2} \quad (5.5)$$

The z -scan measurements can be carried out in open aperture configuration (OA), meaning that no aperture is placed before the detector. Therefore, the detector is continuously measuring the total transmitted intensity as a function of the position of the sample. Since only the impinging intensity at the sample is

changing as the sample is moving, any deviation in the total transmitted intensity must be due to nonlinear absorptive effects, such as saturable absorption or reverse saturable absorption.

Using this configuration, the nonlinear absorption coefficient can be estimated, using the numerical model that was first described by M. Sheik-Bahae *et al.* [BSWH90], and optimized by M. Dinu *et al.* [DiQG03]:

$$T_{OA}(z) \approx 1 - \frac{1}{2\sqrt{2}} \frac{\alpha_2 I_0 L_{eff}}{1 + x^2} \quad (5.6)$$

Where L_{eff} is the sample effective thickness, defined in previous chapters, and $x = z / z_0$, being z the relative position of the sample in the setup. For materials exhibiting nonlinear absorptive effects, the shape of the measured curves is directly related to the sign of α_2 . Thus, materials with SA ($\alpha_2 < 0$) show a change in transmission in the form of a peak, as shown in Fig. 5.3(a), while, on contrary, a valley is generated for materials exhibiting RSA ($\alpha_2 > 0$).

Z-scan measurements can also be performed by placing a small aperture just before the detector, which is known as closed aperture configuration (CA). By doing this, only a small fraction of the beam is transmitted through the aperture. Besides the nonlinear absorption, if the beam experiences any nonlinear phase shift due to the sample, $\langle \Delta\phi \rangle$, as it is translated through the focal region, then the fraction of light measured by the detector will vary due to the Kerr-lens effect generated in the material by the intense laser beam. Thereby, the obtained z-scan curves give information about both, the nonlinear absorption and the nonlinear refraction, n_2 , and the transmittance can be expressed as [DiQG03]:

$$T_{CA}(z) \approx 1 + \frac{4x \langle \Delta\phi \rangle}{(1 + x^2)(9 + x^2)} - \frac{\alpha_2 I_0 L_{eff}}{2\sqrt{2}} \frac{(3 - x^2)}{(1 + x^2)(9 + x^2)} \quad (5.7)$$

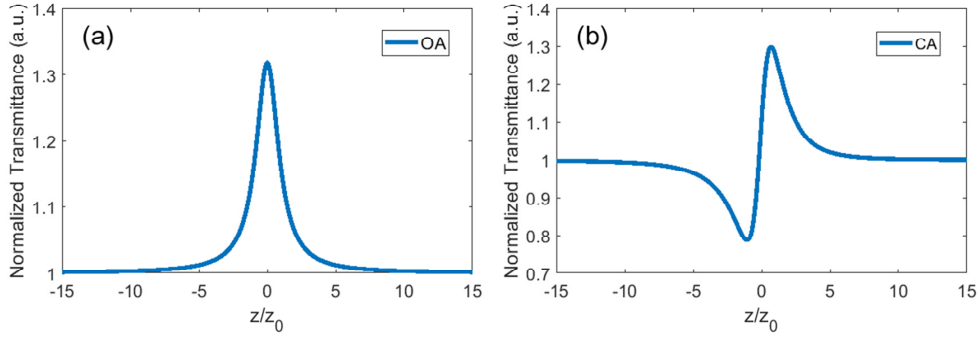


Fig. 5.3: Simulations of z-scan measurements in: (a) open aperture (OA) (with $S = 1$) and (b) closed aperture (CA) (with $S = 0.2$). Material properties: $L_{eff} = 500\mu m$, $\alpha_2 = -1000 cm / GW$, $n_2 = 5 \cdot 10^{-2} cm^2 / GW$.

Where the phase shift is:

$$\langle \Delta \phi \rangle \cong \frac{1}{\sqrt{2}} (1 - S)^{0.25} k L_{eff} n_2 I_0 \quad (5.8)$$

Where $k = 2\pi / \lambda$ and S is the fraction of beam intensity transmitted through the aperture, which usually takes values ranging between $S = 0.1 - 0.4$. In CA configuration the z-scan traces display a characteristic peak-valley shape, which is due to the Kerr-lens behavior, as shown in Fig. 5.3(b).

A scheme of the z-scan setup used in this thesis is shown in Fig. 5.4. An ultrafast fiber laser, delivering ultrashort pulses as short as 200 fs centered at $1.5 \mu m$, has been used as the pumping radiation source. The separation between consecutive pulses is approximately 185 ns, which corresponds to a repetition rate of 5.4 MHz, and the average power is 30 mW. A 99/1 fiber coupler is placed at the output of the laser source. The 1 % of the signal is continuously monitored using a commercial InGaAs-based power meter (Thorlabs S155C attached to PM100USB). The remaining 99% of the signal is launched in free space using a lens collimator. The beam is focused using a 3-cm focal length achromatic lens, leading to a beam radius at beam waist of $w_0 \approx 15\mu m$ with a Rayleigh length of

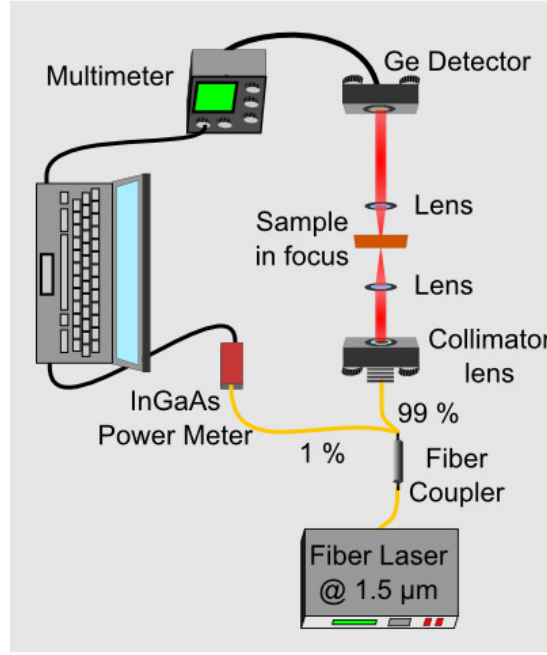


Fig. 5.4: Z-scan experimental setup using a 1.5 μm fiber laser as pumping source and Ge-photodetector as light collector.

$z_0 \approx 450\mu\text{m}$. The sample can travel through the z-axis a distance up to 25 mm, which allows the acquisition of transmittance measurements of the sample being pumped at both, low and high optical intensities. After passing through the sample, the light is collimated using a second 3-cm focal length achromatic lens and collected by a Ge detector with large area, which is connected to a multimeter (Agilent 34401A). All the system is controlled by a home-made Labview program with a computer.

The setup has been entirely developed and fully characterized in the GRIFO facilities at University of Alcalá, in collaboration with Dr. Pedro Corredera of the *Instituto de Física Aplicada* of the CSIC in Madrid.

Saturable absorbers characterization techniques

It is said that a saturable absorber is characterized when the intrinsic parameters that optically defined the material are found. These parameters were introduced in Chapter 4, as for example the linear and non-saturable

transmittances (or reflectances), the modulation depth, the saturation fluence or the damage threshold. All of them can be obtained indistinctly for a device that operates in transmission or in reflection. The main difference resides in the device itself: it is usually called a saturable absorber, SA (also SESA, in the case of semiconductors), when the device is designed to be used in transmission, and a saturable absorber mirror, SAM (also SESAM, in the case of semiconductors), when it presents a mirror at its end for the operation in reflection configuration. In this section, the technique for SESAM characterization will be introduced firstly, along with the experimental setup for this purpose. Finally, it will be explained how the SAs have been characterized in transmission.

The setup that has been developed in this thesis for SESAM characterization is based on the one described by the U. Keller's group, which was first introduced by M. Haiml *et al.* [HaGK04],[MRBI08],[Jang10], and it is depicted in Fig. 5.5.

The same pump laser that was described for z-scan has been used in this setup. The laser signal is continuously monitored with the use of a 99/1 fiber coupler, sending the 1% to a power meter. The 99% remaining is launched into free space using a collimator. A 50/50 beam splitter divides the signal perpendicular into two branches, in one of them a high-reflectivity commercial mirror is placed, while the other branch is where the SESAM to be characterized is positioned, at the focus of a 3-cm focal achromatic lens, in order to increase the fluence impinged on the sample. The light from each branch is reflected back to the beam splitter and sent to the same Ge-detector used in the z-scan setup, connected to a multimeter (Agilent 34405A). The measurements have been carried out blocking each of the beams consecutively.

For calibrating the system, two identical commercial HR-mirrors (Thorlabs, PF10-03-F01) have been placed in each branch. In this way, and knowing the reflectivity value of the mirrors, which is given by the company, the losses in each

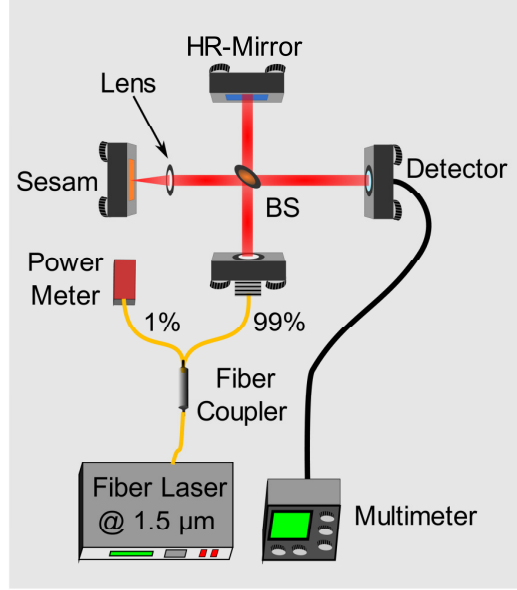


Fig. 5.5: Setup for SESAM characterization comparing reflectivity of the measured device to a known HR-mirror. Using a beam splitter (BS) and a chopper, it is possible to separate in time the four possible states generated between the two branches of the BS.

branch have been estimated. Once the system has been calibrated, the SESAM is placed in the branch with the lens. Varying the power of the incident laser, we can obtain the real reflectivity of the device as a function of the applied power, comparing to the value of the HR-mirror and considering the intrinsic losses of the system. Finally, the reflectivity is represented as a function of the input fluence, F , which is defined as the energy per area, and is usually expressed in $[F] = [\mu J / cm^2]$. The analytical model of the SESAM reflectance as a function of the incoming fluence was given by M. Haiml *et al.* [HaGK04]:

$$R(F) = R_{ns} \frac{\ln \left\{ 1 + \frac{R_{lin}}{R_{ns}} \left[\exp \left(\frac{F}{F_{sat}} \right) - 1 \right] \right\}}{F/F_{sat}} \cdot \exp \left(-\frac{F}{F_2} \right) \quad (5.9)$$

Where R_{lin} and R_{ns} are the linear and non-saturable reflectances, respectively, F_{sat} is the saturation fluence, and F_2 is the induced absorption coefficient, which is related to the nonlinear absorption. In fact, the term: $\exp(-F/F_2)$, represents

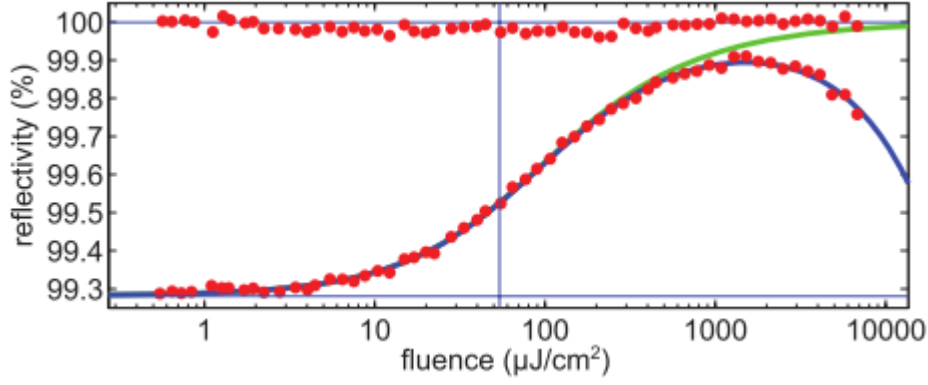


Fig. 5.6: Measurement of a HR-mirror after calibration with linear fitting and an InGaAs SESAM, with fit to equation (5.9), represented with blue line, and neglecting the induced absorption, represented with green line. [MRBI08]

the TPA effect, which typically becomes more relevant in semiconductors when the input fluence is very high. The model was derived using a rate equation describing a two-level system, as occurs in semiconductors with the BV and the CB [HaGK04]. Fig. 5.6 depicts an example of the fitting of this model for a typical InGaAs-based SESAM, finding estimated values of $F_{sat} = 54.7 \pm 1.4 \mu J / cm^2$ and $F_2 = 3.18 \pm 0.13 J / cm^2$ [MRBI08]. The upper curve represents the fitting to experimental data points of a HR-mirror for calibrating the system. In the lower curve, the experimental data points are represented in red, and shows the nonlinear change of the SESAM as a function of the fluence. The blue line represents the fitting to equation (5.9), while green line is the representation to same equation but neglecting the TPA effect.

The properties of the SA in transmission configuration have also been determined by means of the z-scan system. For this purpose, several z-scan curves have been taken varying the laser average power, i.e. the incident fluence (or intensity). From the peak-to-valley height difference in each case, the nonlinear change in transmittance can be found. Since the linear transmittance can be easily estimated, as introduced above, the total transmittance as a function of the impinging fluence can be plotted and the resultant curve is well fit by eq. (5.10):

$$T(F) = T_{ns} \frac{\ln \left\{ 1 + \frac{T_{lin}}{T_{ns}} \left[\exp \left(\frac{F}{F_{sat}} \right) - 1 \right] \right\}}{F/F_{sat}} \cdot \exp \left(-\frac{F}{F_2} \right) \quad (5.10)$$

It must be taken into account that eq. (5.10) is similar to eq. (5.9), but considering the transmittance instead of the reflectance.

Pump and probe measurements

The pump and probe technique allows to study the relaxation dynamics of materials [Kais93]. Fig. 5.7 shows a typical setup for characterizing samples in transmission. In this technique, a pulsed laser beam, is divided into two beams, one of each is of very high intensity (the pump beam), while the other one is of small intensity (the probe beam). The pump beam must carry enough intensity to excite the sample. A delay is introduced in one of the beam paths (in Fig. 5.7 is in the pump beam), in order to separate the pulses that come from each beam in the time-domain. Thus, the optical transmission of the material is measured for different time delays of the pump pulse, revealing the temporal evolution of the material with the excitation.

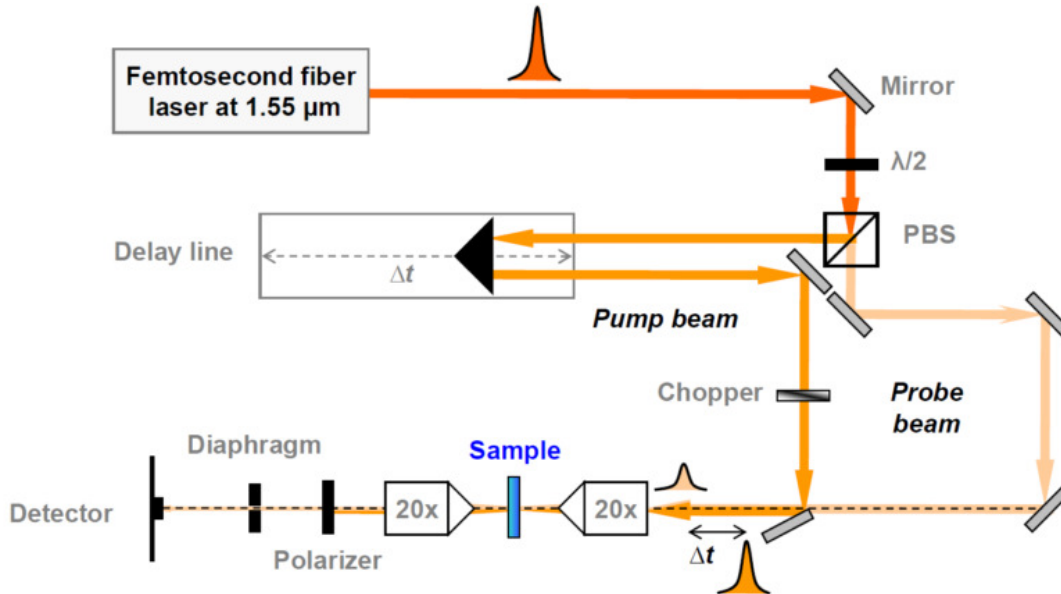


Fig. 5.7: Pump and probe setup configured for transmittance measurements. [Vald11]. PBS: Polarized Beam Splitter

The pump and probe measurements of the InN semiconductors that will be used in this thesis were performed by Dr. S. Valdueza *et al.* Thus, further information about these measurements can be found in following references: [Vald11],[VRNR12].

5.2 Characterization methods of pulsed laser sources

The pulses generated by an ultrafast fiber laser can be characterized in several ways. In this thesis, all the developed lasers have been characterized using the same setup, as shown in Fig. 5.8. The left part of Fig. 5.8 presents the laser to be characterized. In the right part of this figure, two 99/1 fibers couplers are connected in cascade, being the 99% of the first fiber coupler the input of the second fiber coupler. By doing this, different aspects of the laser can be simultaneously monitored. Typically, the 1% of the first fiber coupler is connected to a power meter. The 1% of the second fiber coupler is usually used to measure the laser optical spectrum (being connected to an OSA), the electrical spectrum (using an ESA, Electrical Spectrum Analyzer), or the repetition rate (by means

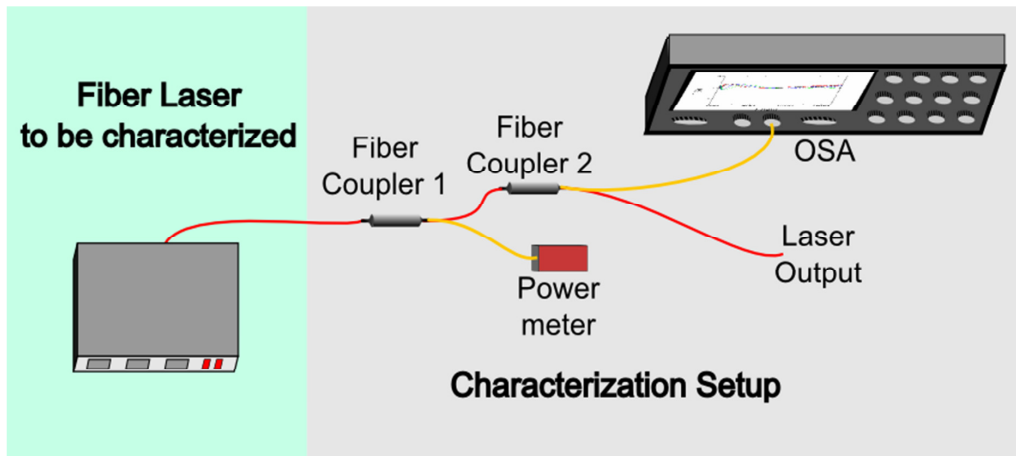


Fig. 5.8: Scheme of an ultrafast fiber laser characterization setup from the laser output of a fiber laser. Two fiber couplers are placed in cascade, allowing to send a small signal to the power meter and the OSA.

of an oscilloscope). The 99% remaining from the second fiber coupler acts as the laser output, but it can also be used to characterize the pulses by means of an optical autocorrelator.

5.2.1 Basic laser concepts

Before introducing the different laser characterization methods, some basic aspects that define short light pulses must be explained. These concepts will be commonly used in following chapters.

- Pulse width ($\Delta\tau$). The pulse width, usually measured in ps or fs for ultrashort pulses (is also known as time-width or pulse-time duration), is usually defined as the FWHM of the time-evolution of the temporal intensity of a pulse.
- Repetition rate (f_{rep}). The repetition rate is the frequency of the pulses emission, $f_{rep} = 1/T_{rep}$, i.e. the amount of pulses per time unit, where T_{rep} is the period of the pulses emission (time separation between emission of two consecutive pulses). Typically, ultrafast fiber lasers have repetition rates between 1-100 MHz.
- Peak power (P_p) and pulse energy (E_p). The peak power is the rate of energy flow in one single pulse, while the pulse energy is the total energy contained in one single pulse. For ultrafast fiber lasers, these two magnitudes are typically in the range of $P_p \approx 50W - 10kW$ and $E_p \approx 10pJ - 10nJ$, respectively. The peak power and pulse energy are related through the pulse duration as follows:

$$P_p = \frac{E_p}{\Delta\tau} \quad (5.11)$$

- Average power (P_{ave}). The average power is the rate of energy flow averaged over one full period. This magnitude can be directly

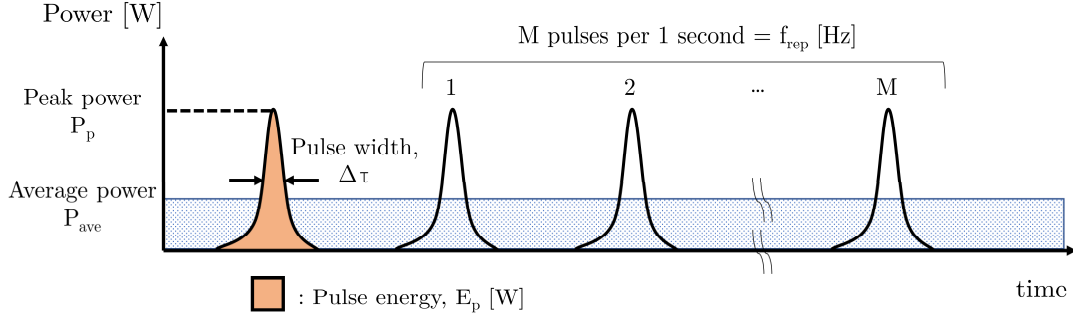


Fig. 5.9: Basic laser concepts schematically explained such as average and peak power, pulse energy, pulse width, pulse energy and repetition rate.

measured by means of a power meter. This quantity gives the average of the power that is circulating in one roundtrip inside the laser cavity. Typically, is in the order of mW.

Moreover, the average power and peak power are related as follows:

$$P_p = P_{ave} \frac{T_{rep}}{\Delta\tau} = \frac{P_{ave}}{f_{rep} \Delta\tau} \quad (5.12)$$

Fig. 5.9 depicts schematically all the magnitudes and concepts introduced.

5.2.2 Autocorrelation

Since the arise of ultrafast lasers, several methods to determine the duration of the generated ultrashort pulses have been proposed. The most common method used, and also the first that was proposed, was a simple nonlinear autocorrelation method (AC) [NaMY89], as depicted in Fig. 5.10. In this technique, the incident pulse is divided into two identical pulses. One of the pulses travels through a delay line, introducing the delay τ , and finally the two pulses cross at a nonlinear crystal, generating second-harmonic effect (SHG), in the form of:

$$E_0^{SHG}(t, \tau) \propto E_0(t) E_0(t - \tau) \quad (5.13)$$

Therefore, we can write the intensity as:

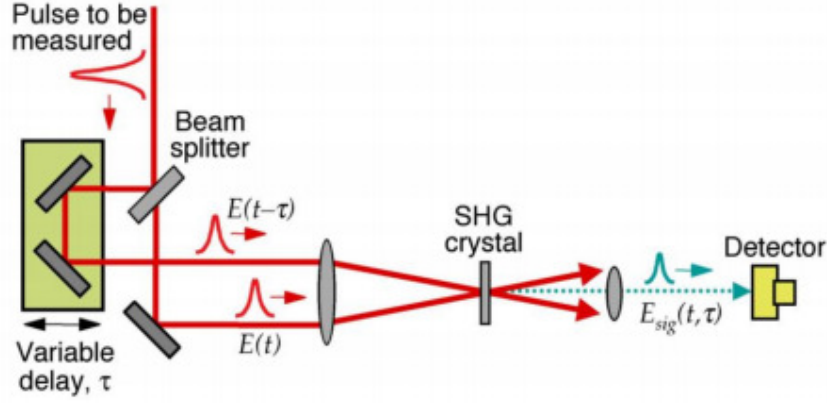


Fig. 5.10: Standard autocorrelation setup with second harmonic generation (SHG) from two identical pulses introducing a delay to one of the pulses. [Treb12]

$$I^{SHG}(t, \tau) \propto I(t)I(t - \tau) \quad (5.14)$$

Since detectors typically are too slow to resolve $I^{SHG}(t, \tau)$ in time, the measurement of (5.14) produces the time integral given by (5.15) [Treb12]:

$$A^{(2)}(\tau) = \int_{-\infty}^{\infty} I(t)I(t - \tau)dt \quad (5.15)$$

Where $A^{(2)}(\tau)$ is usually known as the autocorrelation function (ACF), or simply the autocorrelation. Hence, the pulse intensity can be directly extrapolated from the autocorrelation figures. The full width at half maximum of the curve generated from the autocorrelation, τ_{AC} , and the pulse width, τ_p , are directly related, depending on the form factor of the incident pulse. For example, for Gaussian pulses, we find the relation $\tau_{AC} / \tau_{p,Gaus} \approx 1.41$, while for sech^2 pulses, we have $\tau_{AC} / \tau_{p,\text{sech}^2} \approx 1.54$.

Although autocorrelation is relatively simpler to implement than other techniques, it only provides information about the amplitude of the pulse, but no about its phase. This issue was first solved with the implementation of a technique called frequency resolved optical grating (FROG) in 1993 [Treb12], and later with the technique of spectral phase interferometry for direct electric-field

reconstruction (SPIDER), first introduced in 1998 [IaWa98]. More recently, other techniques for pulse characterization techniques based on the phase scanning have been developed, as for example multiphoton intra-pulse interference phase scan (MIIPS) [LoPD04] or diagnosis-scan (d-scan) [MFAL12].

In this thesis, a commercial autocorrelator (APE-Mini) has been used for estimation of the pulse width. With this device, pulses ranging from 10 fs to 15 ps can be measured. The device calculates internally the ACF, and displays directly the resulting pulse, previous selection of the fitting function, which typically will be Gaussian or sech^2 , for all the measurements taken in this work. Nevertheless, all the curves obtained experimentally from the autocorrelator have been finally again fit, to find the pulse width. As an example, Fig. 5.11 shows the experimental curve obtained from the autocorrelator, denoted by black line and labelled as AC trace, and the corresponding Gaussian fitting, denoted with blue triangles.

As it was discussed in Chapter 3, the time- and frequency-dependence of the pulse shape in pure solitons, generated by an ultrafast fiber laser usually follow a sech^2 function, which was formally introduced in eq. (3.16). However, in

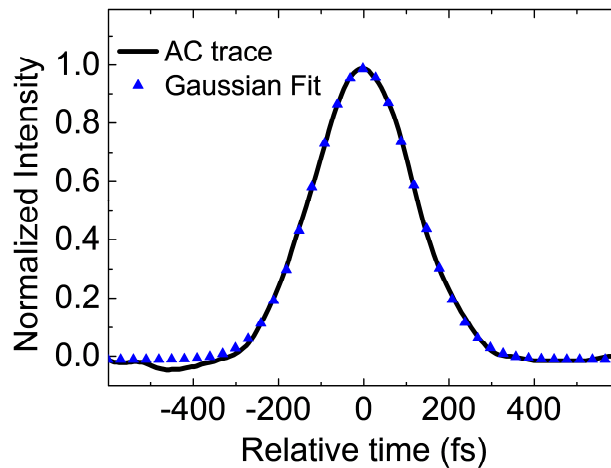


Fig. 5.11: Typical autocorrelator trace (black line) with Gaussian fitting (blue triangles) for InN-based ultrafast fiber laser used in this thesis.

dispersion-managed fiber lasers it is also very common that pulses are described by a gaussian envelope, as introduced in eq. (3.15).

5.2.3 Laser spectra measurements

All the laser spectra have been measured using the same optical spectrum analyzer (OSA, Yokogawa AQ-6315B) that was introduced previously. Typically, just 1% of the laser output is driven to the OSA from the second 99/1 fiber coupler (see Fig. 5.8).

Fig. 5.12 depicts a typical spectrum from the InN-based ultrafast fiber laser that will be presented in detail in Chapter 7. Both, the linear (black line and left vertical axis) and the logarithmic spectrum (green line and right vertical axis) are represented. Same fittings as for the autocorrelator traces have been performed for the characterization of the spectra, namely gaussian and sech^2 fittings, following the same relations expressed in equations (3.16) and (3.15), but changing the time independent variable by the frequency, and $\Delta\tau$ by $\Delta\nu$.

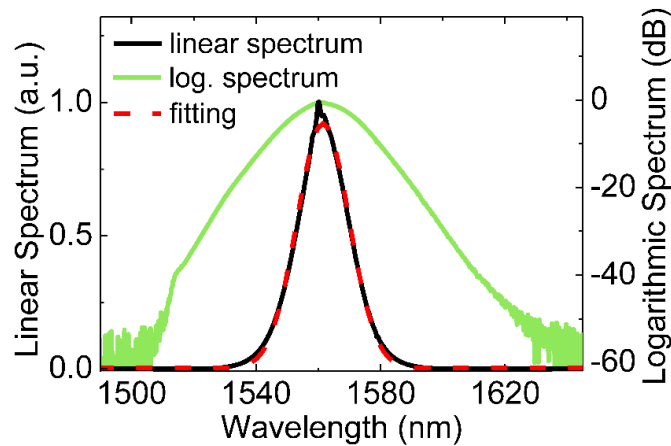


Fig. 5.12: Typical linear (black line) and logarithmic (green line) spectrum from InN-based ultrafast fiber laser used in this thesis, with Gaussian fit (red dashed line). [JMMG17]

5.2.4 ESA and oscilloscope measurements

Mode-locked lasers generate a train of pulses, as it was schematically shown in Fig. 5.9. The consecutive pulses generated are separated a certain time, which is directly related to the resonator length. Using either an electrical spectrum analyzer (ESA) or an oscilloscope, the repetition rate of the laser can be estimated by measuring the frequency or the time separation between consecutive pulses, respectively. It must be pointed out that, despite typically the repetition rate frequency of a Fabry-Perot laser is given by equation (5.16):

$$f_{rep} = \frac{c}{2L} \quad (5.16)$$

Where L is the total length of the cavity, and c the light velocity in the resonator medium (in optical fibers $c \approx 2 \cdot 10^8 m/s$). However, in a fiber laser with a ring resonator, f_{rep} is two-times this value, since the round trip is given by one single trip around the resonator. Thus, the separation between consecutive pulses is given by:

$$T_{rep} = \frac{1}{f_{rep}} \quad (5.17)$$

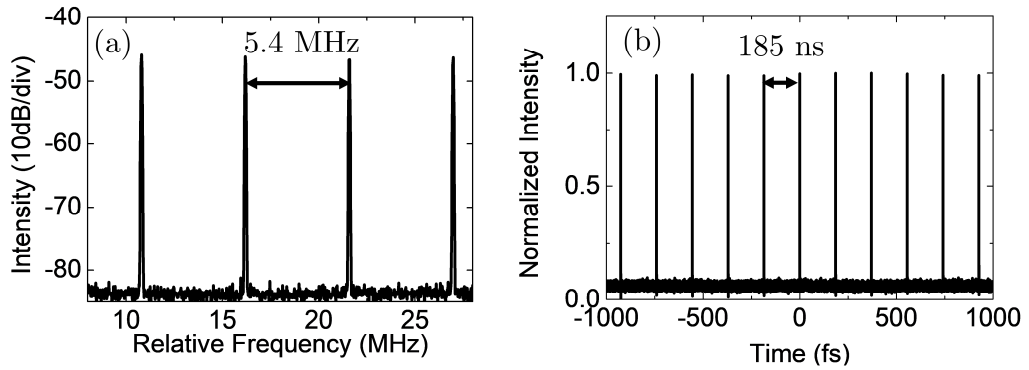


Fig. 5.13: Train of pulses of ultrafast fiber laser presenting: ESA (a) and oscilloscope (b) measurements.

Fig. 5.13 illustrates this property. Particularly, the images in Fig. 5.13 correspond to an experimental ring fiber laser of approximately 38 m long. Fig. 5.13(a) shows an experimental ESA measurement for the laser used as pump source in z-scan and SESAM characterization. It can be estimated that the repetition rate is 5.4 MHz. Additionally, measurements from an ESA give information about the signal-to-noise ratio. However, in all the measurements of this thesis, it has not been possible to do this estimation, since a balanced 20-GHz detector has been used for signal detection and it has been necessary to strongly attenuate the signal in order to avoid the detector damaging. Fig. 5.13(b) depicts the oscilloscope measurement for the same laser. The pulse separation corresponds to 185 ns, which is in agreement to the expected value, corresponding to a 38 m length laser ring cavity. Particularly, the ESA for this purpose presents a 32 GHz bandwidth (Agilent Technologies N9010A), while the oscilloscope presents a 4 GHz bandwidth, with 40 GSa/s (Agilent Technologies MSO9404A).

Chapter 6 Characterization of InN-Based Saturable Absorbers

The aim of this chapter is to show and study the characterization results obtained on novel InN-based saturable absorbers. For this purpose, InN-based bulk layers or quantum structures are considered. First, the structures that will be proposed as SAs are presented. Afterwards, a complete analysis of the structural and optical properties will be carried out. A special emphasis will be made on the optical parameters, but more specifically in the nonlinear properties, as they are required to establish the suitability of the samples as saturable absorbers. The chapter ends with a discussion about the measured properties of the samples, and how these parameters would affect to the performance of mode-locking ultrafast fiber lasers.

6.1 Study of the InN-based samples: structure and growth details

A total of 5 samples are proposed as saturable absorbers devices for operation at telecom wavelengths. The suitability of these devices mainly relies on the nonlinear absorption coefficient and total nonlinear change in absorption (or transmission), i.e. the modulation depth. The complete optical characterization has been carried out at infrared wavelengths, since fiber lasers that use standard

SMF typically operate at 1-1.5 μm . In this thesis, only lasers centered at 1.5 μm will be considered.

The proposed structures are either based on InN bulk materials or InN-based MQWs heterostructures. All the samples have been fabricated following the same conditions, under a N-limited 280 nm/h at 450 $^{\circ}\text{C}$, using the MBE technique. Also, a commercial sapphire with a 10- μm GaN template has been used as substrate in all the proposed samples. The first structure proposed, S1, consists of just a 1- μm -thick bulk InN layer, directly grown on the substrate with no buffer applied. Sample S2 is also composed by a 1- μm -thick bulk InN layer, but with a buffer layer comprising 11 periods of 4.5 nm of InN quantum wells and 7 nm $\text{In}_{0.7}\text{Ga}_{0.3}\text{N}$ barriers, that has been deposited between the InN layer and the substrate. The rest of the proposed samples (S3-S5) are MQWs heterostructures, where the active layer consists of 41 periods of InN, with InGaN barriers presenting different concentrations of In, being $\text{In}_{0.9}\text{Ga}_{0.1}\text{N}$ for S3, $\text{In}_{0.8}\text{Ga}_{0.2}\text{N}$ for S4, and $\text{In}_{0.7}\text{Ga}_{0.3}\text{N}$ for S5.

All the structures have been grown by Dr. Eva Monroy in the INAC-CEA facilities (Grenoble, France). Further details about the samples can be found in references [NGFS07],[Vald11],[VRNR12]. Table 6.1 lists all the structures proposed, which are schematically represented in Fig. 6.1.

Table 6.1 Qualitative description of the proposed InN-based structures as saturable absorbers.

Sample	Structure	Active layer thickness
S1	Bulk InN without buffer	1 μm
S2	Bulk InN with buffer	1 μm
S3	41xMQW (InN/ $\text{In}_{0.9}\text{Ga}_{0.1}\text{N}$)	471.5 nm (4.5 nm / 7 nm)
S4	41xMQW (InN/ $\text{In}_{0.8}\text{Ga}_{0.2}\text{N}$)	471.5 nm (4.5 nm / 7 nm)
S5	41xMQW (InN/ $\text{In}_{0.7}\text{Ga}_{0.3}\text{N}$)	471.5 nm (4.5 nm / 7 nm)

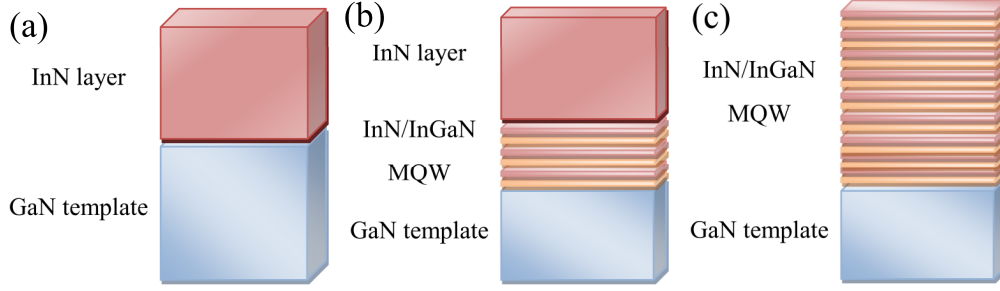


Fig. 6.1: Scheme of the InN-based structures as saturable absorbers, presenting (a) Bulk InN layer without buffer (S1), (b) Bulk InN with MQW buffer layer between substrate and InN (S2), and (c) 41xMQWs heterostructures (S3, S4, S5).

6.2 Structural characterization

The structural analysis of all the samples was carried out by means of atomic force microscopy (AFM), high-resolution X-Ray diffraction (HRXRD) and transmission electron microscopy (TEM) measurements. Further details can be found in refs [NKVC11],[Vald11],[VMMG12].

Fig. 6.2 depicts the AFM images, measured in a $2 \times 2 \text{ } \mu\text{m}^2$ area, for all the samples, labelled (a) to (e) respectively for S1 to S5. The AFM images show the top surface morphology of the materials. From the figures, all the samples exhibit a very low root-mean square roughness, below 2 nm, being particularly flat for the bulk InN with buffer and the $\text{In}_{0.9}\text{Ga}_{0.1}\text{N}$ MQWs, finding values of $\sim 0.5 \text{ nm}$. The introduction of the buffer layer in S2 [Fig. 6.2(b)] eliminates the lattice mismatch existing between the InN layer and the substrate, therefore suppressing the dislocations, which were clearly visible in the AFM image of S1 [Fig. 6.2(a)].

The HRXRD analysis, which can be observed in Fig. 6.3, confirms the good periodicity of the heterostructures, by the several satellite reflections. Measurements for the three MQW heterostructures (S3-S5) are depicted, that can be compared to the bulk InN without buffer structure (S1). The fit to the

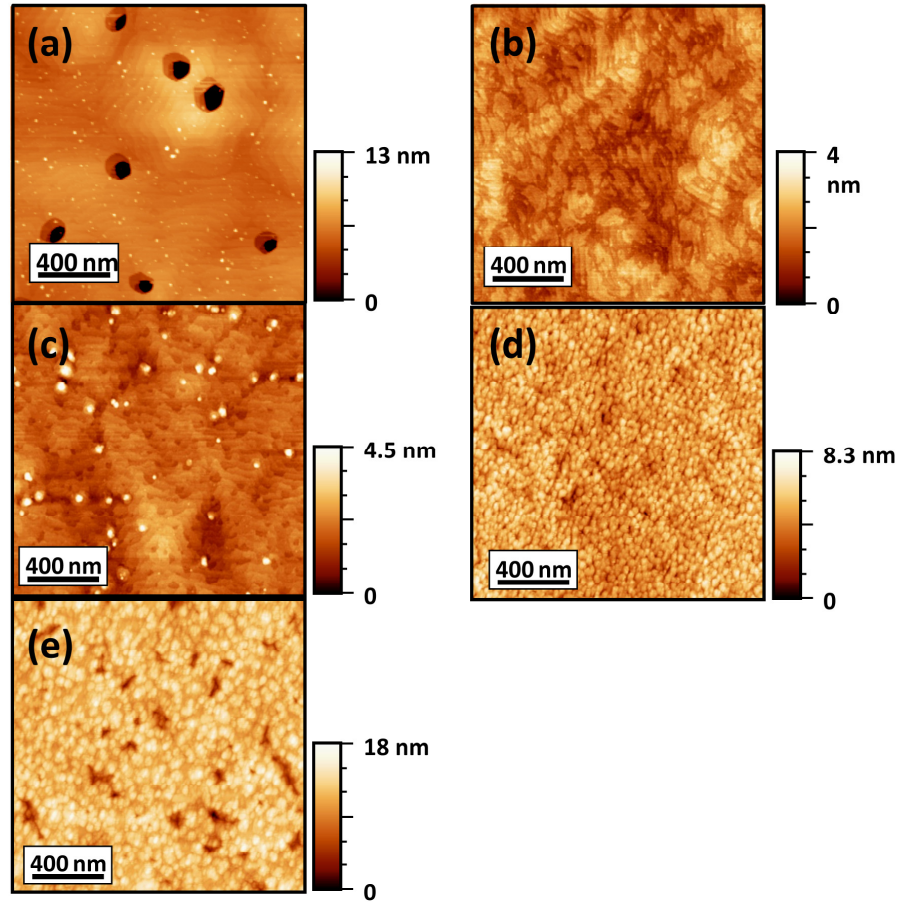


Fig. 6.2: $2 \times 2 \mu\text{m}^2$ AFM images of InN-based structures, corresponding to (a) S1; (b) S2; (c) S3; (d) S4; (e) S5. [Vald11].

theoretical calculations were carried out using X'PERT EPITAXY 40 commercial software. From these calculations, it was concluded that the angular shift of the main InN peak was consistent with the change of In concentration.

Measurements using transmission electron microscopy were also performed, as shown in Fig. 6.4. Conventional TEM analysis for $\text{In}_x\text{Ga}_{1-x}\text{N}$, when In concentration is close to 1, does not result useful, since the atomic number difference typically is not enough to provide a good contrast. For this reason, it is more useful in these kind of structures to perform dark field TEM images [NKVC11]. Particularly, Fig. 6.4(a) represents the bulk InN with buffer (S2), where both layers can be observed. The largest part (upper area), corresponds to the bulk InN layer, while the lowest part of the image is the small area that

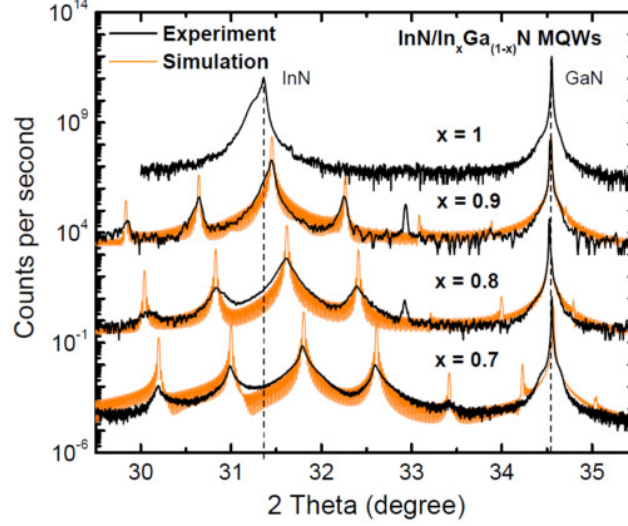


Fig. 6.3: HRXRD measurements (black line) of bulk InN without buffer (S1) and MQWs heterostructures (S3, S4, S5). Best fit to experimental data obtained by theoretical calculations (orange line) is presented for each case. The measurements have been shifted upwards for clarity. [Vald11], [NKVC11].

contains the superlattice, formed by the 11 periods of InN/In_{0.7}Ga_{0.3}N. The introduction of this superlattice helps to reduce dislocations, which are mostly of edge and mixed type [VMMG12], enhancing the crystal quality. Fig. 6.4(b) represents the dark field TEM of sample S3. As attested by the inserted intensity profile, we have a good uniformity of the well and barrier thicknesses, in agreement of those estimated by HRXRD [NKVC11].

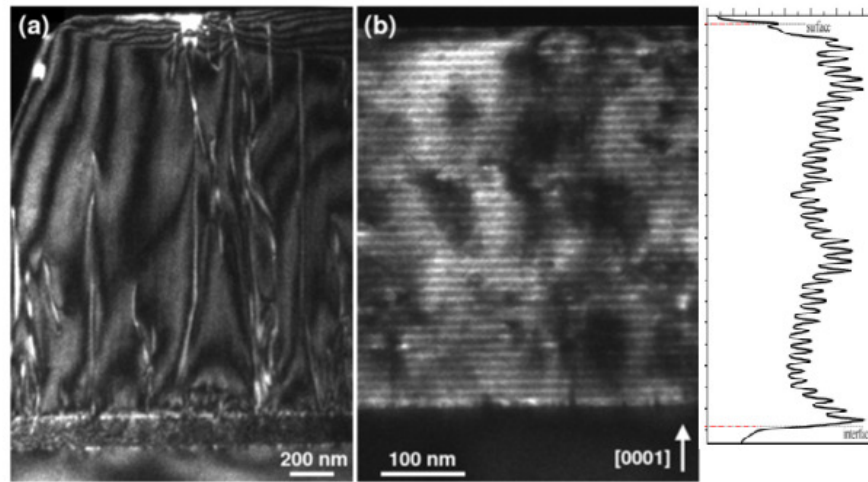


Fig. 6.4: Dark field TEM picture ($g=0002$) of: (a) Bulk InN with buffer layer (S2), and (b) the In_{0.9}Ga_{0.1}N MQW sample (S3). [VRNR12]

6.3 Optical characterization

The aim of this section is to optically characterize the different InN-based structures, in order to prove whether they are able for mode-locking laser applications or not. For this purpose, linear and nonlinear optical measurements are performed.

6.3.1 Linear optical properties

The refractive indexes of the structures have been obtained from the literature. For bulk InN and GaN at $1.55 \mu\text{m}$ are $n_{0,\text{InN}}(1.55\mu\text{m}) = 2.95$, $n_{0,\text{GaN}}(1.55\mu\text{m}) \approx 2.36$, respectively [AACM07]. Due to the small layer thicknesses of MQW structures, it can be assumed that, at $1.55 \mu\text{m}$, they present an effective refractive index that can be estimated considering the value for the wells (InN) and the value for $\text{In}_x\text{Ga}_{1-x}\text{N}$, which was calculated by M. Anani *et. al* [AACM07]. Thus, for the MQW presenting barriers with different In concentration, we have $n_{0,\text{In}_{0.9}\text{Ga}_{0.1}\text{N}}(1.55\mu\text{m}) \approx 2.8 - 2.9$, $n_{0,\text{In}_{0.8}\text{Ga}_{0.2}\text{N}}(1.55\mu\text{m}) \approx 2.6 - 2.7$ and $n_{0,\text{In}_{0.7}\text{Ga}_{0.3}\text{N}}(1.55\mu\text{m}) \approx 2.5 - 2.6$, directly estimated from the bowing curve between the bulk InN and bulk GaN. Thereby, for estimating the effective linear refractive indexes for each of the MQWs structures, S3, S4 and S5, it must be taken into account the contribution of both, the well and the barrier, and their respective length. From these considerations, we find that the refractive indexes are approximately: $n_{0,S3}(1.55\mu\text{m}) \approx 2.9$, $n_{0,S4}(1.55\mu\text{m}) \approx 2.7$ and $n_{0,S5}(1.55\mu\text{m}) \approx 2.6$.

6.3.1.1 Transmission measurements

The transmittance spectrum of each sample, $T(\lambda)$, has been measured under normal incidence using visible to near infrared radiation (from 0.5 to $2.8 \mu\text{m}$). In Fig. 6.5, the optical spectra of the 5 proposed samples are represented (S1-S5).

There is a notable difference between the bulk structures and the MQW spectra. Among the MQW heterostructures, S3 shows the most shifted transmittance spectrum to the infrared, while S5 the less. This is consistent with the expected curve, due to the larger amount of In mole fraction of the barriers. The linear absorption coefficients, $\alpha_0(\lambda)$, have been directly estimated using the Beer-Lambert law, introduced in Chapter 3 and neglecting the reflectance, finding the following expression:

$$\alpha_0(\lambda) = \frac{-\ln[T(\lambda)]}{l} \quad (6.1)$$

Where l is the layer thickness. Thus, at $1.55 \mu\text{m}$, we find that:

$$\begin{aligned} \alpha_{0,S3} &= (6.3 \pm 0.9) \cdot 10^3 \text{ cm}^{-1} \\ \alpha_{0,S4} &= (5.1 \pm 0.8) \cdot 10^3 \text{ cm}^{-1} \\ \alpha_{0,S5} &= (4.0 \pm 0.7) \cdot 10^3 \text{ cm}^{-1} \end{aligned} \quad (6.2)$$

There is an observable shift to larger wavelengths of the InN with the buffer layer with respect to the InN without buffer, which implies that S2 shows stronger absorption at $1.55 \mu\text{m}$ than S1. The estimated linear absorption coefficients for

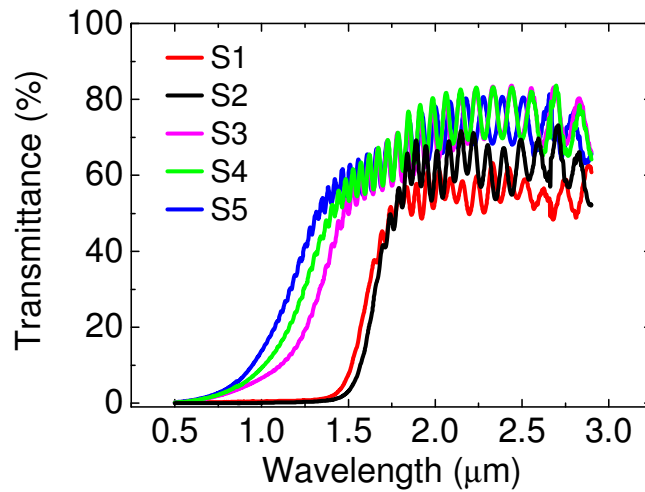


Fig. 6.5: Optical spectra comparison of the five InN-based structures proposed as SA (S1-S5).

these samples are: $\alpha_{0,S1} = (1.4 \pm 0.3) \cdot 10^4 \text{ cm}^{-1}$ and $\alpha_{0,S2} = (2.0 \pm 0.4) \cdot 10^4 \text{ cm}^{-1}$. Moreover, band gap energies of the bulk structures have been estimated using Tauc's approximation [Tauc68], as shown in Fig. 6.6, by fitting linearly the curve obtained after representing $(\alpha E)^2$ versus E . By doing this, we have obtained $E_{G,S1} = 0.80 \pm 0.10 \text{ eV} \rightarrow (\lambda = 1.55 \mu\text{m})$ and $E_{G,S2} = 0.77 \pm 0.10 \text{ eV} \rightarrow (\lambda = 1.61 \mu\text{m})$. J. Wu *et. al* demonstrated that the absorption coefficient and the residual doping are inversely related for InN layers, mainly due to strong Burstein-Moss effect [WWLA04]. Thus, the shift in the band gap energy is probably related to a reduction of the carrier concentration in S2, which has been estimated in $1 \cdot 10^{19} \text{ cm}^{-3}$ for the bulk InN without buffer and $4 - 5 \cdot 10^{18} \text{ cm}^{-3}$ for the InN with the buffer layer [WWLA04]. Moreover, the transmittance of S2 is slightly higher than S1 in the transparent region (for wavelengths above the band gap), indicating larger refractive index values. This can also be attributed to the reduction of defects in the structure, since less photons can be trapped by the material. It has not been possible to estimate the band gap energy of the MQWs

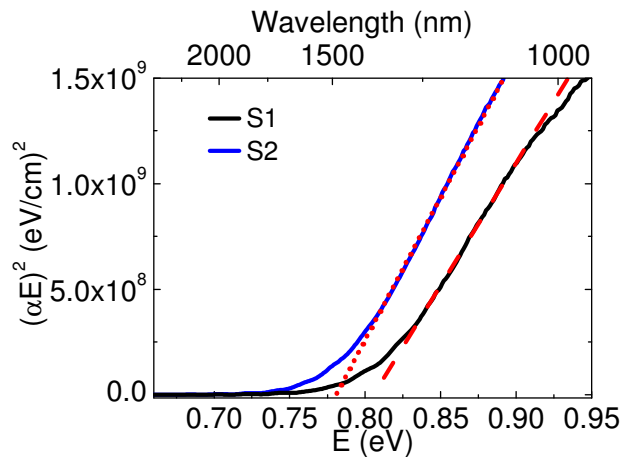


Fig. 6.6: Representations of $(\alpha E)^2$ versus E for Tauc's fit, to estimate the optical bandgap of bulk InN-based SA without buffer, S1 (black line with dashed fit curve), and bulk InN SA with buffer layer, S2 (blue line with dotted fit curve). [JMMG17],[JMMG18]

heterostructures under the Tauc's approximation, since the resultant energy obtained would correspond to the barrier band gap energy, instead of the wells.

6.3.1.2 Photoluminescence

Photoluminescence (PL) measurements at low temperature ($T = 5$ K) of all the samples were carried out by F. B. Naranjo *et. al*, using an Ar laser, centered at $\lambda = 514nm$ as pumping source [NKVC11]. Fig. 6.7(a) compares the emission spectra obtained experimentally for S1 and S2. It can be appreciated that the central peak of the emission of S2 is slightly shifted to larger wavelengths than S1. This result is in good agreement to the band gap difference between these two samples, which was discussed earlier, and it can be explained in terms of the difference in carrier concentration between the two bulk samples. Fig. 6.7(b) shows the experimental emission spectra of S1, S3 and S4. The PL of S5 was not observed under these measurements conditions. From the curves, it was observed that the emission peak blue shifts from 0.67 eV to 0.72 eV, when increasing the indium content in the structures. The inset of the figure depicts the recombination

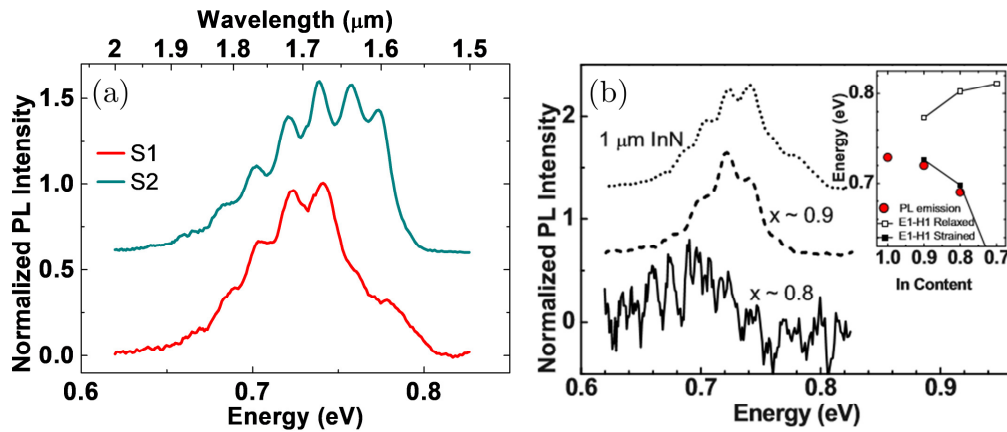


Fig. 6.7: Low temperature PL emission spectra of: (a) Samples S1 (red) and S2 (cyan). (b) Samples S1, S3 and S4. No PL was observed for S5. Inset shows the estimated recombination energies as a function of the In content for the cases of fully relaxed structure (hollow squares) and fully strained on InN (filled squares). Filled red circles are the experimental PL peak energies. [NKVC11]

energies of the samples, considering the structures fully relaxed (hollow squares) and fully strained on InN (filled squares), calculated using Nextnano³ software. The values are in good agreement to the experimental PL peak energy values, represented by filled red circles in the graph. These results obtained were explained in terms of the huge piezo-electric fields, that typically these structures present [NKVC11].

6.3.2 Nonlinear optical properties

In this section, results of the nonlinear optical characterization of the samples are presented and discussed.

6.3.2.1 Pump and Probe measurements

The pump and probe technique was used for estimation of the interband relaxation time of the structures. Samples S2 and S3 were measured at room temperature. The excitation source was an ultrafast laser, delivering pulses with 100 fs time width, centered at 1.55 μm , at a repetition rate of 100 MHz. With these values, the pump beam peak intensity was estimated in 0.35 GW/cm², while the probe beam peak intensity was about 1 order of magnitude lower. Fig. 6.8 shows the relaxation curves for each sample. From the observations of S2, it can be concluded that at least 2 relaxation paths are present. After study the material response as a function of the applied power, it was found that the relaxation time can be reduced from 30 to 13 ps, when the excitation carrier density increased from $n_{exc} \approx 4.3 \cdot 10^{18} \text{ cm}^{-3}$ to $n_{exc} \approx 3.8 \cdot 10^{19} \text{ cm}^{-3}$ as represented in the inset of the figure. This relaxation path was attributed to Auger recombination, while the other relaxation path, of $\tau \approx 70 \text{ ps}$, was related to a non-radiative process, probably via the defects present in the structure. On the other hand, the MQW

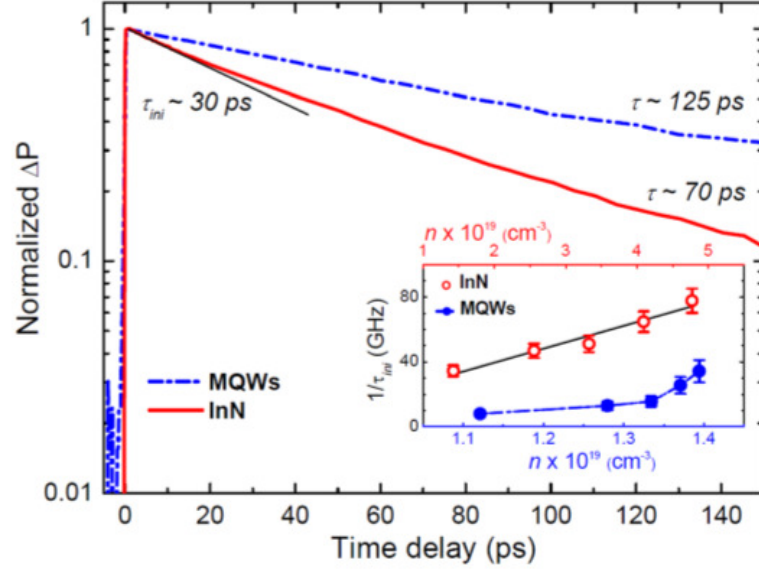


Fig. 6.8: Relaxation curve measured by pump and probe technique for S2 and S3 samples. [VRNR12]

sample only exhibited a single relaxation path, estimated in $\tau \approx 125 \text{ ps}$, considerably slower than the value measured for the bulk sample. The curve represented in the inset shows that the decay becomes non-exponential for larger pump intensities. This feature can be attributed to the many body and electron screening effects. Further details can be found in references [Vald11],[VMMG12]. All the relaxation times measured are significantly slower than InGaAs-based heterostructures, graphene and carbon nanotubes, that typically exhibited values under 1 ps [FMFK12],[YaMX14], which are the most common materials used in the literature at $1.5 \text{ } \mu\text{m}$.

6.3.2.2 Z-scan analysis

The nonlinear absorption measurements of all the samples have been carried out by means of the z-scan technique in open aperture. The excitation laser source used was an ultrafast fiber laser, delivering $\sim 250 \text{ fs}$ pulses with a repetition rate of 5 MHz and up to 35 mW average power. With the setup described in Chapter 5, a peak intensity up to 14.5 GW/cm^2 can be achieved. However, first the system was calibrated using a commercial silicon substrate as reference sample with a

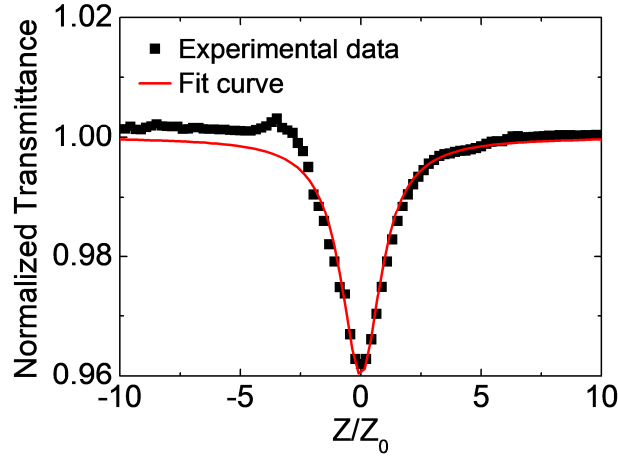


Fig. 6.9: Z-scan experimental data points of 325 μm -thick commercial silicon substrate, using the setup described in Chapter 5. Solid red line corresponds to fitting curve.

nominal thickness of 325 μm (Semiconductor Wafer Inc, SWI). Fig. 6.9 shows the experimental measured data points and the fit curve to equation (5.6). The material exhibited reverse saturable absorption effect, finding a nonlinear absorption coefficient of $\alpha_2(1.5\mu\text{m}) = 0.32 \pm 0.08 \text{ cm/GW}$. This value is in the same order of magnitude than the value measured by M. Dinu *et. al* for silicon, $\alpha_2(1.5\mu\text{m}) \approx 0.8 \text{ cm/GW}$ [DiQG03]. Thus, we can conclude that our system will give reliable estimations of the nonlinear absorption coefficients of the analyzed samples.

The commercial substrate (10 μm -thick GaN over sapphire) was measured separately using same excitation laser, as represented by the black crosses with linear fit in both Fig. 6.10 and Fig. 6.11. Neither SA nor RSA effects were observed in the substrates used. However, a small change of about 0.5 % in transmittance was observed. This small change was attributed to lens effect, since the sample has one side polished manually. Nevertheless, this change in transmittance was much smaller than the observed changes in the rest of the samples due to nonlinear absorption, as it will be shown.

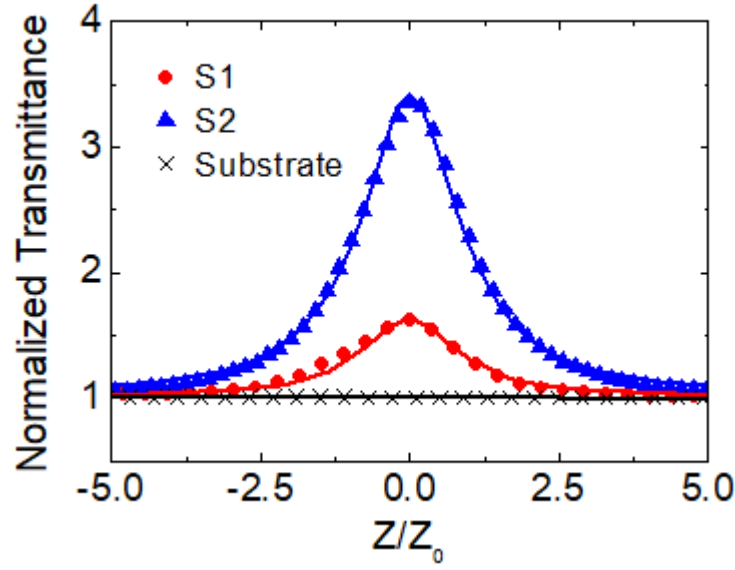


Fig. 6.10: Z-scan analysis of the InN bulk structures. S1 is represented by red circles, and S2 by blue triangles. Solid lines correspond to the fittings. Black crosses correspond to measurements of the substrate alone.

Fig. 6.10 depicts the z-scan measurements for the bulk InN with and without buffer layer (S1 and S2, respectively) samples. The active region of both samples is 1- μm -thick InN layer. However, the effective length is different for each structure, since the linear absorption coefficient was different. Thus, $L_{\text{eff},S1} = 538\text{nm}$ and $L_{\text{eff},S2} = 432\text{nm}$. Using these values, a very high nonlinear absorption coefficient of $\alpha_{2,S1} = -3465 \pm 690\text{cm/GW}$ has been estimated for the bulk InN without buffer, while even larger, $\alpha_{2,S2} = -13600 \pm 2700\text{cm/GW}$ for the InN with the buffer layer. Moreover, it is remarkable the nonlinear change experimented by S2, with over a 230 % of change in transmittance. This huge nonlinear change can be explained in terms of the large linear absorption of this sample and taking into account that the bleaching level for both InN samples must be very similar. Nevertheless, bulk InN without buffer also demonstrated a very large nonlinear effect, with over a 60% change in the transmittance.

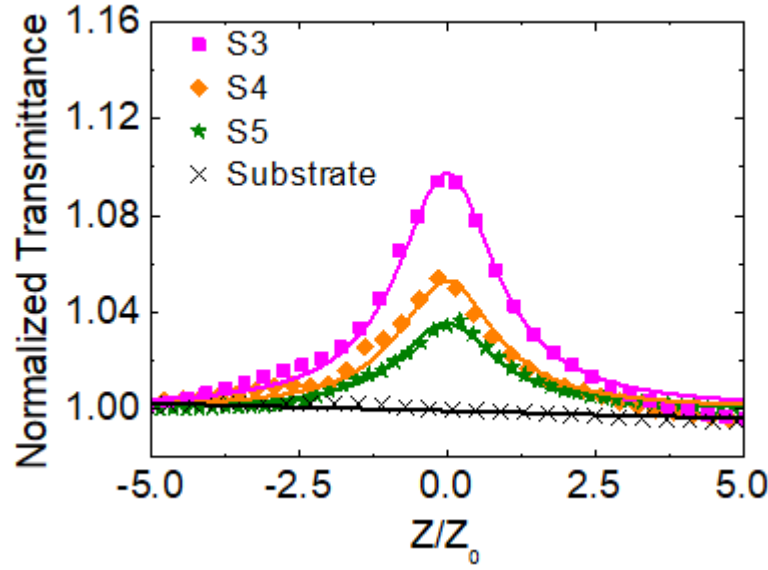


Fig. 6.11: Comparison of the z-scan measurements of the MQW heterostructures. Magenta squares represent S3. Orange diamonds represent S4. Green stars S5. Solid lines correspond to the fittings. Black crosses correspond to measurements of the substrate alone.

The z-scan measurements of the MQW samples are shown in Fig. 6.11. From the analysis of the experimental data, it can be observed that the total nonlinear changes are much smaller than for bulk samples. This was expected, as the linear absorption is much lower for the MQW heterostructures (T over 50 % at 1550 nm) than for the bulk InN samples (T lower than 25 % at 1550 nm). Since S3 is the most resonant among the MQW samples, it has been the one that experimented a larger nonlinear change, as expected. The effective lengths are almost the same for the three structures, being $L_{eff,S3} = 174nm$, $L_{eff,S4} = 176nm$ and $L_{eff,S5} = 178nm$. All the samples had proved saturable absorption effect, with large estimated nonlinear absorption coefficients from the fittings of $\alpha_{2,S3} = -1480 \pm 300 cm/GW$ for InN/In_{0.9}Ga_{0.1}N, $\alpha_{2,S4} = -795 \pm 160 cm/GW$ for InN/In_{0.8}Ga_{0.2}N, and $\alpha_{2,S5} = -505 \pm 100 cm/GW$ for InN/In_{0.7}Ga_{0.3}N. The total

change in transmittance measured for S3, S4 and S5 was approximately 9 %, 5 % and 4 %, respectively.

6.3.2.3 SA characterization measurements

The performance of the analyzed layers as saturable absorbers has been studied by means of z-scan measurements performed by varying the average power of the laser, i.e. the incident peak intensity. As an example, Fig. 6.12 depicts the different z-scan curves obtained for different peak intensities for sample S2. From the peak-to-valley height, the change of transmittance as a function of the fluence was obtained. Since the linear transmittance was already well-known for each sample, we can represent this curve, which is well fit by eq. (5.10). The RSA contribution can be neglected from this equation, since it has not been observed experimentally (it is expected the appearance of this effect at larger fluences).

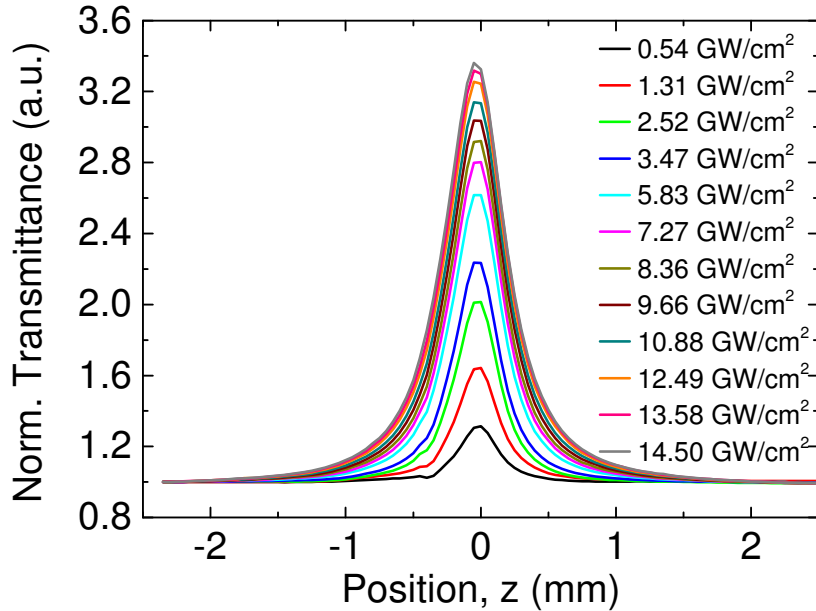


Fig. 6.12: Z-scan measurements at different incident peak intensities for S2.

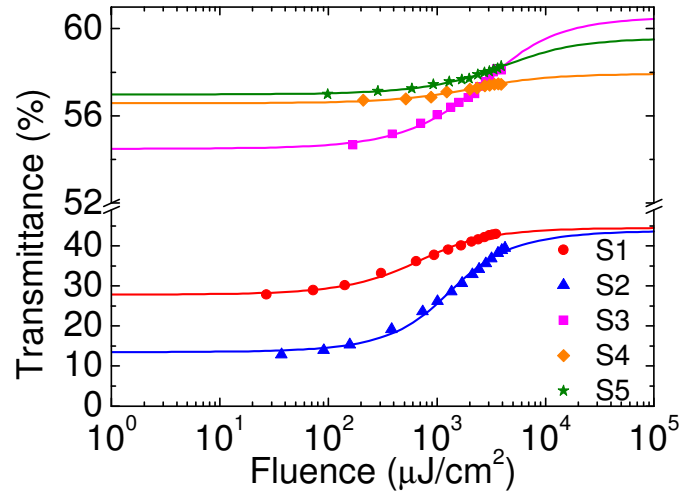


Fig. 6.13: Representation of the transmittance as a function of the fluence impinged to the materials for saturable absorption characterization. S1 represented by red circles, S2 by blue triangles, S3 by magenta squares, S4 by orange diamonds and S5 by green stars. Fitting is represented for each sample.

Fig. 6.13 shows the maximum transmittance data points as a function of the impinged fluence for each layer. The nonlinear change in the transmittance is considerably higher in bulk structures than in the MQW structures. The results from the fitting are summarized in Table 6.2, namely the saturation fluence (F_{sat}) linear transmittance (T_{lin}), the non-saturable transmittance (T_{ns}) and the modulation depth (ΔT).

S2 it is expected as the best saturable absorber device from all the presented in this thesis, mainly due to the very large modulation depth (over 30 %) and larger linear absorption, despite it presents a higher saturation fluence than S1. On the other hand, the MQW-based devices not only they have not exhibited large modulation depths, but their saturation fluences are extremely high, in the order of mJ/cm². This can be explained in terms of the field screening effect that typically appears in these structures, thus needing more energy to overcome this

Table 6.2 Parameters obtained from the fluence-transmittance curves represented in Fig. 6.13 using the eq. (5.10), namely, the saturation fluence (F_{sat}), linear and non-saturable transmittances (T_{lin} , T_{ns} respectively) and the modulation depth (ΔT).

Sample	S1	S2	S3	S4	S5
F_{sat} ($\mu\text{J}/\text{cm}^2$)	315 ± 31	425 ± 43	1580 ± 158	1350 ± 135	2475 ± 248
T_{lin} (%)	28 ± 3	13 ± 1	55 ± 6	56 ± 6	57 ± 6
T_{ns} (%)	45 ± 5	44 ± 4	61 ± 6	58 ± 6	59 ± 6
ΔT (%)	> 16	> 30	~ 6	> 2	~ 2

field, which is almost opposite to the light propagation direction. For this reason, they cannot be expected as efficient devices, contrarily to the InN bulk-based devices.

It must be pointed out that, from the measurements performed, all the samples have demonstrated to support huge fluences of $5 \text{ mJ}/\text{cm}^2$ (which corresponds to peak intensity of $20 \text{ GW}/\text{cm}^2$), without any apparent sign of optical damage. Thus, it is expected that our structures can operate at extremely high fluences. This is an improvement against many typically used materials for infrared applications, such as InGaAs heterostructures (damage threshold of $8 \text{ GW}/\text{cm}^2$)[FMFK12], graphene devices (damage threshold of $2 \text{ GW}/\text{cm}^2$)[YaMX14], or carbon nanotubes (damage threshold of $50 \text{ KW}/\text{cm}^2$)[YaMX14]. On the other hand, all these structures usually exhibited lower saturation fluences than our proposed devices

6.4 Conclusions

In conclusion, InN-based structures have been formally presented and fully characterized in the near infrared. Regarding the structural characterization, all the samples exhibited smooth surfaces, measured by AFM. The HRXRD revealed

highly periodic structures with sharp interfaces. Dark-field TEM images revealed large information about the structures. On one hand, it proved a large reduction of defects in the InN layer with the buffer (S2) with respect the bulk InN without buffer layer (S1), due to the insertion of the multilayer between the bulk layer and the substrate. On the other hand, the MQW samples show good uniformity of the well and the barrier thickness, in agreement with the HRXRD measurements.

In relation to the optical properties, measurements in the near infrared were developed. Table 6.3 summarizes, for each sample, all the relevant properties for saturable absorber characterization.

Bulk InN layers have demonstrated excellent properties. The estimated optical band gap makes these structures ideal for operation in the telecommunications C-Band, since they are very resonant. Moreover, they have exhibited a huge nonlinear effect, that has been characterized at 1.5 μm . Particularly, S2 proved over 30 % of modulation depth in transmittance, which is higher than most of the saturable absorbers and SESAM devices that can be found in the literature at telecom wavelengths. S1 also prove a large modulation depth over 16 %. Moreover, it is still a challenge to find the damage threshold of the samples, since the huge fluences generated from our pumping systems were not enough to optically damage any of the samples. This feature was attributed to the excellent thermal stability III-nitrides have always demonstrated [VoKP97]. On contrary, the high saturation fluences that have been estimated is a disadvantage with respect to many other devices, since more energy is required to reach the full bleaching level of the material. This feature could lead to an increase of the total losses in the laser resonator. Nevertheless, we can conclude that both samples could be used for mode-locking fiber lasers, attending to their properties, and

Table 6.3 General overview of the different characterization values obtained for each sample. Band gap energy, E_{gap} ; Linear absorption coefficient, α_0 ; Effective length, L_{eff} ; Nonlinear absorption coefficient, α_2 ; Saturation fluence, F_{sat} ; Linear transmittance, T_{lin} ; Modulation depth, ΔT ; Recovery time, τ ; Peak intensity for recovery time measurements, I_0 .

Sample	S1	S2	S3	S4	S5
E_{gap} (eV)	0.80	0.77	---	---	---
α_0 (cm^{-1})	$1.4 \cdot 10^4$	$2 \cdot 10^4$	$6.3 \cdot 10^3$	$5.1 \cdot 10^3$	$4.0 \cdot 10^3$
L_{eff} (nm)	538	432	174	176	178
α_2 (cm/GW)	-3465	-13600	-1480	-795	-505
F_{sat} ($\mu\text{J}/\text{cm}^2$)	315	425	1580	1350	2475
T_{lin} (%)	28	13	55	56	57
ΔT (%)	> 16	> 30	~ 6	> 2	~ 2
τ (ps)	---	30-13	125	---	---
I_0 (GW/cm^2)	----	0.35-3.1	0.35	---	---

particularly S2 could lead to better performance than S1 due to the larger modulation depth.

Regarding the MQW heterostructures, despite the estimated nonlinear absorption coefficients were high (particularly for S3, with $\alpha_2 = -1480 \text{ cm} / \text{GW}$) not only the calculated modulation depths were much lower than for the case of InN bulk devices (below 6 %), but also, they demonstrated very high saturation fluences, in the order of mJ / cm^2 . Thus, these heterostructures can still not be considered as efficient devices for mode-locking applications, mainly due to the necessary energy to reach the bleaching level.

Chapter 7 Ultrafast Fiber Lasers using InN as Saturable Absorber in Transmission

In this chapter, the developed ultrafast mode-locked fiber lasers operating at 1.5 μm , using bulk InN-based saturable absorbers are presented. The SAs are set in transmission configuration within an optical fiber ring resonator. Two lasers are described following the same resonator but using different SAs, the first using the bulk InN-based structure without buffer layer, S1, and the second laser using the bulk InN with the buffer layer, S2. The properties of both samples were analyzed in Chapter 6. Among the two samples, the latter has demonstrated better performance, delivering shorter pulses, with a time width around 220 fs, and higher peak power and pulse energy. Moreover, different laser configurations have been studied, in order to seek for the largest values of peak power and pulse energy. Afterwards, a deep discussion about the principle of operation has been carried out. Finally, we have compared the developed lasers with other fiber lasers operating at telecom wavelengths.

7.1 InN-based ultrafast fiber lasers

As it was demonstrated previously, although MQW-based structures present large nonlinear absorption coefficients, their modulation depth was small in comparison to the InN-based bulk devices and the saturation fluence was much larger. Therefore, it has not been possible to reach a stable mode-locking

operation. Thus, the S3, S4 and S5 devices have proved to be not efficient enough for passively mode-locked fiber lasers at 1.5 μm . On contrary, the bulk InN layers demonstrated to be efficient saturable absorbers at these wavelengths, being resonant at telecom wavelengths, i.e. presenting larger absorption, and exhibiting very large modulation depths, which are necessary conditions for ML applications. Thereby, two fiber lasers have been fabricated using samples S1 and S2. For comparison between them, they have been designed following the same fiber ring cavity, which is shown in Fig. 7.1. A commercial Er-doped fiber amplifier (EDFA, Accelink, TV Series), with up to 24 dBm output power, has been used as gain medium, presenting ~ 16 m of doped fiber, with normal-dispersion of $GVD_{EDF} \approx 0.016 \text{ ps}^2 / \text{m}$. The rest of the components use standard single-mode fiber (SMF28) which presents anomalous-dispersion of $GVD_{SMF} \approx -0.021 \text{ ps}^2 / \text{m}$: a variable attenuator to control the losses in the cavity and an optical fiber coupler, resulting in a total ~ 40 m cavity. Thus, the net cavity dispersion is $\sim -0.25 \text{ ps}^2$.

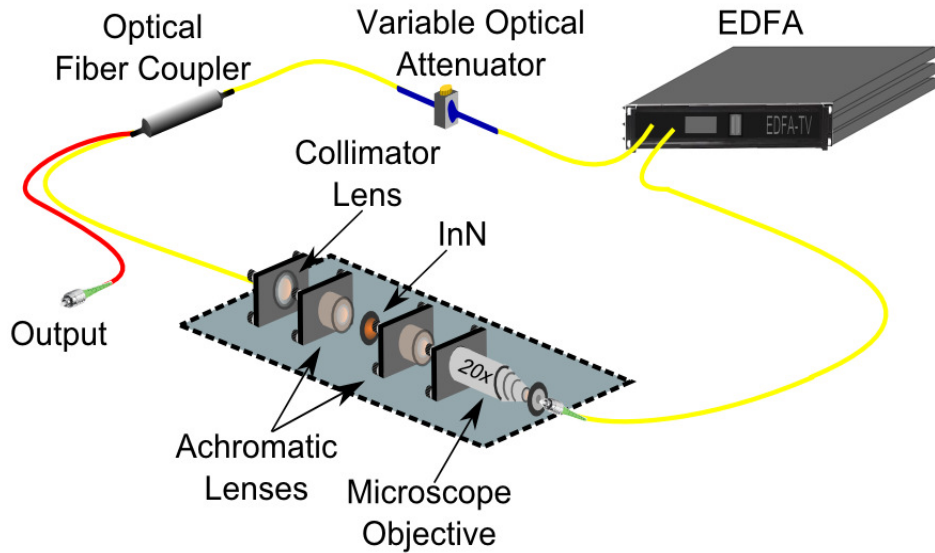


Fig. 7.1: Scheme of the C-band ultrafast mode-locked fiber laser using InN bulk as saturable absorber. [JMMG17]

The InN-based SA is placed in a free space region, between two-achromatic lenses, in order to increase the fluence that impinges the material. A collimator lens (Thorlabs, F280SMA-1550) and 20x microscope objective have been used to launch and collect the light respectively between the optical fiber and the free space. The laser behaves as a dispersion-managed cavity, meaning that exist areas with different sign of dispersion, being the net dispersion anomalous. Further discussion about laser properties and principle of operation will be presented later in more detail. The different characterization measurements of the laser have been carried out simultaneously, as was described in Chapter 5.

Fig. 7.2 depicts the electrical spectrum for the particular case of the developed laser using S1. Since the cavity used is also the same for S2, it should be noted that the electrical spectrum is very similar in both cases. The repetition rate is $f_{rep} \approx 5.25 MHz$, which leads to a separation between consecutive pulses of ~ 190 ns. These values are in good agreement with the total cavity length. Moreover, the peak-to-noise ratio is over 45 dB.

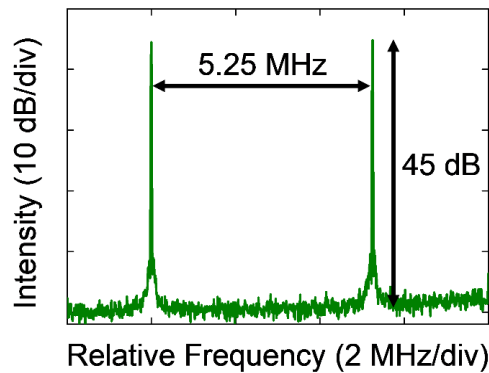


Fig. 7.2: Electrical spectrum of the bulk InN-based SA without buffer ultrafast laser cavity at ML operation. [JMMG18]

7.1.1 Ultrafast fiber laser using bulk InN-based saturable absorber without buffer

The first ultrafast fiber laser that is going to be presented in this thesis has been fabricated using the bulk InN-based SA without the buffer layer (S1). A 90/10 fiber coupler launches 10% of the signal as the laser output, while the 90% remaining is being recirculated. Fig. 7.3 shows typical autocorrelator trace (a) and spectrum (b) of the laser in mode-locking operation. The figures have been obtained for the particular case when attenuation is minimum, being the average output power 9.7 mW, finding pulses with a temporal full width at half maximum (FWHM) of $\Delta\tau = 254 \pm 6\text{fs}$ [see Fig. 7.3(a)] and a spectral width of $\Delta\lambda = 16.1 \pm 0.5\text{nm}$ [see Fig. 7.3(b)]. All the measured spectra are peak centered at $\lambda_c \approx 1562\text{nm}$.

All the autocorrelator traces and spectra measured are well described by a hyperbolic-secant-squared function (sech^2). A characterization of the pulse generation and properties as a function of the average power that is circulating in the resonator (i.e. the average output power) has been carried out. This has been performed by varying the optical losses within the fiber ring by means of a variable optical attenuator. By doing this, different operation regimes have been

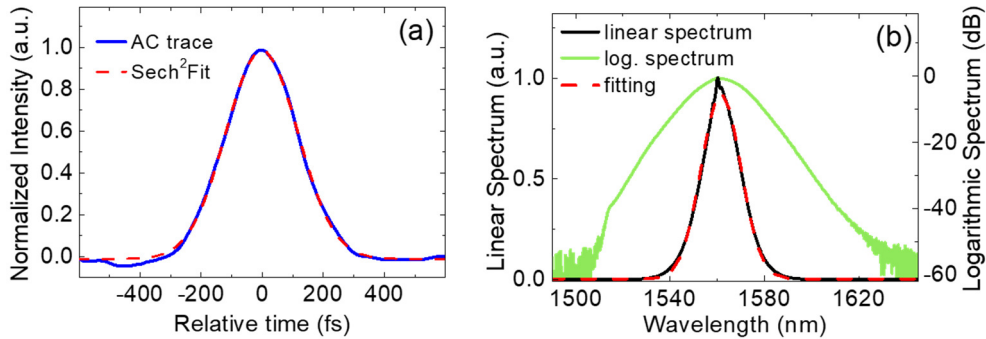


Fig. 7.3: For the minimum attenuation in the cavity: (a) Autocorrelator trace with a temporal duration of 252 fs; (b) Typical laser spectrum, centered at 1562 nm, with a FWHM of 16 nm. [JMMG17]

observed, depending on the power circulating inside the resonator (but characterized as the laser output power), namely continuous wave (CW), a transition range with the simultaneous emission of both, CW and mode-locked components, and the mode-locked regime. Fig. 7.4(a) depicts the peak power as a function of the average output power for the different laser output regimes. It has been experimentally observed that the mode-locking operation self-started [SHLS08] for output average powers above a threshold value of $P_{out} \approx 5.5mW$. Furthermore, typical spectra have been represented as insets of Fig. 7.4(a) for each operation regime. The three spectra have been normalized around $1.56 \mu m$, showing the expected spectral broadening under mode-locking operation (the abscise span is the same, $100 nm$, for all the spectra). Note that in the CW regime no pulses are generated, so that no peak power has been measured, while in the transition range the peak powers have been estimated considering the amount of CW which appears in each of the spectra.

Tuning the variable optical attenuator from the minimum attenuation ($P_{out} \approx 9.7mW$) to the mode-locking threshold results in a variation of the pulse

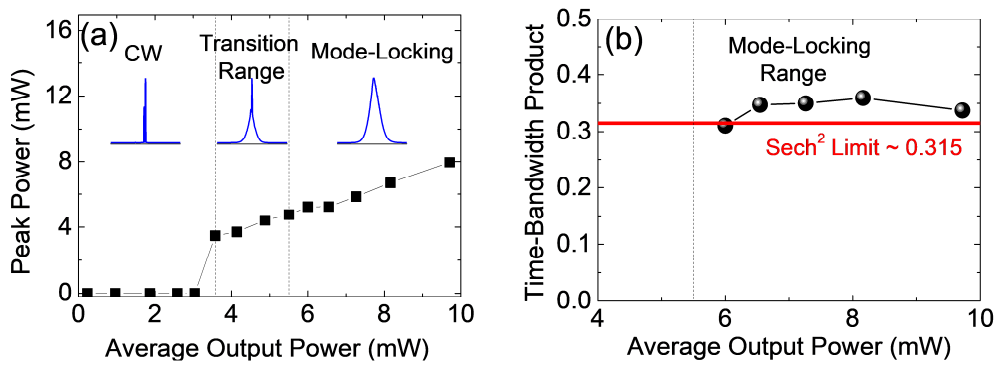


Fig. 7.4: Characterization of the ultrafast fiber laser using S1 as SA. (a) Variation of the peak power as a function of the average output power, showing the different laser operation regimes. The normalized linear spectra, centered at $1.56 \mu m$ with a span of $100 nm$, are shown for each regime. (b) Time-Bandwidth Product as a function of the ring average power. The solid line represents the $sech^2$ limit. [JMMG17]

widths from $\Delta\tau = 258 \pm 6\text{fs}$ to $\Delta\tau = 239 \pm 6\text{fs}$, with the spectral width varying from $\Delta\lambda = 15.2 \pm 0.5\text{nm}$ to $\Delta\lambda = 17.1 \pm 0.5\text{nm}$, respectively. From these values, the calculated peak power, shown in Fig. 7.4(a), varies from 7.95 kW to 4.75 kW, respectively. Thereby, the pulse energy ranges between 2 nJ to 1.13 nJ in the ML operation regime. Fig. 7.4(b) depicts the Time-Bandwidth product (TBP) for the ML values measured, finding TBP values oscillating between 0.32-0.35, close to the transform-limited value for sech^2 pulses ($TBP_{\text{sech}^2} = 0.315$).

In order to study configurations to increase the output peak powers and pulse energies delivered from the laser, two different approaches have been proposed. The first and simplest approach is to fabricate longer cavities, by simply inserting additional optical fiber to the resonator. The second approach has been to amplify the laser output, developing a master oscillator power amplifier (MOPA) configuration [AkSG08],[KoSn64],[LFSA06]. This has been carried out by connecting a second EDFA, which maximum average output power is 40 dBm (Keopsys KPS-BT2-C), to the laser output.

7.1.1.1 Long ultrafast fiber laser cavities

The first proposed way to improve the laser output properties for high pulse energy generation was performed by introducing additional single-mode fiber in the laser using S1, between the saturable absorber and the EDFA input (see Fig. 7.1), which leads to a reduction of the repetition rate. Fig. 7.5(a) and (b) compare the measured traces from the autocorrelator and spectra for different lengths of additional fiber, up to 200 m, reaching approximately a reduction of the repetition rate by a factor of 5, as depicted in Fig. 7.5(c). Table 7.1 summarizes the obtained results, once the FWHM has been estimated in each case, showing negligible changes in the pulse duration, the spectral width or average power. This means that the peak power (P_p) and pulse energy (E_p) are

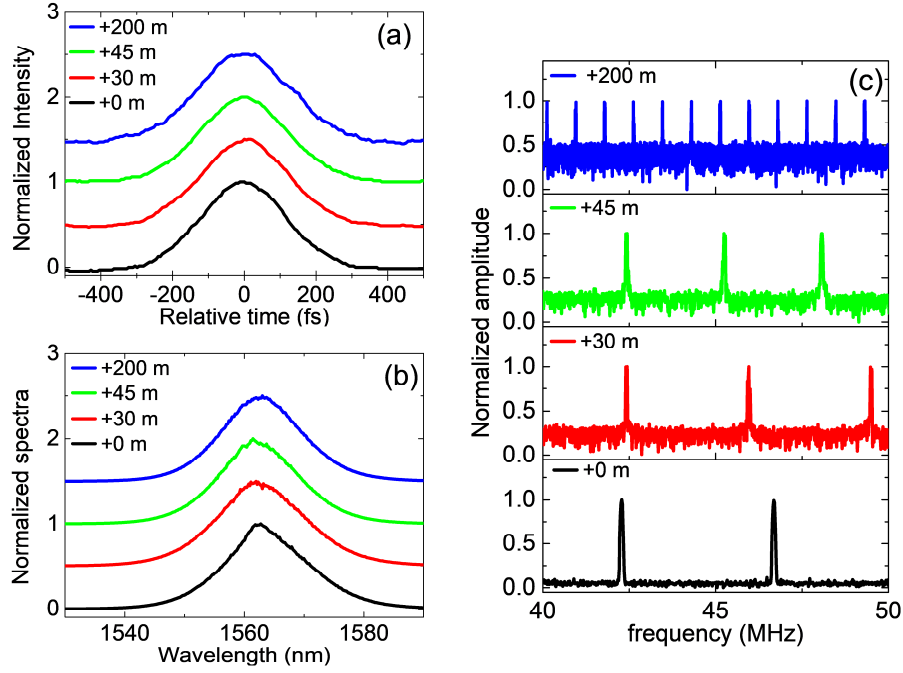


Fig. 7.5: Laser stability for different cavity lengths (from the standard configuration to +200 m of additional fiber): (a) Autocorrelator traces (vertically shifted for clarity), (b) normalized optical spectra (vertically shifted for clarity), and (c) Normalized electrical spectra. [JMMG17]

being multiplied by a factor of 5, by simply introducing 200 m of additional fiber to the standard configuration. Furthermore, the stability in pulse duration and spectral width implies that the TBP remains close to the transform-limited value for all these new configurations.

It should be noted that the additional fiber also introduces a change in average dispersion, which could compensate the increase in pulse energy, thus maintaining the soliton pulse duration relatively stable. In the case of the presented laser cavity and assuming constant the nonlinear fiber coefficient, γ , the insertion of additional fiber with different lengths (30 m, 45 m, 200 m), leads to a change in the average cavity dispersion, D_{ave} . Thus, a 5-times increase in energy could be mostly explained by an equivalent increase in the average dispersion, remaining the pulse duration basically unchanged. For instance, for the case when the cavity

Table 7.1 Experimental results comparing different laser cavity configurations, differing in the length of an additional single-mode fiber inserted between the output coupler and the variable attenuator (see Fig. 7.1). [JMMG17]

Additional fiber length	+ 0 m	+ 30 m	+ 45 m	+ 200 m
Average Power (mW)	9.7	9.7	9.7	9.6
Repetition rate (MHz)	5.25	3.54	2.84	0.84
$\Delta\tau$ (fs)	254 ± 6	265 ± 6	274 ± 6	277 ± 6
$\Delta\lambda$ (nm)	16.0 ± 0.5	17.1 ± 0.5	15.7 ± 0.5	15.5 ± 0.5
P_p (kW)	7.9	10.3	12.5	25.7
E_p (nJ)	2.0	2.7	3.4	11.4
TBP	0.34	0.38	0.36	0.36

length was ~ 40 m, the total estimated GVD was ~ -0.25 ps², being the average GVD coefficient ~ -0.00625 ps²/m. Now, for the case of insertion of 30 m, the total GVD becomes ~ -0.899 ps², resulting in an average GVD coefficient of ~ -0.0126 ps²/m. So, for this particular case, the almost two-fold increase in pulse energy with negligible pulse broadening can be quite well linked to an equivalent increase of the average dispersion coefficient. Note that these values of dispersion have been estimated according to usual literature values. For the 200 m SMF insertion, however, the estimated increase in average GVD coefficient is only a factor of roughly 3.5, which does not exactly match with the obtained energy increase, but that could also be explained considering a smaller nonlinear coefficient in the particular SMF fiber roll used (note that, being all SMFs, the different rolls used have different manufacturing techniques PECVD, VAD, etc.), small variations in the estimated dispersion parameters, and the actual slightly

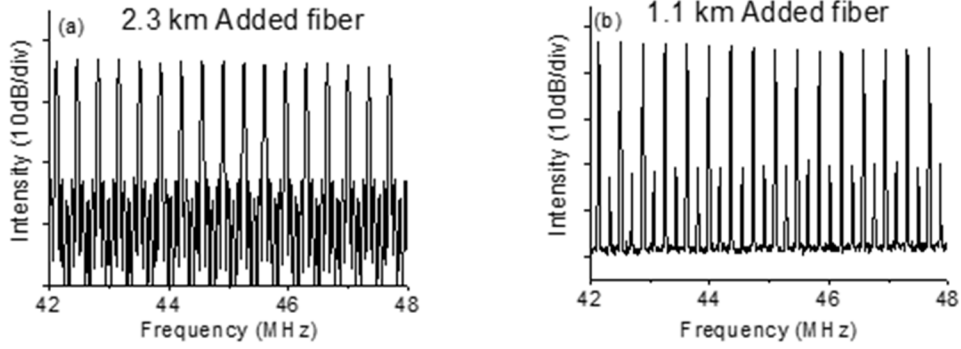


Fig. 7.6: Electrical spectrum of the laser output when inserting (a) 2.3 km of additional fiber, and (b) 1.1 km of additional fiber.

larger pulse width in the case of the 200 m insertion. Thus, it is actually possible to explain that the pulse-length remains almost unaffected in the studied situations based on the soliton area theorem, represented by equation (7.1):

$$E_p \Delta\tau = \frac{2|D_{ave}|}{\gamma} \quad (7.1)$$

However, when longer cavities were implemented, by the insertion of approximately 1- or 2-km of additional fiber, soliton energy quantization effect was observed [TZZL05]. As an example, Fig. 7.6(a) and (b) depict the electrical spectra measured for the particular cases as a result of inserting 2.3 km and 1.1 km, respectively. For the first case, the repetition rate observed experimentally was 350 KHz, which is ~ 4 times greater than the expected one of 88 kHz, according to the resonator length. This means that the 4th harmonic soliton was observed. The 2nd harmonic soliton has been also observed, when adding 1.1 km fiber length to the resonator, where the measured repetition rate was 360 kHz while the expected one was 184 KHz.

7.1.1.2 Post-amplification of the laser

In order to investigate the maximum achievable peak power, the laser output has been amplified using a MOPA configuration, placing another EDFA at the

output of the laser. The master oscillator for this case was the laser with the S1 saturable absorber with no additional fiber in the resonator. The second EDFA can deliver up to 40 dBm (10 W) of average power. However, the average power of this EDFA has been strongly limited, since for very high powers signatures of pulse break-up and supercontinuum generation were observed. Therefore, the output amplification has been limited in this work to values where the pulses still presented good-quality.

Fig. 7.7(a) and (b) show spectra and autocorrelator traces, respectively, for different analyzed cases, maintaining the operation point of the master oscillator near the threshold. By changing the gain of the additional amplifier, the average output power was tuned up to 358 mW, observing the effect of soliton self-frequency shift, which red-shifted the maximum of the emission spectra to 1575 nm. It is clearly visible the appearance of side-lobes when increasing the power. Since the appearance of these side-lobes, the pulse powers of Fig. 7.7(b) have been calculated by integrating the measured energy in the central peak. It

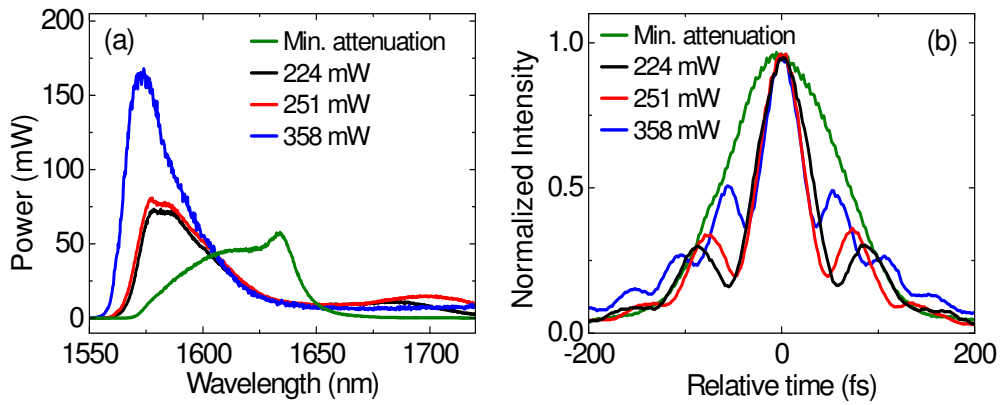


Fig. 7.7: Ultrafast mode-locked fiber oscillator using InN saturable absorber with output fiber gain: (a) spectra, and (b) autocorrelator traces for different amplification values, operating close to the oscillator threshold, with master oscillator output average power of 5.5 mW. The legend indicates the average output power in each case. The green line corresponds to the case of minimum attenuation in the oscillator, i.e. far from the threshold, with master oscillator output average power of 9.7 mW, and minimum output amplification ($P_{Av} = 207$ mW). [JMMG17]

has been estimated that only approximately 50% of the whole pulse energy remains in the central peak for the case of maximum average power (358 mW), and 60% for the other two cases shown. Fig. 7.7(b) depicts pulse widths ranging from $65 \pm 6\text{fs}$ to $53 \pm 6\text{fs}$. This temporal compression of the pulses results in pulse peak power varying from 0.42 MW to 0.7 MW. The temporal pulse compression is attributed to self-phase modulation (SPM) in the output amplifier (causing spectral broadening), followed by a subsequent compression in the anomalously dispersive output fiber. Fig. 7.7(a) and (b) also show the spectrum and autocorrelator trace, respectively, for the particular case when the output amplification is minimum and the variable attenuator inside the ring laser cavity is totally open (mode-locking far from the threshold). The measured spectrum is also shifted to larger wavelengths (up to 1633 nm), due to Raman self-frequency shift. Under these conditions, the measured output average power is 207 mW, and the pulse width is $120 \pm 6\text{fs}$, which implies that the peak power reaches 358 kW. Further increasing the power by output amplification leads to the appearance of side-lobes around the central emission peak, evidencing the increasing effect of SPM. The introduction of the described amplification stage after the mode-locked fiber oscillator (MOPA) leads to additional temporal compression of pulses, which, in turn results in an additional enhancement of the peak power. Fig. 7.7(b) illustrates the appearance of pulse degradation and side-lobes when applying higher amplification.

7.1.2 Ultrafast fiber laser using bulk InN-based saturable absorber with buffer layer

A fiber laser using the bulk InN-based with the buffer layer (S2) as saturable absorber has been developed. For comparison with the previous laser presented using S1, the resonator used has been the same for both cases, which was

introduced in Fig. 7.1. The only difference in the cavity design with respect to the previous laser presented, using bulk InN structure without buffer, is that now a 70/30 fiber coupler can be used, instead of the 90/10. This feature leads to obtained higher average output power values, as it will be discussed afterwards.

An analysis of the variation of the laser properties as a function of the power circulating inside the cavity (thus, the energy applied to the SA) has been carried out. The laser has proved to operate in mode-locked regime for values of output average power higher than 21 mW, which means that approximately 50 mW are being recirculated through the 70% branch of the fiber coupler. Moreover, the transition range in this case was barely observable experimentally, almost passing directly from the CW to the ML operation mode. The maximum average output power the laser can deliver is 30.6 mW, due to the amplifier used. In this range of ML operation, pulse duration oscillates between $\Delta\tau = (220 - 235) \pm 6\text{ fs}$, corresponding the first value to the case for minimum attenuation ($P_{out} = 30.6\text{ mW}$), and growing linearly for larger attenuation (larger losses). Analogously, opposite occurs to the spectral width, which oscillates between $\Delta\lambda = (21.5 - 17.6) \pm 0.5\text{ nm}$, decreasing linearly as a function of average power.

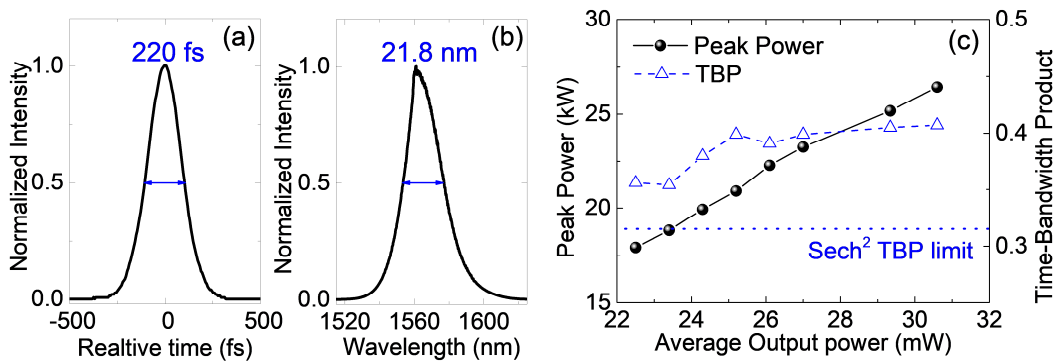


Fig. 7.8: Typical laser output without variable attenuator at 30.6 mW output average power showing: (a) Experimental autocorrelator trace and (b) linear optical spectrum, giving FWHM values for each case. (c) Laser analysis as a function of the average output power, presenting the estimated peak power (fill black circles) and the time-bandwidth product (empty blue triangles). [JMMG18]

Fig. 7.8 (a) and (b) show a typical autocorrelator trace and spectrum of the laser output respectively, for the case of minimum attenuation. The rest of measured autocorrelator traces and spectra are very similar in shape to the ones depicted in Fig. 7.8. Fig. 7.8(c) depicts the calculated peak power (full black circles) and TBP (empty blue triangles) values for the laser operating in the ML regime. TBP ranged between 0.35-0.41, which are not far to the sech^2 limit, that is 0.315. On the other hand, peak power ranges between 26.5-18 kW, for minimum to maximum attenuation in ML operation, respectively, which corresponds to high pulse energies, from 5.8-4.3 nJ.

Despite S2 presents a higher saturation fluence than S1, the mode-locking regime has been achieved more efficiently. This feature is probably related to the product of the linear absorption (α_0) times the InN layer length (L). A larger value of the linear absorption implies that the InN layer can eliminate more efficiently the continuous-wave component present in the transition range, therefore converting this regime of operation into stable mode-locking. Particularly, for the case of S1, it can be estimated $\alpha_{0,S1}L \approx 1.4$, while $\alpha_{0,S2}L \approx 2.0$ for S2. In these estimations, the values of the linear absorption were given in Chapter 6 ($\alpha_{0,S1} \approx 1.4 \cdot 10^4 \text{ cm}^{-1}$, $\alpha_{0,S2} \approx 2.0 \cdot 10^4 \text{ cm}^{-1}$) and $L = 1 \mu\text{m}$ for both samples. For this reason, the transition range in the laser using S2 has been reduced, experiencing almost an immediate change between the CW to the ML regime, when increasing the power above the threshold value. Thus, it has been possible to reach stable mode-locking using a 70/30 fiber coupler, while for sample S1 only the transition range was observably when using this same fiber coupler. Fig. 7.9 represents the experimental spectrum measured for the laser developed using S1 and a 70/30 fiber coupler. From the figure, it is appreciable that the lower part of the spectrum corresponds to a broad spectrum, characteristic of the mode-locking, but also a strong CW component is observable. Under the same

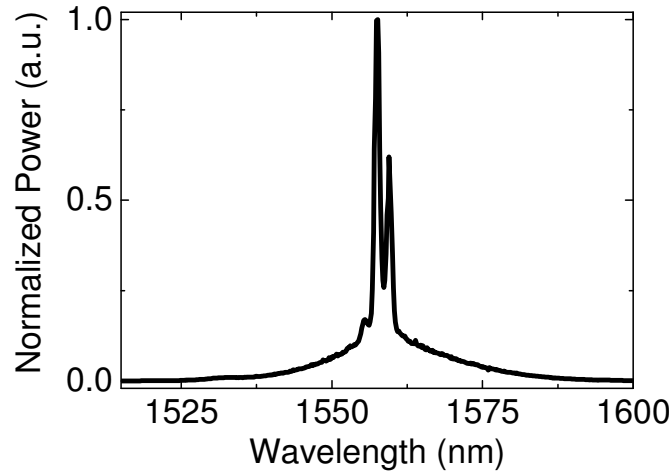


Fig. 7.9: Experimental measured spectrum for laser using S1 as saturable absorber and a 70/30 fiber coupler.

conditions, the larger linear absorption of S2 eliminates the CW component, leading to a stable ML regime. This feature, along with the shorter pulse widths measured (~ 220 -fs for S2, while ~ 250 fs for S1), which can be explained in terms of the larger modulation depth this sample exhibited upon S1 [Haus75a],[Haus75b], led to over a 3-fold increase of peak power and pulse energy in the laser performance.

7.2 Discussion

7.2.1 Principle of operation

No multiple-pulse (soliton energy quantization effect) behavior has been observed for any of the ultrafast lasers presented power ranges and different cases studied. In fact, this effect has only been observed when increasing the pulse energy to very high values, when developing much larger cavities after inserting additional SMF fiber rolls, above 1-km-long. Moreover, in both of the lasers presented, the InN-based saturable absorbers have been placed so that their $\langle 0001 \rangle$ crystallographic axis is aligned with the laser cavity. In such a

configuration, the optical asymmetry within the basal plane of InN is too small to induce remarkable changes with polarization of the incident light [GSWG06]. Thus, the mode-locking operation is independent of the laser polarization. This feature has been confirmed by introducing a polarization control element inside the cavity, which does not induce important changes in the emission properties of the laser for any polarization state.

It should be noted that, in the cases presented, the lasers are actually not cavities that generate pure solitons, but rather dispersion-managed cavities (i.e. they have regions of normal and anomalous dispersion, and overall a low anomalous dispersion). In this type of lasers, the pulse along the cavity is breathing, meaning that it stretches and compresses temporally in each roundtrip as it passes through each sign of dispersion. The shortest achievable pulses in these fiber lasers usually occur when extracting the light in the single-mode fiber after the Er-doped fiber amplifier [ChSG11]. When these strongly chirped pulses with high power reach the single-mode fiber, self-phase modulation effect (SPM) becomes predominant, inducing a temporal compression, in our case leading to the measured $\sim 200\text{-}250$ fs FWHM. InN acts as a very efficient slow saturable absorber, which leads to stable mode-locking with pulse duration well below its recovery time due to the formation of solitons, providing that the intracavity fluence is well above the saturation fluence of the absorber [KuAK98].

Despite the pulses generated in dispersion managed cavities are more often fit by a Gaussian function [TuBF12], the ultrafast fiber cavities that we have presented in this chapter generated pulses that almost fit equally good to a sech^2 than to a Gaussian function. As an example, the fitting error for the autocorrelator traces of the bulk InN-based without buffer SA laser has been estimated in 0.3 % for sech^2 , and 0.4 % for the Gaussian fit, while 0.4 % for both fittings of the bulk InN-based SA with buffer laser. Furthermore, it is remarkable

the absence of Kelly sidebands in all the measured spectra for both lasers presented, which is a common feature in dispersion-managed cavities. This is attributed to a reduction of the phase-matched coupling to resonant sidebands by the change in dispersion from anomalous to normal between regions within the cavity (S. K. Turitsyn et al. [TuBF12]). Also, assuming a total net dispersion of -0.25 ps^2 , the soliton period can be estimated in approximately $Z_0 < 1 \text{ m}$. Thus, we can assume that the laser is in the case of $L \gg Z_0$. As introduced by M. L. Dennis and I. N. Duling III [DeDu94], for $L \gg Z_0$, the initial dispersive wave spreads too far from the soliton to interfere with any successive dispersive wave, so likewise no sidebands will be observed.

In the laser presented using InN without buffer, a transition range appeared between the CW and ML regimes, while this transition operation regime was greatly diminished for the laser using S2 as saturable absorber, due to the larger $\alpha_0 L$ product, as it was explained previously. Nevertheless, it is possible that the laser developed using S2 still has some smaller transition range. This operation regime has been studied by means of real-time oscilloscope measurements of the train of pulses. Fig. 7.10 compares the train of pulses generated in mode-locking regime [Fig. 7.10 (a)] and in the transition range [Fig. 7.10 (b)]. Each figure

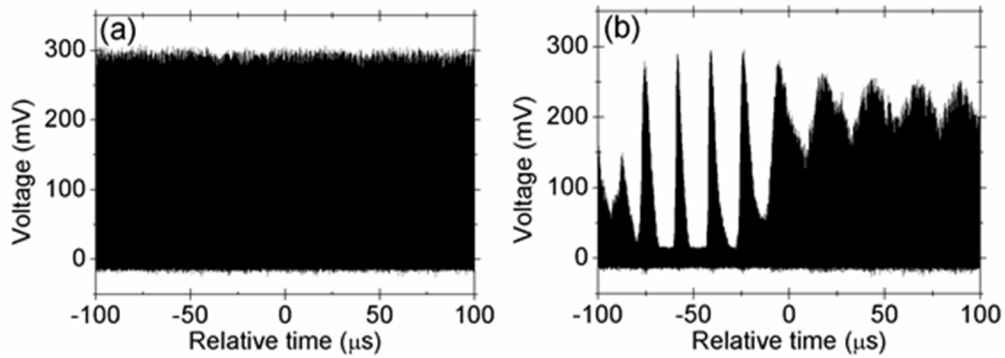


Fig. 7.10: Oscilloscope traces showing the train of pulses delivered by the laser, with the laser operating in (a) stable mode-locking range, and (b) the transition range.

presents a total of 8 million points, extended through a 200 μs window, representing over 1000 consecutive pulses. It was observed that the peaks measured in the transition range appear randomly, which could be due to a working operation regime where the laser is continuously alternating between the mode-locking and the continuous wave. This can be explained as follows: in the transition state, the energy that is circulating in the cavity is not enough to fully saturate the saturable absorber. Sometimes, this energy becomes randomly higher and the SA gets almost saturated (delivering pulses), but always below the required saturation state to reach a stable mode-locking. Thus, the laser appears as oscillating between the two stable modes (ML and CW). However, this is different from other mode-locked lasers where regular soliton explosions have been reported [LLYH16].

7.2.2 Comparison with other ultrafast fiber lasers

Considering that the distances from the optical coupler to the characterization systems (OSA, power meter, etc.) and to the saturable absorber are approximately the same ($\sim 3\text{-}4\text{ m}$), we can expect that the pulse reaching the SA is almost as short as has been measured by the autocorrelator, but 9 times higher in average power, in the case of using the 90/10 fiber coupler. This assumption allows us to estimate a value of the fluence handled by the saturable absorbers. For this purpose, it has been assumed pulses of $\Delta\tau \approx 250\text{ fs}$, and $P_{out} \approx 10\text{ mW}$ (which corresponds to an average power of $\sim 90\text{ mW}$ at the 90% branch of the fiber coupler). With these values, we find that both saturable absorbers can support fluences over $F = 12\text{ mJ} / \text{cm}^2$ (an optical intensity of $I \approx 40\text{ GW} / \text{cm}^2$). However, it has been proved that the SESAM can support a fluence higher than $100\text{ mJ}/\text{cm}^2$ (more than $350\text{ GW}/\text{cm}^2$) optically undamaged [GJMC17], which is over an order of magnitude larger than the rest of commonly used SESAMs,

operating at 1550 nm. This fluence is far beyond the damage fluence of graphene used as saturable absorber (damage threshold, $I_{\max} \approx 2 \text{ GW} / \text{cm}^2$) [SHTP10],[ZTKZ10], which implies a practical limitation for the fiber lasers based on graphene in comparison with nitrides. On the other hand, graphene-based saturable absorbers lead to ultrafast lasers in mode-locked regime that barely deliver pulses below 500 fs. Comparing the results obtained with other lasers that incorporate carbon nanotubes [SYTJ04],[PSHC12], it can be concluded that, despite these lasers can deliver very short pulses (in the order of ~ 100 fs) they are even more limited in both, power and pulse energy than the ones based on graphene (damage threshold, $I_{\max} \approx 50 \text{ kW} / \text{cm}^2$), with pulse energies in the order of hundreds of pJ, about 1-2 orders of magnitude lower than the presented lasers based on nitride saturable absorbers.

Commercial mode-locked femtosecond fiber lasers are mostly based on Kerr-lens effect [TIHN93],[HaIT94] or the use nonlinear polarization rotators [TaZh07] or GaAs-based heterostructures as saturable absorbers. The first two cases, even though leading to sub-100 fs pulses, present the disadvantage of being highly polarization dependent, needing readjustments to compensate polarization changes in the system. Lasers using GaAs-based heterostructures as SESAM present mainly three drawbacks. First, the enhancement of the nonlinear effect of these SESAMs relies on complicated low-dimensional heterostructures. They are also typically polarization dependent. Finally, they are up-limited in power due to the damage threshold of the material [FMFK12].

7.3 Conclusions

In conclusion, ultrafast mode-locked fiber lasers delivering ~ 220 -250 fs operating at telecom wavelengths and using InN-based saturable absorbers in

transmission have been presented. It is the first time that InN has been proposed as SA in the near infrared, in order to fabricate mode-locking lasers. On one hand, the ultrafast fiber laser developed using a bulk InN structure, directly grown on a sapphire substrate with GaN template without the presence of a buffer layer (S1), has demonstrated high stability and pulses with ~ 8 kW peak power and high-energy of 2 nJ. Being a bulk material on a commercial substrate, not only this SA is one of the simplest that can be found in the literature, but also it is easily reproducible. On the other hand, a bulk InN structure with a buffer layer (S2) has demonstrated over a 3-fold increase of the laser performance with respect to S1, due on one hand to the larger linear absorption, expressed as the product of α_0 and the InN length, L , and on the other hand to the enhanced nonlinear properties of the sample, which has reduced the pulse width. This SA with the buffer layer exhibits all the benefits that were demonstrated by the grown directly on GaN-template substrates, but a better performance in the laser output properties.

Also, the insertion of these InN-based SAs within the fiber cavity results in a laser showing polarization independence, which is a clear advantage upon most lasers that can be found in the literature. This feature also makes the laser to be extremely robust against ambient fluctuations and mechanical variations. Furthermore, InN has proved to support enormous fluences, without showing optical damage, contrary to most of known saturable absorbers known in the literature operating at the same wavelength. As a disadvantage, InN devices had demonstrated higher saturation fluences than other saturable absorbers, which is a property to be overcome in future work, since a larger energy is required to achieve the necessary nonlinear change to reach the mode-locking operation regime, introducing higher losses in the resonator. Nevertheless, from all the

aspects mentioned, InN can be placed as a suitable candidate to passively mode-locked high-power fiber lasers in the near infrared.

Finally, two different approaches in order to find the limits in peak power and pulse energies have been demonstrated. The first one has been to develop very large fiber cavities, by the insertion of additional SMF to the fiber resonator. The laser output properties had appeared to be almost unaffected, up to additional 200 m of SMF, while reducing the repetition rate, leading to an almost 5-fold increase in peak power and pulse energy. The second approach was the demonstration of MOPA configuration, by amplifying the laser output using a second EDFA. This approach proved extremely high peak powers (over 500 kW), but also pulse-breaking, with the appearance of side-lobes.

Chapter 8 Ultrafast Mode-Locked Fiber Laser using InN-Based Semiconductor Saturable Absorber Mirror

In this chapter, the first ultrafast fiber laser operating at telecom wavelengths that uses InN-based semiconductor saturable absorber mirror (SESAM) will be presented. Particularly, the developed SESAM is based on the InN structure without buffer layer, S1, which was demonstrated as saturable absorber for passive mode-locked a fiber laser, in Chapter 7, depositing a thin layer of aluminum has been deposited on top of the structure by sputtering technique. The results obtained from the characterization of the laser will be presented and the advantages upon the laser using SA in transmission will be discussed. Moreover, a comparison between the laser fabricated using InN-based SESAM and a commercial InGaAs-based SESAM has been performed, followed by a discussion about the strengths of each structure.

8.1 SESAM fabrication and characterization

The SESAM proposed is based on the bulk InN-based structure without the buffer layer (S1), which was previously described and fully characterized in Chapter 6. A 300-nm-thick aluminum layer has been deposited on top of the InN layer by sputtering technique at room temperature, acting as the mirror of the device. Aluminum grants high reflectance with a small thickness (nominally

$\sim 96\%$ at $1.5 \mu\text{m}$ for a thickness of 300 nm). Moreover, the deposition using sputtering technique makes the mirror to be much simpler than other SESAMs that can be found in the literature, which typically involve distributed Bragg reflectors (DBR, [CGNK11],[HTFH17]). The sputtering chamber used for this purpose is placed at the facilities of the Group of Photonics Engineering, at University of Alcalá.

Fig. 8.1 shows the measurements of the 300-nm-thick Al mirror deposited on a GaN-on-sapphire substrate at different impinging laser fluence, (F), obtained using the characterization setup described in Chapter 5. The reflectance is represented by black triangles, showing a negligible change of the reflectance, less than 0.2% , with an average reflectance of $\sim 94 \%$. Fig. 8.1 also depicts with blue circles the nonlinear behavior of the reflectance of the InN-based SESAM as a function of F . From the fitting of the experimental data to eq. (5.9), a saturation fluence of $F_{sat} = 226 \pm 23 \mu\text{J} / \text{cm}^2$ has been estimated (this value implies the saturation intensity to be $I_{sat} = 2.0 \text{ GW} / \text{cm}^2$). The linear and the non-saturable reflectance of the SESAM have been directly estimated from the fitting, finding

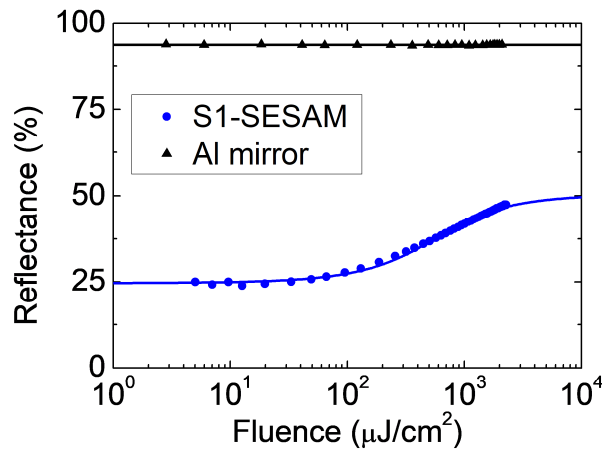


Fig. 8.1: Curve of the measured reflectance (%) of InN-based SESAM (blue circles) and a 300-nm-thick Al mirror deposited on a GaN-on-sapphire substrate (black triangles), as a function of the incident fluence ($\mu\text{J}/\text{cm}^2$) where symbols are the experimental data and the line represents the fitting to Eq. (5.9).

$R_{in} = 25 \pm 3\%$ and $R_{ns} = 50 \pm 5\%$. Therefore, the saturation fluence is approximately 0.7 times lower than the one obtained for S1 in transmission configuration ($F_{sat} = 315 \pm 31 \mu J / cm^2$), while the modulation depth has been increased from $\Delta T \approx 16\%$ in transmission to $\Delta R \approx 25\%$ in reflection. These improvements are partially attributed to the increase of the effective length of the active layer in the SESAM configuration, but also to the fact that characterization of the SESAM requires of a better alignment (the impinging beam incidence needs to be normal to the sample), than in the case of the sample in transmission. The measurement has been performed up to a maximum fluence of 2.5 mJ/cm^2 , which is the limit of the system, due to the excitation source used, described in Chapter 5 (see Fig. 8.1). However, as it was discussed in Chapter 7, InN layers have proved to support fluences higher than 100 mJ/cm^2 (above 350 GW/cm^2) optically undamaged [GJMC17], much larger than the rest of commonly used SESAMs, operating at 1550 nm . Moreover, Fig. 8.1 shows a very noticeable nonlinear change in the reflectance, which, combined with the supported high fluence, represents a clear advantage of InN over other materials proposed as saturable absorbers at telecom wavelengths, as for example GaAs-based quantum wells ($I_{sat} = 0.6 \text{ GW} / cm^2$, damage threshold at 8 GW/cm^2) [FMFK12], graphene ($I_{sat} = 0.1 - 0.5 \text{ GW} / cm^2$, damage threshold at 2 GW/cm^2) [SHTP10],[ZTKZ10], or carbon nanotubes ($I_{sat} = 0.05 \text{ GW} / cm^2$, damage threshold at 50 KW/cm^2) [SYTJ04], [PSHC12].

A commercial InGaAs-based SESAM has been used for comparison with the results obtained from our developed SESAM. Particularly, it is the SAM-1550-55-2ps-x from BATOP Optoelectronics, which consists of a bulk InGaAs-based thin layer on DBR mirror [Bato00]. The optical linear reflectance has been provided by the manufacturer and is represented in Fig. 8.2(a). It can

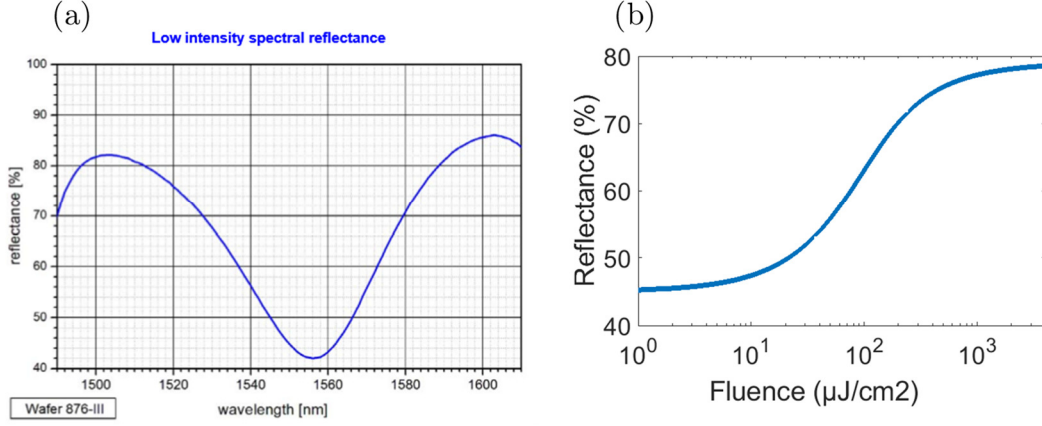


Fig. 8.2: For the commercial InGaAs-based SESAM: (a) Linear reflectance, measured at low intensity incident beam. (b) Simulation of the reflectance as a function of the fluence impinging the structure.

be observed that a minimum of reflectance appears at approximately 1550 nm, where linear reflectance between 40 - 45 % is found. It has not been possible to measure correctly the SESAM nonlinear parameters experimentally, since the active layer presents a strong dependence on the polarization, which hinders the use of the setup for SESAM characterization described in Chapter 5. Thus, the data have been directly obtained from the data sheet provided by the company. Following this data sheet, the expected nonlinear behavior has been simulated. Particularly, the following data have been provided from the company: a saturation fluence of $F_{sat} = 40 \mu J / cm^2$, which is near 5 times lower than the InN-based SESAM, and a damage threshold of 1 mJ/cm², much lower than our device. The material exhibits a relaxation time of ~ 2 ps. The linear absorbance is $A_{lin} = 55\%$ and the non-saturable loss in absorption is $A_{ns} = 21\%$. According to the manufacturer, the transmittance of the device can be neglected. Thus, the reflectance of the SESAM can be estimated as:

$$R = 1 - A \quad (8.1)$$

By doing this, the linear and non-saturable reflectances have been estimated, finding that $R_{lin} = 45\%$ and $R_{ns} = 79\%$, respectively. From, these values, a

modulation depth of $\Delta R = 34\%$ has been estimated. Using these estimated coefficients, the graph presenting the nonlinear change in reflectance as a function of the incident fluence has been simulated and represented in Fig. 8.2(b). It should be noted that this simulation does not take into account the effect of reverse saturation absorption, since the manufacturer did not provide this nonlinear coefficient, so it has not been possible to simulate this effect in the figure, but it should be taken into account when a regime of high incident fluences is reached. This fact could probably lead to a reduction of the efficient modulation depth.

8.2 Ultrafast fiber laser using InN-based SESAM

Once the InN-based SESAM has been optically characterized, it has been introduced within a fiber ring laser cavity, similarly to the lasers developed in Chapter 7. The main difference is the introduction of a fiber circulator.

The developed laser cavity is shown in Fig. 8.3. It comprises a fiber resonator where an EDFA (operating at fixed pump power) acts as the gain medium. The

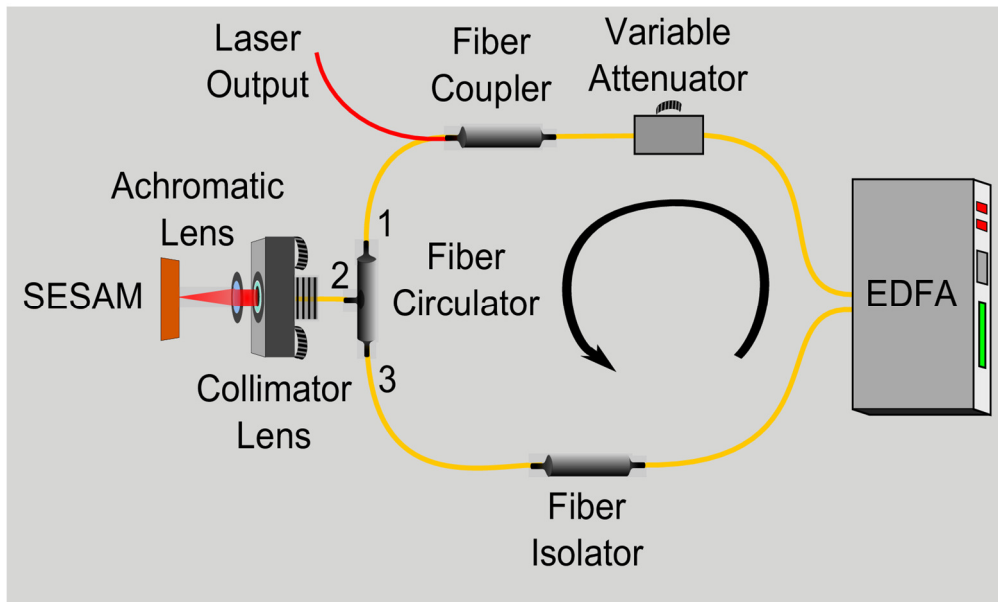


Fig. 8.3: Scheme of the 1.5 μm ultrafast mode-locked laser using InN based SESAM. The black arrow denotes the direction of the light travelling along the cavity. [JMGN18]

Er-doped fiber shows normal group velocity dispersion ($GVD_{EDF} = 0.016 ps^2 / m$), whereas the rest of the components use standard single-mode fiber (SMF) with $GVD_{SMF} = -0.021 ps^2 / m$. The total length of the laser is approximately 40 m, including 16 m of Er-doped fiber. Thus, the laser has an estimated dispersion of $\sim -0.25 ps^2$, which means that it operates in the regime of anomalous dispersion. A fiber coupler is placed after the EDFA to deliver part of the light as the laser output. Different fiber couplers have been used in this study. A 90/10 fiber coupler has been used to study the different operation regimes of the laser and to compare with the laser that used the S1 structure in transmission. In addition, a 70/30 and a 50/50 fiber coupler have been used to obtain the best performance of the laser in terms of peak power and pulse energy. For the 90/10 and the 70/30 couplers, a variable optical attenuator has been placed between the EDFA and the fiber coupler, to control the average power in the resonator (see Fig. 8.3). A fiber circulator is connected to a free space optical system, formed by a collimator lens, a 3-cm-focal achromatic lens and the SESAM. This free space system allows not only to focus the beam on the SESAM but also collecting again the back-reflection from this device (see Fig. 8.3).

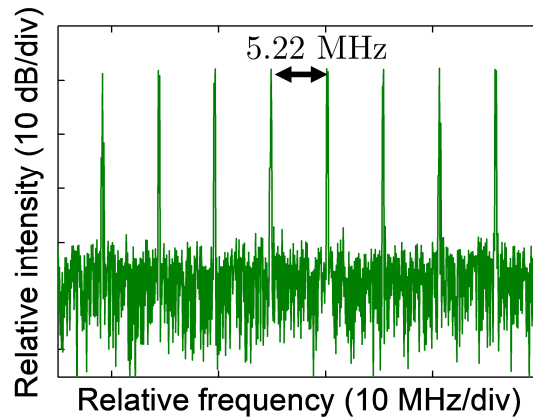


Fig. 8.4: Frequency-domain spectrum of the ultrafast InN-based fiber laser. [JMGN18]

When the EDFA pumping is switched on, the laser delivers a stable train of ultrashort pulses in self-starting operation, if the power impinging the SESAM is above a certain threshold. Fig. 8.4 shows part of the electrical spectrum of the laser. The separation between consecutive pulses is 5.22 MHz. in good agreement with the cavity length. The Resolution-Bandwidth of the measurement was 50 kHz, with 1001 data points and an attenuation of 10 dB.

8.2.1 Laser characterization using 90/10 fiber coupler

The laser performance has been firstly analyzed using a 90/10 fiber coupler, to allow the comparison with the results presented in Chapter 7 for the S1 saturable absorber in transmission configuration. A variable attenuator has been used to introduce a controlled loss in the cavity, in order to characterize the changes of the laser output as a function of the power inside the cavity. The laser output has been characterized from the 10 % branch of the fiber coupler, using the scheme that was introduced in Chapter 5. Fig. 8.5 depicts the experimental results obtained for the different operation modes of the laser. Particularly, Fig. 8.5(a) shows the typical spectra for each operation regime, from continuous wave and the transition range where both, CW and mode-locking coexist, to conventional mode-locking operation of the laser. The laser evolves from CW to mode-locking when increasing the average power circulating in the resonator. Fig. 8.5(b) depicts the evolution of the peak power as a function of the average output power for both the SESAM (black circles) and the SA in transmission configuration (blue squares). The three different operation regimes are observed in both laser configurations but are characterized by different onset values of average output power. Hollow symbols represent the CW and transition range regimes. Among them, the continuous wave symbols present no peak power, since no pulses are emitted. Full symbols represent the mode-locked regime. The laser using the

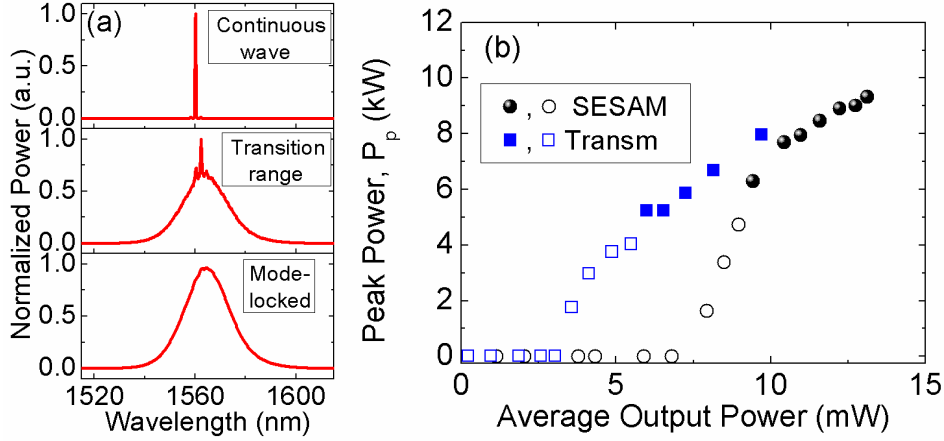


Fig. 8.5: Experimental results of the laser presented in Fig. 8.3 including a fiber attenuator, for a 90/10 fiber coupler: (a) Representation of the typical normalized linear spectra centered at 1565 nm, with 100 nm span for each operation regime (CW, transition range and ML). (a) Peak power calculated as a function of the output power for the 90/10 fiber coupler. Black circles represent the results for the SESAM-based laser, and blue squares for the laser using SA in transmission. For each laser results, the empty marker denotes both the CW measurements and the transition range, while filled markers represent the ML results.

SESAM configuration leads to higher average output power, and thus higher peak power, than the laser in transmission configuration. This feature can be attributed on one hand, to the reduction of the saturation fluence and on the other hand, to the better alignment required for using the SESAM in the resonator. The laser with SESAM shows continuous wave operation up to $P_{out} = 7.9mW$. For values above this threshold, the laser enters the transition range, and reaches the mode-locking regime, above $P_{out} = 9.4mW$. The maximum output average power the laser can deliver using the 90/10 fiber coupler is $P_{out} = 13.1mW$ (corresponding to a peak power of $P_p = 9.3kW$). In the mode-locked regime, pulse width ranges between $\Delta\tau = (258 - 271) \pm 6fs$, as shown in left axis of Fig. 8.6, which has been estimated from the autocorrelator traces and considering a Gaussian fit. The spectral width oscillates between $\Delta\lambda = (21.4 - 21.5) \pm 0.5nm$, whereas all the spectra are centered at $\lambda_c = 1565nm$. These values do not experiment major changes as a function of the output average power, meaning that the variation

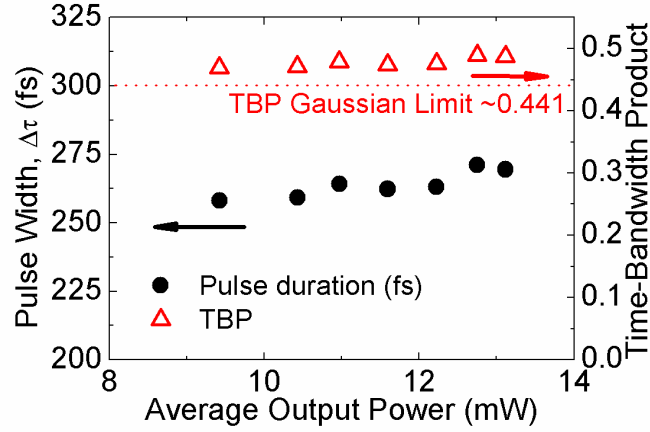


Fig. 8.6: Results for the SESAM-based laser, namely the variation of the pulse duration (black squares, left axis) and time-bandwidth product (red triangles, right axis) as a function of the output average laser power in mode-locking range. [JMGN18]

observed using the 90/10 fiber coupler for both, the peak power (7.0 kW to 9.3 kW) [represented in Fig. 8.5(b)] and pulse energy (1.8 nJ to 2.5 nJ), can be mainly attributed to variations of the average power inside the cavity. The right axis of Fig. 8.6 shows the TBP for the analyzed cases in the mode-locking regime. Fig. 8.6 confirms the high stability of the output pulses as a function of the output average power. At the same time, the pulses are close to the transform-limited situation, which for Gaussian pulses is ~ 0.441 . In this case, the TBP oscillates between 0.47-0.49. This feature implies that the pulses might present some chirp,

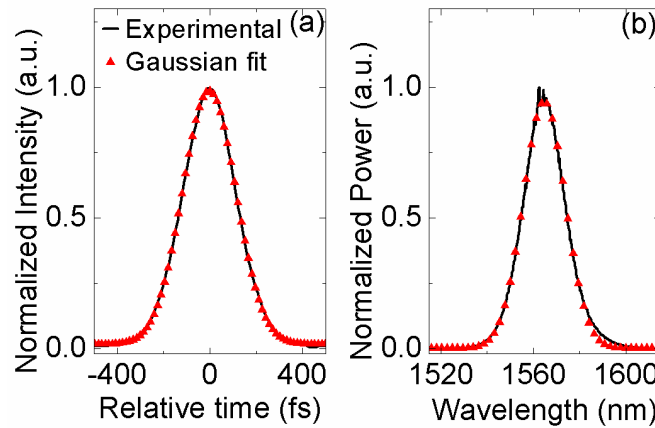


Fig. 8.7: Experimental measurements (black squares) and fits (red lines) when using a 90/10 fiber coupler for output pulses presenting: (a) Autocorrelator trace and (b) optical linear spectrum. [JMGN18]

which could probably be reduced by means of pulse de-chirping correction methods resulting in a further shortening of the time duration. Nevertheless, this pulse reshaping is beyond the objectives of this thesis

Fig. 8.7 shows the typical autocorrelator trace and spectrum for the conditions of minimum attenuation ($P_{out} = 13.1mW$), previously presented in Fig. 8.5(b). The experimental curves obtained have been fit to a Gaussian function. Both, the measured autocorrelator traces and spectra for all the experimental data in the mode-locking range present very similar shape. For the particular case presented in the figure, a time width of $\Delta\tau = 270 \pm 6fs$ was obtained. The spectrum shown in Fig. 8.7(b) has a FWHM of $\Delta\lambda = 21.4 \pm 0.5nm$.

The laser properties have also been studied with two other fiber couplers, namely 70/30 and a 50/50, meaning 30% and 50% of power driven to the output of the laser, respectively, as it will be shown afterwards.

8.2.2 Laser characterization using 70/30 fiber coupler

For the configuration with a 70/30 coupler, the variable attenuator has been maintained in the resonator. Fig. 8.8 shows the relation between the output peak power and average power, whereas the data have been obtained varying the attenuation in the resonator. As it occurred in the laser fabricated with sample S2 (see Chapter 7), the transition range has been reduced and only two operation regimes have been clearly observed: the continuous wave and the mode-locked. The discussion about this feature will be given below. The threshold output average power between the operation modes observed was found in $P_{out} = 21mW$ ($P_p = 18kW$), whereas the maximum output average power the laser can deliver with this fiber coupler is $P_{out} = 26.5mW$ ($P_p = 22.2kW$) [see Fig. 8.8(a)]. The insets of Fig. 8.8(a) show the typical spectra measured for each operation regime.

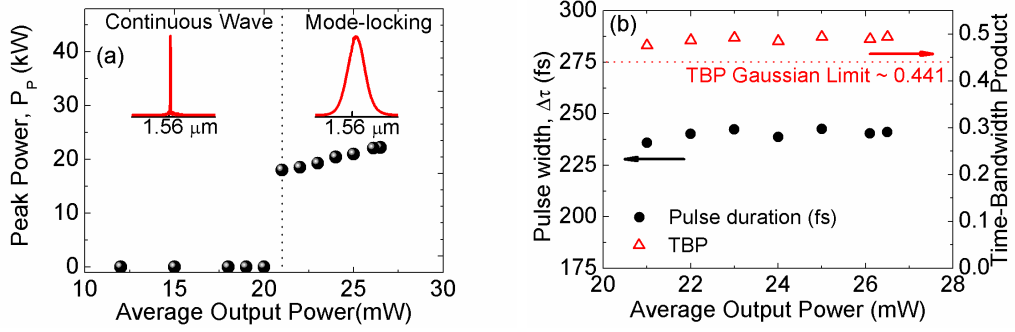


Fig. 8.8: Experimental results of the laser using a 70/30 fiber coupler: (a) Peak power as a function of average output power. Insets show normalized linear spectra centered at $1.56 \mu\text{m}$ with 100 nm span for each operation regime. (b) Variation of the pulse duration (black squares, left axis) and time-bandwidth product (red triangles, right axis) as a function of the output average laser power in mode-locking range. [JMGN18]

The FWHM estimated time widths ranged from $\Delta\tau = 235 \pm 6 \text{ fs}$ to $\Delta\tau = 245 \pm 6 \text{ fs}$. The spectral width ranges between $\Delta\lambda = 24.2 \pm 0.5 \text{ nm}$ and $\Delta\lambda = 24.6 \pm 0.5 \text{ nm}$, while all the spectra are centered at $\lambda_c = 1565 \text{ nm}$. From these values, the peak power and pulse energies vary from 18 kW to 22.2 kW, and 4 nJ to 5 nJ, respectively. Fig. 8.8(b) depicts the TBP of the laser output as a function of the average output power which, similarly to the previous case presented, it oscillates between 0.47-0.49, finding very similar values to the case of the 90/10 fiber coupler.

Fig. 8.9 compares the spectra of the laser using the sample S1 in transmission (black line) and the developed SESAM (red line). Both spectra have been taken using a 70/30 fiber coupler and at maximum possible average output power of the system (with minimum attenuation introduced by the variable attenuator placed inside the cavity). The laser using the SESAM presents a wide spectrum, corresponding to a stable mode-locking regime, while the laser using the SA in transmission is still in the transition range and no stable pulse generation can be observed. Similarly to the discussion in Chapter 7, this situation can be explained

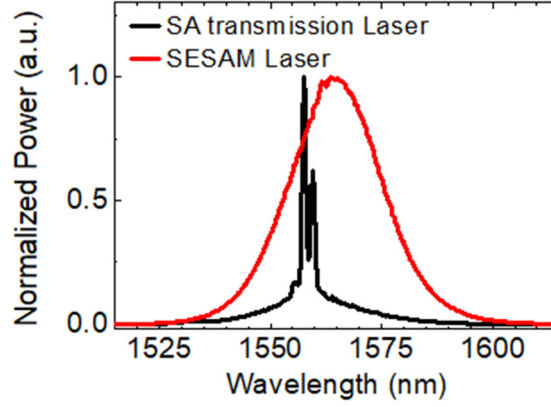


Fig. 8.9: Spectra comparison at maximum possible average power using 70/30 fiber coupler for the laser using SESAM and with the SA in transmission. [JMGN18]

in terms of an increase of the product $\alpha_0 L$, as it will be discussed at the end of section 8.2.3.

8.2.3 Laser characterization using 50/50 fiber coupler

The maximum peak power achievable by this laser oscillator using the same commercial EDFA has been explored using a 50/50 fiber coupler. With the amplifier used along this work, this is the best coupling relation for maximizing the average output power in the laser presented, since no stable mode-locked was achieved using a 40/60, and only the transition range was observed. For the case that is presented in this section, the fiber attenuator has been removed, leading to an increase of the repetition rate, up to 5.5 MHz (reduction of the cavity length of ~ 2 m). Under this configuration, a maximum average output power of $P_{out} = 55.5 mW$ was achieved. Fig. 8.10 shows the measured autocorrelator trace [Fig. 8.10(a)] and the spectrum [Fig. 8.10(b)] with the Gaussian fit for each curve. A pulse width of $\Delta\tau = 241 \pm 6 fs$ and spectral width of $\Delta\lambda = 25.0 \pm 0.5 nm$ (TBP=0.50) have been calculated, leading to a value of peak power as high as $P_p = 42 kW$ and a pulse energy of $E_p = 10 nJ$. For a better comparison between the transmission and reflection configurations, Fig. 8.10(b) additionally depicts

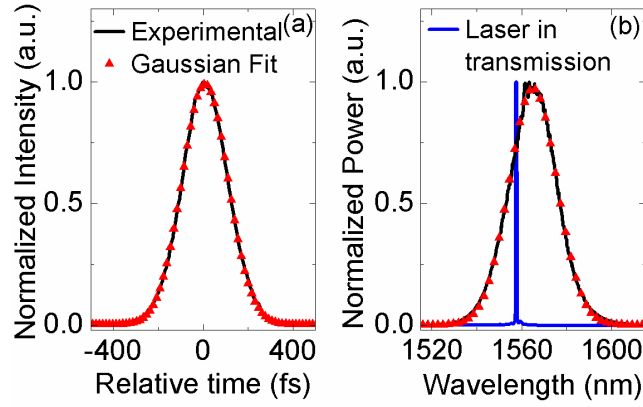


Fig. 8.10: Experimental measurements (black squares) and fits (red lines) when using a 50/50 fiber coupler presenting: (a) Autocorrelator trace and (b) optical linear spectrum. The spectrum at maximum average power for the laser in transmission using the same fiber coupler is represented in blue line. [JMG18]

the measured spectrum for the laser using the saturable absorber S1 in transmission with a 50/50 fiber coupler at the maximum possible average power (blue line). Under this situation, the laser in transmission configuration can only operate in continuous wave regime, while the SESAM configuration yields the highest possible output peak power, with no major modification in the pulse duration over the 90/10 or 70/30 configuration.

It must be highlighted that for the laser in transmission configuration studied in Chapter 7, no mode-locked regime has been reached using neither the 70/30 or the 50/50 fiber couplers. This feature can be explained similarly as in Chapter 7 for the discussion made for the lasers using samples S1 and S2 as saturable absorbers in transmission. The conclusion that the larger the product $\alpha_0 L$ was, the more efficient a saturable absorber became, for the achievement of stable ML was reached. This feature was attributed to the fact that the saturable absorber can eliminate more efficiently the continuous-wave component of the signal, converting the previously observed transition range into ML operation regime. In the case of the SESAM using S1, the product $\alpha_0 L$ has been doubled, compared to the same sample in transmission, since the light propagates twice through the

InN layer in one-single roundtrip and can be estimated as $(\alpha_0 L)_{S1,SESAM} \approx 2.8$. For the samples S1 and S2 in transmission, introduced in previous chapter, the following estimations were reached: $(\alpha_0 L)_{S1,Transm} \approx 1.4$ and $(\alpha_0 L)_{S2,Transm} \approx 2.0$, respectively. For this reason, it has been possible to achieve stable mode-locking regime in the laser not only using a 70/30 fiber coupler (as in the case of using S2 as SA in transmission), but also a 50/50 fiber coupler.

8.3 Ultrafast laser using commercial SESAM

An ultrafast fiber laser using the commercial GaAs-based SESAM, presented in section 8.1 has been developed, in order to compare the obtained results with the InN based SESAM laser. For this reason, the optical resonator is approximately the same that was used for the InN-based SESAM. However, due to the polarization dependence of the commercial SESAM, it has been necessary to add a polarization controller to the resonator, being the total length of the cavity around 41.5 m. This device was inserted between the circulator and the EDFA input, as it is shown in Fig. 8.11. Using typical values of GVD given in

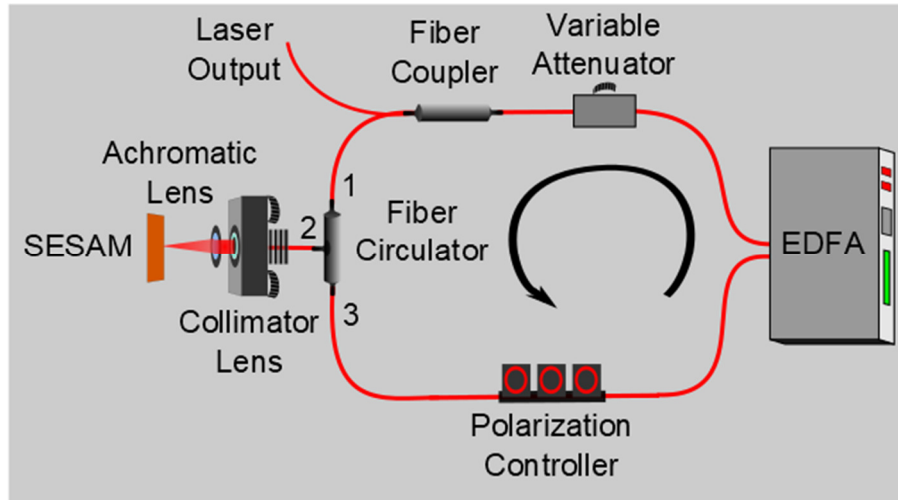


Fig. 8.11: Scheme of the 1.5 μm ultrafast mode-locked laser using commercial GaAs-based SESAM, similar to the one presented in Fig. 8.3, but including a polarization controller. The black arrow denotes the direction of the light propagation in the cavity.

previous section, the net dispersion was estimated in $\sim -0.28 \text{ ps}^2$, where 16 m correspond to EDF and 25.5 m to SMF.

For comparison with the previous laser presented, the fiber coupler used for this experiment was a 70/30, recirculating the 70% and delivering the remaining 30% as the laser output. Fig. 8.12(a) depicts the peak power as a function of the average output power for the laser using GaAs-based SESAM. The thresholds between operation regimes have been reduced, in comparison with the laser using InN-based SESAM. For instance, the CW is only observable for average output powers below 4 mW. Above this value, the laser enters in the transition range, where both CW and ML coexist. For values above $P_{out} \geq 10.5 \text{ mW}$, the laser reaches stable mode-locking operation.

Secondly, varying the polarization by means of the polarization controller, not only the fundamental soliton generated is observable, but also the 2nd harmonic, for power ranging from $P_{out} = 10.5 \text{ mW}$ to $P_{out} = 18.0 \text{ mW}$. Moreover, the 3rd harmonic is observable too, varying the polarization in the range of

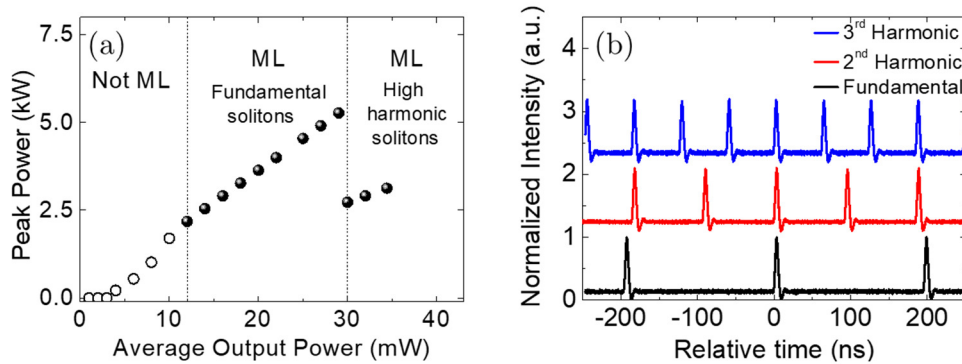


Fig. 8.12: (a) Representation of the peak power as a function of the average output power of the laser using the GaAs-based commercial SESAM. Different operation modes have been observed, namely CW and transition range (empty markers, in not ML operation), standard ML (with fundamental solitons), and ML with high-harmonic solitons circulating in the resonator (filled markers). (b) For high-output-power of $P_{out} = 28 \text{ mW}$ in the ML regime, oscilloscope traces with Y-axis-offset for observation of the fundamental soliton (black) and the 2nd and 3rd harmonics (red and blue lines, respectively).

$P_{out} = 18.0 - 30.0mW$. However, for high-powers of more than $P_{out} \geq 30.0mW$, it has not been possible to observe the first-order soliton for any polarization selected in the polarization controller. Therefore, it was only possible to achieve either the 2nd or 3rd harmonic. Fig. 8.12(b) depicts the oscilloscope curves obtained at $P_{out} = 28.0mW$. The ML operation with fundamental soliton and 2nd and 3rd harmonics have been observed experimentally by just adjusting the polarization. From the fundamental soliton curve, it has been measured that consecutive pulses are separated approximately $T_{rep} \approx 200ns$, which leads to a repetition rate of $f_{rep} \approx 5MHz$, in good agreement with the cavity length. In the higher-harmonic cases, this time separation has been estimated in $T_{rep} \approx 97ns$ and $T_{rep} \approx 65ns$ for the 2nd and 3rd harmonics, respectively.

Fig. 8.13(a) shows a typical autocorrelator trace of the laser output for operation in the mode-locking regime of fundamental solitons, at $P_{out} = 28.0mW$. From the gaussian fit performed, the pulse duration was estimated in $\Delta\tau = 1.0 \pm 0.1ps$. Moreover, the pulse width oscillates between $\Delta\tau = (0.9 - 1.1) \pm 0.1ps$ in all the ML operation regime, with no appreciable

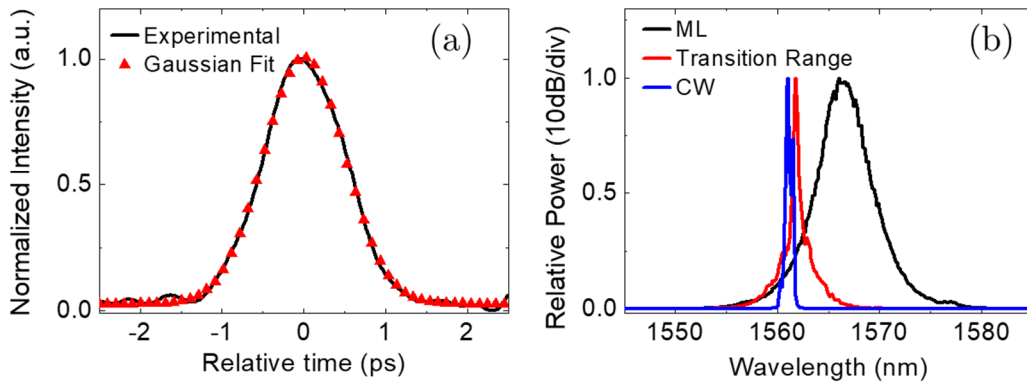


Fig. 8.13: Typical results for ultrafast fiber laser using GaAs commercial SESAM at $P_{out}=28$ mW, presenting: (a) Autocorrelator trace, and (b) optical spectrum. The figures have been obtained for particular case of minimum attenuation.

changes in shape. From these values, the peak power and pulse energy increase as a function of the output average power from $P_P(P_{out} = 11mW) = 2.2kW$ and $E_P(P_{out} = 11mW) = 2.4nJ$ to $P_P(P_{out} = 29mW) = 5.3kW$ and $E_P(P_{out} = 29mW) = 5.8nJ$, respectively. Fig. 8.13(b) represents typical spectra taken for the different operation modes of the laser, namely continuous wave (blue line, $P_{out} = 3.0mW$, transition range (red line, $P_{out} = 8.0mW$ and mode-locking (black line, $P_{out} = 28.0mW$). In general, the spectra generated in the mode-locking regime with fundamental solitons are very similar. It can be appreciated the Raman-shift towards larger wavelengths of the spectra as a function of the increasing power. In the ML regime, the spectral width, estimated from fitting the experimental data to Gaussian function, oscillated between $\Delta\lambda = 6.0 - 6.8 \pm 0.5nm$.

Fig. 8.14 shows different spectra measured for the maximum achievable power ($P_{out} = 34.4mW$), varying the polarization in the cavity by means of the

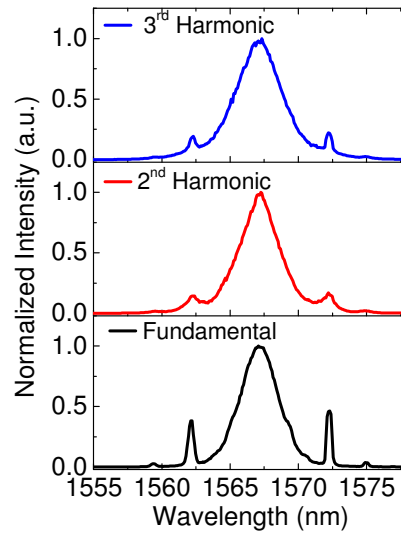


Fig. 8.14: Spectra taken at high-output power ($P_{out} = 34.4mW$) varying the polarization in the cavity. The operation with the 2nd and 3rd harmonics was stable, while operation with fundamental soliton was highly unstable.

polarization controller. For high-power conditions, Kelly side-bands appear. However, these side-bands seem to be reduced, due to the transfer of part of their energy to the new solitons generated in the case of 2nd and 3rd harmonic generated. The laser with operation of fundamental soliton was very unstable, continuously changing and lasting only few seconds in this state, leading to a more stable operation with the generation of higher harmonics. Note from Fig. 8.12(a) that both the peak power and pulse energy have been scaled according to the number of solitons generated, as a consequence of the soliton energy quantization effect.

From the experiments that have been carried out using the GaAs-based commercial SESAM, we can conclude that the operation power range is limited, even when the ML threshold has been reduced, which can be mainly attributed to the lower value of the saturation fluence and non-saturable losses of the device, in comparison with the InN-based SESAM. For instance, for $P_{out} \geq 30.0mW$, it has not been possible to achieve stable fundamental soliton (only higher harmonics), while no energy quantization effect was observed for any of the InN-based lasers presented in this thesis, not even in the cases when increasing the energy by the introduction of additional SMF to the resonator (see section 7.1.1.1).

Also, it must be pointed that, despite the company set the damage threshold of the device in 1 mJ/cm², no optical damage has been observed in the GaAs-based SESAM, even for the maximum achievable fluence impinging the device, which was ~ 8.6 mJ/cm² (an optical intensity of 9.6 GW/cm²).

8.4 Discussion

Analogously to the lasers presented in Chapter 7, the laser using the InN-based SESAM does not exhibit soliton explosion behavior, not even in the transition

range. It is believed that, in this transition state both, the ML and CW coexist simultaneously. Moreover, no soliton energy quantization effect has been observed in the laser presented. Nevertheless, the Kelly sidebands have not been observed in any of the spectra in the ML range.

Contrary to the lasers shown in Chapter 7, the solitons generated from the laser cavities presented in this chapter are better fit from a Gaussian profile than sech^2 . Nevertheless, the curves obtained experimentally are well fit by both functions, where Gaussian fittings had given an error about 0.3 % in all cases and sech^2 of approximately 0.4-0.5 %. This feature, is probably due to the changes carried out in the resonator, resulting in a cavity with larger dispersion changes, as is common in dispersion managed lasers [TuBF12].

Following the previous analysis performed using different fiber couplers, it can be stated that the developed SESAM introduces substantial advantages over the saturable absorber using same InN layer (S1) in transmission configuration. First of all, the InN-based SESAM takes advantage of all the good properties that were demonstrated and discussed in Chapter 7 for the saturable absorbers in transmission, such as conferring the laser polarization independence or to support fluences higher than 100 mJ/cm² (more than 350 GW/cm²) optically undamaged [GJMC17]. Also, the nonlinear behavior of the device has been enhanced, with reduction of the saturation fluence (from $F_{sat} = 315 \pm 31 \mu J / cm^2$ in transmission to $F_{sat} = 226 \pm 23 \mu J / cm^2$ in reflection) and rising the modulation depth (from $\Delta T = 16\%$ to $\Delta R = 25\%$). Furthermore, the product $\alpha_0 L$ has been doubled, since the light passes twice through the InN layer. As it was discussed above, this fact introduces large benefits to the efficiency of the mode-locking generation, transforming the transition range into ML regime, through the absorption of the continuous wave component. For this reason, it has been possible to fabricate the

laser placing a 50/50 fiber coupler, while for the same sample in transmission configuration only a 90/10 was able to be used. In this way, the maximum peak power and pulse energy achievable for stable mode-locking, using the same EDFA and attenuation components was $P_{P,SESAM} = 42kW$ and $E_{P,SESAM} = 10nJ$ (50/50 coupler), while in transmission the results were $P_{P,Transm} = 7.9kW$, $E_{P,Transm} = 2.0nJ$, respectively (90/10 coupler), both lasers presenting similar temporal widths. This implies over a 5-fold increase in the laser performance when using the SESAM configuration. These results are even more valuable, considering the simplicity of the SESAM fabrication, by depositing a very thin Al layer over the active region by a low-cost technique, as is sputtering.

Finally, a ring fiber laser using a commercial GaAs-based SESAM has been developed, in order to compare its performance with the results obtained using the InN-based SESAM. For this purpose, the resonator proposed has been developed using exactly the same components, with exception to the insertion of a polarization controller, in order to achieve efficiently the nonlinear effect in the commercial SESAM. This feature is a clear disadvantage upon the InN-based SESAM, since the strong polarization dependence makes the laser very sensitive to any external fluctuations in the environment, such as temperature, vibrations, etc. that could affect to the polarization. Also, the pulses generated are almost 4 times shorter in the case of InN SESAM (~ 250 fs), compared to the GaAs-based SESAM (~ 1 ps). The commercial SESAM presents a saturation fluence and non-saturable losses lower than the InN-based device. This has reduced the mode-locking threshold due to the reduction of the total losses in the system. On contrary, the commercial SESAM has demonstrated limited operation for high-powers applied to the device, being impossible to efficiently achieve the fundamental soliton, while only exhibiting higher harmonics. This feature implies the power range operation to be very limited. Regarding the laser using InN-based

SESAM, no sign of soliton energy quantization effect has been observed in any of the lasers presented in this chapter or in the lasers presented in Chapter 7. Therefore, taking into account this feature and the enormous fluences that InN layers have demonstrated to support, it is expected that, with the use of different gain media, the power range operation of InN-based ultrafast fiber lasers can be extended much further.

8.5 Conclusions

In conclusion, the first ultrafast fiber laser operating at telecom wavelengths, using InN-based SESAM has been presented. The SESAM has been developed using the bulk InN-based saturable absorber without buffer (S1), consisting in the deposition of 300 nm of Al as top layer of the structure, due mainly to its simplicity of fabrication and reproducibility. Thereby, we can expect even a better performance using more absorptive InN layers, as it was demonstrated in Chapter 7. The use of a SESAM device instead of the SA in transmission have introduced significant benefits, as for example the increase of $\alpha_0 L$ product, leading to better performances of the developed laser, but also the enhance of the nonlinear properties such as the increase of the modulation depth (up to $\Delta R \approx 25\%$) and the drop of the saturation fluence ($F_{sat} = 226 \mu J / cm^2$), compared to the structure in transmission configuration. Moreover, the device that has been presented in this chapter is much simpler than typical SESAMs which can be found in the literature, which typically not only employ complex heterostructures for the active region (MQWs; MQDs, etc.), but also complicated multilayers acting as mirrors (DBRs).

The laser delivers ultrashort pulses, with a time width of $\Delta \tau \approx 250 fs$. The repetition rate has been estimated close to 5 MHz, with maximum average power

up to 55 mW. These values lead to a maximum obtained peak power of $P_p = 42kW$ and high pulse energy of $E_p = 10nJ$. After comparing the developed laser using the InN-based SESAM with a commercial GaAs-based SESAM, several conclusions have arisen. First of all, it must be highlighted the importance of the polarization independence that InN-based structures have proved. This is a clear advantage against the majority of passive ML fiber lasers, which typically use devices as saturable absorbers and present strong polarization dependence. For this reason, the laser systems are very sensitive to any temperature alterations or vibrations in the environment, contrary to the lasers developed using InN. Furthermore, InN has proved to support enormous fluences, contrary to most of known materials proposed as SA operating at telecom wavelengths, which could be an important property for the development of ultrafast lasers delivering very high peak powers. This feature has been attributed to the excellent thermal properties of the III-nitrides semiconductors, largely discussed in previous chapters. Otherwise, despite the saturation fluence of InN in SESAM configuration has been reduced with respect to the sample in transmission configuration, it is still a larger value than the estimated for other saturable absorbers operating at the same wavelength.

Nevertheless, for the all reasons exposed, this novel InN-based SESAM can be considered as a suitable candidate to passively mode-locked high-power fiber lasers in the near infrared.

Chapter 9 General Conclusions and Future Work

This last chapter gives an overview of the conclusions obtained in each experimental chapter, while also allowing to drive some general conclusions about the topic of this thesis. In addition, this chapter provides some perspectives on what research lines of this thesis could be followed, giving also some ideas that have emerged during the development of this work.

9.1 General conclusions

9.1.1 InN-based saturable absorbers

Several InN-based structures have been evaluated along this thesis as saturable absorbers, namely two bulk InN layers (S1, S2) with different band gap energies (thus different carrier concentrations) but resonant at telecom wavelengths and three InN/In_xGa_{1-x}N MQW heterostructures (S3, S4, S5), with decreasing In mole fractions of $x = 0.9$, 0.8 and 0.7 . All the samples were fabricated by plasma-assisted molecular beam epitaxy, in a nitrogen-controlled atmosphere and in all cases the active layers were grown on a commercial GaN-on-sapphire substrate. Bulk structures have demonstrated large nonlinear absorption and

therefore are ideal SAs in the wavelength band of interest. On the contrary, the results obtained after characterizing the nonlinear optical behavior of the MQW structures demonstrate that it is still a challenge to develop efficient SAs with these heterostructures.

The two different bulk structures that have been used in this thesis present a 1- μm -thick layer of InN as active layer. However, in one of the samples (S2), a buffer layer, formed by 11 periods of InN/In_{0.7}Ga_{0.3}N MQW, was deposited between the InN layer and the substrate. It was demonstrated that this buffer layer led to the enhancement of both the linear and nonlinear absorption at 1.55 μm , with respect to the bulk InN structure without buffer (S1). This is due to the reduction of the free carrier density in the material, which leads to a band gap shift to larger wavelengths [WWLA04]. Also, the insertion of the buffer layer reduced the defects in the InN layer. As an example, the modulation depth of S1 was estimated above 15%, while over 30% was estimated for S2. Furthermore, both structures have proved enormous damage thresholds above 100 mJ/cm² [GJMC17]. This high damage threshold converts the proposed structures as promising materials for high-power applications at telecom wavelengths. This property, along with the high thermal and chemical stability of III-nitrides [Wu09] is a clear advantage upon most proposed saturable absorbers that can be found in the literature operating at the same wavelength, such as graphene, carbon nanotubes or GaAs-based structures. On the other hand, the saturation fluence of InN-based saturable absorbers seems to be larger than the appointed saturable absorbers, being something to be improved in further studies, since more energy is necessary to reach the nonlinear regime.

Concerning the MQW heterostructures proposed, all the set has proved saturable absorption effect, when being pumped at high intensities at 1.55 μm . However, not only the measured nonlinear effects were remarkably smaller than

in the bulk structures, but also the saturation fluences were extremely high (over $1\text{mJ} / \text{cm}^2$). Among the three samples proposed, only InN/In_{0.9}Ga_{0.1}N (S3) has shown a modulation depth larger than 6%. From these values obtained, it can be concluded that these samples still cannot be considered as efficient devices for mode-locking applications, which was the main purpose of this work.

9.1.2 InN-based ultrafast fiber lasers

Novel ultrafast mode-locked fiber lasers operating at 1.5 μm have been presented. The novelty of these lasers resides on the use of the developed InN-based saturable absorbers and SESAMs. It must be highlighted that the technique developed in this thesis of using III-nitrides as SA for fabricating infrared passive ultrafast mode-locking lasers has been patented [JMNG16]. Since the MQW-based devices do not attain the required nonlinear behavior, it has not been possible to fabricate mode-locked fiber lasers using these devices.

The developed lasers can be separated into two different types. On one hand, we have demonstrated passive ultrafast fiber lasers that proposed the use of saturable absorbers in transmission. On the other hand, an InN-based SESAM has been fabricated and optically characterized. The performance of the laser developed using this SESAM is compared with a similar laser but using a commercial GaAs-based SESAM.

Concerning the lasers using the InN-based SAs in transmission, the two different bulk samples, S1 and S2, have been placed within the same fiber resonator, in order to compare their performances. From this research, we can reach the following conclusions:

- Ultrashort pulses have been generated, with time widths ranging from $\Delta\tau = 220\text{fs}$ to $\Delta\tau = 250\text{fs}$, and almost transform-limited spectra, ranging around $\Delta\lambda = 15 - 22\text{nm}$. Particularly, the laser fabricated using sample

S2 demonstrated slightly shorter pulses than the one using S1. This was attributed to the larger modulation depth of this device [Haus75a].

- Both lasers have proved to be essentially polarization independent, which makes them extremely robust against temperature and mechanical fluctuations. This was attributed to the high symmetry of the wurtzite structures, which is even enhanced when being pumped along the growth direction, as it was introduced in Chapter 3.
- The time-bandwidth product remains stable in all the analyzed cases and close to the transform-limited situation.
- Despite presenting a larger saturation fluence value, the larger product of the active layer and linear absorption of the InN-based SA with buffer layer ($\alpha_0 L = 2.0$) with respect to the sample without the buffer layer ($\alpha_0 L = 1.4$) has led to a device that reaches mode-locking regime of operation more efficiently, by reducing the transition range through the absorption of the continuous wave component.
- As a result from the previous point, a 3-fold improvement on the performance of the laser using S2 with respect S1 has been demonstrated, obtaining a peak power of 26.5 kW and pulse energy of 5.8 nJ (7.95 kW and 2 nJ for sample S1). These improvements are mainly attributed to the possibility of using a 70/30 fiber coupler in the ring resonator instead of the 90/10 for sample S1. Moreover, the pulse shapes and spectra generated are very similar for both lasers.
- Very high peak power and pulse energies have been obtained, using two different approaches. On one hand, the resonator was modified, by the insertion of additional standard single-mode optical fiber (up to 200 m). This technique allowed to obtain a 5-fold increase of the output values, since the pulse properties experimented no major changes, but the repetition rate was reduced. On the other hand, the MOPA configuration of the laser was demonstrated by placing a second EDFA at the laser output, in order to seek for the maximum values that could be achieved.

Using this technique, a huge peak power value larger than 500 kW was achieved.

- From all the reasons exposed, the laser fabricated using S2 demonstrated a better performance than the one fabricated using S1. However, the easier fabrication procedure and reproducibility of S1 makes it also a very promising saturable absorber device.

The conclusions arisen from fabricated lasers using SESAMs for passive mode-locking the cavity are summarized in the following. Particularly, an InN-based SESAM has been fabricated from S1, after depositing a thin Al-layer (300 nm) on top of the InN layer. The results obtained from the laser have been compared to a laser fabricated using a commercial GaAs-based SESAM. The laser components were the same in both cases, with exception of the insertion of a polarization control system, that was necessary to efficiently observe the nonlinear absorption of the commercial SESAM. Both devices present approximately the same modulation depth. Thus, from the comparison of the laser performances, we can reach the following conclusions:

- The InN-based SESAM preserves all the good properties that were attributed to the InN material, such as the large nonlinear behavior and damage threshold or the almost polarization independency.
- Considering that the active layer is formed by a bulk InN film, while the mirror has been fabricated by the deposition of a thin Al layer, not only it is easily reproducible, but also it can be considered as one of the simplest SESAMs that can be found in the literature, where usually complicated active layers are proposed (typically heterostructures) while also using DBRs as mirrors.
- The fabrication of the InN-based SESAM not only has led to an enhancement of the nonlinear properties compared to the transmissive SA, since the effective thickness has been increased, but has also produced a rise of the product of the linear absorption times the material thickness

($\alpha_0 L = 2.8$). These features have led to a >5 -fold increase of the laser performance with respect to the laser developed using the material in transmission ($P_{peak} = 42kW; E_{pulse} = 10nJ$).

- Pulses with $\Delta\tau = 250 - 270fs$ time widths and $\Delta\lambda = 21 - 24nm$ of spectral widths have been demonstrated for the laser using the InN-based SA, much lower than the results obtained for the GaAs-based commercial SESAM using same laser configuration and amplifier, around $\Delta\tau = 1ps$ (with $\Delta\lambda = 6.0 - 6.8nm$).
- The almost total independence of the polarization of the laser using the InN-based SESAM is a clear advantage over the laser using the commercial SESAM, since not only the stability is much higher, but also it has demonstrated great ruggedness and insensibility to temperature and mechanical fluctuations, and variations of the optical fiber. Moreover, the range of power operation using the GaAs-based SESAM is very limited, with observation of soliton energy quantization effect, while this effect has not been observed in any of the InN-based lasers presented.
- As a disadvantage, the lower saturation fluence of the commercial SESAM reduces the total losses in the system, thus reducing the threshold for mode-locking operation. On the other hand, the laser using the GaAs-based SESAM has not proved to be efficient at high impinging powers, with observation of the soliton energy quantization effect. This effect has not been observed in any of the lasers using InN-based SAs (including SESAM).

In summary, we have successfully demonstrated and characterized novel ultrafast fiber lasers operating at telecom wavelengths, using InN-based devices for passively modulating the intrinsic losses within the cavity. It is the first time that InN has been used for this purpose. Yet, for all the reasons exposed, we can consider this material as a real candidate for developing high-energy and high-power ultrafast lasers at telecom wavelengths.

9.2 Future work

Two different future lines have been proposed, taking into account the results obtained along this thesis. First, the importance of seeking new bulk materials or heterostructures based on III-nitrides and the improvement of the presented ones will be discussed. Afterwards, discussion about the laser design will be made, giving alternative laser designs or resonators. By doing this, it is expected that some of the generated output pulse properties could be enhanced.

9.2.1 Saturable absorbers

InN-based SAs optimization

Despite the excellent properties the InN-based SAs have proved, such as a very high damage threshold, or almost complete polarization independence, these devices can still be further improved. Some ideas are given about the development and optimization of the structures, which can be carried out in future works. Also, other III-nitride structures are alternatively proposed:

- Reduction of the saturation fluence. This could be done by n-type doping of the InN layers. This feature could lead to a reduction of the mode-locking threshold and could possibly allow an all-fiber laser arrangement, placing the SESAM at the tip of a fiber connector [PPPP06], [ZWWB17].
- Reduction of the non-saturable losses. This goal could be achieved by eliminating the substrate. However, it is difficult to remove sapphire due to its large hardness. Nevertheless, recently some techniques are being proposed, mostly based on laser lift-off [SKST13].
- InN-based heterostructures as SA. Despite along this thesis only bulk structures have proved successful mode-locking operation, most SESAMs operating at 1.5 μm in the literature typically rely on MQW or MQD heterostructures. An in-depth study of III-nitride heterostructures could lead to a complete understanding of why the MQWs proposed in this

thesis have not exhibited the excellent results that the bulk devices have. Moreover, by implementing MQW or MQD heterostructures, the nonlinear properties of the device could be enhanced, including e.g. the saturation fluence.

9.2.2 Ultrafast fiber laser design

The lasers developed in this thesis have demonstrated excellent results. However, some aspects can be studied in more detail and other cavities can be explored, using the bulk InN-based devices. The following ideas can be explored:

- Simulation of the laser cavity. For this purpose, the dispersion of both the SMF and EDF must be measured precisely, in order to find the net average dispersion. Also, it is highly recommended to try to measure experimentally not only the autocorrelator traces, but also find both the electric field the phase of the pulses. This can be performed through techniques such as frequency-resolved optical gating [TDFS97] or multiphoton intrapulse interference phase scan [CCCH16].
- Replace the commercial EDFA used by a controlled length of pumped Er-doped fiber. By doing this, it is expected on one hand to increment the signal-to-noise ratio, since the EDFA used has a poor noise figure, and on the other hand to have better control of the total energy applied to the SA.
- Investigate long-fiber cavities. All the lasers shown in this work had proved no energy quantization effect for cavities shorter than 250 m. Therefore, a study to find the longest cavity that can be fabricated would be of great importance to the scientific community, since the SESAM that we have fabricated has proved to support enormous fluences without any sign of optical damage. This study could lead to very high peak powers and pulse energies. Moreover, this study could also lead to generation of strong nonlinearities, since some of these effects were observed when trying to increase the output laser power.

- Implementation of an all-normal dispersion fiber laser. Taking into account the high damage threshold of InN and that this type of lasers typically produces pulses with tens of ps, the power applied to the SESAM could be further increased (up to the appearance of nonlinear effects in the optical fiber). Thus, after de-chirping the generated pulses would typically lead to a pulse width of hundreds of fs and outstanding pulse energies.
- Development of ultrafast fiber lasers with very high repetition rates. This could be explored via generation of higher soliton orders, which typically appear when incrementing the total energy circulating inside the cavity [KPLJ16] or with the development of very short cavities.

List of Publications

The following publications have contributed for this doctoral dissertation

International Journals

- 1. InN-based optical waveguides developed by RF sputtering for all-optical applications at 1.55 μm .** L. Monteagudo-Lerma, F. B. Naranjo, M. Jiménez-Rodríguez, P. A. Postigo, E. Barrios, P. Corredera and M. González-Herráez. *IEEE Photonics Technology Letters*, 27, 2015.
- 2. III-nitride-based waveguides for ultrafast all-optical signal processing at 1.55 μm .** L. Monteagudo-Lerma, F. B. Naranjo, S. Valdueza-Felip, M. Jimenez-Rodríguez, E. Monroy, P. A. Postigo, P. Corredera and M. Gonzalez-Herráez. *Phys. Status Solidi A*, 213(5), 2015.
- 3. Effect of doping on the far-infrared intersubband transitions in nonpolar m-plane GaN/AlGaIn heterostructures.** C. B. Lim, A. Ajay, C. Bougerol, J. Lähnemann, F. Donatini, J. Schörmann, E. Bellet-Amalric, D. A. Browne, M. Jiménez-Rodríguez and E. Monroy. *Nanotechnology* 27(14), 2016.
- 4. P-i-n InGaIn homojunctions (10–40% In) synthesized by plasma-assisted molecular beam epitaxy with extended photoresponse to 600 nm.** S. Valdueza-Felip, A. Ajay, L. Redaelli, M.P. Chauvat, P. Ruterana, T. Cremel,

- M. Jiménez-Rodríguez, K. Kheng and E. Monroy. *Solar Energy Materials & Solar Cells*, 160, 2017.
5. **Ge doping of GaN beyond the Mott transition.** A. Ajay, J. Schörmann, M. Jiménez-Rodríguez, C. B. Lim, F. Walther, M. Rohnke, I. Mouton, L. Amichi, C. Bougerol and M. I. Den Hertog. *Journal of Physics D: Applied Physics*, 49(14), 2016.
 6. **Development of AlInN photoconductors deposited by sputtering.** A. Núñez Cascajero, M. Jiménez-Rodríguez, E. Monroy, M. González-Herráez and F. B. Naranjo. *Physica Status Solidi (A) Applied Research*, 214(9), 2017.
 7. **Widely power-tunable polarization-independent ultrafast mode-locked fiber laser using bulk InN as saturable absorber.** M. Jiménez-Rodríguez, L. Monteagudo-Lerma, E. Monroy, M. González-Herráez and F. B. Naranjo. *Optics Express*, 25(5), 2017.
 8. **A New Ultrafast and High Peak Power Fiber Laser operating at 1.5 μm using InN as Saturable Absorber.** M. Jiménez-Rodríguez, L. Monteagudo-Lerma, E. Monroy, F. B. Naranjo and M. González-Herráez. *Proceedings Optical Fiber Communication Conference (W1F.4)*, 2017.
 9. **Ultrafast Fiber Laser using InN as Saturable Absorber Mirror.** M. Jiménez-Rodríguez, E. Monroy, M. González-Herráez and F. B. Naranjo. *Journal of Lightwave Technology*, 36(11), 2018.
 10. **Effect of the residual doping on the performance of InN epilayers as saturable absorbers for ultrafast fiber lasers at 1.55 μm .** M. Jiménez-Rodríguez, L. Monroy, E. Monroy, M. González-Herráez and F. B. Naranjo. *To be submitted to Applied Physics Letters*, 2018.

National Book Chapters

1. **Estudio y aplicaciones de láseres de pulsos ultracortos basados en anclaje de modos.** M. Jiménez Rodríguez, A. Núñez-Cascajero; L. Monteagudo-Lerma; F. B. Naranjo and M. González-Herráez. *Quintas Jornadas de Jóvenes Investigadores de la Universidad de Alcalá*, ISBN: 978-84-16133-98-7, 2016.
2. **Desarrollo de nitruros basados en InN para aplicaciones fotovoltaicas.** A. Núñez-Cascajero, L. Monteagudo-Lerma, M. Jiménez-Rodríguez, S. Valdueza-Felip, E. Monroy, A. Ruiz, M. González-Herráez and F. B. Naranjo. *Quintas Jornadas de Jóvenes Investigadores de la Universidad de Alcalá*, ISBN: 978-84-16133-98-7, 2016.

Contributions to conferences

- 28 contributions to international and national conferences.

Patents

- **Láser Pulsado anclado en modos con absorbente saturable.** M. Jiménez-Rodríguez, L. Monteagudo-Lerma, F. B. Naranjo, M. González-Herráez, E. Monroy, A. Villafranca (P201600461), currently in PCT extension, 2016.

Bibliography

- [AACM07] ANANI, M. ; ABID, H. ; CHAMA, Z. ; MATHIEU, C. ; SAYEDE, A. ; KHELIFA, B.: InxGa1-xN refractive index calculations. In: *Microelectronics Journal* 38 (2007), Nr. 2 SPEC. ISS., Pages. 262–266
- [Agra01] AGRAWAL, G. P.: *Nonlinear Fiber Optics 4th Edition* : Academic Press, 2001 — ISBN 9780080479743
- [Agra90] AGRAWAL, G. P.: Effect of intrapulse stimulated Raman scattering on soliton-effect pulse compression in optical fibers. In: *Optics Letters* 15 (1990), Nr. 4, Pages. 224
- [AhLC14] AHN, H. ; LEE, M. T. ; CHANG, Y. M.: Spectral dependence of third-order nonlinear optical properties in InN. In: *Applied Physics Letters* 104 (2014), Nr. 20
- [AkSG08] AKHMEDIEV, N. ; SOTO-CRESPO, J. M. ; GRELU, PH: Roadmap to ultra-short record high-energy pulses out of laser oscillators. In: *Physics Letters, Section A: General, Atomic and Solid State Physics* 372 (2008), Pages. 3124–3128
- [Angu14] ANGULO, X.: *Ultra-Long Range Brillouin Optical Time Domain Analysis*, PhD thesis, Universidad of Alcalá, 2014
- [ANMV03] ANTOINE-VINCENT, N. ; NATALI, F. ; MIHAIOVIC, M. ; VASSON, A. ; LEYMARIE, J. ; DISSEIX, P. ; BYRNE, D. ; SEMOND, F. ; U. A.: Determination of the refractive indices of AlN, GaN, and Al[sub x]Ga[sub 1-x]N grown on (111)Si substrates. In: *Journal of Applied Physics* 93 (2003), Nr. 9, Pages. 5222
- [BaTe91] BAHAA, S. ; TEICH, M. C.: *Fundamentals of Photonics*. 5, 1991 — ISBN 0471839655
- [Bato00] BATOP: http://www.batop.de/information/SAM_infos.html.

- [BFHP62] BASS, M. ; FRANKEN, P. A. ; HILL, A. E. ; PETERS, C. W. ; WEINREICH, G.: Optical mixing. In: *Physical Review Letters* 8 (1962), Nr. 1, Pages. 18
- [BFWW62] BASS, M. ; FRANKEN, P. A. ; WARD, J. F. ; WEINREICH, G.: Optical rectification. In: *Physical Review Letters* 9 (1962), Nr. 11, Pages. 446–448
- [BHZW87] BEAUD, P. ; HODEL, W. ; ZYSSET, B. ; WEBER, H. P.: Ultrashort pulse propagation, pulse breakup, and fundamental soliton formation in a single-mode optical fiber. In: *IEEE Journal of Quantum Electronics* 23 (1987), Nr. 11, Pages. 1938–1946
- [Boyd08] BOYD, R. W.: *Nonlinear Optics* : Elsevier Inc, 2008 — ISBN 978-0-12-369470-6
- [BRIC95] BARNETT, B. C. ; RAHMAN, L. ; ISLAM, M. N. ; CHEN, Y. C. ; BHATTACHARYA, P. ; RIHA, W. ; REDDY, K. V. ; HOWE, A. T. ; U. A.: High-power erbium-doped fiber laser mode locked by a semiconductor saturable absorber. In: *Optics letters* 20 (1995), Nr. 5, Pages. 471–473
- [BSWH90] BAHAE, M. S. ; SAID, A. A. ; WEI, T. H. ; HAGAN, D. J. ; STRYLAND, E. W. VAN: Sensitive Measurements of Optical Nonlinearities Using a Single Beam. In: *IEEE Journal of Quantum Electronics* 26 (1990), Nr. 4, Pages. 760–769
- [BuTa05] BUTCHER, K. S. A. ; TANSLEY, T. L.: InN, latest development and a review of the band-gap controversy. In: *Superlattices and Microstructures* 38 (2005), Nr. 1, Pages. 1–37
- [CCCH16] COMIN, A. ; CIESIELSKI, R. ; COCA-LÓPEZ, N. ; HARTSCHUH, A.: Phase retrieval of ultrashort laser pulses using a MIIPS algorithm. In: *Optics Express* 24 (2016), Nr. 3, Pages. 2505
- [CGNK11] CABASSE, A. ; GAPONOV, D. ; NDAO, K. ; KHADOUR, A. ; OUDAR, J. L. ; MARTEL, G.: 130 mW average power, 4.6 nJ pulse energy, 10.2 ps pulse duration from an Er³⁺ fiber oscillator passively mode locked by a resonant saturable absorber mirror. In: *Optics Letters* 36 (2011), Nr. 14, Pages. 2620
- [ChFB17] CHAPARRO, D. ; FURFARO, L. ; BALLE, S.: Subpicosecond pulses in a self-starting mode-locked semiconductor-based figure-of-eight fiber laser. In: *Photonics Research* 5 (2017), Nr. 1, Pages. 37
- [ChSG11] CHOULI, S. ; SOTO-CRESPO, J. M. ; GRELU, P.: Optical spectra beyond the amplifier bandwidth limitation in dispersion-managed mode-

- locked fiber lasers. In: *Optics express* 19 (2011), Nr. 4, Pages. 2959–64
- [COMH08] CABASSE, A. ; ORTAÇ, B. ; MARTEL, G. ; HIDEUR, A. ; LIMPET, J.: Dissipative solitons in a passively mode-locked Er-doped fiber with strong normal dispersion. In: *Optics Express* 16 (2008), Nr. 23, Pages. 19322
- [Corn02] CORNING: SMF-28 Single-mode Optical Fiber. In: *Coating* (2002), Pages. 4
- [CoSo04] DEL COSO, R. ; SOLIS, J.: Relation between nonlinear refractive index and third-order susceptibility in absorbing media. In: *J. Opt. Soc.* 21 (2004), Nr. 3, Pages. 640–644
- [DeDu94] DENNIS, M. L. ; DULING, I. N.: Experimental Study of Sideband Generation in Femtosecond Fiber Lasers. In: *IEEE Journal of Quantum Electronics* 30 (1994), Nr. 6, Pages. 1469–1477
- [DiQG03] DINU, M. ; QUOCHI, F. ; GARCIA, H.: Third-order nonlinearities in silicon at telecom wavelengths. In: *Applied Physics Letters* 82 (2003), Nr. 18, Pages. 2954–2956
- [Dres01] DRESSELHAUS, M. S.: *Solid State Physics Part II - Optical Properties of Solids*, 2001
- [Duli91a] DULING III, I. N.: All-fiber ring soliton laser mode locked with a nonlinear mirror. In: *Optics Letters* 16 (1991), Nr. 8, Pages. 539–541
- [Duli91b] DULING, I.N.: Subpicosecond all-fibre erbium laser. In: *Electronics Letters* 27 (1991), Nr. 6, Pages. 544
- [Edga94] EDGAR, J. H.: *Group III Nitrides*: London, INSPEC, 1994 — ISBN 0-85296-818-3
- [FeGS02] FERMAN, M. E. ; GALVANAUSKAS, A. ; SUCHA, G.: *Ultrafast lasers - Technology and Applications*: CRC Press, 2002 — ISBN 9780824708412
- [Feli16] FELICE, D.: *A Study of a Nonlinear Schrodinger Equation for Optical Fibers*, PhD Thesis, Universita degli Studi di Firenze, 2016
- [FMFK12] FEDORYSHYN, Y. ; MA, P. ; FAIST, J. ; KASPAR, P. ; KAPPELER, R. ; BECK, M. ; HOLZMAN, J. F. ; JÄCKEL, H.: Three Operation Modes for Tb / s All-Optical Switching With Intersubband Transitions in InGaAs/AlAs/AlAsSb Quantum Wells. In: *IEEE Journal of Quantum Electronics* 48 (2012), Nr. 7, Pages. 885–890

- [FrMe49] FRANK, F. C. ; VAN DER MERWE, J. H.: One-Dimensional Dislocations. I. Static Theory. In: *Proceedings of the Royal Society A: Mathematical, Physical and Engineering Sciences* 198 (1949), Nr. 1053, Pages. 205–216
- [GJMC17] GALLAZZI, F. ; JIMENEZ-RODRIGUEZ, M. ; MONROY, E. ; CORREDERA, P. ; GONZÁLEZ-HERRÁEZ, M. ; NARANJO, F. B. ; ANIA-CASTAÑÓN, J.D.: Sub-250 fs , 650 kW Peak Power Harmonic Mode-Locked Fiber Laser with InN-based SESAM. In: *European Conference on Optical Communication (ECOC)* (2017)
- [Gonz04] GONZÁLEZ-HERRÁEZ, M.: *Desarrollo De Técnicas No Lineales Para La Medida De La Distribución Longitudinal De Dispersión Cromática En Fibras Ópticas Monomodo*, PhD Thesis, Universidad Politécnica de Madrid, 2004
- [Gord86] GORDON, J. P.: Theory of the soliton self-frequency shift. In: *Opt. Lett.* 11 (1986), Nr. 10, Pages. 662–664
- [GrAk12] GRELU, P. ; AKHMEDIEV, N.: Dissipative solitons for mode-locked lasers. In: *Nature Photonics* 6 (2012), Pages. 84–92
- [Grif99] GRIFFITHS, D. J.: *Introduction to Electrodynamics*. Upper Saddle River, New Jersey : Prentice Hall, 1999 — ISBN 0-13-805326-X
- [GSWG06] GOLDHAHN, R. ; SCHLEY, P. ; WINZER, A. T. ; GOBSCH, G. ; CIMALLA, V. ; AMBACHER, O. ; RAKEL, M. ; COBET, C. ; U. A.: Detailed analysis of the dielectric function for wurtzite InN and In-rich InAlN alloys. In: *Physica Status Solidi (A) Applications and Materials Science* 203 (2006), Nr. 1, Pages. 42–49
- [HaFP64] HARGROVE, L. E. ; FORK, R. L. ; POLLACK, M. A.: Locking of hene laser modes induced by synchronous intracavity modulation. In: *Applied Physics Letters* 5 (1964), Nr. 1, Pages. 4–5
- [HaGK04] HAIML, M. ; GRANGE, R. ; KELLER, U.: Optical characterization of semiconductor saturable absorbers. In: *Applied Physics B* 79 (2004), Nr. 3, Pages. 331–339
- [HaIT94] HAUS, H. A. ; IPPEN, E. P. ; TAMURA, K.: Additive-Pulse Modelocking in Fiber Lasers. In: *IEEE Journal of Quantum Electronics* 30 (1994), Nr. 1, Pages. 200–208
- [Hana09] HANADA, T.: *Oxide and Nitride Semiconductors* : Springer, 2009

— ISBN 978-3-540-88846-8

- [Haus00] HAUS, H. A.: Mode-locking of lasers. In: *IEEE Journal on Selected Topics in Quantum Electronics* 6 (2000), Nr. 6, Pages. 1173–1185
- [Haus75a] HAUS, H. A.: Theory of Mode Locking with a fast Saturable Absorber. In: *Journal of Applied Physics* 46 (1975), Nr. 7, Pages. 3049–3058
- [Haus75b] HAUS, H. A.: Theory of Mode Locking with a Slow Saturable Absorber. In: *IEEE JOURNAL OF QUANTUM ELECTRONICS* 11 (1975), Nr. 9, Pages. 736–746
- [Hech02] HECHT, E.: *Optics (4th ed.)* : Adison Wesley, 2002
- [Hera03] HERAS-VILA, C. D.: *Estudio de efectos ópticos no lineales en fibras monomodo. Medidas del índice de refracción no lineal*, Ph.D. Thesis, Universidad de Zaragoza, 2003
- [HOHF92] HOFER, M. ; OBER, M.H. ; HABERL, F. ; FERMAN, M.E.: Characterization of ultrashort pulse formation in passively mode-locked fiber lasers. In: *IEEE Journal of Quantum Electronics* 28 (1992), Nr. 3, Pages. 720–728
- [HTFH17] HANZARD, P. H. ; TANG, M. ; FANG, L. ; HABOUCHE, A. ; SAGNES, I. ; BACHELET, C. ; GODIN, T. ; OUDAR, J. L. ; U. A.: Dissipative Soliton Fiber Laser Mode-Locked With a Resonant InGaAs-Based Saturable Absorber Mirror. In: *IEEE Photonics Technology Letters* 29 (2017), Nr. 21, Pages. 1772–1775
- [IaWa98] IACONIS, C. ; WALMSLEY, I. A.: Spectral phase interferometry for direct electric-field reconstruction of ultrashort optical pulses. In: *Optics Letters* 23 (1998), Nr. 10, Pages. 792 — ISBN 1-55752-339-0
- [Ino77] INO, S.: Some New Techniques in Reflection High Energy Electron Diffraction (RHEED): Application to Surface Structure Studies. In: *Jpn. J. Appl. Phys.* 16 (1977), Nr. 6, Pages. 891–908
- [IpSD72] IPPEN, E. P. ; SHANK, C. V. ; DIENES, A.: Passive mode locking of the cw dye laser. In: *Applied Physics Letters* 21 (1972), Nr. 8, Pages. 348–350 — ISBN 0003-6951 VO - 21
- [Jang10] JANG, H.: *SESAM Design and Characterization*, Master Thesis, KTH Stockholm, 2010

- [JKMS97] JUNG, I. D. ; KÄRTNER, F. X. ; MATUSCHEK, N. ; SUTTER, D. H. ; MORIER-GENOUD, F. ; ZHANG, G. ; KELLER, U. ; SCHEUER, V. ; U. A.: Self-starting 6.5-fs pulses from a Ti:sapphire laser. In: *Optics Letters* 22 (1997), Nr. 13, Pages. 1009–1011
- [JMGN18] JIMÉNEZ-RODRÍGUEZ, M. ; MONROY, E. ; GONZÁLEZ-HERRÁEZ, M. ; NARANJO, F. B.: Ultrafast Fiber Laser using InN as Saturable Absorber Mirror. In: *Journal of Lightwave Technology* 36 (2018), Nr. 11, Pages. 2175–2182
- [JMMG17] JIMÉNEZ-RODRÍGUEZ, M. ; MONTEAGUDO-LERMA, L. ; MONROY, E. ; GONZÁLEZ-HERRÁEZ, M. ; NARANJO, F. B.: Widely power-tunable polarization-independent ultrafast mode-locked fiber laser using bulk InN as saturable absorber. In: *Optics Express* 25 (2017), Nr. 5, Pages. 5366
- [JMMG18] JIMÉNEZ-RODRÍGUEZ, M. ; MONROY, L. ; MONROY, E. ; GONZÁLEZ-HERRÁEZ, M. ; NARANJO, F. B.: Effect of the residual doping on the performance of InN epilayers as saturable absorbers for ultrafast fiber lasers at 1.55 μm . In: *Submitted to Appl. Phys. Lett.* (2018)
- [JMNG16] JIMENEZ-RODRIGUEZ, MARCO ; MONTEAGUDO-LERMA, LAURA ; NARANJO, FERNANDO B. ; GONZALEZ-HERRAEZ, MIGUEL ; MONROY, EVA ; VILLAFRANCA, AITOR: Laser Pulsado Anclado en Modos con Absorbente Saturable.
- [JuHa38] JUZA, R. ; HAHN, H.: Über die Kristallstrukturen von Cu_3N , GaN und InN Metallamide und Metallnitride. In: *Zeitschrift für anorganische und allgemeine Chemie* 239 (1938), Nr. 3, Pages. 282–287
- [Kais00] KAISERSLAUTERN, UNIVERSITY OF: *Molecular beam epitaxy (MBE)*.
URL <https://www.physik.uni-kl.de/hillebrands/research/methods/molecular-beam-epitaxy/>
- [Kais93] KAISER, W.: *Ultrashort laser pulses: generation and applications*. New York : Springer, 1993
- [Kell03] KELLER, U.: Recent developments in compact ultrafast lasers. In: *Nature* 424 (2003), Nr. 6950, Pages. 831–838
- [KoSn64] KOESTER, C. J. ; SNITZER, E.: Amplification in a Fiber Laser. In: *Applied Optics* 3 (1964), Nr. 10, Pages. 1182
- [KPLJ16] KOO, J. ; PARK, J. ; LEE, J. ; JHON, Y. M. ; LEE, J. H.: Femtosecond harmonic mode-locking of a fiber laser at 3.27 GHz using a bulk-like,

- MoSe₂-based saturable absorber. In: *Optics Express* 24 (2016), Nr. 10, Pages. 10575
- [KuAK98] KURTNER, F. X. ; DER AU, J. A. ; KELLER, U.: Mode-locking with slow and fast saturable absorbers - What's the difference? In: *IEEE Journal on Selected Topics in Quantum Electronics* 4 (1998), Nr. 2, Pages. 159–168
- [LaDG95] LAZARIDIS, P. ; DEBARGE, G. ; GALLION, P.: Time-bandwidth product of chirped sech(2) pulses: application to phase-amplitude-coupling factor measurement. In: *Optics letters* 20 (1995), Nr. 10, Pages. 1160–1162
- [Laho09] LAHOUCADE, L.: *Plasma-Assisted Molecular Beam Epitaxy of (11-22)-Oriented III-Nitrides*, PhD thesis, Institut Polytechnique de Grenoble, 2009
- [LCHK03] LIN, K. H. ; CHERN, G. W. ; HUANG, Y. C. ; KELLER, S. ; DENBAARS, S. P. ; SUN, C. K.: Observation of huge nonlinear absorption enhancement near exciton resonance in GaN. In: *Applied Physics Letters* 83 (2003), Nr. 15, Pages. 3087–3089
- [LFSA06] LIMPET, J. ; FABIAN, R. ; SCHREIBER, T. ; ANDREAS, T.: High-Power Ultrafast Fiber Laser Systems. In: *IEEE Journal of Selected Topics in Quantum Electronics* 12 (2006), Nr. 2, Pages. 233–244
- [LKJL14] LEE, J. ; KOO, J. ; JHON, Y. M. ; LEE, J. H.: A femtosecond pulse erbium fiber laser incorporating a saturable absorber based on bulk-structured Bi₂Te₃ topological insulator. In: *Optics express* 22 (2014), Nr. 5, Pages. 6165–73
- [LKJL15] LEE, J. ; KOO, J. ; JHON, Y. M. ; LEE, J. H.: Femtosecond harmonic mode-locking of a fiber laser based on a bulk-structured Bi₂Te₃ topological insulator. In: *Optics Express* 23 (2015), Nr. 5, Pages. 6359–6369
- [LLYH16] LIU, M. ; LUO, A. P. ; YAN, Y. R. ; HU, S. ; LIU, Y. C. ; CUI, H. ; LUO, Z. C. ; XU, W. C.: Successive soliton explosions in an ultrafast fiber laser. In: *Optics Letters* 41 (2016), Nr. 6, Pages. 1181–1184
- [LoPD04] LOZOVY, V. V. ; PASTIRK, I. ; DANTUS, M.: Multiphoton intrapulse interference IV Ultrashort laser pulse spectral phase characterization and compensation. In: *Optics Letters* 29 (2004), Nr. 7, Pages. 775–777
- [Love44] LOVE, A. E. H.: *Treatise on mathematical theory of elasticity. 4th edition*, 1944 — ISBN 9781107618091

- [Maim60] MAIMAN, T. H.: Stimulated optical radiation in Ruby. In: *Nature* 187 (1960), Nr. 4736, Pages. 493–494
- [Mart06] MARTÍN-LÓPEZ, S.: *Generación de supercontinuo en fibras ópticas monomodo con fuentes de bombeo continuo*, PhD Thesis, Universidad Complutense de Madrid, 2006
- [MCZZ10] MA, D. ; CAI, Y. ; ZHOU, C. ; ZONG, W. ; CHEN, L. ; ZHANG, Z.: 37.4 fs pulse generation in an Er: fiber laser at a 225 MHz repetition rate. In: *Optics letters* 35 (2010), Nr. 17, Pages. 2858–2860
- [MFAL12] MIRANDA, M. ; FORDELL, T. ; ARNOLD, C. ; L’HUILIER, A. ; CRESPO, H.: Simultaneous compression and characterization of ultrashort laser pulses using chirped mirrors and glass wedges. In: *Optics Express* 20 (2012), Nr. 1, Pages. 688
- [MiMo86] MITSCHKE, F. M. ; MOLLENAUER, L. F.: Discovery of the soliton self-frequency shift. In: *Optics Letters* 11 (1986), Nr. 10, Pages. 659
- [MMOS99] MARTIN, R. W. ; MIDDLETON, P. G. ; O’DONNELL, K. P. ; VAN DER STRICHT, W.: Exciton localization and the Stokes’ shift in InGaN epilayers. In: *Applied Physics Letters* 74 (1999), Nr. 2, Pages. 263–265
- [MoGo06] MOLLENAUER, L. F. ; GORDON, J. P.: *Solitons in Optical Fibers: Fundamentals and Applications* : Academic Press, 2006 — ISBN 978-0-12-504190-4
- [MONH02] MATSUOKA, T. ; OKAMOTO, H. ; NAKAO, M. ; HARIMA, H. ; KURIMOTO, E.: Optical bandgap energy of wurtzite InN. In: *Applied Physics Letters* 81 (2002), Nr. 7, Pages. 1246–1248
- [Mont15] MONTEAGUDO-LERMA, L.: *Development of III-nitride-based waveguides for application in all-optical integrated circuits at 1.55 μm* , PhD thesis, Universidad de Alcalá, 2015
- [MRBI08] MAAS, D. J. H. C. ; RUDIN, B. ; BELLANCOURT, A.-R. ; IWANIUK, D. ; MARCHESE, S. V. ; SÜDMEYER, T. ; KELLER, U.: High precision optical characterization of semiconductor saturable absorber mirrors 16971 (2008), Nr. May, Pages. 16966–16971
- [MRJP87] MEARS, R. J. ; REEKIE, L. ; JAUNCEY, I. M. ; PAYNE, D. N.: Low-noise erbium-doped fibre amplifier operating at 1.54 μm . In: *Electronics Letters* 23 (1987), Nr. 19, Pages. 1026–1028

-
- [MSPS81] MILLER, D. A. B. ; SEATON, C. T. ; PRISE, M. E. ; SMITH, S. D.: Band-gap-resonant nonlinear refraction in III-V semiconductors. In: *Physical Review Letters* 47 (1981), Nr. 3, Pages. 197–200
- [Münc09] MÜNCHEN, UNIVERSITÄT: High Resolution X-Ray Diffraction: User guide manual, Walter Schottki Institut (2009)
- [NaMY89] NAGANUMA, K. ; MOGI, K. ; YAMADA, H.: General Method for Ultrashort Light Pulse Chirp Measurement. In: *IEEE Journal of Quantum Electronics* 25 (1989), Nr. 6, Pages. 1225–1233
- [NGFS07] NARANJO, F. B. ; GONZÁLEZ-HERRÁEZ, M. ; FERNÁNDEZ, H. ; SOLIS, J. ; MONROY, E.: Third order nonlinear susceptibility of InN at near band-gap wavelengths. In: *Applied Physics Letters* 90 (2007), Nr. 9, Pages. 91903
- [NiAn06] NICHOLSON, J. W. ; ANDREJCO, M.: A polarization maintaining, dispersion managed, femtosecond figure-eight fiber laser. In: *Optics express* 14 (2006), Nr. 18, Pages. 8160–7
- [Niel06] NIELSEN, C. K.: *Mode Locked Fiber Lasers: Theoretical and Experimental Developments*, PhD Thesis, University of Aarhus, 2006
- [NKVC11] NARANJO, F. B. ; KANDASWAMY, P. K. ; VALDUEZA-FELIP, S. ; CALVO, V. ; GONZÁLEZ-HERRÁEZ, M. ; MARTÍN-LÓPEZ, S. ; CORREDERA, P. ; MÓNDEZ, J. A. ; U. A.: Nonlinear absorption of InN/InGaN multiple-quantum-well structures at optical telecommunication wavelengths. In: *Applied Physics Letters* 98 (2011), Nr. 3, Pages. 31902
- [NSCC02] NARANJO, F. B. ; SÁNCHEZ-GARCÍA, M. A. ; CALLE, F. ; CALLEJA, E. ; JENICHEN, B. ; PLOOG, K. H.: Strong localization in InGaN layers with high In content grown by molecular-beam epitaxy. In: *Applied Physics Letters* 80 (2002), Nr. 2, Pages. 231–233
- [Núñe17] NÚÑEZ-CASCAJERO, A.: *Development of Nitrides Based on InN for Sensor Applications*, PhD thesis, Universidad de Alcalá, 2017
- [Pasc08] PASCHOTTA, R.: *Field Guide to Laser Pulse Generation*. Bellingham, WA : SPIE Press, 2008
- [PeYF03] PEUMANS, P. ; YAKIMOV, A. ; FORREST, S. R.: Small molecular weight organic thin-film photodetectors and solar cells. In: *Journal of Applied Physics* 93 (2003), Nr. 7, Pages. 3693–3723
- [PFSG14] PESSOA, R. S. ; FRAGA, M. A. ; SANTOS, L. V. ; GALVAO, N. K. A.

- M. ; MACIEL, H. S. ; MASSI, M.: Plasma-assisted techniques for growing hard nanostructured coatings: An overview. In: *Anti-Abrasive Nanocoatings: Current and Future Applications*, 2014 — ISBN 9780857092175, Pages. 456–479
- [PoGG96] POLIAN, A. ; GRIMSDITCH, M. ; GRZEGORY, I.: Elastic constants of gallium nitride. In: *Journal of Applied Physics* 79 (1996), Nr. 6, Pages. 3343–3344
- [Poro97] POROWSKI, S.: Growth and properties of single crystalline GaN substrates and homoepitaxial layers. In: *Materials Science and Engineering B Solid State Materials for Advanced Technology* 44 (1997), Nr. 1–3, Pages. 407–413
- [PPPP06] POLYNKIN, P. ; POLYNKIN, A. ; PANASENKO, D. ; PEYGHAMBARIAN, N. ; MANSURIPUR, M. ; MOLONEY, J.: All-fiber passively mode-locked laser oscillator at 1.5 microm with watts-level average output power and high repetition rate. In: *Optics letters* 31 (2006), Nr. 5, Pages. 592–594
- [PSHC12] POPA, D. ; SUN, Z. ; HASAN, T. ; CHO, W. B. ; WANG, F. ; TORRISI, F. ; FERRARI, A. C.: 74-fs nanotube-mode-locked fiber laser. In: *Applied Physics Letters* 101 (2012), Nr. 15
- [SHLG00] SUN, C.K. ; HUANG, Y.-L. ; LIANG, J.-C. ; GAN, K.-G. ; KAO, F.-J. ; KELLER, S. ; MACK, M. P. ; MISHRA, U. ; U. A.: Large near resonance third order nonlinearity in GaN. In: *Optical and Quantum Electronics* 32 (2000), Nr. June 2017, Pages. 619–640
- [SHLS08] SALHI, M. ; HABOUCHA, A. ; LEBLOND, H. ; SANCHEZ, F.: Theoretical study of figure-eight all-fiber laser. In: *Physical Review A - Atomic, Molecular, and Optical Physics* 77 (2008), Nr. 3
- [SHTP10] SUN, Z. ; HASAN, T. ; TORRISI, F. ; POPA, D. ; PRIVITERA, G. ; WANG, F. ; BONACCORSO, F. ; BASKO, D. M. ; U. A.: Graphene mode-locked ultrafast laser. In: *ACS Nano*. 4, 2010, Pages. 803–810
- [SKST13] SHIMOJUKU, M. ; KOJIMA, A. ; SHIMADA, M. ; TOMIZAWA, H. ; AKIMOTO, Y. ; FURUYAMA, H.: A damage-free sapphire substrate removal process to realize highly manufacturable wafer-level white LED package (2013), Pages. 2–3
- [SLWK00] SUN, C.K. ; LIANG, J.-C. ; WANG, J.-C. ; KAO, F.-J. ; KELLER, S. ; MACK, M. P. ; MISHRA, U. ; DENBAARS, S. P.: Two-photon absorption study

- of GaN. In: *Applied Physics Letters* 76 (2000), Nr. 4, Pages. 439
- [SSLS16] SHAKYA, S. ; SUPE, A. ; LAVRINOVICA, I. ; SPOLITIS, S. ; PORINS, J.: Different optical fiber nonlinear coefficient experimental measurements. In: *2016 International Workshop on Fiber Optics in Access Network, FOAN 2016* (2016)
- [SSPS93] SOUZA, E. A. DE ; SOCCOLICH, C. E. ; PLEIBEL, W. ; STOLEN, R. H. ; SIMPSON, J. R. ; DIGIOVANNI, D. J.: Saturable absorber modelocked polarisation maintaining erbium-doped fibre laser. In: *Electronics Letters* 29 (1993), Nr. 5, Pages. 447–449
- [StKr38] STRANSKI, I. N. ; KRASTANOV, L.: Zur Theorie der orientation Ausscheidung von Ionenkristallen aufeinander. In: *Math.-Naturwiss. IIb* (1938), Nr. 146, Pages. 797
- [StMo85] STRICKLAND, D. ; MOUROU, G.: Compression of amplified chirped optical pulses. In: *Optics Communications* 56 (1985), Nr. 3, Pages. 219–221
- [Svel10] SVELTO, O.: *Principles of lasers* : Springer, 2010 — ISBN 9781441913012
- [SWNV00] S. C. JAIN ; WILLANDER, M. ; NARAYAN, J. ; VANOVERSTRAETEN, R.: III–nitrides: Growth, characterization, and properties. In: *Journal of Applied Physics* 87 (2000), Nr. 3, Pages. 965–1006
- [SYTJ04] SET, S. Y. ; YAGUCHI, H. ; TANAKA, Y. ; JABLONSKI, M.: Laser Mode Locking Using a Saturable Absorber Incorporating Carbon Nanotubes. In: *Journal of Lightwave Technology* 22 (2004), Nr. 1, Pages. 51–56
- [TaFo86] TANSLEY, T. L. ; FOLEY, C. P.: Optical band gap of indium nitride. In: *J. Appl. Phys.* 59 (1986), Nr. 9
- [TaHi92] TAMURA, K. ; HAUS, H. A. A. ; IPPEN, E. P.: Self-starting additive pulse mode-locked erbium fibre ring laser. In: *Electronics Letters* 28 (1992), Nr. 24, Pages. 2226–2228
- [Tauc68] TAUC, J.: Optical properties and electronic structure of amorphous Ge and Si. In: *Materials Research Bulletin* 3 (1968), Nr. 1, Pages. 37–46
- [TaZh07] TANG, D. Y. ; ZHAO, L. M.: Generation of 47-fs pulses directly from an erbium-doped fiber laser. In: *Optics letters* 32 (2007), Nr. 1, Pages. 41–43

- [TDFS97] TREBINO, R. ; DELONG, K. W. ; FITTINGHOFF, D. N. ; SWEETSER, J. N. ; KRUMBUGEL, M. A. ; RICHMAN, B. A. ; KANE, D. J.: Measuring ultrashort laser pulses in the time-frequency domain using frequency-resolved optical gating. In: *Review of Scientific Instruments* 68 (1997), Nr. 9, Pages. 3277–3295
- [Thév11] THÉVENAZ, L. (Hrsg.): *Advanced Fiber Optics. Concepts and Technology*. Lausanne (Switzerland) : EPFL Press, 2011 — ISBN 978-2-940222-43-8
- [TIHN93] TAMURA, K. ; IPPEN, E. P. ; HAUS, H. A. ; NELSON, L. E.: 77-Fs Pulse Generation From a Stretched-Pulse Mode-Locked All-Fiber Ring Laser. In: *Optics letters* 18 (1993), Nr. 13, Pages. 1080
- [TJIH93] TAMURA, K. ; JACOBSON, J. ; IPPEN, E. P. ; HAUS, H. A. ; FUJIMOTO, J. G.: Unidirectional Ring Resonators For Self-Starting Passively Mode-Locked Lasers. In: *Optics Letters* 18 (1993), Nr. 3, Pages. 220–222
- [Treb12] TREBINO, R.: *Frequency-resolved optical gating: the measurement of ultrashort laser pulses*. New York : Springer Science+Business Media, 2012 — ISBN 978-1-4613-5432-1
- [TuBF12] TURITSYN, S. K. ; BALE, B. G. ; FEDORUK, M. P.: Dispersion-managed solitons in fibre systems and lasers. In: *Physics Reports* 521, Elsevier B.V. (2012), Nr. 4, Pages. 135–203
- [TWLW09] TSAI, T. R. ; WU, T. H. ; LIAO, J. C. ; WEI, T. H. ; CHIANG, H. P. ; HWANG, J. S. ; TSAI, D. P. ; CHEN, Y. F.: Characterization of nonlinear absorption of InN epitaxial films with femtosecond pulsed transmission Z-scan measurements. In: *Journal of Applied Physics* 105 (2009), Nr. 6, Pages. 15–18
- [TZZL05] TANG, D. Y. ; ZHAO, L. M. ; ZHAO, B. ; LIU, A. Q.: Mechanism of multisoliton formation and soliton energy quantization in passively mode-locked fiber lasers. In: *Physical Review A - Atomic, Molecular, and Optical Physics* 72 (2005), Nr. 4
- [Vald11] VALDUEZA-FELIP, S.: *Nitride-based semiconductor nanostructures for applications in optical communications at 1.5 μ m*, PhD thesis, Universidad de Alcalá, 2011
- [Vech73] VAN VECHTEN, J. A.: Quantum Dielectric Theory of Electronegativity in Covalent Systems. III. Pressure-Temperature Phase

- Diagrams, Heats of Mixing, and Distribution Coefficients. In: *Phys. Rev. B* 7 (1973), Pages. 1479
- [Vega21] VEGARD, L.: Die Konstitution der Mischkristalle und die Raumfüllung der Atome. In: *Journal of Materials Science* 1 (1921), Pages. 79–90
- [VMMG12] VALDUEZA-FELIP, S. ; MONTEAGUDO-LERMA, L. ; MANGENEY, J. ; GONZALEZ-HERRAEZ, M. ; JULIEN, F. H. ; NARANJO, F. B.: Nonlinear absorption at optical telecommunication wavelengths of InN films deposited by RF sputtering. In: *IEEE Photonics Technology Letters* 24 (2012), Nr. 22, Pages. 1998–2000
- [VNGF08] VALDUEZA-FELIP, S. ; NARANJO, F. B. ; GONZALEZ-HERRAEZ, M. ; FERNANDEZ, H. ; SOLIS, J. ; GUILLOT, F. ; MONROY, E. ; NEVOU, L. ; U. A.: Characterization of the resonant third-order nonlinear susceptibility of Si-doped GaN-AlN quantum wells and quantum dots at 1.5 μm . In: *IEEE Photonics Technology Letters* 20 (2008), Nr. 16, Pages. 1366–1368
- [VoKP97] VOGEL, D. ; KRÜGER, P. ; POLLMANN, J.: Structural and electronic properties of group-III nitrides. In: *Physical Review B* 55 (1997), Nr. 19, Pages. 12836–12839
- [VoWe26] VOLMER, M. ; WEBER, A.: Nucleus Formation in Supersaturated Systems. In: *Z. Phys. Chem (Leipzig)* 119 (1926), Pages. 277–301
- [VRNR12] VALDUEZA-FELIP, S. ; RIGUTTI, L. ; NARANJO, F. B. ; RUTERANA, P. ; MANGENEY, J. ; JULIEN, F. H. ; GONZÁLEZ-HERRÁEZ, M. ; MONROY, E.: Carrier localization in InN/InGaN multiple-quantum wells with high In-content. In: *Applied Physics Letters* 101 (2012), Nr. 6, Pages. 1–5
- [VuMe03] VURGAFTMAN, I. ; MEYER, J. R.: Band parameters for nitrogen-containing semiconductors. In: *Journal of Applied Physics* 94 (2003), Pages. 3675–3696
- [VuMR01] VURGAFTMAN, I. ; MEYER, J. R. ; RAM-MOHAN, L. R.: Band parameters for III-V compound semiconductors and their alloys. In: *Journal of Applied Physics* 89 (2001), Nr. 11 I, Pages. 5815–5875
- [WBCF12] WILLNER, A. E. ; BYER, R. L. ; CHANG-HASNAIN, C. J. ; FORREST, S. R. ; KRESSEL, H. ; KOGELNIK, H. ; TEARNEY, G. J. ; TOWNES, C. H. ; U. A.: Optics and photonics: Key enabling technologies. In: *Proceedings of the IEEE*. 100, 2012, Pages. 1604–1643

- [Wein09] WEINER, A. M.: *Ultrafast Optics*, 2009 — ISBN 9780471415398
- [Wrig97] WRIGHT, A. F.: Elastic properties of zinc-blende and wurtzite AlN, GaN, and InN. In: *Journal of Applied Physics* 82 (1997), Nr. 6, Pages. 2833–2839
- [Wu09] WU, J.: When group-III nitrides go infrared: New properties and perspectives. In: *Journal of Applied Physics* 106 (2009), Nr. 1
- [WWLA04] WU, J. ; WALUKIEWICZ, W. ; LI, S. X. ; ARMITAGE, R. ; HO, J. C. ; WEBER, E. R. ; HALLER, E. E. ; LU, H. ; U. A.: Effects of electron concentration on the optical absorption edge of InN. In: *Applied Physics Letters* 84 (2004), Nr. 15, Pages. 2805–2807
- [WWSY03] WU, J. ; WALUKIEWICZ, W. ; SHAN, W. ; YU, K. M. ; AGER III, J. W. ; LI, S. X. ; HALLER, E. E. ; LU, H. ; U. A.: Temperature Dependence of the Fundamental Bandgap of InN. In: *Journal of Applied Physics* 94 (2003), Pages. 4457
- [WWYA02] WU, J. ; WALUKIEWICZ, W. ; YU, K. M. ; AGER, J. W. ; HALLER, E. E. ; LU, H. ; SCHAFF, W. J. ; SAITO, Y. ; U. A.: Unusual properties of the fundamental band gap of InN. In: *Applied Physics Letters* 80 (2002), Nr. 21, Pages. 3967–3969
- [YaMX14] YAMASHITA, S. ; MARTINEZ, A. ; XU, B.: Short pulse fiber lasers mode-locked by carbon nanotubes and graphene. In: *Optical Fiber Technology* 20 (2014), Nr. 6, Pages. 702–713
- [YYLJ09] YAO, W. ; YU, Z. ; LIU, Y. ; JIA, B.: Linear and nonlinear optical absorption coefficients and refractive index changes in strained GaN/AlN quantum dots. In: *Physica E: Low-Dimensional Systems and Nanostructures* 41, Elsevier (2009), Nr. 8, Pages. 1382–1385
- [ZHGS07] ZHANG, Z. Q. ; HE, W. Q. ; GU, C. M. ; SHEN, W. Z. ; OGAWA, H. ; GUO, Q. X.: Determination of the third- and fifth-order nonlinear refractive indices in InN thin films. In: *Applied Physics Letters* 91 (2007), Nr. 22, Pages. 3–5
- [ZTKZ10] ZHANG, H. ; TANG, D. ; KNIZE, R. J. ; ZHAO, L. ; BAO, Q. ; LOH, K. P.: Graphene mode locked, wavelength-tunable, dissipative soliton fiber laser. In: *Applied Physics Letters* 96 (2010), Nr. 11
- [ZWWB17] ZOU, F. ; WANG, Z. ; WANG, Z. ; BAI, Y. ; LI, Q. ; ZHOU, J.: Widely tunable all-fiber SESAM mode-locked Ytterbium laser with a linear cavity.

In: *Optics and Laser Technology* 92, Elsevier Ltd (2017), Nr. January,
Pages. 133–137